Informatics Control Measurement
in Economy and Environment Protection

2/2018

Informatyka Automatyka Pomiary

w gospodarce i ochronie środowiska

www.e-IAPGOS.pl

ISSN 2083-0157

Kwartalnik Naukowo-Technicznу

XIX International Symposium on Theoretical Electrical Engineering – ISTET 2017 (Technische Universität Ilmenau, Germany)

2/2018

kwiecień – czerwiec

Wydanie pod redakcją naukową
prof. dr hab. inż. Waldemara Wójcika

INFORMATYKA AUTOMATYKA POMIARY
W GOSPODARCE i OCHRONIE ŚRODOWISKA
Informatics Control Measurement in Economy and Environment Protection

p-ISSN 2083-0157, e-ISSN 2391-6761, www.e-iapgos.pl

INTERNATIONAL PROGRAMME COMMITTEE – RADA PROGRAMOWO-NAUKOWA

EDITORIAL BOARD – KOMITET REDAKCYJNY

EDITOR STAFF – ZESPÓŁ REDAKCYJNY

EDITORIAL OFFICE – REDAKCJA

Redakcja czasopisma
Informatyka, Automatyka, Pomiary w Gospodarce i Ochronie Środowiska
Instytut Elektroniki i Technik Informacyjnych
Politechnika Lubelska
ul. Nadbystrzycka 38A
20-618 Lublin
tel. +48 81 53 84 309
fax: +48 81 53 84 312
www.e-iapgos.pl
iapgos@pollub.pl

PUBLISHER – WYDAWCA

Politechnika Lubelska
ul. Nadbystrzycka 38D
20-618 Lublin
tel. +48 81 53 84 100
www.pollub.pl

PRINTING HOUSE – DRUKARNIA

Agencja Reklamowa TOP
87-800 Włocławek
ul. Toruńska 148
tel. +48 54 423 20 40
nakład: 100 egzemplarzy

OTHER INFORMATION – INNE INFORMACJE

Czasopismo jest indeksowane w bazach:

BazTech:	baztech.icm.edu.pl
IC Journals Master List:	www.journals.indexcopernicus.com
Google Scholar	scholar.google.pl
POL-index	pbn.nauka.gov.pl

Czasopismo znajduje się w wykazie czasopism naukowych opublikowanym w Komunikacie Ministra Nauki i Szkolnictwa Wyższego z dnia 9 grudnia 2016 r. – część B, pozycja 685 – z liczbą punktów przyznawanych za publikację równą 7.

Zasady publikowania artykułów, przygotowania tekstów, zasady etyczne, procedura recenzowania, wykazy recenzentów oraz pełne teksty artykułów dostępne są na stronie internetowej czasopisma:

www.e-iapgos.pl

W celu zwiększenia oddziaływania czasopisma w środowisku naukowym redakcja zaleca:

- w artykułach publikowanych w IAPGOS cytować artykuły z renomowanych czasopism międzynarodowych (szczególnie indeksowanych w bazach Web of Science oraz Scopus) używając oficjalnych skrótów nazw czasopism,
- w artykułach publikowanych w innych czasopismach (zwłaszcza indeksowanych w bazach Web of Science oraz Scopus) cytować prace publikowane w IAPGOS – zwłaszcza posługując się numerami DOI, np.:
Kluszczyński K. *Modelowanie – umiejętność czy sztuka?* Informatyka, Automatyka, Pomiary w Gospodarce i Ochronie Środowiska – IAPGOS, 1/2016, 4–15, DOI: 10.5604/20830157.1193833.

CONTENTS – SPIS TREŚCI

DOI: 10.5604/01.3001.0012.0695

TRANSIENT MODELING OF AC MACHINES CONSIDERING SECOND ORDER EFFECTS

Olga Korolova, Juan de la Torre Cubillo, Bernd Ponick
Leibniz Universität Hanover, Institute for Drive Systems and Power Electronics

Abstract. *In this paper, the transient simulation of AC machines considering spatial field harmonics and current displacement in rotor bars is examined. The first point of discussion is the sufficient order of the equivalent circuit of the current displacement model for its accurate co-simulation with the higher spatial field harmonics. In the second place, the problem of inversion of the inductance matrix considering the flux linkage through higher spatial harmonics is studied.*

Keywords: AC motors, transient simulation, spatial field harmonics, current displacement

MODELOWANIE STANÓW PRZEJŚCIOWYCH MASZYN PRĄDU PRZEMIENNEGO Z UWZGLĘDNIENIEM EFEKTÓW DRUGIEGO RZĘDU

Streszczenie. *W artykule przeanalizowano symulację stanów przejściowych maszyn prądu przemiennego z uwzględnieniem harmonicznych pola przestrzennego i przesunięcia prądu w prętach wirnika. Po pierwsze przeanalizowano jaki jest wystarczający rząd modelu równoważnego obwodu przesunięcia prądu dla jego dokładnej symulacji wraz z wyższymi harmonicznymi pola przestrzennego. Po drugie, badany jest problem inwersji macierzy induktancji z uwzględnieniem sprzężenia strumienia przez wyższe harmoniczne przestrzenne.*

Słowa kluczowe: maszyny prądu przemiennego, modelowanie stanów przejściowych, wyższe harmoniczne, przestrzenne przesunięcie prądu

Introduction

The work reported in this paper was performed as a part of the interdisciplinary project AMSES whose purpose is the detailed simulation of transient interactions in electromechanical energy systems consisting of mains, power electronics, electrical machines and their driven equipment or driving turbines. For the simulation, the so-called modified component connecting modeling (mCCM) [6] is used which gives an opportunity to connect subsystems describing different physical processes and construction elements using a special software interface. The advantages of this method are widely described in [7], whereas the main focus of this concept is the easy accessibility of all inner processes of the simulated system. Another task of the mCCM is to enable the order reduction of the simulated system in order to reduce the computational effort. As an intermediate step towards solving this problem, this paper focuses on the problems of simulation of different types of AC machines with mCCM for their further integration into the joint electromechanical system. In order to pursue this task, it is necessary to prepare the AC machine model for the analysis and simulation with mCCM, e.g. to bring the ordinary differential equations (ODEs) of an AC machine into a form appropriate for mCCM. This paper focuses on the study of some aspects of mathematical modeling of AC machines as well as on their numerical solution considering parasitic effects such as higher spatial field harmonics and current displacement in the rotor bars. The general approaches of the model development which base on [1–3] and [8] are described in Sec. 1. Since one of the purposes of the interdisciplinary project AMSES is to create subsystem models which are easily scalable to different modeling depths and accuracies, the AC machine models should also provide the opportunity of such scaling. Thus, the question of a reasonable order of the current displacement model for the chosen number of higher harmonics for their co-simulation will be discussed in Sec. 2. Numerical aspects of the transient simulation of AC machines with higher spatial harmonic effects only as well as the problem of adapting this model to the mCCM structure will be described in Sec. 3. The saturation is neglected and the mechanical part is simulated as one-mass system in the analysis performed.

1. Modeling of the higher spatial harmonics and the current displacement effects

The system of ODEs describing the electromagnetic subsystem of each AC machine with three phases in the stator, which is able to consider the higher spatial harmonic effects such as torque pulsations or additional losses as well as the current displacement effect, is formulated in the general form as

$$\mathbf{u} = \frac{d(\mathbf{L}(\varphi)\mathbf{i})}{dt} + \mathbf{R}\mathbf{i} = \mathbf{L}(\varphi)\frac{d\mathbf{i}}{dt} + \frac{\partial \mathbf{L}(\varphi)}{\partial \varphi}\frac{d\varphi}{dt}\mathbf{i} + \mathbf{R}\mathbf{i} \tag{1}$$

with the state space vector

$$\mathbf{i} = \left[i_{S1}, i_{S2}, i_{S3}, i_{R1}, i_{R2}, i_{R3} \ldots\right]^{\mathrm{T}} \tag{2}$$

and the input vector

$$\mathbf{u} = \left[u_{S1}, u_{S2}, u_{S3}, u_{R1}, u_{R2}, u_{R3} \ldots\right]^{\mathrm{T}} \tag{3}$$

where φ is the electrical rotor angle, $\mathbf{i}$ is the vector of currents (indexes S and R stand for stator and rotor, respectively), $\mathbf{u}$ is the vector of the applied voltages and $\mathbf{L}(\varphi)$ and $\mathbf{R}$ are the inductance and resistance matrices, respectively. The vector of currents $\mathbf{i}$ can be expressed in different coordinate frameworks, e.g. in the frequently used two-axis rotating frame (dq) [4]. However, for the modeling of higher harmonics, the stationary coordinate framework (123) is the most convenient approach. As for most numerical solvers, the differential equations need to be written in an explicit form, i.e. $d\mathbf{y}/dt = f(\mathbf{y})$ The ODEs (1) are transformed into this form as

$$\frac{d\mathbf{i}}{dt} = -\mathbf{L}^{-1}(\varphi)\left(\frac{\partial \mathbf{L}(\varphi)}{\partial \varphi}\frac{d\varphi}{dt} + \mathbf{R}\right)\mathbf{i} + \mathbf{L}^{-1}(\varphi)\mathbf{u} \tag{4}$$

The inductance matrix $\mathbf{L}(\varphi)$, considering the higher spatial harmonics produced by the magnetic asymmetries of stator and rotor and by the nonsinusoidal distribution of the mmf in the stator and rotor windings, shows the dependency of all its elements on the angle φ

$$\mathbf{L}(\varphi) = \begin{bmatrix} L_{S1,S1}(\varphi) & L_{S1,S2}(\varphi) & \ldots & L_{S1,R1}(\varphi) & L_{S1,R2}(\varphi) & \ldots \\ L_{S2,S1}(\varphi) & L_{S2,S2}(\varphi) & \ldots & L_{S2,R1}(\varphi) & L_{S2,R2}(\varphi) & \ldots \\ \ldots & \ldots & \ldots & \ldots & \ldots & \ldots \\ L_{R1,S1}(\varphi) & L_{R1,S2}(\varphi) & \ldots & L_{R1,R1}(\varphi) & L_{R1,R2}(\varphi) & \ldots \\ L_{R2,S1}(\varphi) & L_{R2,S2}(\varphi) & \ldots & L_{R2,R1}(\varphi) & L_{R2,R2}(\varphi) & \ldots \\ \ldots & \ldots & \ldots & \ldots & \ldots & \ldots \end{bmatrix} \tag{5}$$

with the inductance of the flux linkage between the phases i and j through the spatial harmonic k

$$L_{i,j}(\varphi) = \sum_{k} \hat{L}_{i,j,k} \cos(\varphi \cdot \nu_k + \alpha_{i,j,k}), \tag{6}$$

where ν_k is the order of the k-th spatial harmonic and $\alpha_{i,j,k}$ is the respective phase angle.

The equations (1)-(5) take different forms dependent on the rotor type of the considered AC machine. Thus, in case of induction machines with squirrel cage rotor or in case of synchronous machines with damper cage, solving of ODEs for each loop of the rotor cage is necessary for the correct simulation which leads to a

significant increase of the computational effort. In case of machines carrying rotor windings with slip rings such as windings of wound rotor induction machines, real measurable currents of the rotor phases are chosen as the state space variables in (2), so that the state space vector takes the form $\mathbf{i} = [i_{S1}, i_{S2}, i_{S3}, i_{R1}, i_{R2}, i_{R3}]^T$. The analysis performed in Sec. 3 is limited to this type of machines.

The results of the transient simulation according to (1)-(5) for a doubly-fed induction machine with the rated data listed in Tab. 1 synchronized by a DC voltage applied between two rotor phases at a speed of $n = 1500$ rpm with the following stationary no-load operation is shown in Fig. 1. The influence of the higher spatial harmonics can be seen both, in the rotor current and in the stator current, as oscillations with the frequencies 250 Hz and 350 Hz in the stator current and 300 Hz in the rotor current. This corresponds to the expected response of the stator current to the field spatial harmonics (-5*p*, 7*p*) produced by rotor mmf distribution and to the expected response of the rotor current to the field harmonics (-5*p*, 7*p*) produced by stator mmf distribution according to the spatial harmonic theory [3]. The oscillations of the rotor current are fairly low because the fundamental of the stator current is low due to (almost) no-load.

Table 1. Rating and dimensions of the test machine (doubly-fed induction machine)

Parameter	Value
power	2080 kW
pole pairs	2
stator frequency	50 Hz
speed	1780 rpm
voltage	690 V (Y)
current	1780 A
moment of inertia	88 kgm^2
stator outer diameter	890 mm

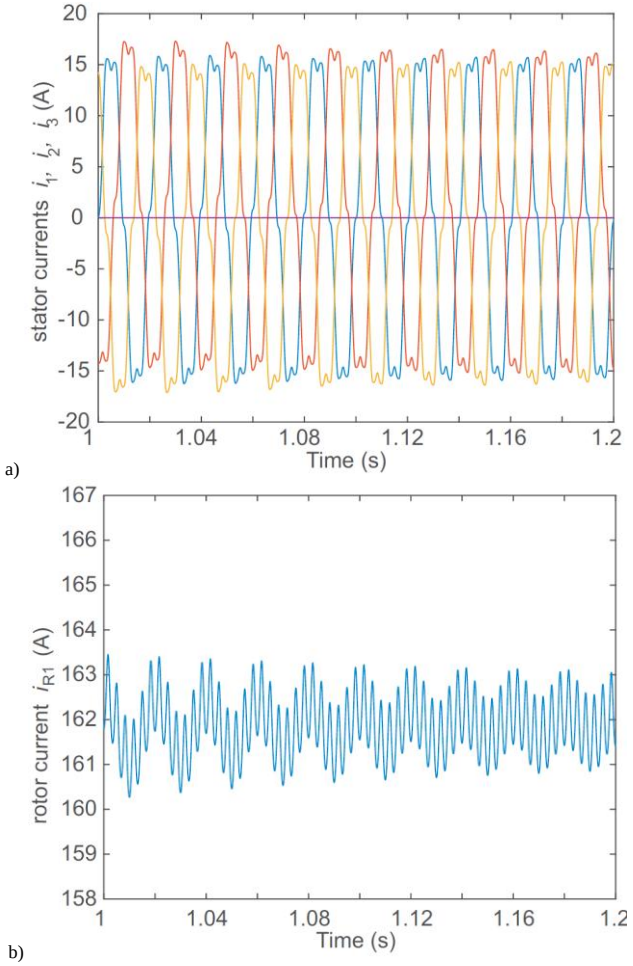

Fig. 1. Fragment of the simulation results for the synchronization process and following stationary no-load operation for the doubly-fed induction machine under consideration of higher spatial harmonics: a) stator currents i_{S1}, i_{S2} and i_{S3}, b) current of one rotor phase i_{R1}

The effect of current displacement can be most frequently observed in cage induction machines with deep bars or with double squirrel cage rotors and to some extent in damper cages of electrically excited synchronous motors in case they are designed for the direct start-up from the mains. Thus, the simulation approach concerning current displacement as well as the analysis performed in Sec. 2 are suitable for the aforementioned types of motors. The combined model for the co-simulation of the higher harmonic effect and the rotor current displacement effect is applicable directly to the wound rotor induction machines and to doubly-fed induction machines as well as to cage induction machines and synchronous machines with damper cages after extending the model with additional loop equations for the rotor cage.

In order to model the current displacement effect in the rotor bars, the equivalent circuit was used based on the discretization of the partial differential equations [3] by fragmentation of the bar geometry similarly to the approach described in [5]. The assumption is made that all rotor bars have the same geometry and that the distribution of the current density over the slot height is the same for all slots. The electromagnetic model of each rotor phase is extended with the equivalent circuit as shown in Fig. 2.

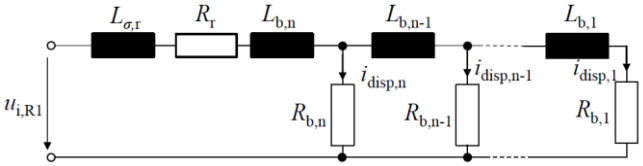

Fig. 2. Equivalent circuit for modeling of the current displacement effect in the rotor bars

The system of ODEs, describing the transient processes in this equivalent circuit for a particular rotor phase R1, if induced voltage u_i is applied as input signal, can be formulated in the matrix form as

$$\frac{d\mathbf{i}_{R1,disp}}{dt} = -\mathbf{L}_{R1,disp}^{-1}\mathbf{R}_{R1,disp}\mathbf{i}_{R1,disp} + \mathbf{L}_{R1,disp}^{-1}\mathbf{B}_{R1,disp}u_{i,R1}, \tag{7}$$

$$i_{R1,disp} = \mathbf{C}_{R1,disp}\mathbf{i}_{R1,disp}, \tag{8}$$

with

$$\mathbf{i}_{R1,disp} = \left[i_{R1,disp,1}, i_{R1,disp,2}, \ldots\right]^T, \tag{9}$$

$$\mathbf{B}_{R1,disp} = \left[0\ldots0,1\right]^T, \quad \mathbf{C}_{R1,disp} = \left[1,1.,..1\right] \tag{10}$$

$$\mathbf{L}_{R1,disp} = \begin{bmatrix} L_{b,1} & 0 & \ldots & \ldots & 0 \\ L_{b,2} & L_{b,2} & 0 & \ldots & 0 \\ \vdots & \vdots & \ddots & \ddots & \vdots \\ L_{b,n}+L_{\sigma,r} & L_{b,n}+L_{\sigma,r} & \ldots & \ldots & L_{b,n}+L_{\sigma,r} \end{bmatrix} \tag{11}$$

$$\mathbf{R}_{R1,disp} = \begin{bmatrix} R_{b,1} & -R_{b,2} & 0 & 0 & \ldots & 0 \\ 0 & R_{b,2} & -R_{b,3} & 0 & \ldots & \vdots \\ \vdots & \vdots & \ddots & \ddots & R_{b,n-1} & -R_{b,n} \\ R_r & R_r & R_r & R_r & R_r & R_{b,n}+R_r \end{bmatrix} \tag{12}$$

where $R_{b,i}$ and $L_{b,i}$ are the resistance and inductance of each fictive parallel conductor inside the rotor bar, respectively, which depend on the slot geometry and on the number of the branches of the equivalent circuit chosen, $L_{\sigma,r}$ and R_r are the leakage reactance and resistance, respectively, which are free from current displacement (e.g. a segment of the short circuit ring) and the currents $i_{R1,disp,k}$ correspond to the currents $i_{disp,k}$ from Fig. 2. In order to integrate the current displacement effect ODEs into the model (1)-(5), the components **i**, **u**, **L**(φ) and **R** are modified as

$$\mathbf{L} = \begin{bmatrix} \begin{bmatrix} L_{S1,S1} & L_{S1,S2} & \ldots. & L_{S1,fd} \\ L_{S2,S1} & L_{S2,S2} & \ldots. & L_{S2,fd} \\ \ldots & \ldots & \ldots & \ldots \\ L_{fd,S1} & L_{fd,S2} & \ldots & L_{fd,fd} \end{bmatrix} & \mathbf{L}_{non-disp,disp} \\ \mathbf{L}_{disp,non-disp} & \mathbf{L}_{disp} \end{bmatrix} \tag{13}$$

$$\mathbf{L}_{non-disp,disp} = \begin{bmatrix} L_{S1,R1} & L_{S1,R2} & \dots \\ L_{S2,R1} & L_{S2,R2} & \dots \\ \dots & \dots & \dots \\ L_{fd,R1} & L_{fd,R2} & \dots \end{bmatrix} \cdot \begin{bmatrix} \mathbf{C}_{R1,disp} & 0 & 0 & \dots \\ 0 & \mathbf{C}_{R2,disp} & 0 & \dots \\ \dots & \dots & \dots & \dots \end{bmatrix} \quad (14)$$

$$\mathbf{L}_{disp,non-disp} = \begin{bmatrix} \mathbf{B}_{R1,disp} & 0 & 0 & \dots \\ 0 & \mathbf{B}_{R2,disp} & 0 & \dots \\ \dots & \dots & \dots & \dots \end{bmatrix} \cdot \begin{bmatrix} L_{R1,S1} & L_{R1,S2} & \dots & L_{R1,fd} \\ L_{R2,S1} & L_{R2,S2} & \dots & L_{R2,fd} \\ \dots & \dots & \dots & .. \end{bmatrix} \quad (15)$$

$$\mathbf{L}_{disp} = \begin{bmatrix} \mathbf{L}_{R1,disp} & 0 & \dots & 0 \\ 0 & \mathbf{L}_{R2,disp} & \dots & 0 \\ \dots & \dots & \dots & .. \end{bmatrix} \quad (16)$$

where $\mathbf{L}_{disp,non-disp}$, $\mathbf{L}_{non-disp,disp}$ are the inductance matrices coupling the phases S1, S2... (and the field winding fd in case of electrically excited synchronous machines) and the phases R1, R2... In this paper, the coupling between the rotor bars through the leakage field is neglected but can be easily considered by adding the respective leakage mutual inductances to the matrix $\mathbf{L}_{disp}$ from (16), whereas the self-inductance of the rotor windings through the main flux should be always considered by adding the respective term to each element of the lower line of $\mathbf{L}_{disp}$. The graphics of the transient simulation obtained using the described model of current displacement for the test machine for its asynchronous start-up without higher spatial harmonic effects simulated with $n = 3$ parallel branches in the equivalent circuit of each rotor phase are shown in Fig. 3. As can be observed from the branch currents $\mathbf{i}_{disp,k}$ which correspond to the current densities inside the rotor bar starting at its bottom for $k = 1$, the current displacement effect is strong at the beginning of the start-up and disappears when reaching synchronous speed as it is expected.

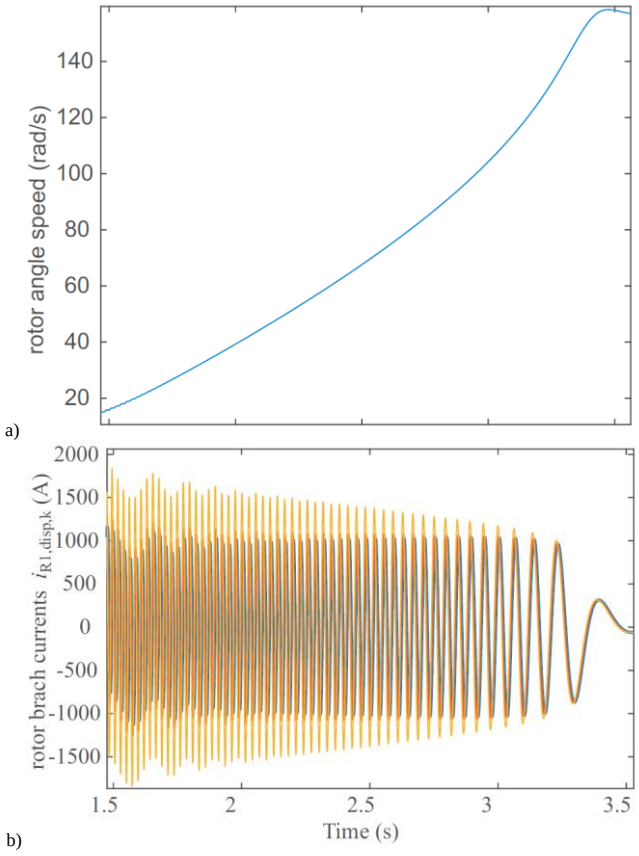

Fig. 3. Results of the simulation of the asynchronous start-up for the test machine under consideration of the current displacement effect in rotor bars: a) rotor speed, b) branch currents in the equivalent circuit for one rotor bar

2. Scaling of the current displacement model for its co-simulation with higher spatial harmonics

As shown in [8], the sufficient number of parallel branches of the equivalent circuit of the rotor (Fig. 2) for an accurate transient simulation is $n = 4$. However, this estimation is relevant for the simulation considering only the spatial fundamental. By introducing the higher spatial harmonics into the model, the voltage induced in the rotor winding in case of $f_1 = 50$ Hz and slip $s = 0$ contains the frequencies

$$f_\nu = f_1 \cdot (\frac{\omega_\nu}{\omega_1} - (1-s) \cdot \frac{\nu}{p}) = \pm 300, \pm 600, \pm 900, \dots Hz \quad (17)$$

where $\omega_\nu / \omega_1 = 1$ for all spatial harmonics produced by the stator winding. These frequencies lead to a much stronger current displacement, so that the equivalent circuit with $n = 4$ elements is not supposed to be accurate enough. The study of the number of branches of the equivalent circuit necessary for the correct simulation for different orders of the spatial harmonics is shown in this section.

As a sufficient criterion of the modeling accuracy, the current displacement factor k_r can be taken as it is shown in Fig. 4. Thus, the current density distribution $\underline{S}$ in one rectangular bar with the height $h = 25$ mm and the width $b = 5$ mm for the constant frequency of the induced voltage $f = 600$ Hz was first calculated analytically according to [3]

$$\underline{S} = \frac{j \cdot 2\pi f \mu_0 \kappa}{(1 + jb\alpha \cdot (e^{(1+j)\beta} - e^{-(1+j)\beta}))} \cdot (e^{(1+j)\alpha x} + e^{-(1+j)\alpha x}) \cdot \underline{i}, \quad (18)$$

where α and β are the factors calculated from the slot geometry [3] and κ is the electrical conductivity. The stationary simulations for the same slot geometry and frequencies were performed with (7)-(16), and the branch currents $i_{R1,disp,k}$ are compared to $|\underline{S}|$ from (18) in Fig. 4. The functions show better correspondence when a higher order of the current displacement model is used. In this case, the factors $k_{r,an}$ and $k_{r,num}$, which represent the overall current displacement factor k_r obtained analytically and numerically, show approximately the same value.

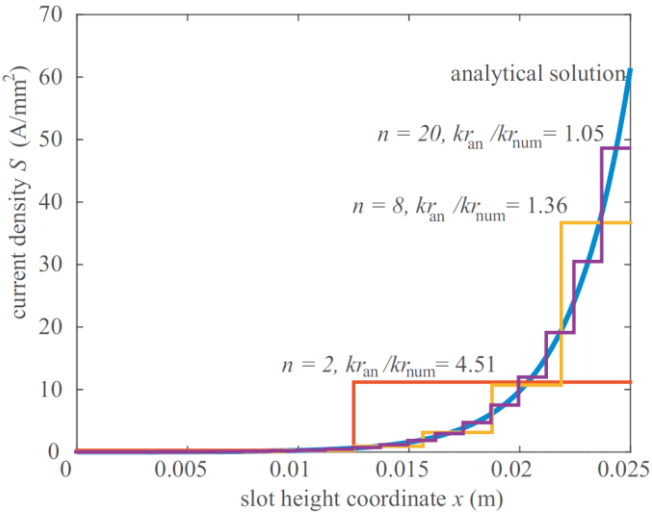

Fig. 4. Current density distribution $|\underline{S}|$ in one rotor bar

The closed-form analytical expression of the current displacement factor for one rotor bar is available for the rectangular slot as [3]

$$k_{r,rect} = \beta \cdot \frac{\sinh 2\beta + \sin 2\beta}{\cosh 2\beta - \cos \beta}. \quad (19)$$

The results of this calculation are shown in Fig. 5 for the same slot geometry as in Fig. 4. Along with the frequency of the induced voltage f, the orders of the spatial harmonics n producing these frequencies at synchronous speed are shown. The current displacement factor $k_{r,num}$ was calculated using the results of the numerical simulation according to (7)-(16) for different numbers of branches n as

$$k_{r,num} = \frac{\mathrm{Re}(\frac{U_i}{\sum I_k})}{R(f=0)}, \tag{20}$$

The numerical solution $k_{r,num}$ converges to the ideal solution $k_{r,an}$ for large values of n. Thus, approximately 25 parallel branches are required for the correct simulation (accuracy of 10% in k_r) of the rotor current response to the voltage induced by harmonics (-23p, 25p). For the lower harmonic orders (-5p, 7p), approximately 10 branches are sufficient to obtain the same accuracy. The same analysis was performed for a round bar with the diameter h = 10 mm. The results are shown in Fig. 6. Generalizing the results obtained, the following criterion for the choice of the appropriate order of the equivalent circuit n is proposed. The rough estimation of the current displacement factor $k_{r,an}$ must be performed first using analytical formulations such as (19) for the rotor induction frequency (17) of the highest simulated harmonic ν_{max}. The order n should be chosen as $n \approx 2 \cdot k_{r,an}$ for an accuracy of approximately 10% in k_r.

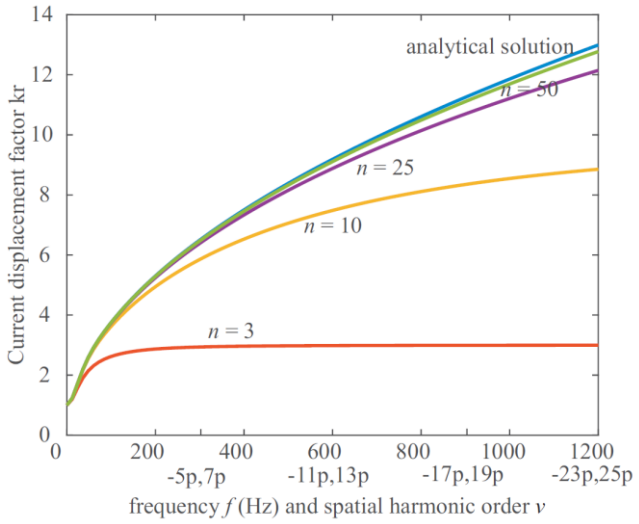

Fig. 5. Current displacement factor k_r dependent on the number of equivalent circuit order n for a rectangular bar

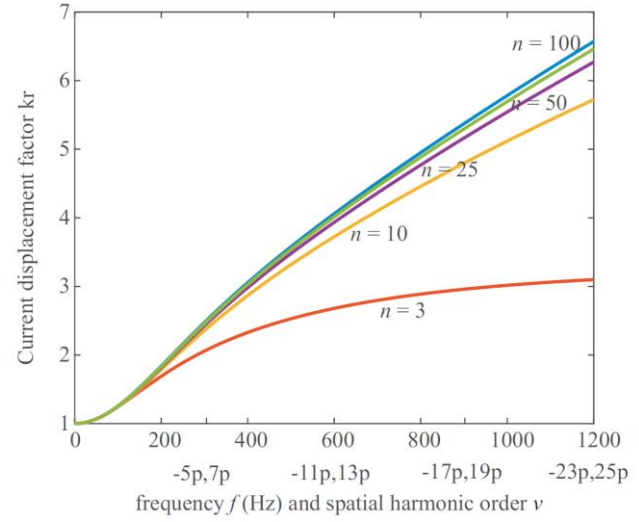

Fig. 6. Current displacement factor k_r dependent on the number of equivalent circuit order n for a round bar

3. Numerical aspects of the higher harmonics simulation

For an efficient analysis of a general AC machine with the modified component connecting modeling (mCCM), different parasitic effects should be split into subsystems for studying their interactions and possibilities of a further order reduction. Transforming the ODEs (1) with current displacement effect into this required form does not show any difficulties and was described in [7]. In order to use all advantages of mCCM for the higher harmonics, the structure of the transient model considering higher spatial harmonics, as shown in Fig. 7 (a), should be achieved. The main features of this structure are: firstly, the function $\mathbf{f}(\mathbf{u}, \mathbf{u}_{v0}, \ldots \mathbf{u}_{vk})$ does not depend on the rotor position φ and, secondly, each function $\mathbf{g}(\mathbf{i}, \nu_i\varphi, \mathbf{u})$ contains only one higher harmonic order ν_i. The direct transformation of (1) into the required form is not possible because of the product of matrices $\mathbf{L}^{-1}(\varphi)$ and $\mathbf{R}$, since each element of the inverse matrix $\mathbf{L}^{-1}(\varphi)$ contains a fraction of the sum of products of harmonic functions with different values of n in the argument.

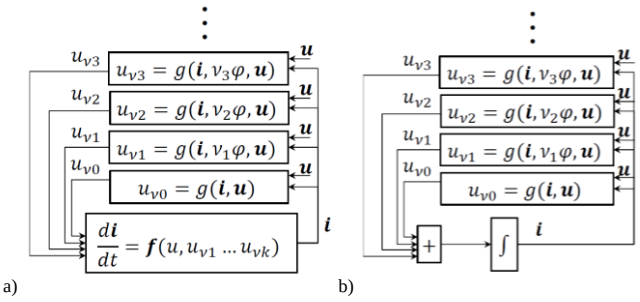

Fig. 7. MCCM structure required for the model of higher harmonics: a) general mCCM structure, b) desired mCCM structure (decoupled harmonics subsystems)

In order to transform (4) into this form, a software tool for the analytical inversion of matrix $\mathbf{L}(\varphi)$ was developed. Using the general matrix inversion rules

$$\mathbf{L}^{-1}(\varphi) = \frac{1}{\det(\mathbf{L}(\varphi))} \cdot \mathrm{adj}(\mathbf{L}(\varphi)), \tag{21}$$

where adj($\mathbf{L}(\varphi)$) is the adjugate of matrix $\mathbf{L}(\varphi)$, and subsequent trigonometrical simplifications, the inverse matrix $\mathbf{L}^{-1}(\varphi)$ is transformed into

$$\mathbf{L}^{-1}(\varphi) = \begin{bmatrix} \frac{\sum_i L_{num,1,1,i}\cos(\nu_i\varphi+\alpha_{1,1,i})}{\sum_j L_{den,j}\cos(\nu_j\varphi+\beta_j)} & \frac{\sum_i L_{num,1,2,i}\cos(\nu_i\varphi+\alpha_{1,2,i})}{\sum_j L_{den,j}\cos(\nu_j\varphi+\beta_j)} & \ldots \\ \frac{\sum_i L_{num,2,1,i}\cos(\nu_i\varphi+\alpha_{2,1,i})}{\sum_j L_{den,j}\cos(\nu_j\varphi+\beta_j)} & \frac{\sum_i L_{num,2,2,i}\cos(\nu_i\varphi+\alpha_{2,2,i})}{\sum_j L_{den,j}\cos(\nu_j\varphi+\beta_j)} & \ldots \\ \ldots & \ldots & \ldots \end{bmatrix} =$$

$$= \frac{\sum_i \mathbf{L}_{num,i}\cos(\nu_i\varphi+\boldsymbol{\alpha}_i)}{\sum_j L_{den,j}\cos(\nu_i\varphi+\beta_i)} \tag{22}$$

Each element of $\mathbf{L}^{-1}(\varphi)$ contains a finite sum of harmonic functions in numerator and denominator. Thus, the part functions $\mathbf{g}(\mathbf{i}, \nu_i\varphi, \mathbf{u})$ for the terms $\mathbf{L}^{-1}(\varphi)$ (-$\mathbf{Ri}$ + $\mathbf{u}$) from (4) can be presented as

$$\mathbf{u}_{num,i} = \mathbf{g}_{num,i}(\mathbf{u}, \mathbf{i}, \nu_i\varphi) = \mathbf{L}_{num,i}\cos(\nu_i\varphi+\boldsymbol{\alpha}_i)(-\mathbf{Ri}+\mathbf{u}) \tag{23}$$

$$u_{den,j} = g_{den,j}(\nu_j\varphi) = L_{den,j}\cos(\nu_j\varphi+\beta_j) \tag{24}$$

The function $\mathbf{f}(\mathbf{u}, \mathbf{u}_{v0}, \mathbf{u}_{v1}\ldots)$ can be expressed as

$$\mathbf{f}(\mathbf{u}, \mathbf{u}_{v0}, \mathbf{u}_{v1}\ldots) = \frac{\mathbf{u}_{num,v0} + \mathbf{u}_{num,v1} + \ldots}{u_{den,v1} + u_{den,v2} + \ldots}, \tag{25}$$

whereas it does not depend explicitly on the rotor position φ, so that the required form from Fig. 7 (a) is accomplished. The same transformation is applied to the product of the matrices $\mathbf{L}^{-1}(\varphi) \cdot \partial\mathbf{L}(\varphi)/\partial\varphi$ in order to obtain the full family of functions $\boldsymbol{g}_{num,i}$. Furthermore, the question was raised whether the elements of the inverse matrix $\mathbf{L}^{-1}(\varphi)$ are possible to be represented as a sum of harmonic functions as shown in Fig. 7 (b) without division operation in each element through the number of simplifications using the regular predictable structure of all elements of the original inductance matrix $\mathbf{L}(\varphi)$. Such simplification of the model considering first harmonic only is possible due to the mathematical feature that the determinant of the inductance matrix

$\det(\mathbf{L}(\varphi)) = const$ is independent of the value of φ. After a number of transformations performed, it was found that the form without division, as in (22), cannot be achieved, so that the structure 7(b) can be considered unattainable for a general case. The analysis of the possible simplifications for particular machines is still an object of study. As an alternative approach to the problem, the Fourier transformation method applied directly to all elements of the inverse matrix $\mathbf{L}^{-1}(\varphi)$ was implemented and tested. According to this method, the inverse matrix $\mathbf{L}^{-1}(\varphi)$ is calculated numerically for $\varphi = 0...2\pi$ with a large number of steps. The spectral analysis of each element of $\mathbf{L}^{-1}(\varphi)$ is performed with the Fourier transformation for the first n harmonics. After this operation, the inverse matrix $\mathbf{L}^{-1}(\varphi)$ can be split into the sum of matrices

$$\mathbf{L}^{-1}(\nu_1\varphi,\nu_2\varphi,\ldots) \approx \mathbf{L}_{0,inv} + \mathbf{L}_{1,inv}(\nu_{inv,1}\varphi) + \mathbf{L}_{2,inv}(\nu_{inv,2}\varphi) + \ldots \quad (26)$$

in order to estimate the impact of each higher harmonic into the system dynamics separately with $\mathbf{g}_i = \mathbf{L}_{i,inv}(\nu_{inv}\varphi)(-\mathbf{Ri} + \mathbf{u})$, as it is shown in Fig. 7 (b). The same transformation is applied to the product of the matrices $\mathbf{L}^{-1}(\varphi)\cdot\partial\mathbf{L}(\varphi)/\partial\varphi$. The model obtained in this way has shown a high sensibility to the accuracy of the Fourier transformation, and its numerical simulation always contains an error due to the truncated terms of the Fourier expansion. The simulation of the stationary operation was performed using this model structure, and the interconnection signals $\mathbf{u}_i = -\mathbf{L}_{i,inv}\mathbf{Ri}$ are exemplarily shown for orders $\nu_{inv,i} = 2p...6p$ in Fig. 8. It can be observed that the harmonics $\nu_{inv,i} = 2p, 5p, 6p...$ in the subsystem components $\mathbf{g}_2(2p\varphi)$, $\mathbf{g}_5(5p\varphi)$, $\mathbf{g}_6(6p\varphi)...$ make the strongest impact in the system dynamics.

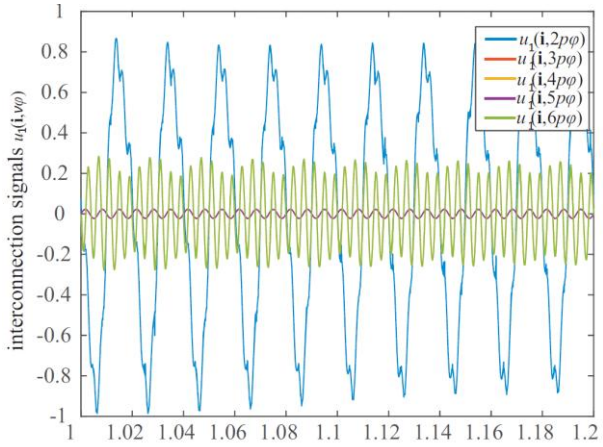

Fig. 8. Example simulation of the higher harmonic effect with the structure required for mCCM as shown in Fig. 7 (b)

4. Conclusion

In this paper, a model for transient simulations of an AC machine considering higher spatial harmonic effects and current displacement in rotor bars is developed, the differential equations for both effects being scalable to different model accuracies. The analysis of the required modeling accuracy of the current displacement effect for different numbers of spatial field harmonics is performed, and an approach for the simplified estimation is proposed. In order to achieve 10% accuracy of the current displacement factor for the harmonics of orders p, $(-5p,7p)$ and $(-23p,25p)$ 3, 10 and 25 elements of the equivalent circuit were necessary for a rectangular bar with the height $h = 25$ mm and the width $b = 5$ mm.

The transformation of the machine model considering higher spatial harmonics into the structure required for an analysis with the component connecting modeling tool was performed. Therefore, the software tool was designed in order to bring all elements of the inverse inductance matrix $\mathbf{L}^{-1}(\varphi)$ by performing analytical inversion into the form $\mathbf{L}^{-1}{}_{j,k}(\varphi) = (L_{num,j,k,1}(\nu_1\varphi) + L_{num,j,k,2}(\nu_2\varphi)\ldots)/(L_{den,1}(\nu_1\varphi) + L_{den,2}(\nu_2\varphi)...)$ in which the interconnection signals of each higher harmonic dynamics could be observed separately. As another approach to this task the approximate inversion using Fourier transformation applied to the inverse inductance matrix $\mathbf{L}^{-1}(\varphi)$ was performed in order to split the impact of higher harmonics on system dynamics into independent parallel branches by achieving the form $\mathbf{L}^{-1}(\varphi) \approx \sum_i \mathbf{L}_{i,inv}(\nu_{inv,i}\varphi)$.

References

[1] Boldea I., Nasar S.: The Induction Machine Handbook. CRC Press, Boca Raton London New York Washington D.C. 2002.
[2] Gao J., Zhang L., Wang X.: AC Machine Systems. Tsinghua University Press and Springer-Verlag, Berlin 2009.
[3] Müller G., Vogt K., Ponick B.: Calculation of Electrical Machines (in German), 6th ed. Wiley-VCH, Weinheim 2012.
[4] Park R.H.: Two Reaction Theory of Synchronous Machines generalized Method of Analysis-Part I. AIEE Transactions 48/1929, 716.
[5] Paszek G.W.: Transient behaviour of the induction machine with high rotor bars. Archiv für Elektrotechnik 63/1981, 77–86.
[6] Popp M., Mathis W., John M., Korolova O., Mertens A., Ponick B.: A Modified CCM Approach for Simulating Hierarchical Interconnected Dynamical Systems. International Symposium on Circuits and Systems, 2017.
[7] Popp M., Mathis W., Korolova O., Ponick B.: A Modified CCM Approach for Simulating Hierarchical Interconnected Dynamical Systems. International Electric Machines and Drives Conference, 2017.
[8] Seinsch H.O.: Transient processes in electrical drives (in German). B.G.Teubner Stuttgart 1991.

M.Sc. Olga Korolova
e-mail: olga.korolova@ial.uni-hannover.de

Olga Korolova received master degree in mechatronics at the Leibniz Universität Hannover in 2013. Since then she is working as a research associate at the Institute for Drive Systems and Power Electronics in Hanover. She focuses on modeling of the transient processes in electrical machines considering parasitic effects. SEW price holder 2015 for developing calculation methods for traction drives

M.Sc. Juan de la Torre Cubillo
e-mail: juan_de_latorre@yahoo.es

Juan de la Torre Cubillo received a Licenciatura (B,Sc. and M.Sc.) in Physics in 2015 from the Universidad Complutense de Madrid. After that he started studying a double degree program "International Mechatronics", at the Leibniz Universität Hannover and St. Petersburg Polytechnic University. Now he is finishing his master thesis on transient processes in motors and working in Ricardo automotive.

Prof. Bernd Ponick
e-mail: ponick@ial.uni-hannover.de

Bernd Ponick received Dipl.-Ing. in 1990 and Dr.-Ing. on el. machines in 1994 from the University of Hanover. After working as head of el. design and Technical Director of Siemens Dynamowerk Berlin he became in 2003 full professor at Leibniz Universität Hanover. His main research activities are prediction and simulation methods for el. machines considering parasitic effects and new applications.

otrzymano/received: 08.12.2017 *przyjęto do druku/accepted: 11.05.2018*

DOI: 10.5604/01.3001.0012.0696

ANALYSIS OF AN ANTI-PARALLEL MEMRISTOR CIRCUIT

Valeri Mladenov, Stoyan Kirilov
Technical University of Sofia, Faculty of Automatics, Department of Theoretical Electrical Engineering

Abstract. *The basic purpose of the present paper is to propose an extended investigation and computer analysis of an anti-parallel memristor circuit with two equivalent memristor elements with different initial values of the state variables using a modified Boundary Condition Memristor (BCM) Model and the finite differences method. The memristor circuit is investigated for sinusoidal supply current at different magnitudes – for soft-switching and hard-switching modes, respectively. The influence of the initial values of the state variables on the circuit's behaviour is presented as well. The equivalent i-v and memristance-flux and the other important relationshipsof the memristor circuit are also analyzed.*

Keywords: memristor; anti-parallel memristor circuit; finite-differences method; equivalent resistance

ANALIZA PRZECIWRÓWNOLEGŁEGO OBWODU MEMRYSTOROWEGO

Streszczenie. *Podstawowym celem niniejszego artykułu jest zaproponowanie rozszerzonego badania i komputerowej analizy przeciwrównoległego układu memrystorowego z dwoma równoważnymi elementami memrystorowymi o różnych wartościach początkowych zmiennych stanu z wykorzystaniem zmodyfikowanego modelu Boundary Condition Memristor (BCM) i metody różnic skończonych. Obwód memrystorowy jest badany dla sinusoidalnego prądu zasilania o różnych wielkościach – odpowiednio dla trybów miękkiego przełączania i twardego przełączania. Przedstawiono również wpływ wartości początkowych zmiennych stanu na zachowanie obwodu. Analizowane są również równoważne charakterystyki prądowo-napięciowe zależność między memrystancją i strumieniem magnetycznym oraz inne ważne cechy obwodu memrystora.*

Słowa kluczowe: memrystor; przeciwrównoległy obwód memrystorowy; metoda różnic skończonych; rezystancja równoważna

Introduction

After the theoretical prediction of the memristor element by Prof. L. Chua [3] in 1971 and the physical realization of the memristor prototype by Stanley Williams in HP research labs [2] in 2008 a lot of scientific papers associated with memristors are published [1, 4, 7, 8]. An anti-parallel memristor circuit with two memristor elements is analyzed in an oscillator circuit in [4] and [8]. The lack of detailed investigation of anti-parallel memristor circuits for sine-wave mode was the basic motivation for the present research. The modified linear drift memristor model proposed here is based on the BCM model [4], but for simplification, the model used here is without sensitivity voltage thresholds. For the analyses, we use an algorithm based on the finite differences method for numerical analysis. The basic purposes of our paper are to derive the main important relationships of the memristor circuit, its equivalent resistance for sine-wave current source power supply and to acquire the main results for hard-switching and soft-switching modes.

The paper is organized as follows. In Section 1 a description of the modified memristor model used for the computer simulations is proposed. In Section 2 a rigorous analysis of the anti-parallel memristor circuit is presented. The basic results from the simulations are presented and discussed in Section 3. The conclusion is shown in Section 4.

1. A description of the used memristor model

The modified BCM memristor model will be discussed using the titanium-dioxide memristor structure [7] given in Fig. 1. The upper region of the TiO_2 structure with a length of w is doped with oxygen vacancies [7]. The second sub-layer is made of pure TiO_2. The length of whole memristor structure is denoted with D [4, 7].

The normalized length of the doped layer of the memristor element, also known as the state variable x could be defined with the following formula [1, 4, 7]:

$$x = \frac{w}{\mathrm{D}} \tag{1}$$

The equivalent resistance of the memristor element could be expressed using the assumption for series linking of the doped and the un-doped regions [7]:

$$R = R_{doped} + R_{un-doped} = \mathrm{R_{ON}}x + \mathrm{R_{OFF}}(1-x) \tag{2}$$

where $\mathrm{R_{ON}}$ and $\mathrm{R_{OFF}}$ are the memristances for fully-closed and fully-open states, for $x = 1$ or $x = 0$, respectively [4, 7].

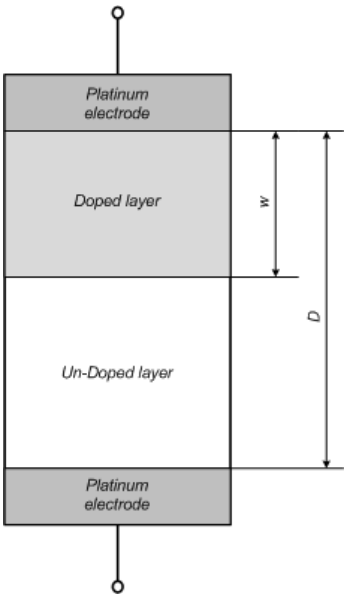

Fig. 1. Structure of the titanium dioxide memristor element

The i-v relation of the memristor element could be expressed using (2) and the state-dependent Ohm's law [2, 7]:

$$u = Ri = \left[\mathrm{R_{ON}}x + \mathrm{R_{OFF}}(1-x)\right]i \tag{3}$$

The voltage drop across the doped region of the memristor element u_w is [2, 4, 7]:

$$u_w = R_{doped}i = \mathrm{R_{ON}}xi = \mathrm{R_{ON}}i\frac{w}{\mathrm{D}} \tag{4}$$

The electric field intensity in the doped layer of the memristor element $\boldsymbol{E}_w$ is [2, 5]:

$$\mathbf{E}_\mathrm{w} = \frac{u_w}{w} = i\frac{\mathrm{R_{ON}}}{\mathrm{D}} \tag{5}$$

The rate of moving the border between doped and un-doped regions of the element is [5, 7]:

$$v = \frac{\mathrm{d}w}{\mathrm{d}t} = \frac{\mathrm{d}}{\mathrm{d}t}(x\mathrm{D}) = \mathrm{D}\frac{\mathrm{d}x}{\mathrm{d}t} = \mu\mathbf{E}_\mathrm{w} \tag{6}$$

where μ is the ionic dopant drift mobility [5, 7]. After transformations of (6) the basic differential state equation of the memristor element is derived [4, 7]:

$$\frac{\mathrm{d}x}{\mathrm{d}t} = \frac{\mu\mathrm{R_{ON}}}{\mathrm{D}^2}i = \mathrm{k}i \tag{7}$$

where k is a constant dependent only on memristor parameters. When we have two or more memristors in an electric circuit formula (7) has to be adapted [1, 4]:

$$\frac{\mathrm{d}x}{\mathrm{d}t} = \eta \frac{\mu \mathrm{R_{ON}}}{\mathrm{D}^2} i = \eta \mathrm{k} i \tag{8}$$

where η is a polarity coefficient [1, 4]. When the memristor element is forward-biased we have η = 1. For reverse-biased memristor we have η = -1 [4]. An anti-parallel circuit with two memristors supplied by a sinusoidal current source is given in Fig. 2. The first memristor M_1 is forward-biased and the second one M_2 is reverse-biased. For the circuit analysis we use a modified BCM model with linear ionic drift and without sensitivity thresholds. The BCM model switch-based algorithm is used here for representation the boundary effects [4].

The BCM model is appropriate for simulation of memristor elements both for soft-switching and hard-switching mode [1, 4, 8]. For soft-switching mode the state variable *x* does not reach its limiting values – 0 and 1, respectively. For hard-switching the state variable *x* reaches its boundary values and for a forward-biased memristor, if the state variable $x = 0$, its value could be changed only if the current through it becomes positive [1, 4]. If *x* increases and becomes equal to 1, the state variable *x* could be changed only if the current is negative. For a reverse-biased memristor operating in a hard-switching mode, if the state variable becomes with a value of $x = 0$, it could be changed if the memristor current is negative. If the state variable *x* becomes equal to 1, it could be changed if the current is positive [4].

2. Analysis of the memristor circuit

The memristor circuit under analysis is given in Fig. 2. It contains two equivalent memristors with different initial values of the state variables x_1 and x_2. The state equations are:

$$\begin{aligned} \frac{\mathrm{d}x_1}{\mathrm{d}t} &= \eta_1 \mathrm{k} i_1 = \mathrm{k} i_1 \\ \frac{\mathrm{d}x_2}{\mathrm{d}t} &= \eta_2 \mathrm{k} i_2 = -\mathrm{k} i_2 \end{aligned} \tag{9}$$

According to the Kirchhoff Current Law we have [2]:

$$j_e(t) = i_1 + i_2 \tag{10}$$

Using (2) we obtain the equivalent resistance R_{12} of the parallel connection of the memristors [2]:

$$\begin{aligned} R_1 &= (\mathrm{R_{ON}} - \mathrm{R_{OFF}})x_1 + \mathrm{R_{OFF}} \\ R_2 &= (\mathrm{R_{ON}} - \mathrm{R_{OFF}})x_2 + \mathrm{R_{OFF}} \\ \Delta\mathrm{R} &= \mathrm{R_{ON}} - \mathrm{R_{OFF}} \\ R_{12} &= \frac{R_1 R_2}{R_1 + R_2} = \frac{(\mathrm{R_{OFF}} + \Delta\mathrm{R}x_1)(\mathrm{R_{OFF}} + \Delta\mathrm{R}x_2)}{2\mathrm{R_{OFF}} + \Delta\mathrm{R}(x_1 + x_2)} \end{aligned} \tag{11}$$

The voltage drop across the memristors is [2]:

$$u = j_e(t) R_{12} = j_e(t) \frac{(\mathrm{R_{OFF}} + \Delta\mathrm{R}x_1)(\mathrm{R_{OFF}} + \Delta\mathrm{R}x_2)}{2\mathrm{R_{OFF}} + \Delta\mathrm{R}(x_1 + x_2)} \tag{12}$$

The currents flowing through the memristors are [2]:

$$\begin{aligned} i_1 &= j_e(t) \frac{(\mathrm{R_{OFF}} + \Delta\mathrm{R}x_2)}{2\mathrm{R_{OFF}} + \Delta\mathrm{R}(x_1 + x_2)} \\ i_2 &= j_e(t) \frac{(\mathrm{R_{OFF}} + \Delta\mathrm{R}x_1)}{2\mathrm{R_{OFF}} + \Delta\mathrm{R}(x_1 + x_2)} \end{aligned} \tag{13}$$

A sinusoidal current source is used for the computer simulation. Using (9), (10) and (11), the KCL and the finite-differences method a pseudo-code is created:

A pseudo-code algorithm for simulations of the anti-parallel memristor circuit with two memristors:

1. begin procedure eta1=1; eta2=-1; Jem=1e-3; f=40; psiu=deg2rad(-60);
2. Ron=100; Roff=16000; deltaR=Ron-Roff; mu=1e-12;
3. D=10e-9; k=(mu*Ron)/(D^2); x01=0.3; x02=0.7; xmin=0; xmax=1;
4. [je,t,deltat,tmin,tmax,N]=sine_gen(Jem,f,psiu);
5. n=1:1:N+1; % sample vector
6. [x1,x2]=memr_x_antipar_MM(je,deltat,tmin,tmax,... x01,x02,k,Roff,deltaR,xmin,xmax);
7. R1 = deltaR*x1 + Roff; R2 = deltaR*x2 + Roff; Req = (R1.*R2)./(R1+R2);
8. u = je.*Req; iM1 = u./R1; iM2 = u./R2; flux = integr(u,deltat,tmin,tmax);
9. function [u,t,deltat,tmin,tmax,N]=sine_gen(um,f,psiu) Steady state sine analysis
10. T=1/f; tmin=0; tmax=8*T; deltat=(tmax-tmin)/1e6;
11. t1 = tmin : deltat : tmax; omega = 2*pi*f; f1 = um*sin(omega*t1 + psiu);
12. u=f1; t=t1; N=tmax/deltat; end function
13. function [x1,x2] = memr _x_ antipar_ MM (je, deltat, tmin, tmax, x01,x02,k,Roff,deltaR,xmin,xmax)
14. N=(tmax-tmin)/deltat; % number of samples; n=1:1:N+1; % obtaining x1 and x2; x1=[ ]; x2=[ ];
15. for n=1, x11=x01; x22=x02; end
16. for n=2:1:N+1
17. A=(deltaR*(x11(n-1)+x22(n-1))+(2*Roff)); % in the denominator
18. x11(n) = x11 (n-1)+((k*je(n-1)*deltat*(deltaR* x22(n1)+Roff))/A);
19. x22(n) = x22 (n-1) - ((k*je(n-1)*deltat*(deltaR* x11(n-1)+Roff))/A);
20. % boundary condition switching x11
21. if x11(n)<=xmin && je(n)<=0
22. x11(n)=xmin;
23. elseif x11(n)>=xmax && je(n)>=0
24. x11(n)=xmax;
25. else x11(n)=x11(n-1)+((k*je(n-1)*deltat*(deltaR* x22(n-1)+Roff))/A); end
26. % boundary condition switching x22
27. if x22(n)<=xmin && je(n)>=0
28. x22(n)=xmin;
29. elseif x22(n)>=xmax && je(n)<=0
30. x22(n)=xmax; else x22(n)=x22(n-1) - ((k*je(n-1) *deltat*(deltaR*x11(n-1)+Roff))/A); end
31. end x1=[x1 x11]; x2=[x2 x22];

end function; end procedure.

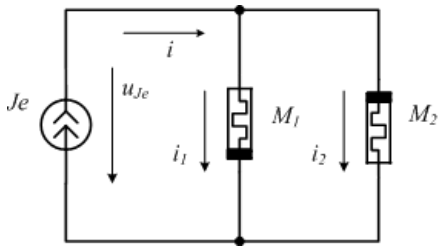

Fig. 2. An anti-parallel memristor circuit under analysis

3. Results by the computer simulation

The anti-parallel memristor circuit given in Fig. 2 is investigated for soft-switching and hard-switching modes, respectively [1, 4] and its computer simulations were made in MATLAB environment [2, 4, 6]. An additional simulation obtained by SIMSCAPE [8] confirms the results given below.

3.1. Soft-switching mode

For analysis of the anti-parallel memristor circuit at soft-switching mode we use a sinusoidal current source with the following signal: $j_e(t) = 0.1 \cdot \sin(2 \cdot \mathrm{pi} \cdot 40 \cdot t - 60°)$, mA. The time diagrams of the source current and the voltage drop across the parallel-connected memristors are presented in Fig. 3. It is obvious that the source current is sinusoidal but the voltage drop across the memristors has a non-sinusoidal form due to the nonlinearity of the memristor elements [7].

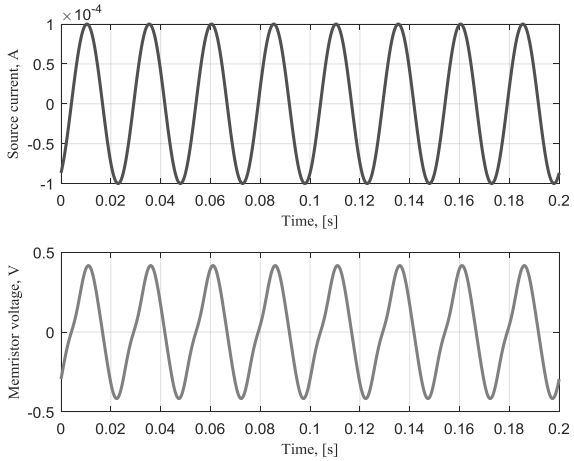

Fig. 3. Time diagrams of the source current and voltage drop across the memristors M_1 and M_2 for soft-switching mode

The time diagrams of the state variables x_1 and x_2 for the memristor elements are given in Fig. 4. It is clear that the state variables do not reach their limiting values. When the state variable x_1 increases then the state variable x_2 decreases due to the anti-parallel biasing.

The state-flux relationships of the memristors M_1 and M_2 are presented in Fig. 5 and Fig. 6, respectively. They are single-valued curves. Due to the anti-parallel connection they have different signs of their derivatives – the first is an increasing curve but the second is a monotonically decreasing curve. When x_1 increases then the state variable x_2 decreases, and vice versa.

The time diagrams of the memristances of the elements are presented in Fig. 7. Due to the anti-parallel connection when R_1 increases then R_2 decreases, and vice versa.

The time diagram of the equivalent resistance R_{12} of the anti-parallel connection is presented in Fig. 8. It is obvious that the parallel resistance of the memristor connection is a time-dependent non-sinusoidal function.

The memristance-flux relationship of the memristor parallel connection is presented in Fig. 9. It is a single-valued function with a local maximum which is obtained for a specific value of R_1 and R_2 according (11).

The current-voltage relationships of the memristors M_1 and M_2 are presented in Fig. 10 and Fig. 11. It is clear that the current intensity for the second memristor M_2 is higher than the current through the memristor M_1. This fact is due to the different initial values of the state variables and the different biasing polarities.

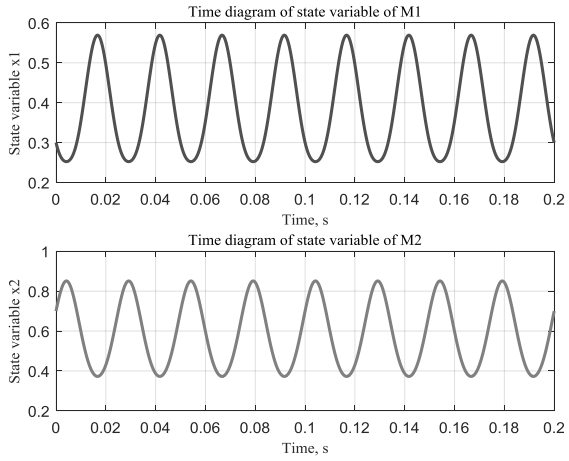

Fig. 4. Time diagrams of the state variables x_1 and x_2 of the memristors for soft-switching mode

The equivalent current-voltage relationship of the memristor parallel connection is presented in Fig. 12. It is a pinched hysteresis loop and it shows us that in this case the parallel connection of two anti-parallel memristor elements has a behaviour of a single memristor element.

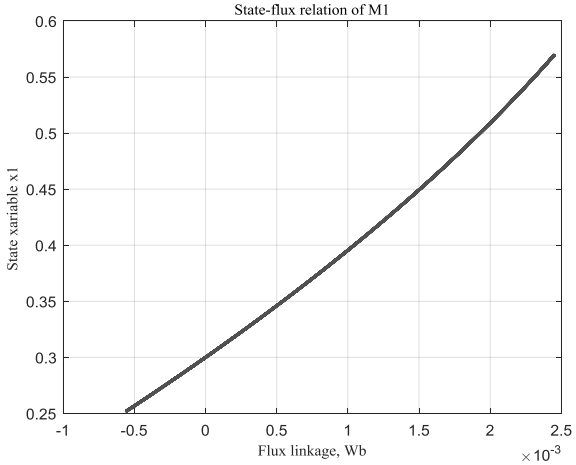

Fig. 5. State-flux relationship of the memristor M_1 for soft-switching mode

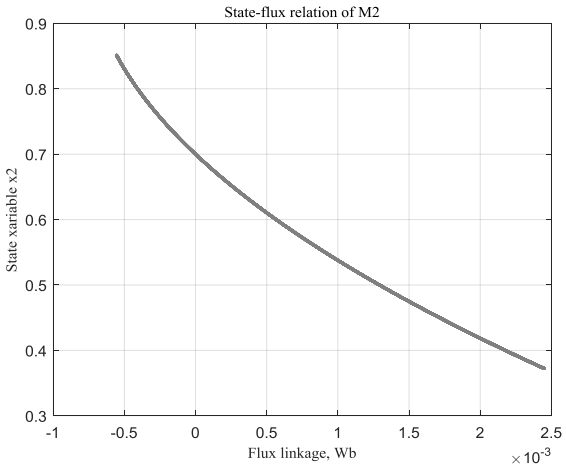

Fig. 6. State-flux relationship of the memristor M_2 for soft-switching mode

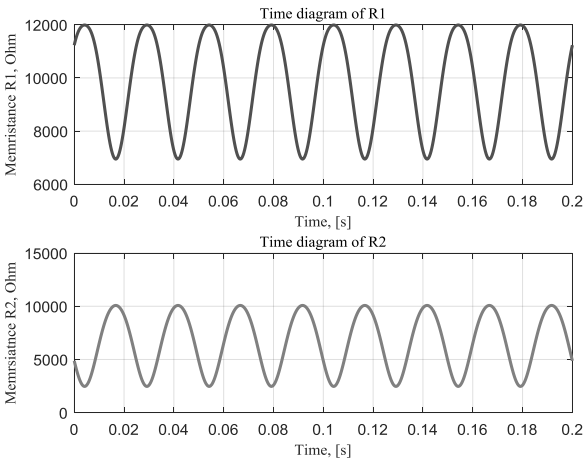

Fig. 7. Time diagrams of the memristances of the elements of the anti-parallel memristor circuit for soft-switching mode

3.2. Hard-switching mode

For analysis of the anti-parallel memristor circuit at hard-switching mode we use a sinusoidal current source with the following signal: $j_e(t)$ = 1·sin (2·pi·40·t - 60°), mA. The time diagrams of the source current and the voltage drop across the memristors are presented in Fig. 13. It is obvious that the source current is sinusoidal but the voltage drop across the memristors has highly a non-sinusoidal form due to the extended memristor

nonlinearity for hard-switching mode. The time diagrams of the state variables for hard-switching mode are presented in Fig. 14. It is clear that the state variables reach their limiting values – 0 and 1. If x_1 has a value of 1 then x_2 is equal to 0, and vice versa.

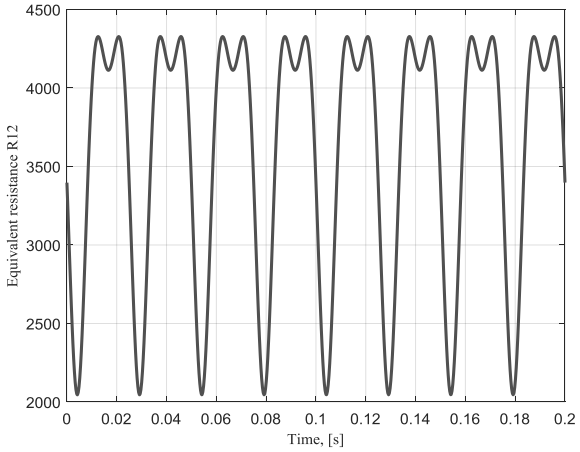

Fig. 8. Time diagram of the equivalent resistance of the anti-parallel memristor circuit for soft-switching mode

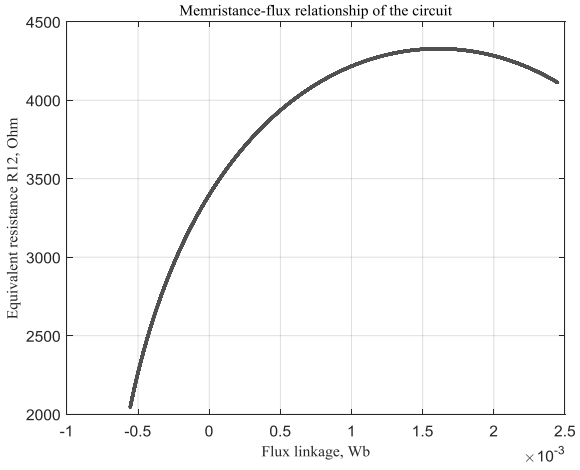

Fig. 9. Memristance-flux relationship of the anti-parallel memristor circuit for soft-switching mode

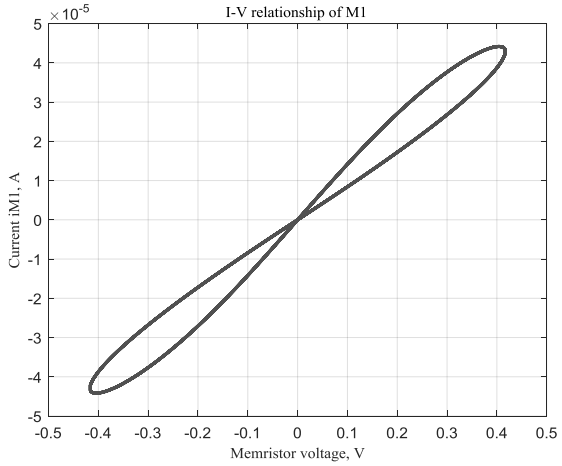

Fig. 10. Current-voltage relationship of the first memristor M_1 for soft-switching

The state-flux relationships of the memristor elements are presented in Fig. 15. It is clear that they are multi-valued hysteresis curves. Due to the different biasing polarities of the memristor elements their slope and respectively the first derivative are different to each other. When x_1 increases to 1 then the state variable x_2 decreases to 0, and vice versa. The memristance-flux relationship of the anti-parallel memristor connection is given in Fig. 16. It is a multi-valued hysteresis curve with a local maximum. After comparison of Fig. 15 and Fig. 16 it could be concluded that the diagram presented in Fig. 16 is derived using the state-flux relationships of the memristors for hard-switching. The memristances of the elements are reverse proportional to the respective state variables.

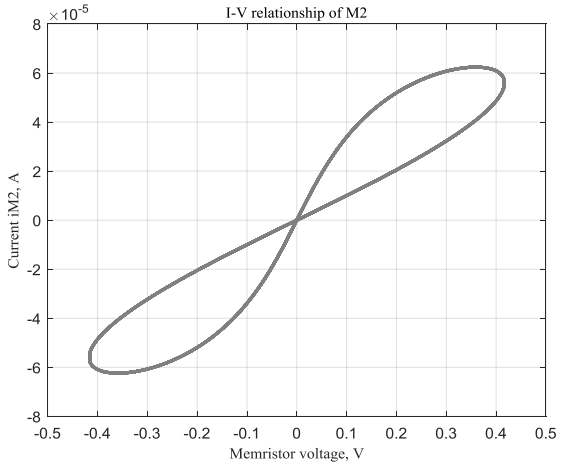

Fig. 11. Current-voltage relationship of the first memristor element M_2 for soft-switching mode

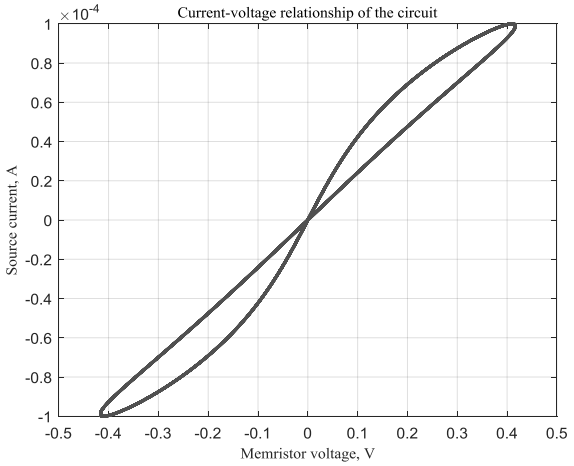

Fig. 12. Current-voltage relationship of the whole anti-parallel memristor circuit for soft-switching mode

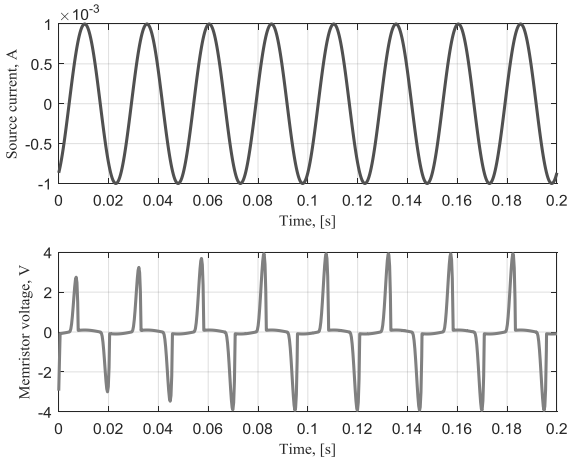

Fig. 13. Time diagrams of the source current and the voltage drop across the memristors M_1 and M_2 for hard-switching mode

The time diagrams of the memristances of the memristor elements are presented in Fig. 17. It is clear that their resistances

reach their limiting values – 100 Ohms and 16 kOhms, respectively, in the same time excluding the transition time intervals between the fully open and fully closed states. The time diagram of the equivalent resistance of the anti-parallel memristor connection is presented in Fig. 18. It is understandable that for more of the time intervals the first or the second memristor operates in a hard-switching mode and has its minimal resistance. Due to this fact the equivalent resistance of the anti-parallel memristor circuit for the long-time intervals has also its minimal value which is lower than 100 Ohms.

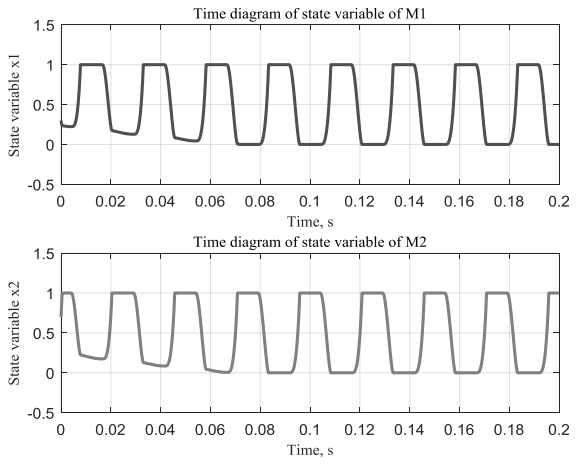

Fig. 14. Time diagrams of the state variables x_1 and x_2 of the memristor elements for hard-switching mode

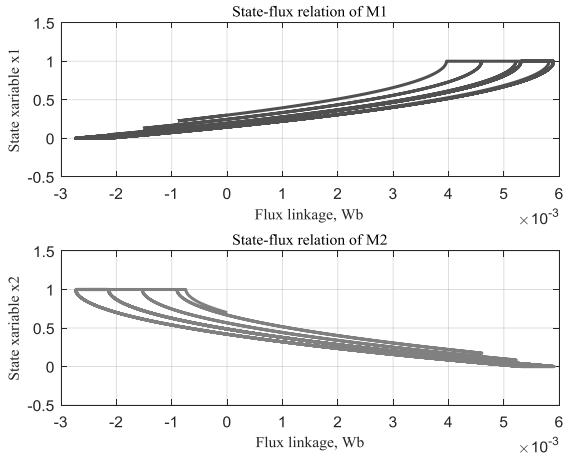

Fig. 15. State-flux relationships of the memristor elements M_1 and M_2 for hard-switching mode

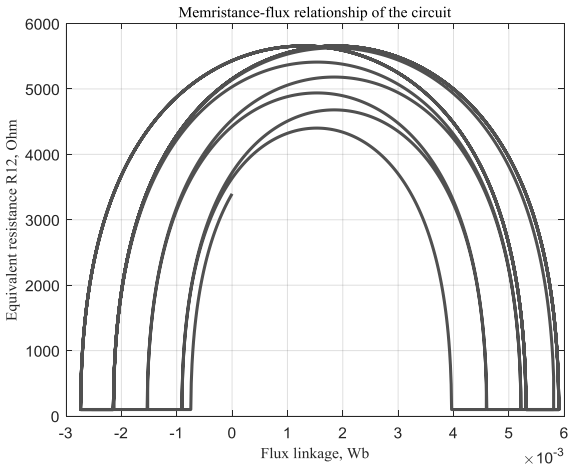

Fig. 16. Memristance-flux relationship of the whole anti-parallel memristor circuit for hard-switching mode

The current-voltage relationships of the memristor elements are presented in Fig. 19. These curves in the present case are anti-symmetrical. For hard-switching mode the memristors have rectifying effect and their behaviour is similar to the operation of the semiconductor diodes. When the first memristor is reaching a fully-open state in the same time interval the second memristor reaches its fully-closed state, and vice-versa.

The current-voltage characteristic of the equivalent anti-parallel memristor circuit is given in Fig. 20. Due to the anti-parallel connection of the memristor elements the equivalent memristor circuit has a symmetrical pinched multi-valued i-v relationship and it have not rectifying properties in this case.

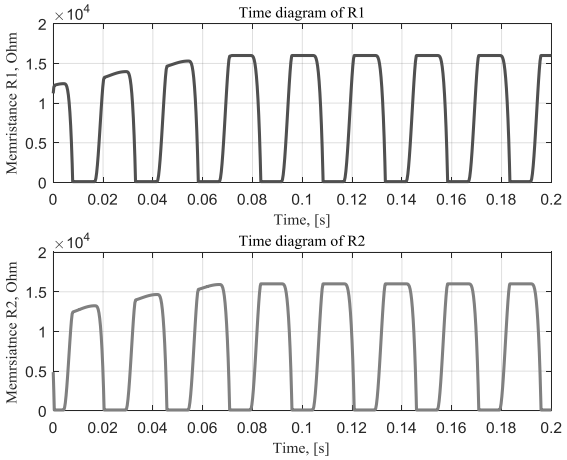

Fig. 17. Time diagrams of the memristances of the elements of the anti-parallel memristor circuit for hard-switching mode

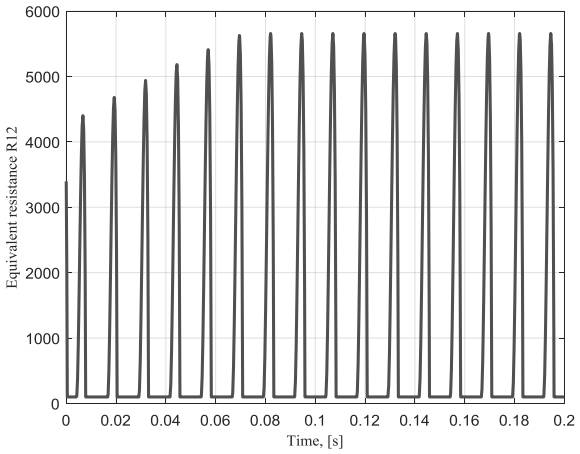

Fig. 18. Time diagram of the equivalent resistance of the anti-parallel memristor circuit for hard-switching mode

Due to the high nonlinearity of the memristor elements for hard-switching mode the respective memristance-flux relationships and the current-voltage characteristics are multi-valued functions. The maximal values of the equivalent memristance of the anti-parallel memristor circuit are from 4400 Ohms to 5600 Ohms. When the total resistance of the anti-parallel memristor circuit under analysis obtain its maximal values then both the memristor elements are operating near to fully-closed state. When the equivalent resistance of the investigated anti-parallel memristor circuit is lower than 100 Ohms then at least one of the memristor elements is in a fully-closed state and the respective state variable is equal to 0.

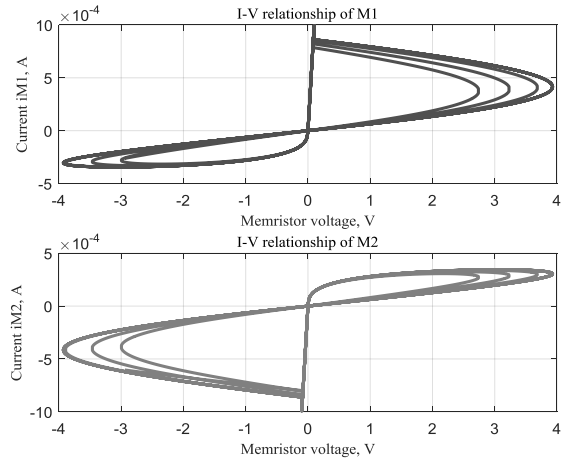

Fig. 19. Current-voltage relationship of the first memristor element M_1 for hard-switching mode

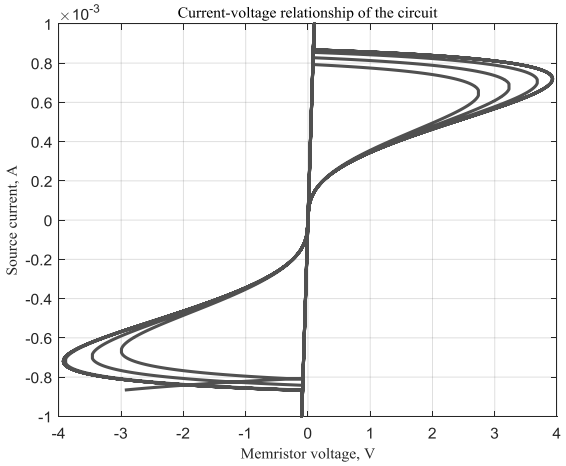

Fig. 20. Current-voltage relationship of the whole anti-parallel memristor circuit for hard-switching mode

4. Conclusion

After finishing the analytical investigations and the computer simulations of the anti-parallel memristor circuit several conclusions could be completed. The computer analysis results confirm the theoretical investigations made in Section 2. The influence of the current source has different effect on the two memristors due to their different polarity biasing. For a sinusoidal source current signal with a magnitude of 0.1 mA both the memristors operate in a soft-switching mode. For soft-switching mode if one of the memristor has increasing conductance in the same time the conductance of the other memristor decreases. The equivalent memristor circuit has a pinched single-valued hysteresis of the current-voltage relationship and in the present case it behaves like a single memristor element. For a sinusoidal signal with a magnitude value of 1 mA both the memristor elements operate in a hard-switching mode. In many time intervals with a relatively long duration the first memristor is in a fully-open state while the second memristor is in a fully-closed state, and vice versa. Then the anti-parallel memristor circuit has minimal resistance lower than 100 Ohms. In the other time intervals both the memristors operate in an active mode so the state variables are in the interval (0, 1). The equivalent current-voltage relationship of the whole anti-parallel memristor circuit is a symmetrical multi-valued curve despite of the fact that each of the memristor elements in the anti-parallel circuit has an anti-symmetrical single-valued current-voltage relationship. Then the equivalent behaviour of the anti-parallel memristor circuit is different from the operation of the rectifying elements. For hard-switching the memristor circuit has a high nonlinearity.

Acknowledgements

The research is supported by national Co-financing (contract № ДКОСТ01/14) of COST Action № IC1401 MemoCIS.

References

[1] Ascoli A., Corinto F., Tetzlaff R.: Generalized Boundary Condition Memristor Model. Int. J. Circ. Theor. Appl. 44/2016, 60–84.
[2] Brandisky K., Georgiev Z., Mladenov V., Stancheva R.: Theoretical Electrical Engineering – Part 1 & 2, KING Publishing House, Sofia 2005.
[3] Chua L.O.: Memristor – The Missing Circuit Element. IEEE Trans. on Circuit Theory CT-18/1971, 507–519.
[4] Corinto F., Ascoli A.: A Boundary Condition-Based Approach to the Modelling of Memristor Nanostructures. IEEE Transactions on Circuits and Systems - I, Regular Papers 59(11)/2012, 2713–2726.
[5] Hristov M., Vassileva T., Manolov M.: Semiconductor elements. New knowledge Publishing House, Sofia 2007.
[6] MATLAB – Version 7.12.0.635 (R2011a) User's Guide. The MathWorks, Inc.
[7] Strukov D.B., Snider G.S., Stewart D.R., Williams R.S.: The missing memristor found. Nature 453(06932)/2008, 80–83.
[8] Walsh A., Carley R., Feely O., Ascoli A: Memristor circuit investigation through a new tutorial toolbox. European Conference on Circuit Theory and Design (ECCTD) – Germany, 2013, 1–4.

Prof. Valeri Mladenov
e-mail: valerim@tu-sofia.bg

Prof. Mladenov has received his Ph.D. in Electrical Engineering from Technical University of Sofia in 1993. He is a Senior Member of IEEE and has awarded for dedication and contributions. He has written more than 300 papers in professional journals and conferences. His research interests are in the field of nonlinear systems, neural networks, artificial intelligence, applied mathematics and signal processing. He serves as a reviewer for a number of scientific journals.

Ph.D. Stoyan Kirilov
e-mail: s_kirilov@tu-sofia.bg

Dr. Kirilov has graduated in Telecommunications in 2010 and he receives his Ph.D. from Technical University of Sofia in Theoretical Electrical Engineering in 2014. Since 2016 he is a Chef Assistant Professor in the same institution. His main scientific and research interests are associated with simulations and modeling of memristors and memristive circuits, electronic elements and devices. He has been a reviewer in several scientific conferences – ICEST, ECCTD.

otrzymano/received: 08.12.2017 *przyjęto do druku/accepted: 11.05.2018*

DOI: 10.5604/01.3001.0012.0697

ADVANCED MEMRISTOR MODEL WITH A MODIFIED BIOLEK WINDOW AND A VOLTAGE-DEPENDENT VARIABLE EXPONENT

Valeri Mladenov, Stoyan Kirilov
Technical University of Sofia, Faculty of Automatics, Department of Theoretical Electrical Engineering

Abstract. *The main idea of the present research is to propose a new nonlinear ionic drift memristor model suitable for computer simulations of memristor elements for different voltages. For this purpose, a modified Biolek window function with a voltage-dependent exponent is applied. The proposed modified memristor model is based on Biolek model and due to this and to the use of a voltage-dependent positive integer exponent in the modified Biolek window function it has a new improved property - changing the model nonlinearity extent dependent on the integer exponent in accordance with the memristor voltage. Several computer simulations were made for soft-switching and hard-switching modes and also for pseudo-sinusoidal alternating voltage with an exponentially increasing amplitude and the respective basic important time diagrams, state-flux and i-v relationships are established.*

Keywords: memristor, nonlinear ionic dopant drift, modified Biolek window function, voltage-dependent exponent

ZAAWANSOWANY MODEL MEMRYSTORA ZE MODYFIKOWANYM OKNEM BIOLEK ORAZ EKSPONENTĄ ZALEŻNĄ OD NAPIĘCIA

Streszczenie. *Główną ideą niniejszej pracy jest zaproponowanie nowego modelu nieliniowego dryfu jonowego, odpowiedniego do komputerowych symulacji elementów memrystorowych dla różnych napięć. W tym celu stosowana jest zmodyfikowana funkcja okna Biolek z wykładnikiem zależnym od napięcia. Zaproponowany zmodyfikowany model memrystora oparty jest na modelu Biolek i dzięki temu oraz zastosowaniu zależnego od napięcia dodatniego współczynnika całkowitego w zmodyfikowanej funkcji okna Biolek ma on nową ulepszoną właściwość - zmieniając nieliniową zależność modelu od wykładnika całkowitego zgodnie z napięciem memrystora. Przeprowadzono kilka symulacji komputerowych dla trybów przełączania miękkiego i twardego, a także dla pseudo-sinusoidalnego napięcia przemiennego z wykładniczo rosnącą amplitudą i ustalono odpowiednie podstawowe wykresy czasowe, i zależności stan-strumień oraz prądowo-napięciowe.*

Słowa kluczowe: memrystor, nieliniowy dryft domieszki jonowej, zmodyfikowana funkcja okna Biolek, wykładnik zależny od napięcia

Introduction

The first physical prototype of the memristor element predicted by Leon Chua in 1971 [5] was invented in the HP research labs by Williams in 2008 [9]. It was based on a semiconductor material – crystalline titanium dioxide partially doped with oxygen vacancies [9]. Since this moment a lot of technical papers associated with memristor elements have been written and several basic memristor models have been proposed [1–3, 6, 10]. Each of the most important memristor models is appropriate for specific electrical regimes and applications [1, 10]. The memristor model proposed by Strukov and Williams [9] is with a linear ionic dopant drift and it is appropriate for low voltages and soft-switching mode. The nonlinear ionic drift model of Biolek is able to represent the memristor behaviour for higher voltages and it is mainly used for hard-switching mode [3]. The BCM model [6] and the Generalized BCM [2] memristor model are versatile and they use a switch-based algorithm for representing the boundary effects. They could be used both for soft-switching and hard-switching modes [1, 2, 6]. The Generalized BCM uses sensitivity thresholds not only for the boundaries but for every value of the state variable of the memristor element [2]. The new model proposed in this paper is based on Biolek model. It uses a modified Biolek window function with a voltage-dependent exponent. The new idea of the model proposed here is that the integer exponent of the modified Biolek window function [3] depends on the memristor voltage. Therefore, the respective extent of nonlinearity of the ionic dopant drift dependent on the positive integer exponent used in the window function could be changed in the operation process in accordance with the voltage of the memristor nanostructure. This functionality is very important for the realistic representation of the physical phenomena of the nonlinear ionic dopant drift [1, 2].

The paper is organized as follows. In Section 1 the motivation for creating the new nonlinear drift model, a description of the memristor structure and operation, and the main idea are given. The proposed new memristor model, its description and discussion and the pseudo-code algorithm for the modified memristor model are presented in Section 2. The results obtained by the computer simulations are presented and discussed in Section 3. The concluding remarks are given in Section 4.

1. Background, motivation and basic idea of the new nonlinear memristor model

The modified memristor model proposed here will be discussed using the titanium-dioxide memristor nanostructure described in [9]. The left region of the TiO_2 structure with a length of w is doped with oxygen vacancies [9]. The second sub-layer is made of pure TiO_2. The length of the whole memristor nanostructure is denoted with D [9] The normalized length of the doped layer, also known as the state variable x of the memristor could be defined with the following formula [1, 9]:

$$x = \frac{w}{\mathrm{D}} \tag{1}$$

The equivalent resistance of the memristor element could be expressed using the assumption for a series connection of the doped and the un-doped regions [9] and the substituting circuit of the memristor given in Fig. 1:

$$R = R_{doped} + R_{un-doped} = \mathrm{R_{ON}}x + \mathrm{R_{OFF}}(1-x) \tag{2}$$

where $\mathrm{R_{ON}}$ and $\mathrm{R_{OFF}}$ are the memristances for fully-closed and fully-open states [6, 9, 10], for $x = 1$ or $x = 0$, respectively.

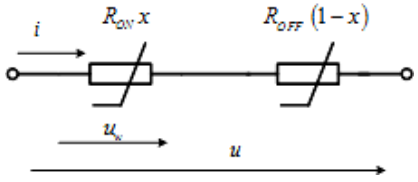

Fig. 1. Substituting circuit of a titanium dioxide memristor

The i-v relationship of the memristor could be expressed using (2) and the state-dependent Ohm's law [4, 9]:

$$u = Ri = \left[\mathrm{R_{ON}}x + \mathrm{R_{OFF}}(1-x)\right]i \tag{3}$$

The voltage drop across the doped region of the memristor element u_w is [7, 9]:

$$u_w = R_{doped}i = \mathrm{R_{ON}}xi = \mathrm{R_{ON}}i\frac{w}{\mathrm{D}} \tag{4}$$

The electric field intensity in the doped layer of the memristor element $\boldsymbol{E_w}$ is [7, 9]:

$$\mathbf{E_w} = \frac{u_w}{w} = i\frac{\mathrm{R_{ON}}}{\mathrm{D}} \tag{5}$$

The rate of moving the boundary between doped and un-doped layers of the element is [7, 9]:

$$v = \frac{\mathrm{d}w}{\mathrm{d}t} = \frac{\mathrm{d}}{\mathrm{d}t}(x\mathrm{D}) = \mathrm{D}\frac{\mathrm{d}x}{\mathrm{d}t} = \mu\mathbf{E}_{\mathrm{w}} \tag{6}$$

where μ is the ionic dopant drift mobility [7, 9]. After transformations of (6) the basic differential equation of the memristor is derived [2, 6, 9]:

$$\frac{\mathrm{d}x}{\mathrm{d}t} = \frac{\mu \mathrm{R}_{\mathrm{ON}}}{\mathrm{D}^2} i = \mathrm{k}i \tag{7}$$

where k is a constant dependent on the memristor parameters. When we have two or more memristors in a circuit then formula (7) must be modified [6, 10]:

$$\frac{\mathrm{d}x}{\mathrm{d}t} = \eta\frac{\mu \mathrm{R}_{\mathrm{ON}}}{\mathrm{D}^2} i = \eta\mathrm{k}i \tag{8}$$

where η is a polarity coefficient [6, 10]. When the memristor element is forward-biased we have η = 1. For a reverse-biased memristor the polarity coefficient is η = -1 [6].

Formula (8) is valid only for very small electrical currents and memristor voltages [1, 6, 9]. For representing the nonlinear ionic drift effect in the general case an additional window function is needed to be used in the right side of (8) [1, 3]:

$$f_B(x,i) = 1 - [x - stp(-i)]^{2\mathrm{p}} \tag{9}$$

where p is a positive integer exponent. The function expressed with (9) is presented for first use by Biolek in [3] and it is also known as a Biolek window function [3].

Then the state equation of the memristor element presented with (8) could be modified using (9) and according to [3] is:

$$\frac{\mathrm{d}x}{\mathrm{d}t} = \eta\mathrm{k}i f_B(x,i) = \eta\mathrm{k}i\left\{1 - [x - stp(-i)]^{2\mathrm{p}}\right\} \tag{10}$$

where $f_B(x)$ is the original Biolek window function [3]. The function *stp(i)* used in (9) and (10) is [3]:

$$stp(i) = \begin{cases} 1, \ if \ i \geq 0 \ (u \geq 0) \\ 0, \ if \ i < 0 \ (u < 0) \end{cases} \tag{11}$$

After substitution of (11) in (10) the following equations are derived [3]:

$$\begin{aligned} \frac{\mathrm{d}x}{\mathrm{d}t} &= \eta\mathrm{k}i\left[1 - (x-1)^{2\mathrm{p}}\right], \ u(t) \leq 0, \ [i(t) \leq 0] \\ \frac{\mathrm{d}x}{\mathrm{d}t} &= \eta\mathrm{k}i\left[1 - x^{2\mathrm{p}}\right], \ u(t) > 0, \ [i(t) > 0] \end{aligned} \tag{12}$$

The original Biolek memristor model discussed here is fully described with equations (3) and (12).

2. The proposed modified new memristor model description and pseudo-code based algorithm

If the memristor voltage increases then the ionic dopant drift nonlinearity increases too [1, 3, 10]. Practically the representation of the increasing the nonlinearity of the ionic dopant drift could be expressed with decreasing of the positive integer exponent in the Biolek window function [1, 3, 6]. The projected relationship between the positive integer exponent of the modified Biolek window function in the proposed memristor model and the absolute value of the memristor voltage could be expressed approximately with a hyperbolic-like function:

$$p = round\left(\frac{10}{|u|+1}\right) \tag{13}$$

where the function '*round*' is used for deriving an integer result. Then the modified Biolek window function $f_{BM}(x,u)$ used in the proposed memristor model is:

$$\begin{aligned} f_{BM}(x,u) &= 1 - (x-1)^{2round\left(\frac{10}{|u|+1}\right)}, \ u(t) \leq 0 \\ f_{BM}(x,u) &= 1 - x^{2round\left(\frac{10}{|u|+1}\right)}, \ u(t) > 0 \end{aligned} \tag{14}$$

Then the proposed memristor model could be fully described using the following equations:

$$\begin{aligned} \frac{\mathrm{d}x}{\mathrm{d}t} &= \eta\mathrm{k}i\left[1 - (x-1)^{2round\left(\frac{10}{|u|+1}\right)}\right], \ u(t) \leq 0, \ [i(t) \leq 0] \\ \frac{\mathrm{d}x}{\mathrm{d}t} &= \eta\mathrm{k}i\left[1 - x^{2round\left(\frac{10}{|u|+1}\right)}\right], \ u(t) > 0, \ [i(t) > 0] \\ u &= Ri = \left[\mathrm{R}_{\mathrm{ON}}x + \mathrm{R}_{\mathrm{OFF}}(1-x)\right]i \end{aligned} \tag{15}$$

where the third equation in (15) is (3) and it represents the state-dependent Ohm's Law for the memristor element [9]. Using (15) and the finite differences method [4] a pseudo-code based algorithm is derived for the computer simulations:

A pseudo-code based algorithm of the proposed model

```
% memristor parameters and voltage characteristics
eta=1; um=0.5; f=40; psiu=deg2rad(-60);
Ron=100; Roff=16000; deltaR=Ron-Roff; mu=1e-12;
D=10e-9; k=(mu*Ron)/(D^2); x0=0.3; xmin=0; xmax=1;
% the function "sine_gen" is used for generating a sinusoidal
% voltage signal
[u,t,deltat,tmin,tmax,N]=sine_gen(um,f,psiu);
% the function "integr" is used for obtaining the magnetic flux
% linkage using the voltage signal
n=1:1:N+1; flux=integr(u,deltat,tmin,tmax);
% the function "biolekvar1" is used for simulation using the
 modified Biolek memristor model
[x,biolekwin,p]=biolekvar1(deltat,u,k,eta,deltaR,Roff,x0,N);
% the function "biolekvar3" is used for simulation using the
original Biolek memristor model
[z,biolekwin3]=biolekvar3(deltat,u,k,eta,deltaR,Roff,x0,N);
Req=deltaR*x+Roff; Req2=deltaR*z+Roff;
iM=u./Req; iM2=u./Req2;
function [u,t,deltat,tmin,tmax,N]=sine_gen(um,f,psiu)
% Steady state sine analysis
T=1/f; tmin=0; tmax=8*T; deltat=(tmax-tmin)/1e5;
t1=tmin:deltat:tmax; omega=2*pi*f;
f1=um*sin(omega*t1+psiu);
%f1=um*exp(2.5*t1).*sin(omega*t1+psiu);
u=f1; t=t1; N=tmax/deltat; End
function psi=integr(u,deltat,tmin,tmax)
N=(tmax-tmin)/deltat; % number of samples
n=1:1:N+1; % sample vector
psi=[ ]; % empty array for the flux linkage
% integrating u with respect to t
for n=1;   psi1(n)=0; end
for n=2:1:N+1;     psi1(n)=psi1(n-1)+u(n-1)*deltat;
end; psi=[psi psi1]; end
function [x,biolekwin,p] =biolekvar1(deltat,u,k,eta,
deltaR,Roff ,x0,N); p=[ ]; x=[ ]; biolekwin=[ ];
for n=1,    x1=x0;    biolekwin1=1;
   p1(n)=round(10./(abs(u(n))+1));
end; for n=2:1:N+1;
   p1(n)=round(10./(abs(u(n))+1));
   A=deltaR*x1(n-1)+Roff;
   if u(n)<=0
   x1(n)=x1(n-1)+(eta*k*u(n-1)*deltat*(1-(x1(n-1)-
1).^(2*p1(n))))/A;
   biolekwin1(n)=1-(((x1(n)-(sign(-u(n))+
1)/2)).^(2*p1(n)));        else
      x1(n)=x1(n-1)+(eta*k*u(n-1)*deltat*(1-(x1(n-
1)).^(2*p1(n))))/A;
      biolekwin1(n)=1-(((x1(n)-(sign(-u(n))+1)/2)).^
(2*p1(n)));        end end    p=[p p1];    x=[x x1];
   biolekwin=[biolekwin biolekwin1]; end
function [x, biolekwin]=biolekvar3 (deltat,u,k,eta,
deltaR, Roff, x0,N); x=[ ]; biolekwin=[ ]; for n=1     x1=x0;
   biolekwin1(n)=1-(((x1(n)-(sign(-u(n))+1)/2)).^(2*1));
```

```
end for n=2:1:N+1;     A=deltaR*x1(n-1)+Roff;
   if u(n)<=0,     x1(n)=x1(n-1)+(eta*k*u(n-1)*deltat
*(1-(x1(n-1)-1)^(2*1)))/A;
   biolekwin1(n)=1-(((x1(n)-(sign(-u(n))+1)/2)).^(2*1));
   else x1(n)=x1(n-1)+(eta*k*u(n-1)*deltat
   *(1-(x1(n-1))^(2*1)))/A;
   biolekwin1(n)=1-(((x1(n)-(sign(-u(n))+1)/2)).^(2*1));
   end end   x=[x x1];  biolekwin=[biolekwin biolekwin1];
   end procedure
```

3. Simulations results

3.1. Soft-switching mode

The computer simulations of the memristor models were made in MATLAB environment [8, 10]. Here we will make a comparison of several results obtained by the use of the original Biolek memristor model and the proposed modified Biolek model. The voltage signal for testing the memristor is: $u(t) = 0.6 \cdot \sin(2 \cdot pi \cdot 40 \cdot t - 60°)$. The time diagrams of the memristor voltage and the respective value of the integer positive exponent are presented in Fig. 2. In this case the integer exponent p changes in the range from 6 to 10 in accordance to the absolute value of the memristor voltage.

The state-flux relationships of the memristor according to the original Biolek model and the proposed modified model are shown in Fig. 3. According to the original Biolek memristor model the state-flux relatioship is a multi-valued curve while fo the same conditions the state-flux relationship of the modified memristor model is almost a single-valued curve which is an advantage of the proposed modified memristor model. The time diagrams of memristor current according to the original Biolek model and the proposed model are presented in Fig. 4. For both the memristor models the current has a non-sinusoidal form due to the memristor nonlinearity. The current-voltage relationships of the memristor element according to the original Biolek memristor model and the proposed modified Biolek memristor model are given in Fig. 5. It is clear that the current-voltage relationships are pinched hysteresis loops both for the original Biolek model and for the proposed modified Biolek memristor model and they almost coincide to each other. For the original Biolek model the i-v relation is a multi-valued curve while for the proposed model it is almost a double-valued curve.

The diagrams of the original Biolek window function $f_B(x,u)$ and of the modified Biolek window function $f_{BM}(x,u)$ derived respectively for the original Biolek memristor model for different values of the positive integer exponent p and for the modified Biolek model with a voltage-dependent exponent are shown in Fig. 6. The range of the state variable for the original Biolek model increases with the growing of the integer exponent p while in the same time the range of the window function decreases. For exponents higher than 1 the original Biolek window function reaches its maximal value of 1. With increasing the positive integer exponent in the original Biolek window function the ionic dopant drift nonlinearity extent decreases.

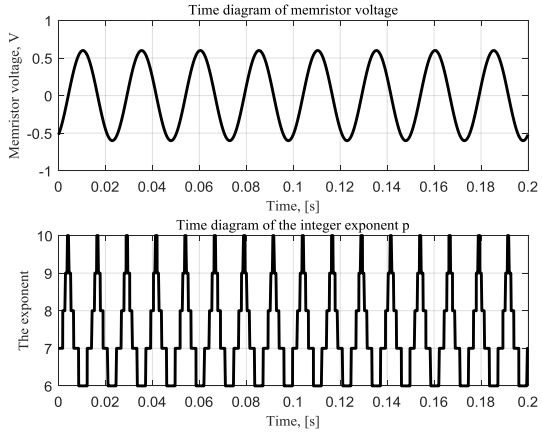

Fig. 2. Time diagrams of memristor voltage and the integer exponent p in the modified Biolek window function for soft-switching mode

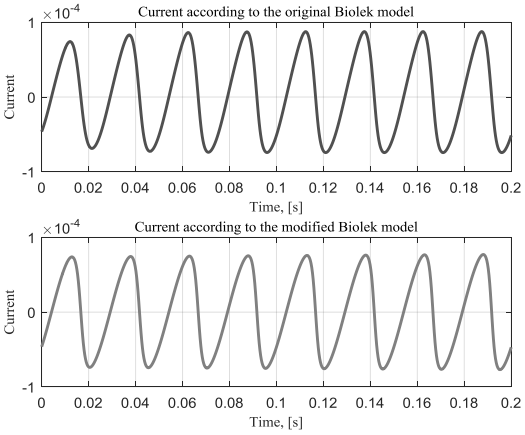

Fig. 4. Time diagrams of memristor current according to the original Biolek memristor model and the modified Biolek model for soft-switching mode

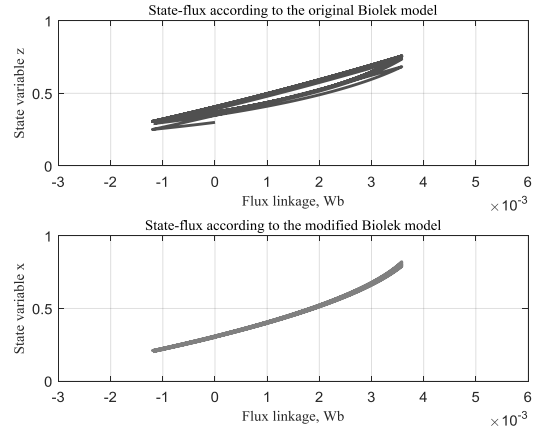

Fig. 3. State-flux relationships of the memristor according to the original Biolek memristor model and the modified Biolek model for soft-switching mode

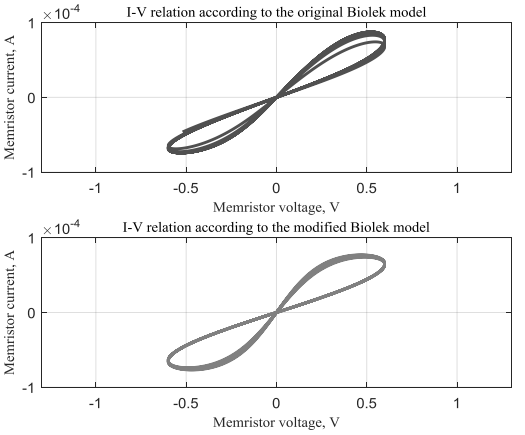

Fig. 5. I-V relationships of the memristor according to the original Biolek memristor model and the modified Biolek model for soft-switching mode

After a comparison of the original Biolek window function for different values of the positive integer exponent *p* with the proposed modified window function it could be concluded that the modified Biolek window function is created from several segments taken from the original Biolek window functions obtained for different positive exponents *p*. According to the proposed modified memristor model the positive integer exponent *p* changes automatically in the simulation process in dependence with the absolute value of the memristor voltage and the operating point of the memristor in the field of the relationship between the modified window function and the state variable *x* is moving on several different segments for different exponents *p*.

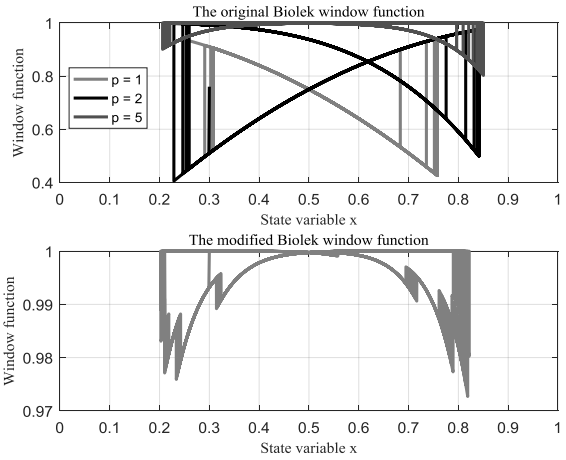

Fig. 6. Diagrams of the window functions according to the original Biolek memristor model and the modified Biolek model for soft-switching mode

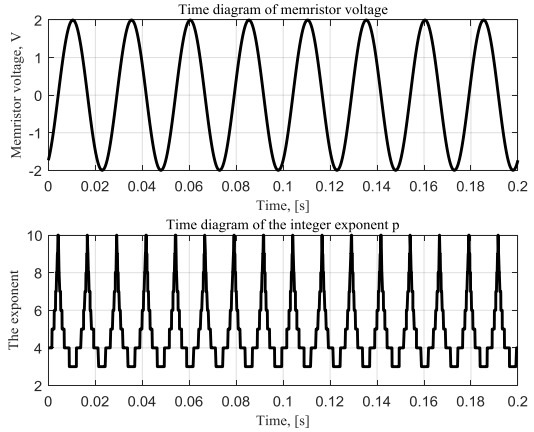

Fig. 7. Time diagrams of memristor voltage and the integer exponent p in the modified Biolek window function for hard-switching mode

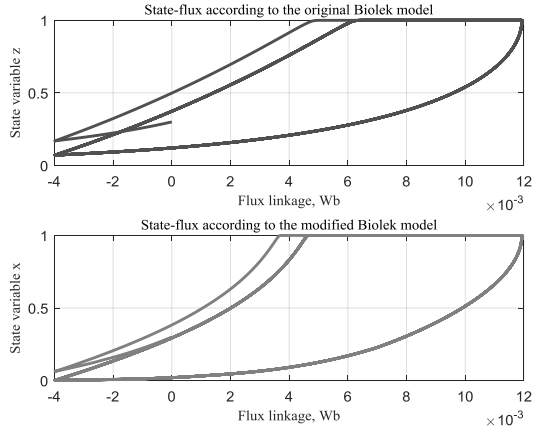

Fig. 8. State-flux relationships according to the original Biolek memristor model and the modified Biolek model for hard-switching mode

3.2. Hard-switching mode

The voltage signal used for the computer simulations in a hard-switching mode is: $u(t) = 2 \cdot \sin(2 \cdot pi \cdot 40 \cdot t - 60°)$. The time diagrams of the memristor voltage and the respective integer positive exponent of the modified Biolek window function are represented in Fig. 7. In the case of hard-switching mode the exponent *p* changes in a larger range (from 3 to 10) than the respective range for soft-switching mode (from 6 to 10) and the respective nonlinearity extent of the ionic drift is higher.

The respective state-flux relationships of the memristor for the original Biolek model and for the proposed modified Biolek model are presented in Fig. 8. It is clear that both the original Biolek model and its modification are able to limit the state variable in the range (0, 1). For the original Biolek memristor model in this case the state variable *x* does not reach the minimal limit of 0 but for the modified memristor model this limit is almost reached.

The time diagrams of the memristor currents according to the original Biolek model and the proposed modified Biolek model are presented in Fig. 9. In both the cases the memristor operates as a rectifying semiconductor diode. According to the proposed memristor model the current maximal value is a little bit higher than the respective maximal value for the original Biolek memristor model.

The current-voltage relationships of the memristor element obtained according to the original Biolek memristor model and the proposed modified Biolek model are presented in Fig. 10. In both the cases the current-voltage relationship is an anti-symmetrical curve and it confirms the rectifying behaviour of the memristor element when it operates in a hard-switching mode [6]. In the present case the respective current-voltage relationships almost match to each other.

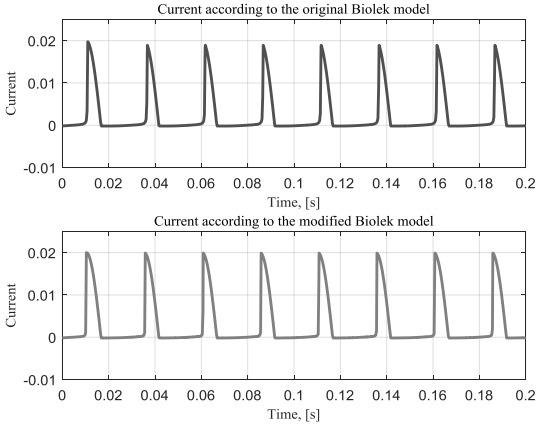

Fig. 9. Time diagrams of memristor current according to the original Biolek memristor model and the modified Biolek model for hard-switching mode

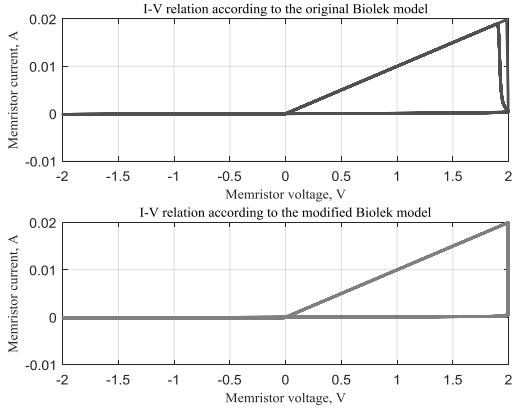

Fig. 10. I-V relationships of the memristor according to the original Biolek memristor model and the modified Biolek model for hard-switching mode

The diagrams of the original Biolek window functions for different positive integer exponents *p* and the modified Biolek window function are presented in Fig. 11. For the original Biolek memristor model if the exponent *p* is higher than 2 the state variable and the window function have their maximal range – from 0 to 1. This phenomenon is also derived for the proposed modified Biolek model for this case. For the original Biolek model the nonlinearity of the model is fixed and the integer exponent p has a value of 1, 2 or 5, while for the modified Biolek model the nonlinearity extent depends on the memristor voltage. Due to the full range of the state variable (from 0 to 1) the hard-switching behaviour of the memristor element is more clearly expressed by the use of the modified Biolek memristor model.

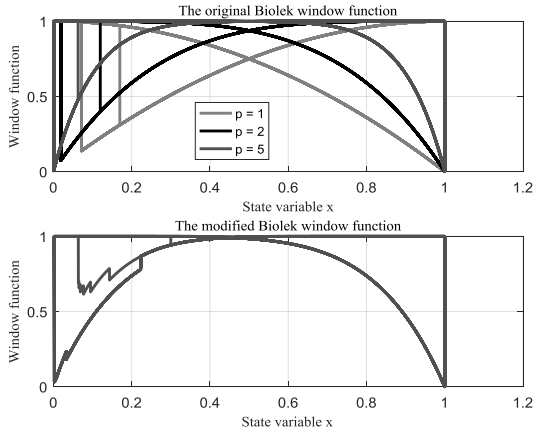

Fig. 11. Diagrams of the window functions according to the original Biolek memristor model and the modified Biolek model for hard-switching mode

3.3. Analysis of the proposed modified memristor model for AC voltage signal with an exponentially increasing magnitude

In this paragraph for testing the proposed modified memristor model we use an AC voltage signal with exponentially increasing magnitude. In this case we could observe the transition between the soft-switching mode and hard-switching mode it the time domain. The voltage signal used for the computer simulations is as follows: $u(t) = 0.6 \cdot \exp(3 \cdot t) \cdot \sin(2 \cdot \mathrm{pi} \cdot 40 \cdot t - 60°)$. The time diagrams of the pseudo-sinusoidal memristor voltage and the respective integer exponent of the modified Biolek window function are presented in Fig. 12. It is easy to observe the change of the exponent range which depends on the voltage. The state-flux relation of the memristor obtained by the use of the original Biolek memristor model and the modified Biolek model are presented in Fig. 13. In both the cases the state-flux relationships are obtained as a multi-valued hysteresis curves. The time diagrams of the memristor currents for the original Biolek memristor model and for the proposed modified Biolek model are presented in Fig. 14. For the original Biolek model the memristor current is with very low level and in the end of the simulation interval the current amplitude increases and the element starts operation in a hard-switching mode. For the proposed modified Biolek memristor model the memristor current is obtained with a magnitude several times higher than the current amplitude derived by the original Biolek model. The current-voltage relationships of the memristor according to the original Biolek model and to the proposed modified model for a pseudo-sinusoidal voltage signal with an exponentially increasing amplitude are presented in Fig. 15. Observing the current-voltage curves one can determine the transition between the soft-switching and hard-switching modes.

For given conditions the soft-switching behaviour is dominating for the original Biolek model while the hard-switching mode is more clearly expressed for the proposed modified Biolek model. The window functions for the original Biolek memristor model for several different positive integer exponents and for the modified memristor model are presented in Fig. 16. In this case the extent of ionic drift nonlinearity for the modified Biolek memristor model changes in the simulation process while for the original Biolek model the integer exponent is fixed. The nonlinearity extent of the ionic dopant drift decreases if we choose a higher value of the positive integer exponent.

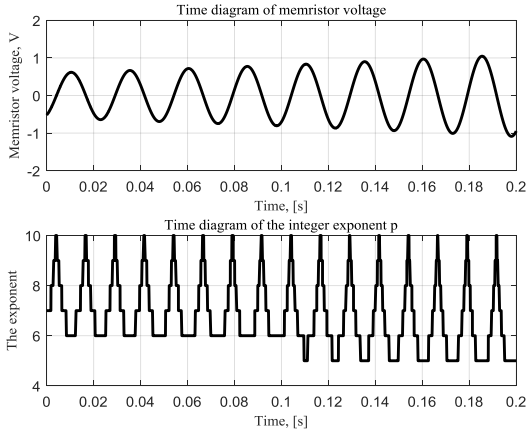

Fig. 12. Time diagrams of the voltage u and the integer exponent p for pseudo-sinusoidal voltage with an exponentially increasing magnitude

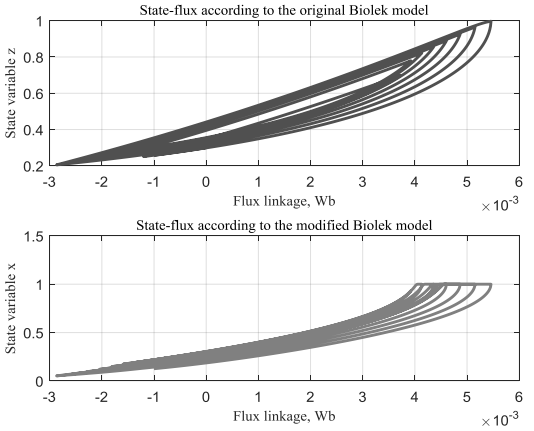

Fig. 13. State-flux relations of the memristor according to the original Biolek memristor model and the modified Biolek model for pseudo-sinusoidal voltage with an exponentially increasing magnitude

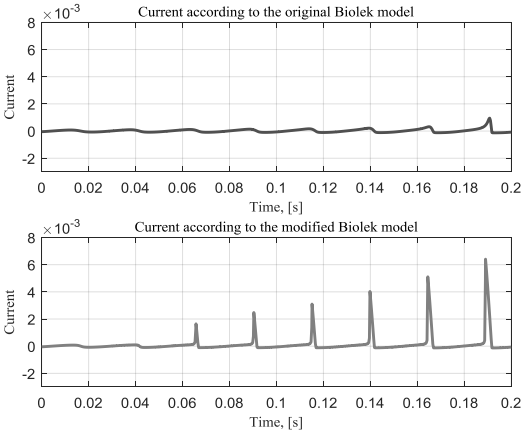

Fig. 14. Time diagrams of the memristor current according to the original Biolek model and the modified Biolek model for pseudo-sinusoidal voltage with an exponentially increasing amplitude

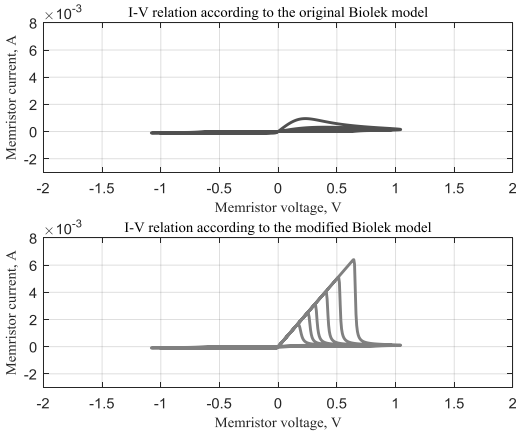

Fig. 15. Current-voltage relationships of the memristor according to the original Biolek memristor model and the modified Biolek model for pseudo-sinusoidal voltage with an exponentially increasing amplitude

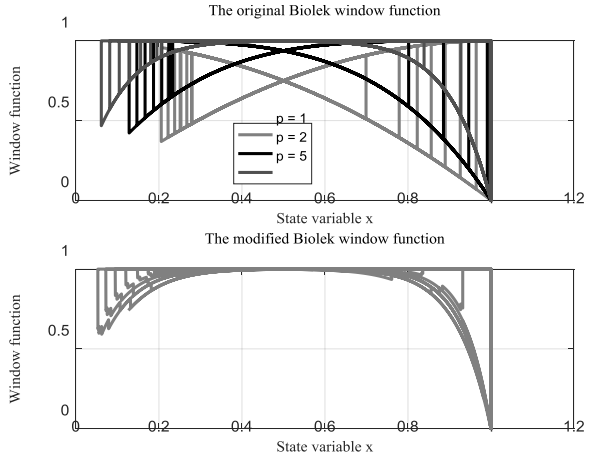

Fig. 16. Window functions diagrams according to the original Biolek memristor model and the modified Biolek memristor model for pseudo-sinusoidal voltage signal with an exponentially increasing magnitude

If we observe the window functions for the original Biolek memristor model presented in the first sub-figure of Fig. 16 then it could be concluded that for the given circumstances if we increase the integer exponent *p* then the state variable tends to reach its minimal value of 0. The proposed modified window function presented in the second sub-figure of Fig. 16 is derived by the use of several segments of the original Biolek window functions for different positive integer exponents. This phenomenon is based on the proposed relationship between the positive integer exponent *p* and the absolute value of the memristor voltage.

4. Conclusion

After the detailed analytical description and the computer simulations of the proposed modified Biolek memristor model in parallel with the original Biolek model investigation several conclusions could be completed. The new modified nonlinear memristor model proposed in this research is based on the Biolek model. It has many of the advantages of the original Biolek memristor model. The proposed model has a nonlinear ionic dopant drift and a mechanism for limitation of the state variable in the range from 0 to 1 confirmed by simulations for hard-switching mode. The new model has a new advantage with respect to the original Biolek model with fixed integer exponent – the ability for realistic representation of ionic dopant drift nonlinearity in accordance to the absolute value of the applied memristor voltage. As it could be seen from the simulation results the state-flux relationships of the modified Biolek model for soft-switching are almost single-valued curves which is an advantage of the new model with respect to the original Biolek model which represents for the same condition multi-valued state-flux relationships of the memristor element.

Acknowledgements

The research is supported by national Co-financing (contract № ДКОСТ01/14) of COST Action № IC1401 MemoCIS.

References

[1] Ascoli A., Corinto F., Senger V., Tetzlaff R.: Memristor Model Comparison. IEEE Circuits and Systems Magazine 2013, 89–105.
[2] Ascoli A., Corinto F., Tetzlaff R.: Generalized Boundary Condition Memristor Model. Int. J. Circ. Theor. Appl. 44/2016, 60–84.
[3] Biolek Z., Biolek D., Biolkova V.: SPICE Model of Memristor with Nonlinear Dopant Drift. Radioengineering 18/2009, 210–214.
[4] Brandisky K., Georgiev Z., Mladenov V., Stancheva R.: Theoretical Electrical Engineering–Part 1 & 2. KING Publishing house, Sofia 2005.
[5] Chua L.: Memristor–The Missing Circuit Element. IEEE Transactions on Circuit Theory 18(5)/1971, 507–519.
[6] Corinto F., Ascoli A.: A Boundary Condition-Based Approach to the Modelling of Memristor Nanostructures. IEEE Transactions on Circuits and Systems - I, Regular Papers 59(11)/2012, 2713–2726.
[7] Hristov M., Vassileva T., Manolov E.: Semiconductor elements. New knowledge, Sofia 2007.
[8] MATLAB–7.12.0.635(R2011a) User's Guide. The MathWorks, Inc.
[9] Strukov D. B., Snider G. S., Stewart D. R., Williams R. S.: The missing memristor found. Nature 453(06932)/2008, 80–83.
[10] Walsh A., Carley R., Feely O., Ascoli A.: Memristor circuit investigation through a new tutorial toolbox. ECCTD 2013, 1–4.

Prof. Valeri Mladenov
e-mail: valerim@tu-sofia.bg

Prof. Mladenov has received his PhD in Electrical Engineering from Technical University of Sofia in 1993. He is a Senior Member of IEEE and has awarded for dedication and contributions. He has written more than 300 papers in professional journals and conferences. His research interests are in the field of nonlinear systems, neural networks, artificial intelligence, applied mathematics and signal processing. He serves as a reviewer for a number of scientific journals.

Ph.D. Stoyan Kirilov
e-mail: s_kirilov@tu-sofia.bg

Dr. Kirilov has graduated in Telecommunications in 2010 and he receives his PhD from Technical University of Sofia in Theoretical Electrical Engineering in 2014. Since 2016 he is a Chef Assistant Professor in the same institution. His main scientific and research interests are associated with simulations and modeling of memristors and memristive circuits, electronic elements and devices. He has been a reviewer in several scientific conferences – ICEST, ECCTD.

otrzymano/received: 08.12.2017 *przyjęto do druku/accepted: 11.05.2018*

DOI: 10.5604/01.3001.0012.0698

MATHEMATICAL MODELING AND CONTROL SYSTEM OF NEARLY ZERO ENERGY BUILDING

Ildar A. Sultanguzin[1], Hannes Toepfer[2], Ivan D. Kalyakin[1], Alexandr V. Govorin[1], Ekaterina V. Zhigulina[1], Sergey Yu. Kurzanov[1], Yury V. Yavorovsky[1]
[1]Department of Industrial Thermal Engineering Systems, National Research University "MPEI", [2]Institute for Information Technology, Technische Universität Ilmenau

Abstract. *The article examines three different kinds of mathematical model of nearly zero energy building. The first model enables to optimize the structure and the definition of key parameters of energy efficient building. The second model is necessary for passive house designing with renewable energy sources. The third model should be used for monitoring and control of energy supply system of nearly zero energy building through year every hour of winter and summer.*

Keywords: control system, mathematical model, monitoring, passive house, zero energy building

MODELOWANIE MATEMATYCZNE I SYSTEM STEROWANIA BUDYNKIEM NIEMAL ZEROENERGETYCZNYM

Streszczenie. *W artykule rozważono trzy różne typy matematycznego modelu budynku o niemal zerowym zużyciu energii. Pierwszy model pozwala zoptymalizować strukturę i definicję kluczowych parametrów budynku energooszczędnego. Drugi model jest niezbędny do zaprojektowania domu pasywnego wykorzystującego odnawialne źródła energii. Trzeci model powinien być stosowany do godzinowego monitorowania i monitorowania systemu energetycznego budynku o niskim zużyciu energii przez cały rok.*

Słowa kluczowe: układ sterowania, model matematyczny, monitoring, dom pasywny, budynek zeroenergetyczny

Introduction

The 4th industrial revolution is a stage of development, which spreads new abilities in science, technologies, life. And the more benefits it provides, the more knowledge is to be known, the more information is to be managed. At present, when we are trying to reduce energy consumption by developing old or creating new technologies, it is vital to modernize the main consumers – buildings, where we live. Year by year buildings become bigger, the amount of occupants is growing, which makes all systems more complicated.

In current work the subject of research is a two-storey nearly zero house with 160 m^2 of living space. The design of its energy supply system can be divided in three stages:

- selection of technologies, which are nearest to optimum;
- creation of mathematical model for each configuration;
- data collection and control system.

1. Optimization model

In Russia construction of energy-efficient buildings with minimum energy consumption – is one of the basic tasks in solving of energy saving problems. Here optimum solutions are to be estimated for north, moderate and south climate zones taking into account their specific characteristics.

The solution for the optimization task through a mathematical model allows to determine the optimum parameters of energy supply system at which power independence of the considered object would be reached. It will allow to use the renewable energy and to preserve fossil fuels that is urgent because of existing reserves exhaustion

The problem of optimization of creation of energy efficient buildings [4, 10] analogously with the optimization problem of integrated steelworks and heat power installations [11] could be formulated as follows (1) – (6).

A problem concerning optimization of the energy supply system of building could be formulated as a mathematical problem in the following manner.

It is necessary to determine such parameters X and a type of the thermal scheme S that is

$$C_\Sigma = F(X, Y(X), Z_K, S, A) \rightarrow min \quad (1)$$

with constraints

- in the form of equations

$$E(X, Y(X)) = 0 \quad (2)$$

- in the form of inequalities

$$Y^* < Y(X) < Y^{**} \quad (3)$$

optimized parameters:
of energy sources

$$X_{SOUR}^* < X_{SOUR} < X_{SOUR}^{**} \quad (4)$$

of energy saving technologies

$$X_{TECH}^* < X_{TECH} < X_{TECH}^{**} \quad (5)$$

of energy storages

$$X_{STOR}^* < X_{STOR} < X_{STOR}^{**} \quad (6)$$

for $A = A_0$, where X – is a set of independent parameters, Y – is a set of the dependent parameters determined through system of the equations (2).

In order that energy efficiency optimization was conducted by the form of the thermal scheme of power technologies at building, it is necessary that the indicator S includes all possible varieties of thermal schemes types defined as a result of the analysis of functioning of energy supply system. Indicators of external factors at the solution of this task are considered to be set, i.e. $A = A_0$. Mainly the climatic conditions, technical and economic values necessary for determination of separate elements of the power equipment costs, costs of fuel, depreciation, repair, etc. enter set of indicators A.

As criterion of optimization C_Σ the minimum of the total expenses including capital and operational expenditure for construction and the equipment, cost of the consumed energy resources and damage from impact of harmful emissions on the environment during the building life cycle could be chosen.

As the optimized parameters X could be used:

- various energy resources (natural gas, biomass, electric power, solar energy, wind power, warmth of soil, etc.);
- modern construction materials (gas-concrete blocks, mineral basalt wool, expanded polystyrene, polyurethane foam, etc.);
- energy saving technologies (heat pumps, recuperation of air and water waste heat, solar collector, solar photovoltaic (PV) panels, wind power installations);
- covering of basic and pick loads for energy supply of building (heating, hot water supply, ventilation, conditioning, power supply);
- volume of energy storages (the accumulators of hot water, rechargeable batteries, compressed air energy storage, etc.).

The solution of an optimizing task on mathematical model will allow determining the optimum parameters of energy supply system at which power independence of the considered object would be reached. It will allow preserving fossil fuels that is urgent at exhaustion of their reserves.

2. Passive House Model

The designing mathematical model is created in PHPP (Passive House Planning Package) and designPH software [3, 6], and it allows find the parameters of energy supply system with the lowest energy consumption (see Fig. 1).

According to passive house concept and PHPP software we could find decision which allows to decrease the energy consumption to 38 kWh/(m^2a) [10]. Next step is the active house concept implementation for designing nearly zero energy building, based on the renewable energy resources (solar energy, wind energy).

In current work the subject of research is a two-storey net zero house with 160 m^2 of living space. The designing of its energy system can be divided in three stages:

- selection of technologies, which are the nearest to optimum;
- creation of mathematical model for each configuration;
- data manipulation.

Configuration with geothermal heat pump as main energy source and gas boiler as auxiliary, solar collectors, photovoltaic panels as additional renewable energy source was selected. The mathematical model is created in PHPP (Passive House Planning Package) and designPH software, and it allows to find parameters of system with the lowest energy consumption.

The results of energy demand calculations for different system configurations are presented in the Table Configuration "Compact heat pump (HP) unit" ("compact heat pump") means the usage the air heat that is removed from the premises as the low-grade heat source.

Configuration with geothermal heat pump as main energy source, wooden fireplace, gas boiler, ventilation with heat recovery, solar collectors, photovoltaic panels, as auxiliary energy sources has been selected (Fig. 2).

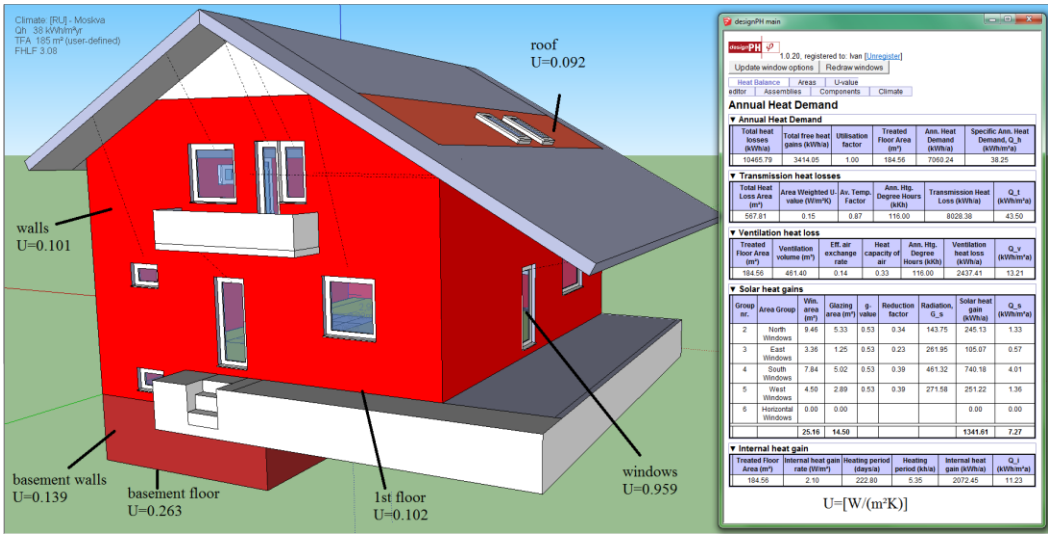

Fig. 1. Result of design of building in design PH and PHPP software

Table 1. Results of energy demand calculations for different system configurations

	Geothermal heat pump	Gas boiler	„Compact HP unit"	Water-air heat pump
Primary energy demand, $\frac{kW \cdot h}{a}$	8089	13099	10004	13233
Specific primary energy demand, $\frac{kW \cdot h}{m^2 \cdot a}$	108	126	113	135
Specific space heating energy demand, $\frac{kW \cdot h}{m^2 \cdot a}$	42	46	42	41

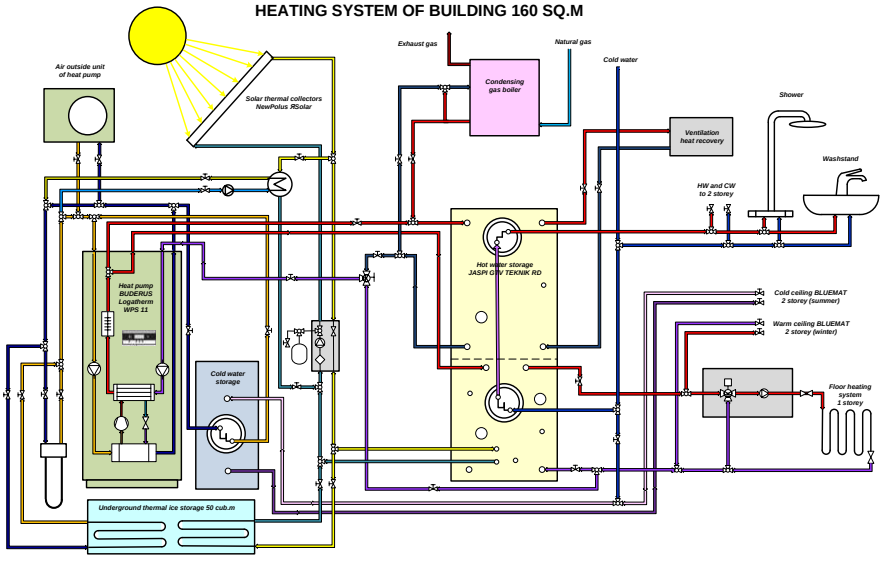

Fig. 2. Heating system of the building under consideration

3. Monitoring and control system

The next stage is to define how to collect sensory information and to influence the required element, how to manage data and to control all the parameters in every significant part of energy supply system. The creation of monitoring and control system has a great importance.

Now the task is to create a model of control system and define its optimal configuration for the most effective exploitation of energy supply system in winter and summer. The main problem of multi-energy systems in buildings is to combine the performance of different sources of energy to hold comfortable microclimatic parameters and achieve nearly zero energy balance any time. And beside the problem of energy streams management at present moment, there is more significant one – season energy storage. The remote operation should be organized in order to minimize the energy consumption in periods when the building is vacant.

Automated building management system (BMS) is designed to automate the processes and operations that are implemented in modern buildings. In literature BMS usually implies the automation of building engineering systems: ventilation, heating and air conditioning, water supply and sewerage, electricity and lighting, etc.

There are upper level and lower level organization of the smart home (see Fig. 3). The upper level is the interaction of man and control your smart home based on interfaces. The lower level is the direct interaction of a unified system of collecting and processing information and various device-based data transfer protocols. Data transfer protocol - a set of agreements interface logic levels that define the data exchange between different programs.

Wired and wireless protocols have a number of advantages and disadvantages. Wired ones require a large number of wires around the house for all appliances, but less susceptible to interference like wireless and have significantly less electromagnetic impact on human health. It is quite easy to organize wireless protocols, that almost do not require the carrying out communications with the exception of power supply.

The project of Building Management System (BMS) [9] implies realization of intelligent climate, lighting, appliances and security controls that consider and comprise the following:

- heat load regulators depending on the outdoor air temperature and on the individual schedules,
- load redistribution between the systems when using the multiple energy systems in the building,
- safety sensors usage for water overheating in the heating circuit, prevention burner extinction,
- intelligent control of water flow, of water turning off, of heating water in the tanks batteries, depending on the schedule and consumption,
- intelligent control of the lighting will include controlling not only the switching on and off lighting, but also the position of the curtains, shutters and blinds,
- intelligent control of electrical appliances,
- security sensors application: sensors of gas contamination, fire, flooding.

For thermal and electric energy saving in heating, ventilation and air-conditioning there should be organized daily parameters control in each room, given the people presence and working in the premises of various household appliances and lighting, insulation, open doors.

Thermal and electric energy savings for heating hot water can be achieved by taking into account the consumption during the day and thereby regulating the amount of hot water supply during the day. It is possible to provide the flow of hot and cold water directly to the moment when it is used, same as it is organized in public areas in order to save heat, electricity and water consumption. In case of damage or depressurization of the water system the water flow should be stopped.

Energy savings can be achieved by automatic disconnection of lighting in those areas where there are no people or in those areas where sufficient illumination through daylight. Savings could be achieved by de-energizing part of the smart building system that is not used. Also there should be created profiles with settings for a specific user or a specific situation for better efficiency and convenience.

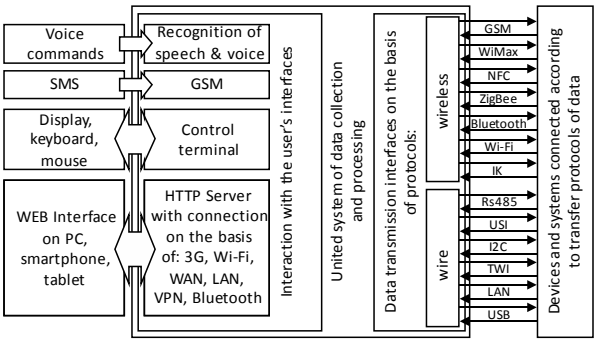

Fig. 3. Key diagram of the scheduled intelligent house organization

It is possible to achieve high-quality results on energy saving and comfortable living due to integration data systems into a unified system of collecting and processing information.

The principle of creating and functioning of the road traffic system management monitoring based on wireless sensors and data transmission via Internet [12] can be used in monitoring systems and smart house management. In particular, on the basis of meteorological forecast for 1 – 2 days obtained via the Internet may be the best option for the energy system of the smart home. When the weather forecast is changing, then the control programs of the energy supply system of the smart house will also be changed. The system of smart environments for energy savings consist of sensors embedded in an environment that allow a control system to perceive its current state [13].

The method for forecasting the load for space heating in a single-family house is presented in [1]. The forecasting model is built using data from houses located in Denmark, combined with local climate measurements and weather forecasts. Every hour the hourly heat load for each house the following two days is forecasted. Identification of a model, which is suitable for all the houses, is carried out. New approach to online forecasting of power production from PV systems explains in [2]. The suggested method is a two-stage method where first a statistical normalization of the solar power is obtained using a clear sky model. In the work [13] the heat dynamics of a storage tank were modelled on the basis of data and maximum likelihood methods. The grey-box model was used for Economic Model Predictive Control (MPC) of the energy in the tank. The control objective was to balance the energy from a solar collector and the heat consumption in a residential house. It is proposed to integrate a price-sensitive control to enable the storage tank to serve a smart energy system in which flexible consumers are expected to help balance fluctuating renewable energy sources like wind and solar. Through simulations, the impact of applying Economic MPC shows annual electricity cost savings up to 25–30% [7].

Another work [15] shows that the building automation systems (BAS) are capable of managing building operational performance in an efficient and convenient way. The amount of real-time monitoring and control data in BAS grows continually in the building life cycle, which stimulates an intense demand for powerful big data analysis tools in BAS. Time series data mining methodology for temporal knowledge discovery in big BAS data is presented in this paper. The methodology has been applied to analyze the BAS data retrieved from a real building.

Large amounts of data are increasingly accumulated in the energy sector with the continuous application of sensors, wireless transmission, network communication, and cloud computing technologies [5]. It considers the sources and characteristics of energy big data. Also, a process model of big data driven smart energy management is proposed. There are four important aspects of BAS: power generation side management, microgrid

and renewable energy management, asset management and collaborative operation, as well as demand side management. It points out the challenges of big data-driven smart energy management in IT infrastructure, data collection and governance, data integration and sharing, processing and analysis, security and privacy, and professionals [5]. It is necessary to use the system approach of big data analysis for smart energy management on the base of the last investigations in the field of monitoring and control systems [1, 2, 5, 7, 8, 12–15].

4. Conclusion

The investigated nearly zero energy building has been examined by means of three different kinds of mathematical model that were developed via PHPP and the designPH software. First model is needed for optimization of structure and definition of key parameters of energy efficient building. Second model has been used for design of passive house with renewable energy sources in energy supply system. Third model should be used for monitoring and control of energy supply system of nearly zero energy building through year every hour of winter, spring, summer and autumn.

It is necessary to pursue collaborative Russian-German research in decision of optimization task, in modeling of buildings, and in development of monitoring and control of nearly zero energy buildings.

References

[1] Bacher P., Madsen H., Nielsen H.A., Perers B.: Short-term heat load forecasting for single family houses. Energy and Buildings 38/2006, 63–71.
[2] Bacher P., Madsen H., Nielsen H.A.: Online short-term solar power forecasting. Solar Energy 83/2009, 1772–1783.
[3] Cemesova A. et al.: PassivBIM: Enhancing interoperability between BIM and low energy design software. Automation in Construction 57/2015, 17–32.
[4] Fabrizio E. et al.: A model to design and optimize multi-energy systems in buildings at the design concept stage. Renewable Energy 35/2010, 644–655.
[5] Fan Ch. et al.: Temporal knowledge discovery in big BAS data for building energy management. Energy and Buildings 109/2015, 75–89.
[6] Feist V.: Die Hauptlagen nach der Projektierung der passiven Häuser. Konti Print, Moscow 2015.
[7] Halvgaard R. et al.: Model predictive control for a smart solar tank based on weather and consumption forecasts. Energy Procedia 30/2012, 270–278.
[8] Michailidis I.T. et al.: Proactive control for solar energy exploitation: A german high-inertia building case study. Applied Energy 155/2015, 409–420.
[9] Oti A.H. et al.: A framework for the utilization of Building Management System data in building information models for building design and operation. Automation in Construction 72/2016, 195–210.
[10] Sultanguzin I., Kalyakin I., Govorin A., et.al.: Optimization of the energy efficient active house. 3 Ingenieurtag 2016. Neseff-Netzwerktreffen 2016. Tagungsband. Branden-burgische Technische Universität. Cottbus-Senftenberg. 14-15 November 2016, 8–12.
[11] Sultanguzin I.A., Isaev M.V., Kurzanov S.Yu.: Optimizing the production of coke, coal chemicals, and steel on the basis of environmental and energy criteria. Metallurgist 54/2011, 600–607.
[12] Toepfer H., Goetze M., Chervakova E., Hutschenreuther T.: On the Use of Wireless Sensors Within a Traffic Monitoring System. Proceedings of the International Academic Forum AMO–SPITSE–NESEFF. Smolensk Publishing "Universum", Moscow–Smolensk 2016.
[13] Torunski E. et al.: A review of smart environments for energy savings. Procedia Computer Science 10/2012, 205–214.
[14] Wang Y., Kuckelkorn J., Liu Y.: State of art review on methodologies for control strategies in low energy buildings in the period from 2006 to 2016. Energy & Buildings 147/2017, 27–40.
[15] Zhou K. et al.: Big data driven smart energy management: From big data to big insights. Renewable and Sustainable Energy Reviews 56/2016, 215–225.

Prof. Ildar A. Sultanguzin
e-mail: sultanguzinia@mpei.ru

Professor of the Department of Industrial Thermal Engineering Systems, National Research University "MPEI", Moscow, Russia.
He had defended a Ph.D. thesis "Rational Creation of Converter Gas Accumulation System under Pressure on the Base of Mathematical Modelling" in December 1985 and a doctoral dissertation "Scientific and Technical Foundation of Integrated Steelworks Energotechnological System Modeling and Optimization" in September 2005.

Prof. Hannes Toepfer
e-mail: Hannes.Toepfer@tu-ilmenau.de

He gained the Dr.-Ing. (equiv. Ph.D,) in 1996 and in 2003 the habilitation degree. From 2009 on, he is a Full Professor at Technische Universität Ilmenau and heading the Advanced Electromagnetics Lab with a research focus on electromagnetic sensors. He is a senior member of the IEEE.

B.Sc. Ivan D. Kalyakin
e-mail: albanec1@mail.ru

I. Kalyakin is a student of Moscow Power Engineering Institute and is getting a Master`s Degree course at the department of Industrial Heat-and- power Systems. The theme of the bachelor`s work was "The design of energy-supply system of nearly zero energy building". He is interested in mathematical modeling and have skills of work in such software, as Passive House Planning Package, SketchUp, AutoCad, MathCad, Aspen Hysys.

M.Sc. Alexandr V. Govorin
e-mail: a.govorin@mail.ru

He is Ph.D. student at the Department of Industrial Heat Power Engineering Systems, NRU MPEI, Russia

Ph.D. Ekaterina V. Zhigulina
e-mail: zhigulinayv@mpei.ru

She is associate professor at the Dept. of Industrial Heat Power Engineering Systems, Deputy director of Energy Efficiency Issues Institute, NRU MPEI, Russia.
E. Zhigulina is a co-author of 2 books (in Russian) and around 25 papers in peer-reviewed journals for a total of about 30 papers in journals, book chapters, and conference proceedings.

Ph.D. Sergey Yu. Kurzanov
e-mail: KurzanovSU@mpei.ru

He is Associate Professor of the Department of Industrial Heat Power Engineering Systems, NRU MPEI, Russia.
S. Kurzanov is a co-author of 2 books (in Russian) and around 15 papers in peer-reviewed journals for a total of about 25 papers in journals, book chapters, and conference proceedings.

Ph.D. Yury V. Yavorovsky
e-mail: YavorivskyYV@mpei.ru

He is Head of the Department of Industrial Heat Power Engineering Systems, NRU MPEI, Russia.
Y. Yavorivsky is a co-author of 4 books (in Russian) and around 32 papers in peer-reviewed journals for a total of about 40 papers in journals, book chapters, and conference proceedings.

otrzymano/received: 08.12.2017 *przyjęto do druku/accepted: 11.05.2018*

DOI: 10.5604/01.3001.0012.0699

HARMONIC DOMAIN MODEL OF AN OPEN-LOOP CONTROLLED PWM CONVERTER

Malte John, Axel Mertens
Leibniz Universität Hannover, Institute for Drive Systems and Power Electronics

Abstract. *An harmonic domain model is developed for open-loop controlled voltage source inverters, which provides the steady-state solution for integer multiples of the fundamental frequency. The convolution of the switching function spectrum with the converter currents and voltages is used to describe the coupling of the AC side and the DC side. The modeling is based on a single phase leg and is extended to a single-phase and a three-phase voltage source inverter, which results in a non-linear algebraic equation system. For open-loop control the switching function is independent of the converter currents and voltages and the model is simplified to a linear equation system. This straightforward and fast model is verified by time domain simulations and experimental results. The modeling can be adapted to systems of coupled converters, which is presented for a back-to-back converter system showing the harmonic interaction of the connected subsystems.*

Keywords: frequency-domain analysis, Power conversion harmonics

CZĘSTOTLIWOŚCIOWY KONWERTER PWM ZE STEROWANIEM W OTWARTEJ PĘTLI

Streszczenie. *Opracowano model w domenie częstotliwości dla falowników napięcia sterowanych w otwartej pętli, który zapewnia rozwiązanie w stanie ustalonym dla całkowitych wielokrotności częstotliwości podstawowej. Splot spektrum funkcyjnego przełączania z prądami i napięciami przemiennika służy do opisania sprzężenia strony prądu przemiennego i prądu stałego. Modelowanie opiera się na pojedynczej fazie i jest rozszerzone na falownik jednofazowy i trójfazowy, co skutkuje nieliniowym układem równań algebraicznych. W przypadku sterowania w otwartej pętli funkcja przełączania jest niezależna od prądów i napięć przekształtnika, a model jest uproszczony do układu równań liniowych. Ten prosty i szybki model jest weryfikowany przez symulacje w dziedzinie czasu i wyniki eksperymentalne. Modelowanie może być dostosowane do systemów przekształtników sprzężonych, które przedstawiono dla systemu konwertera równoległego pokazującego harmoniczne oddziaływanie połączonych podsystemów.*

Słowa kluczowe: analiza w dziedzinie częstotliwości, harmoniczne konwersji mocy

Introduction

The accurate assessment of the harmonic behavior of power electronic converters is required during various design steps, e.g. filter design, capacitor lifetime estimation, converter control, and electromagnetic interference performance. Therefore, the steady-state behavior of the pulse-width modulated (PWM) voltage source inverter (VSI) is widely studied. Describing the converter switching state with a switching function s, the impact of the PWM process on the voltages and currents can be described. Double Fourier integral analysis [3, 4], is used to derive the output voltage spectrum analytically. Assuming a constant DC link voltage and a sinusoidal input signal with constant modulation index M, the output voltage spectrum u_{ac} is derived as the multiplication of the phase leg switching functions s and the half of the DC link voltage $u_{\mathrm{dc}}/2$. Furthermore, the spectrum of the DC link current is developed in [2] using double Fourier integral analysis and in [8] by convolving the spectrum of the switching functions and the spectrum of the phase currents. In [11] an expression for the switching function spectrum for arbitrary band-limited input signals is developed, which allows to incorporate harmonic input signals and overcomes the limitation to single-frequency input signals.

With these methods the relationships of the converter voltages and currents are described accurately. However, the converter is connected to an electrical circuit of sources, loads, linear and non-linear components. Forming a closed-loop system, the DC-side quantities influence the AC-side quantities, and vice versa. Therefore, all system equations have to be solved together, in order to cover the reactions.

Modeling the interaction of coupled-converter systems is a challenging task, due to the complexity of the system and the number of modeled effects. In [4] the harmonic and interharmonic behavior of a drive system of a passive rectifier and a VSI feeding an induction motor is studied in the time-domain. The coupling of all system quantities is covered, however it remains unclear if the equations are solved simultaneously and therefore covers any reactions. A closed-loop controlled DC/DC converter system is modeled in [12]. The harmonic interaction is covered in a matrix representation. However, a small-signal assumption is used for the harmonic interaction in the PWM process.

Solving the system equations in the frequency domain allows a direct solution for the steady state, which provides an additional tool for the engineer allowing a different view on the system. Moreover, the computing time can be lower than for time-domain simulations, as no transients are modeled. The harmonic domain is introduced as a subspace of the frequency domain, where only integer multiples of a fundamental frequency are defined. A system of non-linear equations describes the steady state with the harmonics as coupled variables. Solutions can be obtained by iterative methods that have been reported for various AC/DC converter systems [1].

Extensive studies have been published for AC/DC converter systems based on line-commutated converters [10] and use a convolution method to determine the AC/DC conversion and solve the system equations based on the Newton method.

The harmonic domain modeling has been adapted to a PWM-VSI based STATCOM in [6] with a modulator model, which is an extension of a modulator model for a six-pulse thyristor bridge in [10]. In [9] a harmonic domain model for a single-phase and a three-phase VSI for photovoltaic systems is presented. Both publications use iterative solution methods. The switching function spectra are solved in the time domain, requiring the solution to be separated from the solution of the system equations.

In this paper, the harmonic domain model of the single-phase and three-phase VSI is derived. We show that for open-loop control the non-linearity of AC/DC conversion is simplified to a linear equation system by means of discrete convolution. The resulting equation system is linear, allowing a direct, non-iterative solution method. The models are easily extended to a coupled converter system.

1. Model development

1.1. Model of one VSI phase leg

The fundamental building block of a VSI is one inverter phase leg (one half bridge) (Fig. 1). The upper and lower IGBTs in each phase leg ν are switched comparatively. Assuming ideal switching behavior without interlocking time (“dead time”), each phase leg can be replaced by a single-pole double-throw switch with the switching function

$$s_\nu \in \{-1,1\} \tag{1}$$

The switching function is used to provide the algebraic connection of the AC-side voltage and current ($u_{\mathrm{ac}}, i_{\mathrm{ac}}$) and the DC-side voltage and current ($u_{\mathrm{dc}}, i_{\mathrm{dc}}$).

$$i_{\mathrm{dc}\nu}(t) = \frac{1}{2}\left(i_{\mathrm{dcp}\nu}(t) - i_{\mathrm{dcn}\nu}(t)\right) = \frac{1}{2}\cdot s_\nu(t)\cdot i_{\mathrm{ac}\nu}(t) \tag{2}$$

$$u_{\mathrm{ac}\nu}(t) = \frac{1}{2}\cdot s_\nu(t)\cdot u_{\mathrm{dc}}(t) \tag{3}$$

Note that the DC-side current of a single half bridge is merely a fictive current. Transforming the equations to the harmonic domain yields a discrete convolution of the spectra for the calculation of the k-th harmonic of the fundamental angular frequency ω_0 denoted with the subscript '$,k$':

$$\underline{i}_{\mathrm{dc}\nu,k} = \left[\frac{1}{2}\cdot \underline{\boldsymbol{s}}_\nu(k) * \underline{\boldsymbol{i}}_{\mathrm{ac}\nu}(k)\right]_{,k} = \frac{1}{2}\cdot \sum_{m=-\infty}^{\infty} \underline{s}_{\nu,m}\cdot \underline{i}_{\mathrm{ac}\nu,(k-m)} \tag{4}$$

$$\underline{u}_{\mathrm{ac},k} = \left[\frac{1}{2}\cdot \underline{\boldsymbol{s}}_\nu(k) * \underline{\boldsymbol{u}}_{\mathrm{dc}}(k)\right]_{,k} = \frac{1}{2}\cdot \sum_{m=-\infty}^{\infty} \underline{s}_{\nu,m}\cdot \underline{u}_{\mathrm{dc}\nu,(k-m)} \tag{5}$$

The spectrum of the switching function is represented in the vector $\underline{\boldsymbol{s}}_\nu(k)$ that contains the complex Fourier coefficients as the elements $\underline{s}_{\nu,k}$:

$$s_\nu(t) = \sum_{k=-\infty}^{\infty} \underline{s}_{\nu,k}\cdot \mathrm{e}^{\mathrm{j}k\omega_0 t} \tag{6}$$

In general, the convolution represents the coupling of the harmonics of the converter currents and voltages of AC and DC side.

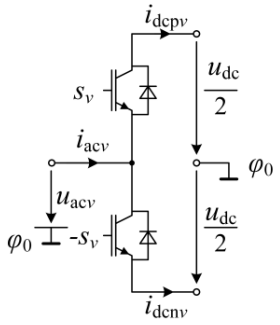

Fig. 1. One inverter phase leg

1.2. Single-phase VSI model

The single-phase VSI in Fig. 2 consists of two inverter phase legs (one full bridge). The inductance L_{ac} and the resistance R_{ac} represent a linear AC-side filter, and the capacitance C_{dc} and the resistance R_{dc} a linear DC-side filter. Disturbances (e.g. grid, machine or other converter) are incorporated by a voltage source u_{dis} on the AC side and by a current source i_{dis} on the DC side. The connection of the two phase legs yields

$$i_{\mathrm{ac}}(t) = i_{\mathrm{ac1}}(t) = -i_{\mathrm{ac2}}(t) \tag{7}$$

$$u_{\mathrm{ac}}(t) = u_{\mathrm{ac1}}(t) - u_{\mathrm{ac2}}(t), \tag{8}$$

and the converter system equations are obtained by applying the equations of one inverter phase leg to the single-phase VSI:

$$i_{\mathrm{dc}}(t) = \frac{1}{2}\cdot\left(s_1(t) - s_2(t)\right)\cdot i_{\mathrm{ac}}(t) \tag{9}$$

$$u_{\mathrm{ac}}(t) = \frac{1}{2}\cdot\left(s_1(t) - s_2(t)\right)\cdot u_{\mathrm{dc}}(t) \tag{10}$$

The linear AC-side and DC-side filters are described for each harmonic individually by their harmonic transfer functions with the AC-side impedance

$$\underline{z}_{\mathrm{ac},k} = \frac{1}{\underline{y}_{\mathrm{ac},k}} = R_{\mathrm{ac}} + \mathrm{j}k\omega_0 L_{\mathrm{ac}}\,, \tag{11}$$

and the DC-side admittance

$$\underline{y}_{\mathrm{dc},k} = \frac{1}{\underline{z}_{\mathrm{dc},k}} = \frac{1}{R_{\mathrm{dc}}} + \mathrm{j}k\omega_0 C_{\mathrm{dc}}\,. \tag{12}$$

The complete converter system is described by the following four equations:

$$\underline{i}_{\mathrm{ac},k} = y_{\mathrm{ac},k}\cdot\left(\underline{u}_{\mathrm{dis},k} - \underline{u}_{\mathrm{ac},k}\right) \tag{13}$$

$$\underline{u}_{\mathrm{dc},k} = \underline{z}_{\mathrm{dc},k}\cdot\left(\underline{i}_{\mathrm{dis},k} + \underline{i}_{\mathrm{dc},k}\right) \tag{14}$$

$$\begin{aligned}\underline{i}_{\mathrm{dc},k} &= \left[\frac{1}{2}\cdot\left(\underline{\boldsymbol{s}}_1(k) - \underline{\boldsymbol{s}}_2(k)\right) * \underline{\boldsymbol{i}}_{\mathrm{ac}}(k)\right]_{,k} \\ &= \frac{1}{2}\cdot\sum_{m=-\infty}^{\infty}\left(\underline{s}_{1,m} - \underline{s}_{2,m}\right)\cdot \underline{i}_{\mathrm{ac},(k-m)}\end{aligned} \tag{15}$$

$$\begin{aligned}\underline{u}_{\mathrm{ac},k} &= \left[\frac{1}{2}\cdot\left(\underline{\boldsymbol{s}}_1(k) - \underline{\boldsymbol{s}}_2(k)\right) * \underline{\boldsymbol{u}}_{\mathrm{dc}}(k)\right]_{,k} \\ &= \frac{1}{2}\cdot\sum_{m=-\infty}^{\infty}\left(\underline{s}_{1,m} - \underline{s}_{2,m}\right)\cdot \underline{u}_{\mathrm{dc},(k-m)}\end{aligned} \tag{16}$$

The equations (13) to (16) describe the system for one harmonic. Limiting the description to $k_{\max}$ harmonics, the vectors $\underline{\boldsymbol{u}}_{\mathrm{ac}}, \underline{\boldsymbol{i}}_{\mathrm{ac}}, \underline{\boldsymbol{u}}_{\mathrm{dc}}, \underline{\boldsymbol{i}}_{\mathrm{dc}}$ have the length $l = 2\cdot k_{\max} + 1$. The equations can be used to eliminate three of the unknown spectra. Equation (17) gives the final equation for the k-th harmonic with $\underline{\vec{U}}_{\mathrm{dc}}$ as the remaining variable. $\boldsymbol{D}\left(\underline{\boldsymbol{y}}_{\mathrm{ac}}(k)\right)$ is a diagonal matrix with $\underline{y}_{\mathrm{ac},k}$ as the k-th diagonal element.

$$\begin{aligned}&\underline{y}_{\mathrm{dc},k}\,\underline{u}_{\mathrm{dc},k} + \\ &\frac{1}{4}\left[\left(\underline{\boldsymbol{s}}_1(k) - \underline{\boldsymbol{s}}_2(k)\right) * \boldsymbol{D}\left(\underline{\boldsymbol{y}}_{\mathrm{ac}}(k)\right)\left(\underline{\boldsymbol{s}}_1(k) - \underline{\boldsymbol{s}}_2(k)\right) * \underline{\boldsymbol{u}}_{\mathrm{dc}}(k)\right]_{,k} = \\ &\underline{i}_{\mathrm{dis},k} + \frac{1}{2}\left[\left(\underline{\boldsymbol{s}}_1(k) - \underline{\boldsymbol{s}}_2(k)\right) * \boldsymbol{D}\left(\boldsymbol{y}_{\mathrm{ac}}(k)\right)\boldsymbol{u}_{\mathrm{dis}}(k)\right]_{,k}\end{aligned} \tag{17}$$

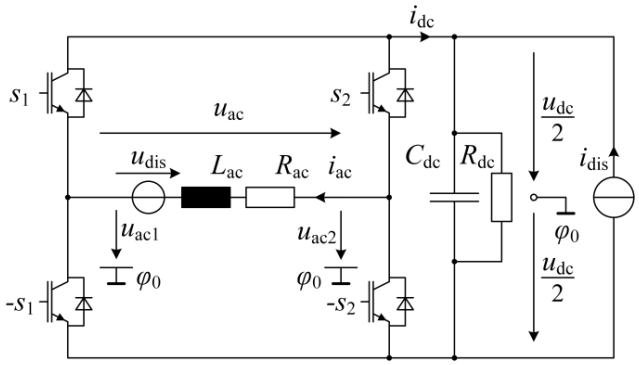

Fig. 2. Single-phase VSI

1.3. Three-phase VSI model

The three-phase VSI in Fig. 3 comprises three phase legs (three half-bridges).

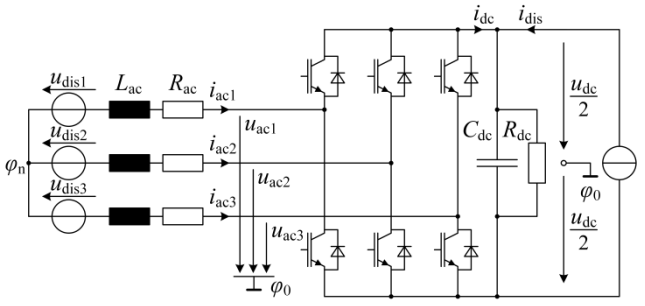

Fig. 3. Three-phase VSI

The AC-side disturbance consists of three individual voltage sources connected to the neutral point φ_n Adapting the previous equations to the three phase legs, denoted with $\nu \in \{1,2,3\}$, yields:

$$i_\mathrm{dc}(t) = \frac{1}{2} \cdot \sum_{\nu=1}^{3} s_\nu(t) \cdot i_{\mathrm{ac}\nu}(t) \tag{18}$$

$$u_{\mathrm{ac}\nu}(t) = \frac{1}{2} \cdot s_\nu(t) \cdot u_\mathrm{dc}(t) \tag{19}$$

$$\vec{I}_\mathrm{dc} = \frac{1}{2} \cdot \sum_{\nu=1}^{3} \vec{S}_\nu * \vec{I}_{\mathrm{ac}\nu} \tag{20}$$

$$\vec{U}_{\mathrm{ac}\nu} = \frac{1}{2} \cdot \vec{S}_\nu * \vec{U}_\mathrm{dc} \tag{21}$$

The relationship of the DC-side current and voltage is the same as for the single-phase VSI in (14). A symmetrical filter for a three-phase system has the form

$$\underline{\boldsymbol{Y}}_{\mathrm{ac},k} = \underline{y}_{\mathrm{ac},k} \cdot \frac{1}{3} \begin{bmatrix} 2 & -1 & -1 \\ -1 & 2 & -1 \\ -1 & -1 & 2 \end{bmatrix}. \tag{22}$$

With $y_{\mathrm{ac},k}$ defined in (11), the relationship of the AC-side currents and voltages can be denoted in vector form:

$$\underline{\boldsymbol{i}}_{\mathrm{ac},k} = \underline{\boldsymbol{Y}}_{\mathrm{ac},k} \cdot (\underline{\boldsymbol{u}}_{\mathrm{dis},k} - \underline{\boldsymbol{u}}_{\mathrm{ac},k}) \tag{23}$$

Higher order filters and unsymmetrical filters can be modeled by adapting the admittance matrix $\underline{\boldsymbol{Y}}_{\mathrm{ac},k}$.

1.4. Model for coupled VSI

Connecting two converters A and B in the DC link (back-to-back configuration) allows the coupling of two AC networks of different fundamental frequencies, e.g. a drive system with grid connection and variable speed drive. The DC-side current of converter A (i_dcA) can be considered as the disturbance current of converter B, and vice versa. In order to represent the interaction of both systems, the overall equation system has to be solved together using the coupling relationship of the DC link:

$$\underline{y}_{\mathrm{dc},k} \cdot \underline{u}_{\mathrm{dc},k} = \underline{i}_{\mathrm{dcA},k} + \underline{i}_{\mathrm{dcB},k} \tag{24}$$

The fundamental frequency of the overall system is the greatest common divisor of both systems' fundamental frequencies:

$$f_0 = \gcd(f_{0\mathrm{A}}, f_{0\mathrm{B}}) \tag{25}$$

A connection of two converters on the AC side can be applied similarly by substituting the disturbance voltage of one system with the AC-side voltage of the other system.

2. Solution method and results

For an open-loop controlled converter, the modulator input is independent of the system variables. Therefore, the spectrum of the switching function $\underline{\boldsymbol{s}}_\nu$ can be calculated in advance. As it forms a discrete line spectrum, a discrete convolution results in no loss of accuracy. The switching spectrum can be seen as a set of parameters, and (17) becomes a linear equation.

Limiting the number of harmonics to k_max, an approximation is performed, leading to a linear equation system $\underline{\boldsymbol{A}}\,\underline{\boldsymbol{x}} = \underline{\boldsymbol{b}}$. The system matrix $\underline{\boldsymbol{A}}$ contains the linear transfer functions and the switching function spectrum, $\underline{\boldsymbol{x}}$ comprises all harmonic variables, and $\underline{\boldsymbol{b}}$ includes the harmonics of the disturbances. All system variables are vectors with the length $l = 2 \cdot k_\mathrm{max} + 1$, as each harmonic is represented as complex Fourier coefficients with their positive and negative frequency components and the direct component.

The spectrum of the switching function is defined by the modulation process and described for various modulation methods in [7] using double Fourier integral analysis. The analysis assumes a pure sinusoidal input signal with a fixed modulation index M in the linear control range (for PWM $0 \le M \le 1$). Symmetrical regularly sampled PWM yields the time domain expression of the switching functions, cf. [7]:

$$\begin{aligned} s_\nu(t) = \frac{2}{\pi} \sum_{\substack{m=0 \\ m>0}}^{\infty} \sum_{n=-\infty}^{\infty} \frac{1}{q} J_n\left(q \frac{\pi}{2} M\right) \sin\left([q+n]\frac{\pi}{2}\right) \\ \cdot \cos(m(\omega_\mathrm{c} t + \theta_\mathrm{c}) + n(\omega_0 t + \theta_0)) \end{aligned} \tag{26}$$

$J_n(\xi)$ is the n-th order Bessel function with the argument ξ, $q = m + n\frac{\omega_0}{\omega_\mathrm{c}}$, ω_0 and ω_c are the fundamental and the carrier angular frequency, and θ_0 and θ_c are the fundamental and the carrier phase shift, respectively.

The VSI models use the spectrum of the switching function. Therefore, the complex Fourier coefficients $\underline{s}_{\nu,k}$ of the switching function are obtained by converting (26) in the form of (6). [7] also provides the Fourier representation using real coefficients (a_k, b_k) that can be transformed to the complex representation.

2.1. Single-phase VSI

Using the equations (13) to (16), the single-phase VSI (Fig. 2) can be described as the linear equation system $\underline{\boldsymbol{A}}\,\underline{\boldsymbol{x}} = \underline{\boldsymbol{b}}$:

$$\begin{bmatrix} \boldsymbol{E} & \boldsymbol{0} & \boldsymbol{H} & \boldsymbol{0} \\ \boldsymbol{E} & \boldsymbol{D}(\underline{\boldsymbol{z}}_\mathrm{ac}) & \boldsymbol{0} & \boldsymbol{0} \\ \boldsymbol{0} & \boldsymbol{0} & \boldsymbol{D}(\underline{\boldsymbol{y}}_\mathrm{ac}) & -\boldsymbol{E} \\ \boldsymbol{0} & \boldsymbol{H} & \boldsymbol{E} & \boldsymbol{0} \end{bmatrix} \begin{bmatrix} \underline{\boldsymbol{u}}_\mathrm{ac} \\ \underline{\boldsymbol{i}}_\mathrm{ac} \\ \underline{\boldsymbol{u}}_\mathrm{dc} \\ \underline{\boldsymbol{i}}_\mathrm{dc} \end{bmatrix} = \begin{bmatrix} \boldsymbol{0} \\ \underline{\boldsymbol{u}}_\mathrm{dis} \\ -\underline{\boldsymbol{i}}_\mathrm{dis} \\ \boldsymbol{0} \end{bmatrix} \tag{27}$$

All elements of the matrix $\boldsymbol{A}$ are submatrices of the size $l \times l$. The convolution matrix $\boldsymbol{H}$ is defined as the matrix that describes the convolution as a matrix multiplication

$$\underline{\boldsymbol{H}}\,\underline{\boldsymbol{u}} = \frac{1}{2}(\underline{\boldsymbol{s}}_1 - \underline{\boldsymbol{s}}_2) * \underline{\boldsymbol{u}} \tag{28}$$

$\boldsymbol{E}$ denotes the identity matrix, $\boldsymbol{0}$ is the zero matrix and $\boldsymbol{D}(.)$ is a diagonal matrix. The convolution matrix $\boldsymbol{H}$ can be easily implemented in Matlab using the function *convmtx*, resulting in a matrix of size$(2l-1) \times l$, where the convolution matrix $\boldsymbol{H}$ is the centered submatrix of size $l \times l$. The resulting block diagram of the open-loop controlled converter is given in Fig. 4.

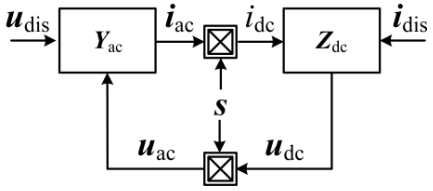

Fig. 4. Block diagram for an open-loop controlled VSI

Using (17) would result in a more compact description of the system, which can effect the numerical inversion to perform $\boldsymbol{x} = \boldsymbol{A}^{-1}\boldsymbol{b}$.

Fig. 5 shows the results for the parameters of the system given in Table 1. The modulation index has been chosen to $M = 0.4$ with zero phase shift between the fundamental components of u_dis and the modulator input ($\theta_0 = 0$). Disturbances are applied with $u_\mathrm{dis} = 40\,\mathrm{V}\sin(\omega_0 t) + 4\,\mathrm{V}\sin(11\,\omega_0)$ and $i_\mathrm{dis} = 10\,\mathrm{A} + 2\,\mathrm{A}\sin(6\,\omega_0 t)$. The harmonic domain model considers 200 harmonics ($k_\mathrm{max} = 200$). The results of the analytical model in black are compared to results of a time-domain simulation in Simulink/Plecs in red, which are the Fourier coefficients of one fundamental period of the time-domain signals after all transients being completed. There is a good agreement of both models' results.

Table 1. Styles predefined in IAPGOS template

Parameter	Symbol	Value
AC-side inductance	L_{ac}	17.5 mH
AC-side resistance	R_{ac}	300 mΩ
DC-side capacitance	C_{dc}	480 µF
DC-side resistance	R_{dc}	18 Ω
Fundamental frequency	f_0	50 Hz
Carrier frequency	f_c	1.5 kHz

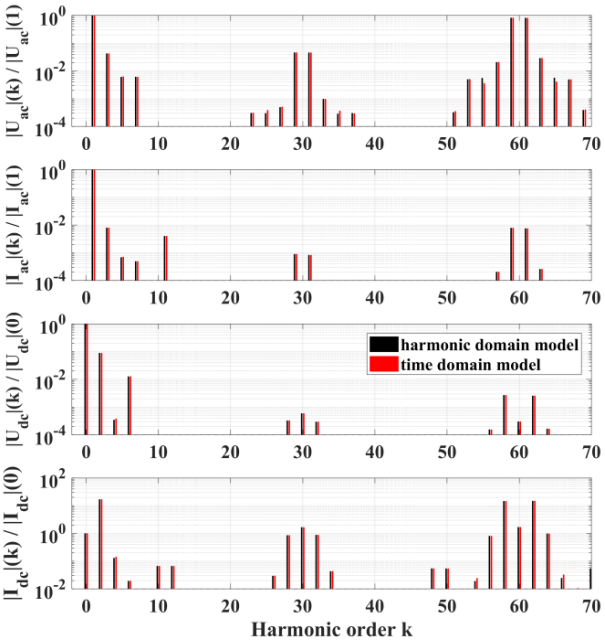

Fig. 5. Comparison of harmonic domain model (black) and time domain simulations (red) for a single-phase VSI

2.2. Three-phase VSI

For a three-phase VSI the solution method is merely an adaption to the three-phase system. Unsymmetrical filter and disturbance voltages can be applied in the model.

Fig. 6 provides a comparison of the proposed harmonic domain model, time domain simulations in Simulink/Plecs, and experimental results. The parameters of the system are the same as for the single-phase VSI in Table 1. The modulation index is set to $M = 1$. A second converter system is used to generate the symmetrical three-phase disturbance voltage with a RMS line-line voltage of 40 V. A phase-locked loop (PLL) assures no phase shifting between the fundamental components of u_{dis} and the modulator input ($\theta_0 = 0$). There is no influence of the PLL in the steady-state behavior.

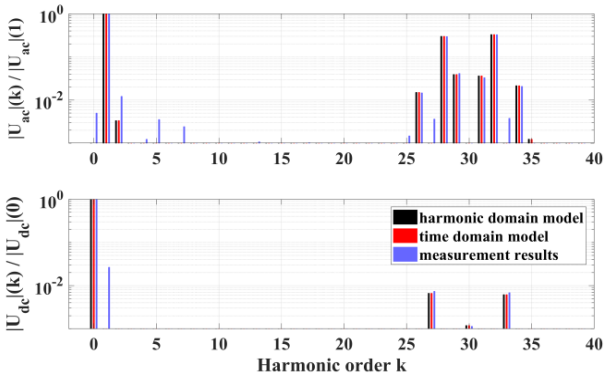

Fig. 6. Comparison of harmonic domain model (black), time domain simulations (red), and measurement results (blue) for a three-phase VSI

The harmonic domain model (black) and the time domain simulations (red) show a good conformity. There is no interlocking time modeled in both cases, which causes the deviations from the experimental results (blue), where an interlocking time is mandatory. The effects can be modeled using the approach presented in [5]. This leads to a dependency of the switching function on the phase leg current and therefore to a non-linear equation system.

2.3. Back-to-Back VSI

Two single-phase VSI are connected in a common DC link to show the interaction of converter systems. System A has a fundamental frequency of $f_{0A} = 50$ Hz and system B a fundamental frequency of $f_{0B} = 40$ Hz. For this purpose, the overall fundamental frequency is chosen to 10 Hz. Fig. 7 compares the harmonic domain model with time domain simulations. For clarity only the first 25 harmonics are shown. The single-phase- VSI of system A creates a strong 100 Hz component in the DC link, which is passed on to system B as the interharmonic of $2 \cdot f_{0A} - f_{0B} = 60$ Hz (and $2 \cdot f_{0A} + f_{0B} = 120$ Hz). The propagation back to the DC link is visible as 20 Hz (and 100 Hz). Besides other harmonics and interharmonics a 30 Hz and 70 Hz component can be explained. Again, there is a good accordance of the harmonic domain and time domain models.

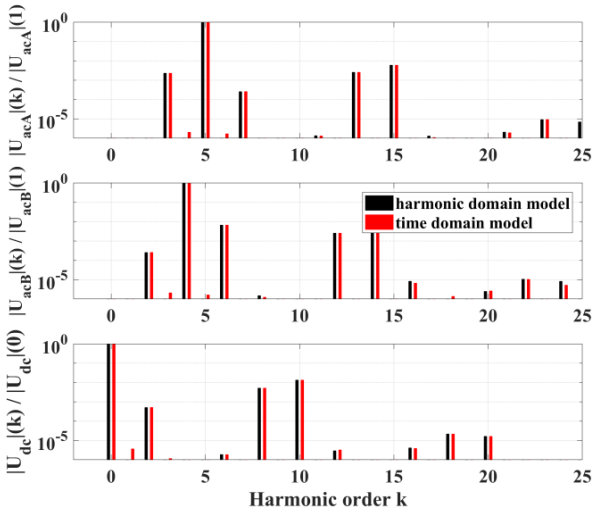

Fig. 7. Comparison of harmonic domain model (black) and time domain simulations (red) for two single-phase VSI in back-to-back configuration

3. Conclusions

As the fundamental building block of voltage source inverters, the phase leg has been analyzed in the harmonic domain and used to build models for the single- and the three-phase VSI. Applying open-loop control, the switching function spectrum is independent of the system variables. The outcome is a straightforward and quickly computable model for the steady-state spectrum, as the system equations become linear.

Whenever the switching function is dependent of the system variables, the equation system is non-linear, and an algorithm for non-linear equation systems is required, e.g. the Newton method. This includes modeling the interlocking time or closed-loop control. Moreover, the load, filters and disturbances can be non-linear or dependent on the system variables, requiring iterative solution methods.

The analytical models of single VSI can be adapted to arbitrarily coupled converter systems to analyze the harmonic interaction of the subsystems.

Acknowledgements

The authors would like to thank the Volkswagen Foundation for the financial support of this work within the project AMSES (Aggregated Models for the Simulation of Electromechanical Power Systems).

References

[1] Arrillaga J., Watson N.R.: The Harmonic Domain revisited. 13th International Conference on Harmonics and Quality of Power, 2008.
[2] Bierhoff M.H., Fuchs F.W.: DC-Link Harmonics of Three-Phase Voltage-Source Converters Influenced by the Pulsewidth-Modulation Strategy–An Analysis. IEEE Transactions on Industrial Electronics. 55(5)/2008, 2085–2092.
[3] Black H.S.: Modulation Theory. Van Nostrand, Princeton 1953.
[4] Chang G.W., Chen S.K., Su H.J., Wang P.K.: Accurate Assessment of Harmonic and Interharmonic Currents Generated by VSI-Fed Drives Under Unbalanced Supply Voltages. IEEE Transactions on Power Delivery 26(2)/2011, 1083–1091.
[5] Chierchie F., Stefanazzi L., Paolini E.E., Oliva A.R.: Frequency Analysis of PWM Inverters With Dead-Time for Arbitrary Modulating Signals. IEEE Transactions on Power Electronics 29(6)/2014, 2850–2860.
[6] Collins C.D., Bathurst G.N., Watson N.R., Wood A.R.: Harmonic domain approach to STATCOM modelling. Transmission and Distribution IEE Proceedings - Generation 152(2)/2005, 194–200.
[7] Holmes G., Lipo T.A.: Pulse Width Modulation for Power Converters: Principles and Practice. Wiley-IEEE Press, 2003.
[8] McGrath B.P., Holmes D.G.: A General Analytical Method for Calculating Inverter DC-Link Current Harmonics. IEEE Transactions on Industry Applications 45(5)/2009, 1851–1859.
[9] Nduka O.S., Pal B.C.: Harmonic Domain Modeling of PV System for the Assessment of Grid Integration Impact. IEEE Transactions on Sustainable Energy 8(3)/2017, 1154–1165.
[10] Smith B.C., Watson N.R., Wood A.R., Arrillaga J.: Steady state model of the AC/DC convertor in the harmonic domain. IEE Proceedings - Generation, Transmission and Distribution 142(2)/1995, 109–118.
[11] Song Z., Sarwate D.V.: The frequency spectrum of pulse width modulated signals. Signal Processing 83(10)/2003, 2227–2258.
[12] Yue X., Zhuo F., Yang S., Pei Y., Yi H.: A Matrix-Based Multifrequency Output Impedance Model for Beat Frequency Oscillation Analysis in Distributed Power Systems. In IEEE Journal of Emerging and Selected Topics in Power Electronics 4(1)/2016, 80–92.

M.Sc. Eng. Malte John
e-mail: malte.john@ial.uni-hannover.de

Malte John received the Dipl.-Ing. from Leibniz Universität Hannover, Germany, in 2014.
Since 2014 he has been a Ph.D. student at the Institute for Drive Systems and Power Electronics, Lebniz Universität Hannover, Germany. His main research interests includes the modeling of harmonic interactions of power electronic systems.

Prof. Axel Mertens
e-mail: mertens@ial.uni-hannover.de

Axel Mertens (S'89–M'92) received the Dipl.-Ing. and Dr.-Ing. (Ph.D.) degrees from Rheinisch-Westfaelische Technische Hochschule (RWTH) Aachen University, Germany, in 1987 and 1992, respectively. From 1993 to 2004, he was with Siemens Drive Technologies, Germany. In 2004, he was appointed Professor of power electronics and drives at Leibniz Universität Hannover, Germany. Since 2012, he has been the Head of the Department Converter Technology within the Fraunhofer Institute for Wind Energy and Energy System Technology (IWES).

otrzymano/received: 08.12.2017 *przyjęto do druku/accepted: 11.05.2018*

DOI: 10.5604/01.3001.0012.0700

MAGNETIC FIELD OF COAXIAL SQUARE COILS ENCLOSED WITH HIGH-PERMEABILITY MATERIAL

Anamarija Juhas[1], Neda Pekaric Nad[1], Hannes H. Toepfer[2]
[1]University of Novi Sad, Faculty of Technical Science/Department of Power, Electronic and Telecommunication Engineering, [2]Technische Universität Ilmenau, Department of Advanced Electromagnetics

Abstract*. In this paper, the method of images is used to model the effects of enclosure made of high-permeability material on magnetic field of square coils. Closed-form description for the images, along with the case study involving square Helmholtz coils, is provided.*

Keywords: Helmholtz coils, magnetic field, method of images

POLE MAGNETYCZNE WSPÓŁOSIOWYCH KWADRATOWYCH CEWEK ZAMKNIĘTYCH W MATERIALE O WYSOKIEJ PERMEANCJI

Streszczenie. *W artykule opisano wykorzystanie metody obrazów do modelowania wpływu obudowy wykonanej z materiału o dużej przenikalności magnetycznej w obszarze kwadratowych cewek. Przedstawiono opis obrazów dla zamkniętej formy wraz ze studium przypadku z kwadratowymi cewkami Helmholtza.*

Słowa kluczowe: cewki Helmholtza, pole magnetyczne, metoda obrazów

Introduction

This paper is devoted to the analysis of magnetic field of square loops enclosed with high-permeability material. Systems like this can be found inside shielded exposure equipment for biological experiments [21], inside passive shielded rooms with MRI equipment [13], or inside shielded electronic equipment to protect it from external fields [1]. As shown in [21], the μ-metal box can be used to enlarge the volume of uniform magnetic field inside the system of four coaxial square coils.

The paper is organized as follows. In Section 1 we provide formulation of the problem, describe our model as well as magnetic field calculation which is based on the method of current images. In Section 2, we extend our considerations to the system of two coaxial loops in the presence of magnetic enclosure. In this section we consider Helmholtz coils as an important special case. In Section 3, we provide the concluding remarks and some possible extensions of the presented results. The expressions used in the calculations of the magnetic flux density vector of the original and all image loops are provided in Appendix.

1. Formulation of the problem

Here we consider the effect of enclosure made of high-permeability material on the magnetic field of the square loop. The geometry of the problem is presented in Fig. 1. We assume that the loop is made of a conductor of zero radius. In order to simplify the analysis, we further assume that the walls of the enclosure are infinitely thick. As shown in [18], the effects of finite thickness of the walls of magnetic materials is more pronounced if the relative permeability is less than 100 (e.g. for some soft ferrites).

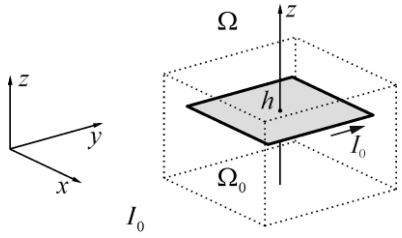

Fig. 1. Geometry of the square loop enclosed with high-permeability material

A square loop of side dimensions $2a$ surrounded by the air (region Ω_0) is enclosed with high-permeability material (region Ω) occupying $|x|\geq d/2$, $|y|\geq d/2$, $|z|\geq d/2$. To be more precise, region Ω_0 is hole inside the infinite block of high-permeability material. The shape of the hole is the cube with side dimensions equal to d and center at the origin. The coordinates of the center of the loop are $(0,0,h)$ where $|h|<d/2$. The sides of the loop are either parallel or orthogonal to the sides of the cube. In our model, the permeability of the magnetic material is constant and equal to μ. Conductivity of both media is equal to zero.

In order to take into account the influence of the enclosure on the magnetic field, the method of current images is used. It is well known that the method of images is powerful tool when the geometry of boundaries is simple. According to the method of images, magnetic flux density can be calculated by introducing the image loops (see e.g. [11, 22]). The positions and the currents of the image loops ensure proper boundary conditions at all interfaces between the two media. The method of images enables calculation of the magnetic field in all regions except inside the conductor of the loop.

According to the method of images, the magnetic field in region Ω_0 can be determined by removing magnetic material and introducing an infinite set of the image loops. In what follows, the nth layer of images $(n\geq 1)$ refers to the set of all images which are located between two concentric cubes with centers at the origin and side dimensions $(2n-1)d$ and $(2n+1)d$. Accordingly, the images in the first layer are located between the cubes of side dimensions d and $3d$, the images in the second layer are located between the cubes of side dimensions $3d$ and $5d$, etc. The number of the images in the nth layer is equal to $(2n+1)^3-(2n-1)^3=24n^2+2$ (corresponding to 26 images in the first layer, 98 in the second, 218 in the third, etc.). Let us denote

$$\alpha=\frac{\mu-\mu_0}{\mu+\mu_0}. \tag{1}$$

The centers and the currents of the image loops in the nth layer can be obtained as

$$C(n_x,n_y,n_z)=(n_x d,n_y d,n_z d+(-1)^{n_z}h), \tag{2}$$

$$I(n_x,n_y,n_z)=(-\alpha)^{|n_x|+|n_y|}\cdot\alpha^{|n_z|}I_0, \tag{3}$$

respectively, where α is given by (1), I_0 denotes the current in the original loop, and n_x, n_y and n_z are integers satisfying

$$\max(|n_x|,|n_y|,|n_z|)=n. \tag{4}$$

The positive value of the current in the image loop means that its direction is the same as in the original loop. Contrary, the negative value corresponds to the current in opposite direction. The axis of each image loop is parallel to the axis of the original loop. According to (2)-(3), 3-tuple (n_x,n_y,n_z) completely describes the image. The order of the layer to which the image loop belongs can be determined from (4). Moreover, the centers of all image loops

in the nth layer can be generated by using the following procedure

i) $n_x = \pm n,\ -n \le n_y \le n,\ -n \le n_z \le n,$

ii) $-n < n_x < n,\ n_y = \pm n,\ -n \le n_z \le n,$

iii) $-n < n_x < n,\ -n < n_y < n,\ n_z = \pm n.$

Let us consider the first layer $(n=1)$ of the images. For $n=1$, first step of the above procedure reads: $n_x = \pm 1$, $-1 \le n_y \le 1$, $-1 \le n_z \le 1$. This step generates 18 images listed as images 1-18 in Table 1. The second step $-1 < n_x < 1$, $n_y = \pm 1$, $-1 \le n_z \le 1$, generates 6 images listed as images 19-24 in Table 1. Finally, the third step $-1 < n_x < 1$, $-1 < n_y < 1$, $n_z = \pm 1$, generates the last two images in Table 1. The coordinates of the center of each image loop are calculated from (2). The current in each image loop is obtained from (3).

Table 1. The first layer of images

Image no.	n_x	n_y	n_z	$C(n_x,n_y,n_z)$	$I(n_x,n_y,n_z)$
1	–1	–1	–1	$(-d,-d,-d-h)$	$\alpha^3 I_0$
2	–1	0	–1	$(-d,0,-d-h)$	$-\alpha^2 I_0$
3	–1	1	–1	$(-d,d,-d-h)$	$\alpha^3 I_0$
4	–1	–1	0	$(-d,-d,h)$	$\alpha^2 I_0$
5	–1	0	0	$(-d,0,h)$	$-\alpha I_0$
6	–1	1	0	$(-d,d,h)$	$\alpha^2 I_0$
7	–1	–1	1	$(-d,-d,d-h)$	$\alpha^3 I_0$
8	–1	0	1	$(-d,0,d-h)$	$-\alpha^2 I_0$
9	–1	1	1	$(-d,d,d-h)$	$\alpha^3 I_0$
10	1	–1	–1	$(d,-d,-d-h)$	$\alpha^3 I_0$
11	1	0	–1	$(d,0,-d-h)$	$-\alpha^2 I_0$
12	1	1	–1	$(d,d,-d-h)$	$\alpha^3 I_0$
13	1	–1	0	$(d,-d,h)$	$\alpha^2 I_0$
14	1	0	0	$(d,0,h)$	$-\alpha I_0$
15	1	1	0	(d,d,h)	$\alpha^2 I_0$
16	1	–1	1	$(d,-d,d-h)$	$\alpha^3 I_0$
17	1	0	1	$(d,0,d-h)$	$-\alpha^2 I_0$
18	1	1	1	$(d,d,d-h)$	$\alpha^3 I_0$
19	0	–1	–1	$(0,-d,-d-h)$	$-\alpha^2 I_0$
20	0	1	–1	$(0,d,-d-h)$	$-\alpha^2 I_0$
21	0	–1	0	$(0,-d,h)$	$-\alpha I_0$
22	0	1	0	$(0,d,h)$	$-\alpha I_0$
23	0	–1	1	$(0,-d,d-h)$	$-\alpha^2 I_0$
24	0	1	1	$(0,d,d-h)$	$-\alpha^2 I_0$
25	0	0	–1	$(0,0,-d-h)$	αI_0
26	0	0	1	$(0,0,d-h)$	αI_0

The positions of the centers of all image loops in the first layer are shown in Fig. 2. The numbers in the squares correspond to the numbers of the images in Table 1. Numerical values used in this example are $d = 0.5\,\text{m}$ and $h = 0.2\,\text{m}$. The center $(0,0,h)$ of the original loop (source loop) is marked with downward triangle dot. In order to improve the clarity of the figure, the centers that belong to the planes $z = -d-h = -0.7\,\text{m}$, $z = h = 0.2\,\text{m}$ or $z = d-h = 0.3\,\text{m}$ are interconnected with black solid lines. The region Ω_0 is region inside the cube plotted with green lines. The centers of all image loops in the first layer are located between the cubes of side dimensions $d = 0.5\,\text{m}$ (green lines) and $3d = 1.5\,\text{m}$ (red lines).

In the following example, we compare the magnetic flux density of the square loop with and without enclosure (Fig. 3a). Moreover, we compare the calculated values of the magnetic flux density of the enclosed square loop by taking into account only the first (Fig. 3b), and both the first and the second layer of the images (Fig. 3c). The magnetic flux density is calculated in the region Ω_0 at the plane $y = 0$. The expressions used in the calculations of the magnetic flux density of the original and image loops are provided in the Appendix. Resultant magnetic flux density in the region Ω_0 is obtained by superposition of the fields of the original loop and the image loops. Numerical values used in the calculations are $I_0 = 1\,\text{A}$, $d = 0.5\,\text{m}$, $a = 0.2\,\text{m}$, $h = 0.2\,\text{m}$ and $\alpha = 1$ (corresponding to $\mu/\mu_0 \to \infty$). Since the air is linear medium, and currents in all image loops are linearly proportional to the current in the original loop (see (3)), it follows that resultant magnetic flux density is also linearly proportional to the current in the original loop. Therefore, the presented results can be easily scaled up or down for arbitrary current.

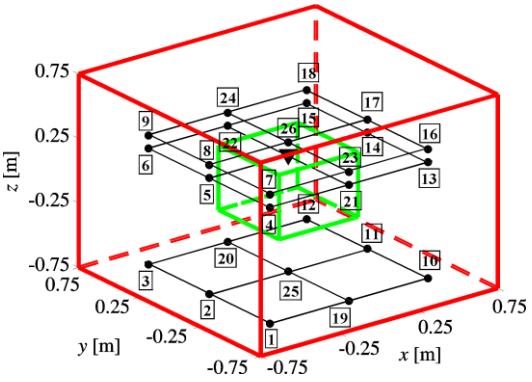

Fig. 2. The centers of all image loops in the first layer (black dots) and the center of the original loop (downward triangle dot)

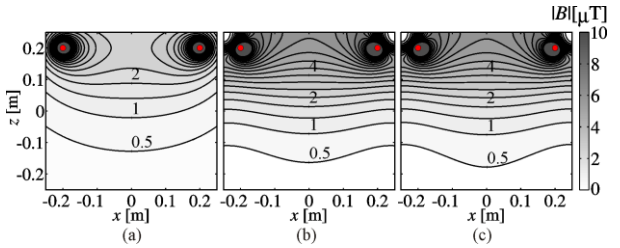

Fig. 3. Magnetic flux density of a square loop at the plane $y = 0$ (a) without enclosure, (b) with enclosure by taking into account only the first layer of images and (c) with enclosure by taking into account both the first and the second layer of images

According to the definition of the layer of images, the distance between the original loop and the layer increases with increasing order of the layer. Moreover, the number of images in the layer also increases with the order of the layer. Thus, it is not obvious that the magnetic field of the higher order layers is significantly weaker than the magnetic field of lower order layers. However, comparing Figs. 3b and 3c it follows that the effect of the second layer of images on the magnetic flux density is very weak. We also investigated the impact of the layers up to sixth order. Our numerical experiments showed that higher order layers $(3 \le n \le 6)$ can be completely neglected in the magnetic flux density calculations, because they produce very weak field in comparison to the field of the original loop. We also conclude that in calculations only the first layer of images should be included. We arrived to the same conclusion for the other values of $\alpha \ge 0.5$.

2. Case study: system of two coaxial square loops

The exposure systems for bio-magnetic experiments in *in vitro* studies are usually based on systems of coaxial coils connected in series and enclosed with high-conductivity and/or high-permeability material (see e.g. [14, 21]). The enclosure represents either commercial incubator or it serves as a shield from the background fields.

In this section we extend our analysis to the system of two loops enclosed with high-permeability material. The loops are assumed to be identical, coaxial and parallel. As an important special case we consider square Helmholtz coils. We investigate the effect of the enclosure and variation of the length of the sides of the coil (relative to the length of the edges of the enclosure) on magnetic field and its uniformity.

The geometry of two identical square loops having common axis and enclosed with high-permeability material is presented in Fig. 4. The coils are located at planes $z = h$ and $z = -h$. All other data are the same as in the previous section (Fig. 1).

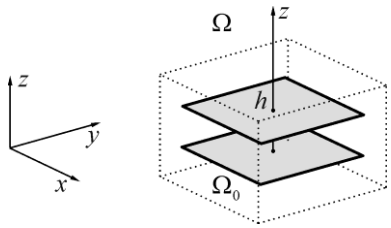

Fig. 4. System of two coaxial and parallel square loops enclosed with high-permeability material

2.1. Helmholtz coils with enclosure

Helmholtz coils are widely used to generate uniform magnetic field needed for bio-magnetic experiments (e.g. [14]), for the testing of equipment (e.g. [16, 23]), as well as for calibration of magnetic field sensors (e.g. [5, 10]). In all mentioned applications, it is of significance to obtain as large as possible volume of the uniform field.

General analysis of the magnetic field in Helmholtz coils and its uniformity in the absence of magnetic materials are well known, e.g. [6, 8, 9, 20]). Analysis of sensitivity of Helmholtz coils on imperfections of design parameters are conducted in a number of papers, see e.g. [2–4, 7, 17].

According to our best knowledge, this is the first consideration of the uniformity of magnetic field inside square Helmholtz coils enclosed with high-permeability material. In this subsection it is shown that the volume of uniform magnetic field may increase in the presence of the enclosure.

As an example we calculate magnetic flux density of square Helmholtz coils in the air (Fig. 5a), and with the enclosure by taking into account only the first layer of images (Fig. 5b). The magnetic flux density is calculated in the region Ω_0 at the plane $y = 0$. The values used in the calculations are $I_0 = 1\text{A}$, $d = 0.5\text{m}$, $a = 0.2\text{m}$, $h = 0.5445a = 0.1089\text{m}$ and $\alpha = 1$. It is easy to observe that the magnetic flux density around the center of the system is increased in the presence of the enclosure and at the same time, the volume of high uniformity of magnetic field is enlarged. In this example we also found that the effects of the second layer are weak and that the effects of the layers of order higher than two can be completely neglected.

The magnetic field non-uniformity u within the system of the loops (expressed as a percentage) can be defined as [2]

$$u[\%] = \left|1 - B(x,y,z)/B_0\right| \cdot 100, \tag{5}$$

where B_0 denotes the magnetic flux density at the center of the system (which for the coordinate system adopted in this paper coincides with the origin) and $B(x,y,z)$ denotes magnetic flux density at point (x,y,z). Due to the symmetry of the system, magnetic flux density has only z–component on z–axis (axis of the system). According to the definition (5), the value $u = 0$ corresponds to uniform field and low values of u indicate low level of field non-uniformity. For most bio-magnetic experiments magnetic field non-uniformities of less than 10% or 5% are acceptable [15]. Very rare, non-uniformity of less than 1% is required. The lines in Fig. 6 represent the contours of 1%, 2%, 5% and 10% of non-uniformity of the magnetic field at the plane $y = 0$.

Furthermore, we analyze non-uniformity of the magnetic field at the planes $z = 0$, $z = 0.1\text{m}$, and $z = 0.15\text{m}$. Contour lines of 1%, 2%, 5% and 10% of non-uniformity are presented in Fig. 7, Fig. 8 and Fig. 9, respectively. Dashed red lines indicate the positions of the square loops. Additionally, from the shape of the contours of constant non-uniformity u, it follows that u can be considered as a function of z and $r_{xy} = \sqrt{x^2 + y^2}$.

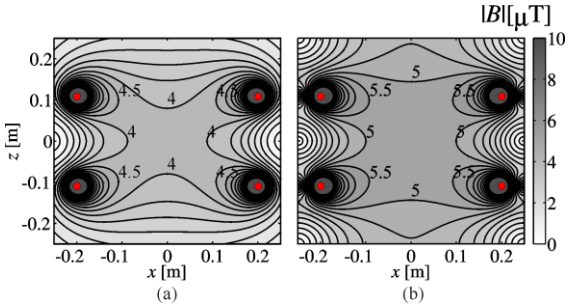

Fig. 5. Magnetic flux density of Helmholtz coils at the plane y = 0 (a) without enclosure and (b) with enclosure by taking into account only the first layer of images

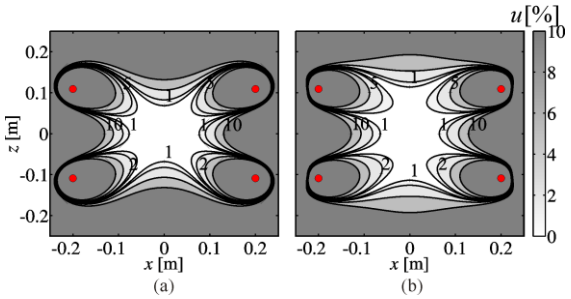

Fig. 6. Non-uniformity of the magnetic flux density of Helmholtz coils at the plane y = 0 (a) without enclosure and (b) with enclosure

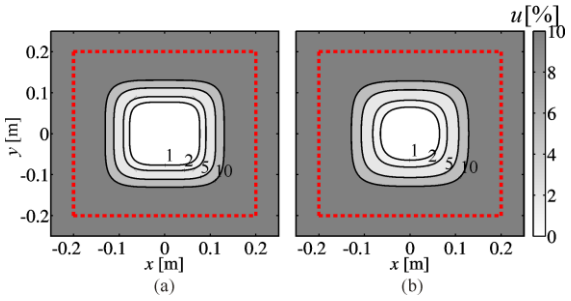

Fig. 7. Non-uniformity of magnetic flux density of Helmholtz coils at the plane z = 0 (a) without enclosure and (b) with enclosure

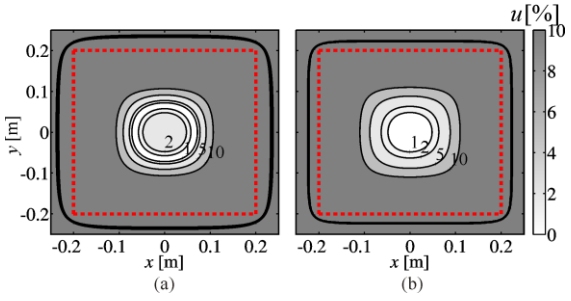

Fig. 8. Non-uniformity of magnetic flux density of Helmholtz coils at the plane z = 0.1 m (a) without enclosure and (b) with enclosure

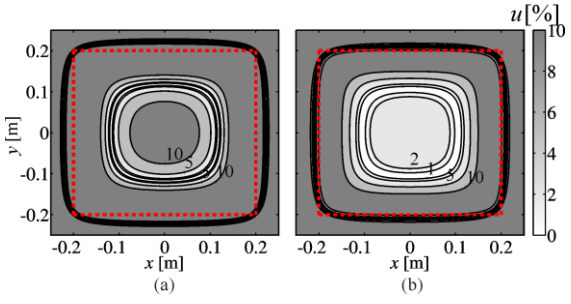

Fig. 9. Non-uniformity of magnetic flux density of Helmholtz coils at the plane z = 0.15 m (a) without enclosure and (b) with enclosure

Boundaries of the volume within 5% and 10% of non-uniformity inside Helmholtz coils with and without enclosure are summarized in Table 2. According to Table 2, the influence of the enclosure on lateral dimensions of the volume of uniform field is weak. On the other hand, the z–coordinates where $u \le 5\%$ is attained, are $|z/a| \le 0.76$ and $|z/a| \le 0.53$ for Helmholtz coils with and without enclosure, respectively. The z–coordinates where non-uniformity $u \le 10\%$ is attained are $|z/a| \le 0.90$ and $|z/a| \le 0.66$ for Helmholtz coils with and without enclosure, respectively. Consequently, the volume of the uniform field is significantly enlarged in the presence of the enclosure.

Table 2. Boundaries of volume of uniform field inside Helmholtz coils with and without enclosure

u	without enclosure	with enclosure
5%	$r_{xy}/a \le 0.45$	$r_{xy}/a \le 0.44$
	$\|z/a\| \le 0.53$	$\|z/a\| \le 0.76$
10%	$r_{xy}/a \le 0.54$	$r_{xy}/a \le 0.55$
	$\|z/a\| \le 0.66$	$\|z/a\| \le 0.90$

The aforementioned definition of non-uniformity (5) includes the magnetic flux density magnitude. However, the polarization of the uniform field should be linear, with the direction of the magnetic flux density vector along z–axis. In what follows, we consider two measures for non-uniformity of the z–component of magnetic flux density.

Let us first introduce relative difference between z–component of the magnetic flux density $B_z(0,0,z)$ at a point on the axis of the system and B_0 at the center of the system (that is, at the origin)

$$\varepsilon[\%] = \left[1 - B_z(0,0,z)/B_0\right] \cdot 100, \tag{6}$$

as proposed in [23]. For Helmholtz coils, fraction h/a is constant. Therefore, ε depends only on d/a and z/a where a denotes half-length of the sides of the loops and d denotes length of the edges of the enclosure. From the geometry of the system, it immediately follows that $d/a > 2$ and $d/a > 2|z/a|$. Plots of the contours of absolute value of ε as a function of d/a and $|z/a|$ for Helmholtz coils without enclosure and with enclosure are presented in Figs. 10(a) and 10(b), respectively. The volumes with $|\varepsilon| \le 5\%$ and $|\varepsilon| \le 10\%$ are considerably increased in the presence of the enclosure for $d/a < 3$ ($d/a = 2.5$ in the previous example presented in Figs. 6-9). For $d/a > 3$, the enclosure is not close enough to the coils and its influence is weak. However, for $d/a < 3$, the presence of the enclosure causes the increase of the height of the volume of the uniform field. This increase can be explained through the contribution of the four images in the first layer that are coaxial with the original loops and having the current in the same direction as in the original loops. Thus two original loops along with these four images form a system of six coaxial and parallel loops. Such virtual system may provide elongated volume of uniform magnetic field compared to the system consisting of the two coils alone.

Furthermore, let us introduce relative difference between z–component of the magnetic flux density $B_z(x,0,z)$ at point $(x,0,z)$ and B_0,

$$\xi[\%] = \left[1 - B_z(x,0,z)/B_0\right] \cdot 100. \tag{7}$$

According to (7), ξ depends on d/a, x/a, and z/a. Plots of the contour lines of absolute value of ξ for Helmholtz coils with enclosure, $d/a \in [2,3]$ and the following six values of $|z/a|$, $|z/a| \in \{0, 0.15, 0.3, 0.45, 0.6, 0.75\}$ are presented in Figs. 11(a)-(f), respectively. These figures confirm that high uniformity of the z–component of the magnetic flux density can be also achieved in the presence of the enclosure.

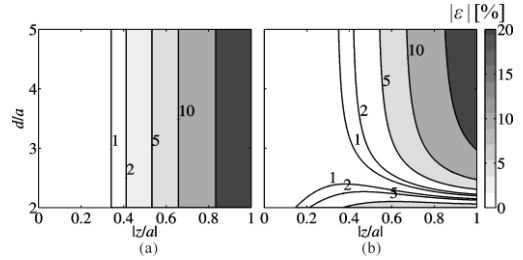

Fig. 10. Absolute values of relative difference ε for Helmholtz coils (a) without enclosure and (b) with enclosure

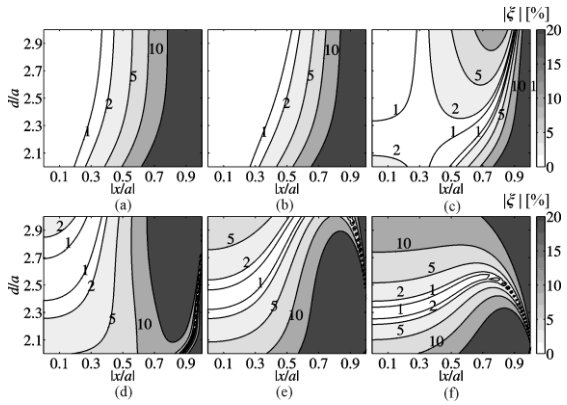

Fig. 11. Absolute values of relative difference ξ for Helmholtz coils with enclosure for (a) $|z/a|=0$, (b) $|z/a|=0.15$, (c) $|z/a|=0.3$, (d) $|z/a|=0.45$, (e) $|z/a|=0.6$, (f) $|z/a|=0.75$

3. Conclusion

In this paper we analyze magnetic field of the square loop enclosed with a high-permeability material having infinitely thick walls. Closed form expressions for the positions and centers of an infinite set of the images are provided. The images are grouped into the subsets, so-called layers of images. The contribution of the layers to the magnetic field is investigated numerically. It is shown that the impact of the second layer is very weak, and the impact of the layers of the order higher than two can be completely neglected, providing that $\alpha \ge 0.5$ (corresponding to $\mu \ge 3\mu_0$). In calculations of magnetic field only contributions of the images in the first layer should be included.

In Section 2 we consider the system of two coaxial and parallel identical square coils enclosed with high-permeability material with infinitely thick walls. Square Helmholtz coils, as an important special case, are considered in detail. We show that the volume of the uniform magnetic field inside the Helmholtz coils can be significantly increased in the presence of the enclosure. A possible application of these results is in the design of exposure system for in-vitro bio-magnetic experiments based on Helmholtz coils. Such system is usually placed inside the commercial incubator with heating elements, which produce magnetic field. Apart from shielding this field, the box made of high-permeability material can be used to enlarge the volume of uniform magnetic field inside the Helmholtz coils.

In this paper, we assume that the walls of the enclosure are infinitely thick, and made of material having constant permeability and zero conductivity. These conditions can be approximately fulfilled by using ferrite with relative permeability higher than 100 [18], providing that the saturation is avoided. Moreover, before the practical realization, the sensitivity of the magnetic field uniformity on the imperfections of the dimensions of the coils and their positions inside the box should be analyzed.

The presented work might be easily extended to include considerations of the systems of three or more coaxial and parallel square coils enclosed with high-permeability material. In future work we will also consider the enclosed systems of coaxial and parallel circular coils.

Appendix

In this appendix we provide the expressions that enable fast and easy calculation of the magnetic flux density vector of the original and the image square loops.

A square loop in homogeneous medium of constant permeability μ is shown in Fig. 12. The side dimensions of the loop are $2a$, center of the loop is at (x_0, y_0, z_0), the plane of the loop is parallel to $xy-$plane and the edges of the loop are parallel to either x or y axis.

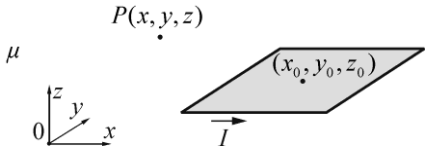

Fig. 12. Square loop

Following the derivation presented in [12], it is easy to show that the components of the magnetic flux density at point $P(x, y, z)$ can be expressed as

$$B_x(x,y,z) = \frac{\mu I (z - z_0)}{4\pi} \sum_{k=1}^{4} \frac{(-1)^{k+1}}{r_k (r_k + d_k)}, \tag{8}$$

$$B_y(x,y,z) = \frac{\mu I (z - z_0)}{4\pi} \sum_{k=1}^{4} \frac{(-1)^{k+1}}{r_k (r_k + c_k)}, \tag{9}$$

$$B_z(x,y,z) = \frac{\mu I}{4\pi} \sum_{k=1}^{4} (-1)^k \left[\frac{c_k}{r_k (r_k + d_k)} + \frac{d_k}{r_k (r_k + c_k)} \right], \tag{10}$$

where

$$\begin{aligned} c_1 &= (x - x_0) + a, & d_1 &= (y - y_0) + a, \\ c_2 &= (x - x_0) - a, & d_2 &= (y - y_0) + a, \\ c_3 &= (x - x_0) - a, & d_3 &= (y - y_0) - a, \\ c_4 &= (x - x_0) + a, & d_4 &= (y - y_0) - a, \end{aligned} \tag{11}$$

and

$$r_k = \sqrt{c_k^2 + d_k^2 + (z - z_0)^2}, \qquad k = 1, \ldots, 4. \tag{12}$$

Magnetic flux density on the axis of the square coil can be obtained by substituting $x = x_0$ and $y = y_0$ into (8)-(12). After some rearrangements it follows that

$$\begin{aligned} B_x(x_0, y_0, z) &= 0, \\ B_y(x_0, y_0, z) &= 0, \\ B_z(x_0, y_0, z) &= \frac{2\mu I a^2}{\pi \left[a^2 + (z - z_0)^2 \right] \sqrt{2a^2 + (z - z_0)^2}}. \end{aligned} \tag{13}$$

Finally, z–component of the magnetic flux density at the center of the loop is equal to

$$B_z(x_0, y_0, z_0) = \frac{\sqrt{2}\mu I}{\pi a}. \tag{14}$$

Acknowledgement

This work is supported by Serbian Ministry of Education, Science and Technology Development as a part of the Project TP32016.

References

[1] Ahuir J. V.: Going wireless with magnetic shielding. A on Note ANP016, Wurth Electronic Inc. 2013, http://www.we-online.com/web (available 12.12.2017).
[2] Beiranvand R.: Analyzing the uniformity of the generated magnetic field by a practical one-dimensional Helmholtz coils system. Rev. Sci. Instrum. 7/2013, 075109-1–11 [DOI: 10.1063/1.4813275].
[3] Beiranvand R.: Magnetic field uniformity of the practical tri-axial Helmholtz coils systems. Rev. Sci. Instrum. 5/2014, 055115-1–10 [DOI: 10.1063/1.4876480].
[4] Beiranvand R.: Effects of the winding cross section shape on the magnetic field uniformity of the high field circular Helmholtz coil systems. IEEE Trans. Ind. Electron. 2017, 7120–7131 [DOI: 10.1109/TIE.2017.2686302].
[5] Bronaugh E. L.: Helmholtz coils for calibration of probes and sensors: Limits of magnetic field accuracy and uniformity. IEEE 1995 Int. Symp. Electromagn. Compatibility, Atlanta. 72–76 [DOI: 10.1109/ISEMC.1995.523521].
[6] Cacak R. K., Craig J. R.: Magnetic field uniformity around near Helmholtz coil configurations. Rev. Sci. Instrum. 11/1969, 1468–1470 [DOI: 10.1063/1.1683829].
[7] Crosser M. S., Scott S., Clark A., Wilt P. M.: On the magnetic field near the center of Helmholtz coils. Rev. Sci. Instrum. 8/2010, 084701-1–6 [DOI: 10.1063/1.3474227].
[8] Crownfield F. K., Jr.: Optimum spacing of coil pairs. Rev. Sci. Instrum. 2/1964, 240–241 [DOI: 10.1063/1.1718796].
[9] Firester A. H.: Design of square Helmholtz coil systems. Rev. Sci. Instrum. 9/1966, 1264–1265 [DOI: 10.1063/1.1720478].
[10] Frix W. M., Karady G. G., Venetz B. A.: Comparison of calibration systems for magnetic field measurement equipment. IEEE Trans. Power Del. 1/1994, 100–108 [DOI: 10.1109/61.277684].
[11] Hammond P.: Electric and magnetic images. Proceedings of the IEE - Part C: Monograph 12/1960, 306–313 [DOI: 10.1049/pi-c.1960.0047].
[12] Juhas A., Pekaric-Nad N., Toepfer H.: Magnetic field of rectangular current loop with sides parallel and perpendicular to the surface of high-permeability material. Serb. J. Electr. Eng. 4/2014, 701–717 [DOI: 10.2298/SJEE1404701J].
[13] Kalafala, A. K.: Optimized configurations for passively shielded magnetic resonance imaging magnets. IEEE Trans. Magn. 2/1993, 1240–1244 [DOI: 10.1109/20.250628].
[14] Kirschvink J. L.: Uniform magnetic fields and double-wrapped coil systems: Improved techniques for the design of bioelectromagnetic experiments. Bioelectromagnetics 1992, 401–411 [DOI: 10.1002/bem.2250130507].
[15] Misakian M.: Exposure systems. EMF Engineering Review Symposium, Charleston, 1998. 4.1-4.6. ftp://ftp.emf-data.org/pub/emf-data/symposium98/topic-04-synopsis.pdf (available 12.12.2017).
[16] Poppenk F. M., Amini R., Brouwer G. F.: Design and application of a Helmholtz cage for testing nano–satellites. Proc. 58th Congress IAF, paper no. IAC-07-C1.8.02, Huderabad, India, 2007. 4650–4659.
[17] Purcell E. W.: Helmholtz coils revisited. Amer. J. Phys. 1989, 18–22 [DOI: 10.1119/1.15860].
[18] Roshen W. A.: Effect of finite thickness of magnetic substrate on planar inductors. IEEE Trans. Magn. 1/1990 270–275 [DOI: 10.1109/20.50553].
[19] Ruark A. E., Peters M. F.: Helmholtz coils for producing uniform magnetic fields. J. Opt. Soc. Am. 1926, 205–212 [DOI: 10.1364/JOSA.13.000205].
[20] Rudd M. E., Craig J. R.: Optimum spacing of square and circular coil pairs. Rev. Sci. Instrum. 9/1968, 1372–1374 [DOI: 10.1063/1.1683678].
[21] Schuderer J., Oesch W., Felber N., Spat D., Kuster N.: In vitro exposure apparatus for ELF magnetic fields. Bioelectromagnetics 2004, 582–591 [DOI: 10.1002/bem.20037].
[22] Turowski J., Turowski M.: Engineering Electrodynamics Electric Machine, Transformer, and Power Equipment Design, CRC Press Taylor & Francis Group 2014.
[23] Wang J., She S., Zhang S.: An improved Helmholtz coil and analysis of its magnetic field homogeneity. Rev. Sci. Instrum. 5/2002, 2175–2179 [DOI: 10.1063/1.1471352].

Ph.D. Anamarija Juhas
e-mail: ajuhas@uns.ac.rs

Anamarija Juhas received Ph.D degree in electrical engineering from the Faculty of Technical Sciences (FTN), University of Novi Sad, in 2009. She is currently an Associate Professor with the Department of Power, Electronic and Telecommunication Engineering at the same Faculty. Her research interests include calculation and measurements of electric and magnetic fields, electromagnetic compatibility, human exposure to electromagnetic fields, memristors and power amplifiers.

Prof. Neda Pekaric Nad
e-mail: pecaric@uns.ac.rs

Neda Pekaric Nad got her Ph.D degree in Electrical engineering from the Faculty of Electrical Engineering (ETF), University of Belgrade, in 1984. For many years she is a Professor at the Department of Power, Electronic and Telecommunication Engineering at the University of Novi Sad. Her research interests include electromagnetic compatibility, as well as study of electric and magnetic fields and their biological effects.

Prof. Hannes H. Toepfer
e-mail: hannes.toepfer@tu-ilmenau.de

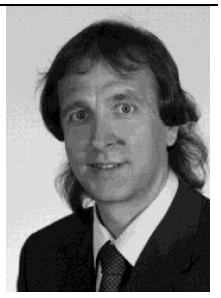

Hannes Toepfer studied Electrical Engineering at the Institute of Technology Ilmenau. From 1991-2002 he worked as an scientific assistant at the Ilmenau University of Technology. In 1996, he received the Dr.-Ing. (equiv. PhD) and in 2003 his postdoctoral qualification (Habilitation). In 2002, he joined the Institute for Microelectronics and Mechatronics Systems where he has been directing the System Design department. In 2009, he became a Full Professor at Technische Universität Ilmenau and heading the Advanced Electromagnetics Group with a research focus on electromagnetic sensors.

otrzymano/received: 08.12.2017 *przyjęto do druku/accepted: 11.05.2018*

DOI: 10.5604/01.3001.0012.0701

A DISTRIBUTED METHOD FOR TRANSIENT SIMULATIONS THAT DYNAMICALLY CONSIDERS SUPPLEMENTARY RESULTS FROM AUTONOMOUS SOFTWARE AGENTS

Matthias Jüttner[1], Sebastian Grabmaier[1], Jonas Rohloff [1], Desirée Vögeli[2], Wolfgang M. Rucker[1], Peter Göhner[2], Michael Weyrich[2]

[1]University of Stuttgart, Institute for Theory of Electrical Engineering, [2]University of Stuttgart, Institute of Industrial Automation and Software Engineering

Abstract. *Based on autonomous software agents capable of calculating individual numerical field problems, a distributed method for solving transient field problems is presented. The software agents are running on distributed resources connected via a network and represent a dynamic calculation environment. Communication and data exchange between multiple agents enables their collaboration and allows decisions based on distributed overall knowledge. As unique characteristics, no central unit influences the solution process at any time. The presented simulation example and its evaluated calculation process proves the method to benefit from redundant resources.*

Keywords: automatic step size control, distributed computing, software agents, transient simulation

ROZPROSZONA METODA DO SYMULACJI STANÓW PRZEJŚCIOWYCH DYNAMICZNIE UWZGLĘDNIAJĄCA DODATKOWE WYNIKI AUTONOMICZNYCH AGENTÓW PROGRAMOWYCH

Streszczenie. *W oparciu o autonomiczne agenty programowe zdolne do obliczania indywidualnych numerycznych problemów pola, przedstawiono rozproszoną metodę rozwiązywania stanów przejściowych pola. Agenty programowe działają na zasobach rozproszonych połączonych za pośrednictwem sieci i reprezentują środowisko obliczeń dynamicznych. Komunikacja i wymiana danych między wieloma agentami umożliwia ich współpracę i pozwala podejmować decyzje w oparciu o rozproszoną wiedzę ogólną. Jako unikalna charakterystyka jest fakt, że żadna jednostka centralna nie wpływa w żadnym momencie na proces rozwiązania. Przedstawiony przykład symulacji i jej oszacowany proces obliczeniowy dowodzi, że metoda umożliwia korzystanie z nadmiarowych zasobów.*

Słowa kluczowe: automatyczna kontrola wielkości kroku, przetwarzanie rozproszone, agenty programowe, symulacja przejściowa

Introduction

Using the finite element method (FEM) to solve transient simulations is mostly done by sequentially calculating discrete time steps. The time stepping is controlled by the error

$$\mathrm{E}_\tau^n = \sqrt{\frac{1}{k}\sum_{i=1}^{k}\left(\frac{|\epsilon_i^n|}{A_{tol,i}+\max(|u_i^{n-1}|,|u_i^n|)\cdot R_{tol,i}}\right)^2} \leq 1 \qquad (1)$$

calculated for each time step n. The number of degrees of freedom (dofs) is given as k, A_{tol} and R_{tol} represent desired tolerances, u_i^n is the approximation of the solution and ϵ_i^n is the solver's estimation of the (local) absolute error [5]. The optimal step size is

$$\Delta t_{\tau,opt}^n = \Delta t^n \cdot (1/\mathrm{E}_\tau^n)^{1/(q+1)} \qquad (2)$$

with q as order of the method and Δt^n as previous step. The optimal steps size is multiplied by a safety factor f and used for calculating the next time step Δt^{n+1} [2]. If $\mathrm{E}_\tau^n \leq 1$ is satisfied the solution $\boldsymbol{u}^n$ is used and a next time step is calculated. Otherwise results are discarded and another step size is chosen.

Alternatives to a sequential calculation sequence represent parallel time integration methods proposed during the last 50 years [4]. In analogy, the developed parallel method aims on a faster calculation compared to a sequential one by performing multiple redundant shootings in parallel and selecting the largest valid steps size by evaluating error criteria like (1). Since redundant resources are provided within common business networks, they are used for calculating redundant shootings and the related partial time steps. A goal oriented usage of these additional resources is the major target of this contribution. For topics like efficiency and scalability, trust is given to the principles of the market for providing results. Within a working market, these issues are automatically evaluated by the participants and there is no need for further attention within the solution strategy.

The following contribution is organized in five sections. While section I gives the introduction for this new way of handling transient simulations, section II describes the implemented calculation framework. In section III the solution process of this framework is explained. The numerical model given in section IV proves the concepts functionality and allows its discussion based on numerical results. Section V finally concludes this contribution and outlines related topics.

1. Calculation system

Here, a distributed calculation system with independent and autonomous calculation units is used to solve transient FEM simulations. The calculation units are implemented based on the paradigm of agent based programming [7]. This enables autonomous and distributed software units to cooperate and to fulfill own goals based on individual strategies. Here, each software agents represents an independent computer with different hard- and software capabilities. This setup is shown in Fig. 1 for p agents within a computer network. Available software capabilities are FEM tools. These are provided to the agents by interfaces and enables them to handle and perform numeric field calculations. In comparison to previous work, capabilities for a transient simulation were added [8].

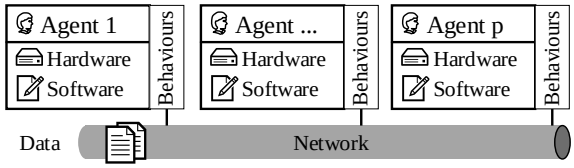

Fig. 1. Software agent system with own resources for field calculation

The agents' goal is to make profit. Therefore, agents apply their behaviours and all their capabilities accordingly. This means that the autonomous agents use their individual scheduler, their own business model and as many resources as considered necessary. It also enables a cooperative usage of the resources by multiple applications within every software agent. In the same way a competition between the agents is started to maximize their profit. Compared to cluster computing agents do not provide calculation time here. They offer individually calculated results that were derived from a global numerical model. Consequently, different solutions coexist within the calculation system. For additional processing steps like transient or coupled simulation or post-processing an adequate payment is expected by the agents. Suitable payment criteria for a user are the calculation time, the re-

maining error or costs for calculation like for a usage of software licences.

Enabling redundant agents to compete within the solution process of a transient numerical simulation, the agents resulting goal is to contribute to the overall solution. Therefore, they perform calculations without fulfilling distributed tasks or parallelize them in a common manner. They gain profit by quickly providing best and cheapest partial simulation results to the user before other competing agents do. For the considered transient simulation, partial tasks arise from different safety factors f for calculating a time step Δt_τ^n. These independent partial tasks are calculated in parallel. Communication between the agents avoids the calculation of duplicated parameter sets. It also enables a globally concerted uniform decision for the largest valid time step $\Delta t_{\tau,max}^n$ fulfilling (1). The iterative solution process with multiple time steps is achieved by exchanging the latest valid result.

2. Numerical method

To implement an adequate global calculation method for transient electrical engineering problems, the method is supposed to handle differential algebraic and stiff simulations [9]. Therefore, an implicit time integration scheme is preferred with a variable and adaptive time stepping based on selected error criteria. Within each time step a nonlinear system of equations is likely and must therefore been solved. The first order predictor of the implemented second order backward differential formulation (bdf) is a given in [2] as

$$\boldsymbol{u}_{pred}^n = \boldsymbol{u}^{n-1} + \frac{\boldsymbol{u}^{n-1}-\boldsymbol{u}^{n-2}}{\Delta t^{n-1}}\Delta t^n. \tag{3}$$

The bdf with a linear damping matrix D and a nonlinear stiffness matrix K^n is given as

$$K^n \boldsymbol{u}^n = -\frac{1}{\Delta t^n\, m_{bdf}^n} D\left(\boldsymbol{u}^n - \boldsymbol{u}_{bdf}^n\right). \tag{4}$$

According to [2], the parameter m_{bdf}^n is weighting the current and previous time step by

$$m_{bdf}^n = \frac{\Delta t^{n-1}+\Delta t^n}{\Delta t^{n-1}+2\Delta t^n}. \tag{5}$$

The second order backward differential term is

$$\boldsymbol{u}_{bdf}^n = w_1^n \boldsymbol{u}^{n-1} - w_2^n \boldsymbol{u}^{n-2} \tag{6}$$

with the weighting factors

$$w_1^n = \frac{(\Delta t^{n-1}+\Delta t^n)^2}{(\Delta t^{n-1})^2+2\Delta t^n \Delta t^{n-1}} \tag{7}$$

and

$$w_2^n = \frac{(\Delta t^n)^2}{(\Delta t^{n-1})^2+2\Delta t^n \Delta t^{n-1}}. \tag{8}$$

Because of the second order accuracy of the time solution, a third order error estimator $\boldsymbol{\epsilon}$ is used. The estimator for $\boldsymbol{u}^n$ and the three previous results $\boldsymbol{u}^{n-1}$, $\boldsymbol{u}^{n-2}$, $\boldsymbol{u}^{n-3}$ is given as

$$\begin{aligned}\boldsymbol{\epsilon}^n = \frac{\Delta t^n + \Delta t^{n-1}}{6}\Bigg[&\frac{1}{\Delta t^n}\left(\boldsymbol{u}^n - \boldsymbol{u}^{n-1}\right)\\ &-\frac{\Delta t^n + \Delta t^{n-1}}{(\Delta t^{n-1})^2}\left(\boldsymbol{u}^{n-1} - \boldsymbol{u}^{n-2}\right)\\ &+\frac{\Delta t^n}{\Delta t^{n-1}\Delta t^{n-2}}\left(\boldsymbol{u}^{n-2} - \boldsymbol{u}^{n-3}\right)\Bigg].\end{aligned} \tag{9}$$

As relative time discretization error (1) is used. Its absolute tolerance $A_{tol,i}$ depends on the type of the dependent variable. Especially for multiphysics systems this absolute tolerance must be chosen appropriately. Analog to (1) relative errors for the nonlinear Newton steps E_ν^n and the iterative linear solver E_μ^n are calculated. A time step Δt^n is valid if all three errors (E_ν^n, E_μ^n, E_τ^n) are within their predefined tolerances. Larger time steps during the simulation lead to large time errors E_τ^n in the numerical result, an increased number of iteration in the linear and the nonlinear solver and might end up in divergence. The optimal time step size for the nonlinear Newton method is

$$\Delta t_{\nu,opt}^n = \Delta t^n \cdot \left(1/\mathrm{E}_\nu^n\right)^{1/r^2} \tag{10}$$

with r as number of Newton iterations. If the required accuracy is not reached during the linear Krylov iterations, Δt^n is repeatedly calculated with a heuristically reduced safety factor ¼ [6]. In case of E_ν^n or E_μ^n are not satisfied during the calculation of Δt^n, the time step is repeatedly calculated with

$$\Delta t_{opt}^n = \min\left(\Delta t_{\nu,opt}^n, \Delta t_{\tau,opt}^n\right) \tag{11}$$

The time step Δt_{opt}^n is also used as approximation of Δt^{n+1}. Since Δt_{opt}^n is only an approximation for Δt^{n+1} the safety factor f is used to avoid its repeated calculation [5].

For a parallel and redundant calculation of the time riod $[t_0, t_{STEP}]$ by a software agents system, each agent j applies a unique time step multiplier f_j to create and perform its simulations. The individual time step of agent j is given as

$$\Delta t_j^n = \Delta t_{opt}^{n-1} \cdot f_j. \tag{12}$$

Fig. 2 shows the resulting configuration of a software agents system. The multiplier f_j is generated based on the number of currently available and potentially contributing software agents. If only one agent is available $f = 5/6$ is chosen according to [2]. In case of more agents, larger time steps speed up the calculation. Smaller time steps avoid a re-initialization in case of no or slow convergence and require less effort during the nonlinear and the linear solver iterations. For a dynamic calculation environment it also makes sense to adapt f according to the amount of available resources after finishing the calculation of a time step. The agent with the largest time step fulfilling all error criteria proposes the solution $\boldsymbol{u}^n$ for the actual time step Δt^n. Same holds for the next optimal step size Δt_{opt}^{n+1}, so other agents are able to derive their time step by using their multiplier f_j. In case off all agents fail the new time step is chosen under the condition that all new time steps multiplied with the factor f_j are smaller than all previous steps. For a global time $t_{STEP} > t_{END}$ the calculation finally ends.

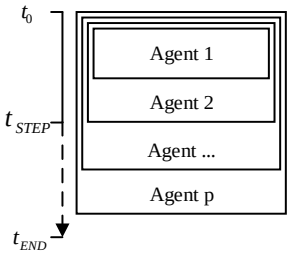

Fig. 2. Time steps selection for autonomous software agents

3. Numerical validation

To demonstrate the performance of the method a tuned circuit is considered. It contains a lumped capacitor with 1mF and an inductor with a coil of 50 thin windings including its nonlinear and lossy core. The eddy current losses and the nonlinear BH-material properties of the magnetic core are evaluated using the FEM based on the geometric 3D model shown in Fig. 3. For its calculation the sector symmetry, its horizontal symmetry and infinite elements at the border of the surrounding air are used [10].

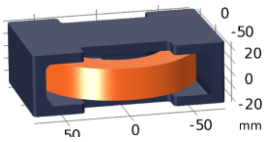

Fig. 3. Geometric model of the nonlinear and lossy inductance

The evaluated differential equation in the magnetic core is

$$\nabla \times \frac{1}{\mu(|\boldsymbol{B}|)} \nabla \times \boldsymbol{A} = -\sigma_{core} \frac{\partial \boldsymbol{A}}{\partial t}, \tag{13}$$

with the scalar permeability μ as nonlinear function of the magnetic flux density $\boldsymbol{B} = \nabla \times \boldsymbol{A}$. Here the modified vector potential $\boldsymbol{A}$ defined by $\boldsymbol{E} = -\partial A/\partial t$ is used. The advantage of this modification is the vanishing electric scalar potential resulting in a smaller equation system [3].

For the surrounding air region and the windings $\mu_r = 1$ is considered. Within the region of the windings the additional source term $\boldsymbol{s}I/a$ is added to the right side to handle the electric current. Here $\boldsymbol{s}$ has a length of one, points in the direction of the homogenized electric current density $\boldsymbol{J}$ and normal to the cross section area a of the coil. The conductivity in the air and coil is set to $\sigma_{air} = 1\ S/m$ to provide a well posed equation system [1]. The core is modelled with an electric conductivity $\sigma_{core} = 10^5\ S/m$. The coupled ordinary differential equations are

$$\frac{\mathrm{N_W}}{a}\int_{\Omega_{coil}} \frac{\partial \boldsymbol{A}}{\partial t}\cdot \boldsymbol{s}\,\mathrm{d}\boldsymbol{x} + U = 0 \tag{14}$$

and

$$I + C\frac{\partial U}{\partial t} = 0 \tag{15}$$

with the number of windings $\mathrm{N_W}$ and the capacitor C. The introduced electric current I leads to the differential algebraic equation system

$$\begin{bmatrix} K(A) & 0 & R^T \\ 0 & 1 & 0 \\ 0 & 0 & 1 \end{bmatrix}\begin{Bmatrix} \boldsymbol{A} \\ U \\ I \end{Bmatrix} + \begin{bmatrix} D & 0 & 0 \\ R & 0 & 0 \\ 0 & C & 0 \end{bmatrix}\frac{\partial}{\partial t}\begin{Bmatrix} \boldsymbol{A} \\ U \\ I \end{Bmatrix} = 0 \tag{16}$$

that also supports a higher accuracy for I during calculation. Initially the capacitor is charged with $U = 20\ V$ and the electric current I is zero. Analogy to (4) the nonlinear stiffness matrix of the FEM model is $K(A)$. Its linear damping matrix is D due to the cores conductivity. The lumped capacitor is considered as C. The integral operator $R := \mathbb{R}^N \to \mathbb{R}$ couples $\boldsymbol{A}$ to the voltage at the capacitor. Via I as auxiliary variable the current density $\boldsymbol{J}$ is impressed into the FEM model by the operator $R^T := \mathbb{R} \to \mathbb{R}^N$. This results in a model with $5 \cdot 10^5$ dof. One of them represents the electric current $I \in \mathbb{R}$ within the resonant circuit and another the electric voltage at the capacitor $U \in \mathbb{R}$. The other dofs are used for the magnetic vector potential $\boldsymbol{A} \in \mathbb{R}^3$ and describe the field variable.

The considered software agents system contains five agents with similar capabilities and hardware resources. They are running on five Intel i5-4690 with 4 cores at 3.5 GHz. For evaluation the time between $t_0 = 0$ and $t_{END} = 100$ ms is chosen. During the calculation process every agent performs at maximum 3 nonlinear iterations with 20 linear iterations per time step Δt^n. These are performed by the biconjugate gradient stabilized method (BiCGStab) with a vector multigrid preconditioner and a direct solver for the coarse problem. The number of Newton iterations are chosen as constant to achieve an equal distribution of the calculation effort. This also avoids idle time or time outs while waiting for partial results. The agents' time step multipliers f_j are chosen as shown in Tab. 1.

Table 1. Time steps applied by the different software agents

Agent 1	Agent 2	Agent 3	Agent 4	Agent 5
0.25	0.5	1.0	1.5	2.0

All valid voltage results of the agents are shown in Fig. 5 for four selected iterations near the minima of U. Agents that do not converge at all are not shown. The maximum time steps fulfilling all error criteria are highlighted with a circle. These results are chosen as next starting point for further time steps. The adaptive time stepping within the method is also shown in Fig. 5 by the distinct width of each iteration.

The calculated time dependent U and I are shown in Fig. 4. Calculation was done within 3 h. Additionally, reference solutions for U and I are given computed with much smaller time steps. They are evaluated on Intel Xeon E5-2630 with eight cores at 2.4 GHz within 8 h and show a good agreement.

The evaluated norm of the magnetic flux density $\boldsymbol{B}$ indicates the saturation and the skin effect within the core at $t = 2$ ms. It is shown in Fig. 6 by cutting the core along the symmetry planes.

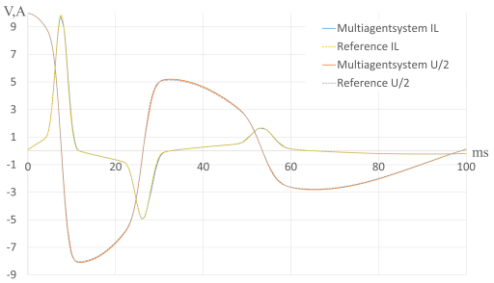

Fig. 4. Result comparison between the agents system and a reference solution

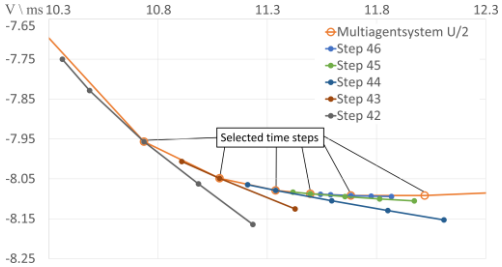

Fig. 5. Time steps of five autonomous software agents cooperatively but also competitively computing a transient FEM simulation

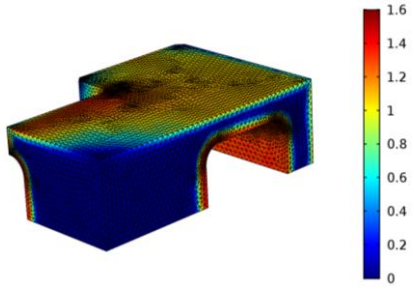

Fig. 6. Tetrahedral mesh of the iron core and norm of the magnetic flux density $\boldsymbol{B}$ in Tesla at 2ms

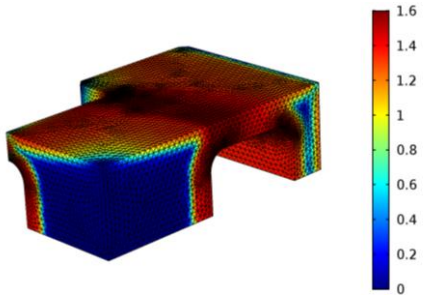

Fig. 7. Tetrahedral mesh of the iron core and norm of the magnetic flux density $\boldsymbol{B}$ in Tesla at 5ms

The mesh properly resolves the decay of the magnetic flux density $\boldsymbol{B}$ due to the skin effect. The magnetic flux density in the core at $t = 5$ms is shown in Fig. 7. There, the magnetic flux has penetrated the complete core and the saturation effect dominates. Due to the data exchange between the agents and their interest on contributing to further tasks all results shown in the Fig. 4–7 exist at every agent.

Here the agents system requires 145 steps to fulfill the error criteria within every time step. Compared to another run of the computation with just one agent with $f_1 = 1$ about 96 iterations are avoided. This is due to the replacement of the propose time step by results of other agents (22 times) and a totally avoided re-initialisation (74 times). The multipliers f_j considered during the solution are shown in Fig. 8. The results mostly confirm $0.5 \leq f \leq 1$ as advised in [2] and automatically chosen by the agents system. The usage of multiple software agents leads to a calculation time reduction of 21 %. Repeating this experiment with other error criteria the time reduction obviously relates to the

number of spared iterations. Highlighting finally, that even in the worst case the presented system is as fast as a calculation without redundant resources.

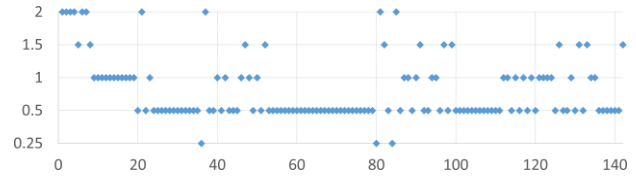

Fig. 8. Multipliers for time steps chosen to fulfill the error criteria

4. Conclusion

Within this contribution a new way of handling transient simulations is presented based on a software agents system. Details about the software agents system and the applied numerical method are given. Demonstrated on the transient simulation of a resonant circuit the method was validated. The results show that the calculation process profits from using redundant resources. Even in the worst case the presented system is as fast as a common calculation system. The additionally achieved flexibility of the calculation process is also beneficial for non-permanent calculation resources.

Acknowledgement

This work was supported by the Deutsche Forschungsgemeinschaft (DFG) under the grants RU 720/15 and WE 5312/8.

References

[1] Bíró O.: Edge element formulations of eddy current problems. Computer Methods in Applied Mechanics and Engineering 169(3-4)/1999, 391–405.
[2] Celaya E.A., Aguirrezabala J.A., Chatzipantelidis P.: Implementation of an Adaptive BDF2 Formula and Comparison with the MATLAB Ode15s. Procedia Computer Science 29/2014, 1014–1026.
[3] Emson C., Trowbridge C.: Transient 3D Eddy Currents Using Modified Magnetic Vector Potentials and Magnetic Scalar Potentials. IEEE Transactions on Magnetics 24(1)/1988, 86–98.
[4] Gander M.J.: 50 Years of Time Parallel Time Integration. Multiple Shooting and Time Domain Decomposition Methods, Cham, Springer, 2015, 69–113.
[5] Hairer E., Nørsett S.P., Wanner G.: Solving ordinary differential equations I. Nonstiff Problems, 2nd ed., Springer, Berlin 2009.
[6] Hindmarsh A.C., Brown P.N., Grant K.E., Lee S.L., Serban R., Shumaker D., Woodward C.S.: SUNDIALS: Suite of nonlinear and differential/algebraic equation solvers. ACM Transactions on Mathematical Software 31(3)/2005, 363–396.
[7] Jennings N.R.: On agent-based software engineering. Artificial Intelligence 117/1999, 277–296.
[8] Jüttner M., Grabmaier S., Vögeli D., Rucker W.M., Göhner P.: Coupled Multiphysics Problems as Market Place for Competing Autonomous Software Agents. IEEE Transactions on Magnetics 53(6)/2017.
[9] Moore P.K., Petzold L.R.: A stepsize control strategy for stiff systems of ordinary differential equations. Applied numerical mathematics 15(4)/1994, 449–463.
[10] Zienkiewicz O.C., Emson C., Bettess P.: A novel boundary infinite element. International Journal for Numerical Methods in Engineering 19(3)/1983, 393–404.

M.Sc. Eng. Matthias Jüttner
e-mail: matthias.jüttner@ite.uni-stuttgart.de

Former academic staff at the Institute for Theory of Electrical Engineering at the University of Stuttgart. Research topics: domain decomposition methods, multiphysics simulations, software agents.

M.Sc. Sebastian Grabmaier
e-mail: sebastian.grabmaier@ite.uni-stuttgart.de

Academic staff member at the Institute for Theory of Electrical Engineering at the University of Stuttgart. Research topics: domain decomposition methods, coupled field problems.

M.Sc. Jonas Rohloff
e-mail: mail@jonas-rohloff.de

Graduated student at the University of Stuttgart. Research topics: calculation of time dependent field problems.

M.Sc. Desirée Vögeli
e-mail: desiree.voegeli@ias.uni-stuttgart.de

Academic staff member at the Institute of Industrial Automation and Software Engineering at the University of Stuttgart. Research topic: agentbased assistance systems for parallel process coordination.

Prof. Wolfgang M. Rucker
e-mail: rucker@ite.uni-stuttgart.de

Former head of the Institute for Theory of Electrical Engineering at the University of Stuttgart.
Research topic: fast calculation of electromagnetic fields.

Prof. Peter Göhner
e-mail: peter.goehner@ias.uni-stuttgart.de

Former head of the Institute of Industrial Automation and Software Engineering at the University of Stuttgart. Research topic: agentbased system in industrial automation.

Prof. Michael Weyrich
e-mail: ias@ias.uni-stuttgart.de

Head of the Institute of Industrial Automation and Software Engineering at the University of Stuttgart. Research topic: methods and tools to reduce software complexity in industrial automation.

otrzymano/received: 08.12.2017 *przyjęto do druku/accepted: 11.05.2018*

DOI: 10.5604/01.3001.0012.0702

MULTISENSORS FOR WHOLE-CELL ANALYTICS

Ingo Tobehn-Steinhäuser[1], Margarita Günther[2], Stefan Görlandt[1], Steffen Herbst[1], Heike Wünscher[1], Thomas Ortlepp[1], Gerald Gerlach[2]

[1]CiS Forschungsinstitut für Mikrosensorik GmbH, [2]Technische Universität Dresden, Solid-State Electronics Laboratory

***Abstract**: Whole-cell biosensors, which can be used in the environmental protection and process measuring technology, in the biotechnology, food and pharmaceutical industry for the on-line control and monitoring of chemical and biochemical processes and for the fast detection of small amounts of solutes, are of great interest. These kind of biosensors comprise microorganisms like genetically modified yeast cells, which react on a specific stimulus, e.g. a residual amount of drugs in the measurement medium with a dependent fluorescence. The receptors of the cells detect specific signal molecules and stimulate the organism to produce a fluorescent protein. In this work, a combined impedimetric-optical read out was used, which can provide the reliable and long-term stable detection of a fluorescence signal accompanied by impedance measurements monitoring cell vitality and activity. A new challenge thereby is a special sensor design which enables the integration of excitation source, photodetector, interdigitated electrodes, and the fluidic system with an effective and long-term-stable packaging.*

Keywords: Diclofenac, impedance spectroscopy, transparent ITO-electrodes, switchable electrical interdigital fingers, multiplexer

MULTISENSORY DLA BIOSENSORÓW PEŁNOKOMÓRKOWYCH

***Streszczenie**: Biosensory pełnokomórkowe cieszą się bardzo dużym zainteresowaniem. Mogą one być wykorzystywane w ochronie środowiska i technologii pomiaru procesów, w branży biotechnologicznej, spożywczej i farmaceutycznej do kontrolowania i monitorowania procesów chemicznych i biochemicznych on-line oraz do szybkiego wykrywania niewielkich ilości substancji rozpuszczonych,. Tego rodzaju biosensory obejmują mikroorganizmy, takie jak genetycznie zmodyfikowane komórki drożdży, które reagują na specyficzny bodziec, np. fluorescencją na resztkowa ilość leków w pożywce pomiarowej. Receptory komórek wykrywają określone cząsteczki sygnałowe i stymulują organizm do wytwarzania białka fluorescencyjnego. W pracy wykorzystano łączony odczyt impedancyjno-optyczny, który może zapewnić niezawodną i długotrwale stabilną detekcję sygnału fluorescencyjnego, któremu towarzyszą pomiary impedancji monitorujące żywotność i aktywność komórek. Nowym wyzwaniem jest specjalna konstrukcja czujnika, która umożliwia integrację źródła pobudzenia, fotodetektora, elektrod palcowych i układu płynowego w jednej obudowie.*

Słowa kluczowe: Diclofenac, spektroskopia impedancyjna, przezroczyste elektrody ITO, przełączane palce elektrodowe, multiplekser

Introduction

Within the framework of the collaborative project BioSAM, a sensor for the detection of the analgesic diclofenac in wastewater was developed. It was used as a prototype by several institutes that worked on different work packages according to their profile. Of the total drug used, diclofenac reaches 70% by excretion via the urine in the wastewater cycle. In Germany, only 63 t per year are prescribed medically. In water treatment plants, diclofenac is removed in only insignificant amounts, so that it enters the water cycle [5]. For example, in a 2008 study on European rivers, diclofenac concentrations in the one- to three-digit nanogram per liter range were measured [2]. From India, the fact is known that the uptake of the substance can lead to death of free-living vultures by kidney failure. Some fish species have also been shown to have harmful effects on the liver and kidneys [1].

In practice, there are already very accurate and reliable analytical methods for the detection of diclofenac in surface water. However, they need an infrastructure such as special laboratories with appropriate staff and logistical efforts. In contrast, the method presented here is inexpensive and suitable for on-site measurements.

The functional principle of the developed whole-cell biosensor is based on the use of genetically modified yeast cells, which produce a fluorescent protein under the influence of diclofenac. The detection of a fluorescence signal was accompanied by impedance measurements monitoring both cell vitality and activity.

1. Experimental setup

1.1. Impedance sensor

In order to enable a combination of optical and electrical measurements, transparent ITO (indium tin oxide; 0.5 µm thick) interdigital structures for impedance spectroscopy were coated on the B270i glass wafers (wafer thickness (1.0 ± 0.1) mm). The prepared structures were optically transparent and conductive. The living cells were immobilized on the glass substrate with two coated ITO-electrode arrays in a four-chamber microfluidic cell. The optical transmitter/receiver module was installed below the glass substrate (figures 1 and 2).

Two ITO-electrode arrays provided the independent impedance measurements for the measuring and reference channels. Each array consists of 24 fingers (with a finger length of 11 mm). Depending on the layout, the distance between the fingers varies between 2.5 µm and 133.5 µm and the width between 5 µm and 186 µm (Fig. 2).

Using a multiplexer, it was possible to connect the finger structures arbitrarily to form arrays or to operate them individually. As a result, the penetration depth of the electric field into the medium could be varied. Thus, the medium and cells could be impedimetrically detected separately from each other [6].

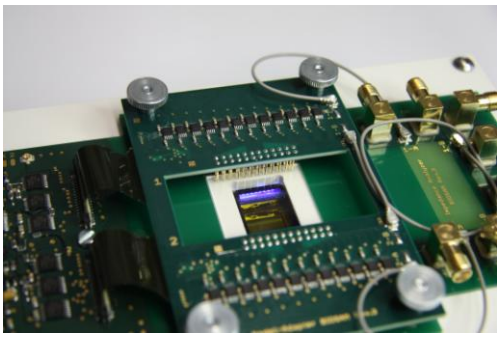

Fig. 1. Circuit board with control-part, multiplexer, interdigital ITO (indium tin oxide) structures and fluorescence sensor for analyte detection (the fluidics interface is not shown)

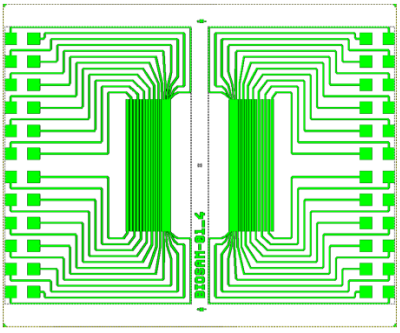

Fig. 2. Layout of the ITO-structures on glass

The multiplexer board consists of a main board and a needle adapter board. The latter was detachably connected to the main board by two ZIF flex connections. It consists of a 2×12 dual analog multiplexer, 2×24 spring contact pins and 4 micro coax connectors [7].

Using a corresponding graphical user interface (GUI), the individual shift registers were controlled via the COM port and the microcontroller in such a way that each of the 2×24 channels could be switched to high or low (GND, ground) signal separately.

One spring contact pin represents one channel. The needle adapter board is pressed down by means of 4-four knurled nuts/screws so that the spring contact pins are pressed onto the contact surfaces of the BioSAM chip. By switching the channels, individual "strips" or "strip pairs" can be activated or deactivated so that the active measuring area is increasing or decreasing.

The output signal is formed by that contributions from the actively switched channels. All inactive channels were switched to ground (GND) and their signals were thus not recorded and did not contribute to the sum signal.

1.2. The optical sensor

The optical sensor consists of two LED light sources (one for each chamber), two filter units and the photodiode (Figs. 3 and 4). The filter units separate the excitation (470 nm) and the fluorescent (510 nm) light as sharply as possible.

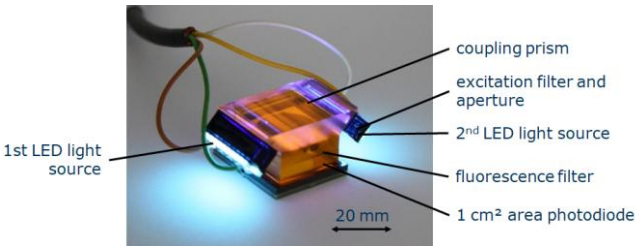

Fig. 3. Optical sensor

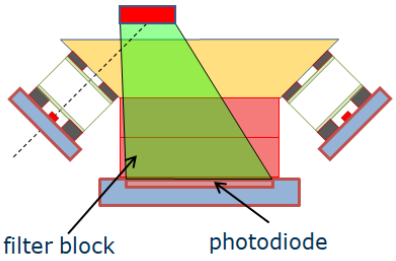

Fig. 4. Schematic cross-section through the optical sensor

2. Measurement results

Test measurements were carried out at CiS Forchungsinstitut für Mikrosensorik, Erfurt, for KCl aqueous solutions by means of a LCR meter 4294A (Agilent Inc.) (Fig. 5). This LCR meter has a measuring range of 40 Hz to 110 MHz whereas the frequency range amounts only to 40 Hz to 1 MHz.

The measurements were performed for the KCl solutions with concentrations of 1 mol/l, 10^{-3} mol/l, 10^{-5} mol/l, and 10^{-7} mol/l. Since potassium and chloride ions have the same ion mobility those solutions are almost potential-neutral and therefore are preferably used as a calibration standard [4]. Additionally, the impedance spectrum of the dry substrate was recorded (Fig. 5).

For measurements with living cells, one of the two chambers served as a reference with only the nutrient medium flowing through it. The presence of cells affects the measuring impedimetric signal by their electrical properties.

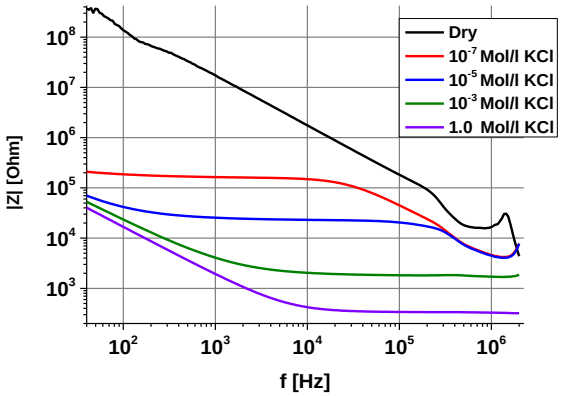

Fig. 5. Impedance spectra for the KCl solutions and for the dry substrate

In general, a cell can be described quite well by means of a equivalent circuit diagram, in which the cell membrane is characterized by two capacitances and the interior of the cell is modeled by an ohmic resistor.

In the combined opto-impedimetric sensor system, the fluorescence signal was optically detected using the CiS fluorescence setup when switching on either one LED row or two LED rows (470 nm, 27 V, 8 mA). The photodiode current was measured by means of a current-voltage converter based on an operational amplifier OP177 and a LabJack U6-PRO card [3].

Figure 6 shows the change of the photodiode current as a function of the diclofenac concentration after a 16 h overflow with MM (minimal medium nutrient solution), mixed with different diclofenac concentrations. The optical signal was determined using the fluorescence setup, which was located below the microfluidic cell with immobilized yeast cells (Saccharomyces cerevisiae BY4741 p426PDR5-tGFP).

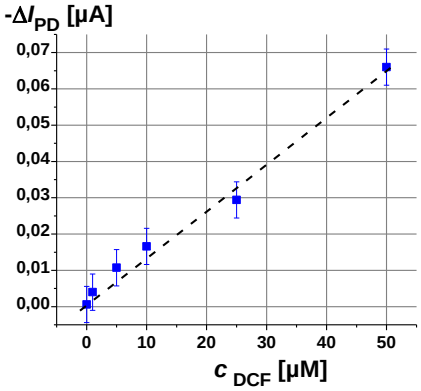

Fig. 6. Photodiode current I_{PD} as a function of the diclofenac concentration c_{DCF}

The results of the impedance measurements are shown in figures 7 and 8. In was found, that the impedance spectrum depends on the electrode configuration, on the composition of the supplied solution as well as on the cell density. Figure 7 compares the spectra for the yeast cells immobilized in gel and for the cell suspension placed on the ITO electrode arrays (glass substrate BioSAM-01_4) in a microfluidic cell. Figure 8 shows the change in the impedance modulus at a frequency of 100 kHz for immobilized yeast cells Saccharomyces cerevisiae BY4741 p426PDR5-tGFP in the medium and in 1 µM diclofenac solution. The time-dependent impedance increase was caused by the cell proliferation.

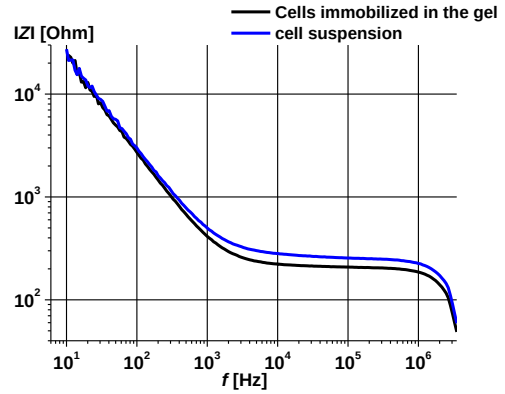

Fig. 7. Impedance spectra for the immobilized cells and for the cell suspension

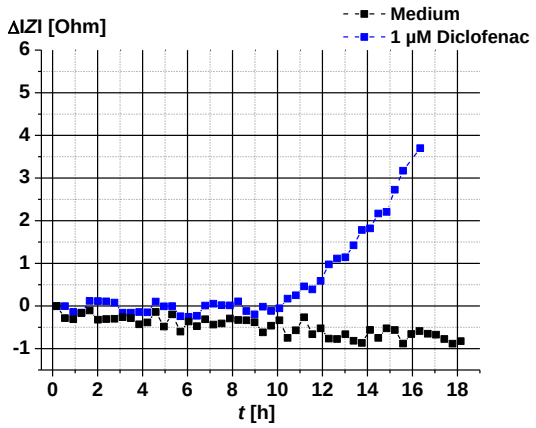

Fig. 8. Change of the impedance modulus at a frequency of 100 kHz for immobilized yeast cells in the medium and in 1 µM diclofenac solution

Such a sensor model based on electrical networks is able to describes the dynamic behavior of immobilized cells and the transport processes at the electrodes. Figure 9 shows the equivalent circuit diagram, whose parameters (Table 1) were adapted to the measured data determined by means of a corresponding ITO electrode configuration.

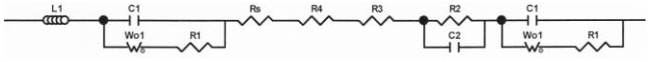

Fig. 9. Equivalent circuit diagram of the cell including the experimental setup (explanation in the text)

Table 1. Parameters of the network model of Fig. 9

Parameter	Immobilized cells		Unit
	2 finger	electrode array	
L_1	$9 \cdot 10^{-8}$	$9 \cdot 10^{-8}$	H
C_1	$6 \cdot 10^{-8}$	$6 \cdot 10^{-8}$	F
R_W	$6{,}5 \cdot 10^{-3}$	$6 \cdot 10^{-3}$	Ω
τ	$1{,}2 \cdot 10^{-10}$	$2{,}4 \cdot 10^{-9}$	s
P	0,42	0,46	
R_1	$2{,}5 \cdot 10^{-3}$	$2{,}5 \cdot 10^{-3}$	Ω
R_2	100	100	Ω
R_3	750	166	Ω
R_4	0	0	Ω
R_s	42	42	Ω
C_2	$5 \cdot 10^{-6}$	$5 \cdot 10^{-6}$	F

The behavior of the electrode can be modeled by means of an open Warburg impedance Z_{Wo}, a charge transfer resistance R_1 and a double-layer capacitance C_1. The cell suspension is described by a RC element (parallel connection of R_2 and C_2) connected in series with a resistor R_s of the solution. The Warburg impedance models the behavior of transport processes (usually diffusion) to electrodes. It is given by

$$Z_{Wo} = R_W \frac{ctnh\left[(j\tau w)^P\right]}{(j\tau w)^P} \quad (1)$$

where τ is the diffusion time, w the angular frequency, and $j = \sqrt{-1}$ the imaginary unit.

3. Conclusions

It was shown that a simultaneous monitoring of optical and impedimetric signals enables inexpensive and robust biosensors based on the whole-cellconcept. Such sensors can be miniaturized and are on-line capable. With further development of the cells towards higher sensitivity (e.g. by an amplification system) and a better signal stability to compare different experiments (e.g. by genomic integration of the PDR5 :: TGFP construct) as well as by the development of a small detection unit to read the fluorescence, in the future such asensor system could contribute to an improved, inline-capable wastewater analysis.

Acknowledgments

Financial support by the German Federal Ministry of Education and Research is kindly acknowledged (HIGS-03WKCL01F).

References

[1] Bidoglio G., Contini S., Gawlik B.M., Locoro G., Loos R., Rimaviciute E.: EU-wide survey of polar organic persistent pollutants in European river waters. Environmental Pollution 157/2009, 561–568.
[2] Falås P., Jewell K.S., Joss A., Ternes, T.A. Wick A: Transformation of diclofenac in hybrid biofilm–activated sludge processes. Water Research 105/2016, 559–567.
[3] Günther M. et al.: Kombinierter optisch-impedimetrischer Ganzzellbiosensor, 13. Dresdner Sensor-Symposium, Dresden 2017, 120–125.
[4] Lide D.R.: Handbook of chemistry and physics – 83rd edition. CRC Press LLC, 2002–2003.
[5] Meißner M.: Arzneimittel in der Umwelt: Natur als Medikamentendeponie, Dtsch Arztebl 105(24)/2008, A-1324 / B-1143 / C-1118.
[6] Pliquett U. et. al.: Schlussbericht. IGF-Vorhaben-Nummer 16925 BR/2; Grundlegende Untersuchungen zu Miniaturelektrodenarrays für die Impedanzspektroskopische zelluläre Biosensorik.
[7] Schröder M. et al.: Hochintegrierte Ganzzellsensoren für die Umwelt- und Medizintechnik. 13. Dresdner Sensor-Symposium, Dresden 2017, 148–152.

Ph.D. Ingo Tobehn-Steinhäuser
e-mail: itobehn@cismst.de

Development engineer in the design department of the CiS Research Institute His current research interests include impedance and temperature measurements.

Ph.D. Margarita Günther
e-mail: mguenthe@mail.zih.tu-dresden.de

M.Sc. Eng. Stefan Görlandt
e-mail: sgoerlandt@cismst.de

M.Sc. Eng. Steffen Herbst
e-mail: sherbst@cismst.de

Ph.D. Heike Wünscher
e-mail: hwuenscher@cismst.de

Prof. Thomas Ortlepp
e-mail: tortlepp@cismst.de

Prof. Gerald Gerlach
e-mail: gerald.gerlach@tu-dresden.de

otrzymano/received: 08.12.2017 *przyjęto do druku/accepted: 11.05.2018*

DOI: 10.5604/01.3001.0012.0703

TOOLS FOR COMPARING THE RESULTS OF THE WORK OF SORTING ALGORITHMS

Larysa Gumeniuk, Vladimir Lotysh, Pavlo Gumeniuk
Lutsk National TechnicalUniversity, Department of Automation and Computer – Integrated Technologies

Abstract. *The program implementation of sorting algorithms is obtained. The program realization of complex for comparison of sorting algorithms is obtained. Using the obtained tools, an analysis of algorithms for sorting by speed was performed depending on the number of members of the data array.*

Keywords: sorting algorithms, program realization, a software package

NARZĘDZIA DO PORÓWNANIA WYNIKÓW PRACY ALGORYTMÓW SORTOWANIA

Streszczenie. *Wykonano program realizujący algorytmy sortowania. Otrzymano programowy układ do porównania algorytmów sortowania. Wykorzystując otrzymane narzędzia, wykonano analizę algorytmów sortowania według prędkości, w zależności od liczby elementów tablicy danych.*

Słowa kluczowe: algorytmy sortowania, realizacja programu, pakiet oprogramowania

Introduction

Often, there is a need to arrange objects based on a single quality: to record number's data in ascending order, arrange people by their height, arrange words in alphabetical order. If you are able to compare any two items from the given set, then this set can always be arranged. The process of organizing information is called "sorting".

The volumes of data arrays reach the sizes that decades ago seemed almost unbelievable. The need to organize large amounts of information that is used to effectively implement a real-time search and processing procedure is increasing. The larger the amount of processed data, the more important is the task of optimizing the algorithms used, including sorting.

Thus, the development and research of methods for sorting data arrays, presenting them in a more convenient and formalized form with subsequent implementation is an urgent task at the present stage of development of high-performance computing instruments.

The purpose of this work is to develop a software package for comparing the results of the algorithms of sorting. The creation of a complex includes the development of algorithms and software for comparing the results of the algorithms of sorting.

1. Problem statement

In the development of tools (software complex) the most common algorithms for data sorting have been analysed. Due to the analysis conducted for the program implementation, the following sorting algorithms were selected:

- Built-in sorting algorithm (Python),
- Quicksort (Hoare sorting),
- Merge sort,
- Heapsort (pyramid sort),
- Binary insertion sort,
- Sorting by using simple (linear) inserts,
- Shell sort,
- Sort by choice,
- Bubble sort,
- Threaded sort,
- Bin sort (Bucket sort),
- Integer sort (Radix sort).

For program realization of selected algorithms scripting programming language is being used.

The scripting languages are used by themselves as complete base tool platforms more frequently. For example, many large commercial applications are now programmed mainly in Perl, PHP or Python. Python belongs to a dynamic typing language class, provides the programmer with an automatic "garbage collection" and convenient high-level data structures, such as dictionaries, lists, tuples, etc. Python combines striking power with a simple and understandable syntax, thought-out modularity and scalability.

The Python language interpreter is freely distributed under the Python Software Foundation (PSF) License, which is to some extent even more democratic than the GNU General Public License.

For Python there are libraries for access to the DBMS (on the Windows platform, access to the DB is possible through ADO). There are extension modules for Python under Windows and Unix/Linux for access to Oracle, Sybase, Informix, MySQL and SQLite.

The implementation of tools for comparing results is done in the Delphi programming language.

For temporarily storing data about the speed of program implementation of sorting algorithms, SQLite database is selected. The program is lined up with a library and the engine becomes an integral part of the program.

SQLite stores the entire database (including definitions, tables, indexes, and data) in a single standard file on the computer that is running the program.

Database Management System "SQLite" is a program that is provided under "open source" terms.

The SQLite library itself is written in C and is included in the Python installation application. A number of wrappers and components have been developed to work with Delphi. To implement the Delphi-SQLite connection, the ZeosLIB components have been selected.

ZeosLib is an open source project that supports multiple database management systems for Delphi, FreePascal, Kylix and BCBuilder: MySQL, PostgreSQL, Interbase, Firebird, MS SQL, Sybase, Oracle, SQLite. ZeosLib uses native DBMS libraries, but can also use its own modified libraries. Usually it's used for configuring and linking components to each other and the host.

The software implementation of the selected algorithms has been carried out in the programming language Python version 3.4.3. SQLite3 database version 3.7.0.1 was used to save data.

To save the data of calculation of the sorting algorithm time to obtain information about the average, median, and fashion, we use the box_plot database table box created using the SQLite3 DBMS.

The table structure is designed to store the data of ten runs of each sorting algorithm with a fixed value of the number of members of the Nb data array.

To analyse the obtained data a software package was developed, which includes: application for calculation (average, median, mode) and visualization of the obtained results; Application for analysis of the received data (regression equation, time) of the sorting process and their 2D and 3D visualization; an application for comparing graphs of sorting time dependence on the number of sorting elements.

Let's take a closer look at each of the applications.

2. Main results

Data Mining application – has the ability to download data from the box's database, namely the box_plot table, display it in tabular form, calculate the average, median, mode, maximum value and minimum value, and visualize this data in the form of a graph (Figure 1).

The application Chart_m is intended to calculate the total sorting time, creating the sorting time graphical dependence on the number of array elements for this sorting method (2D and 3D), maintaining the obtained dependence into the BMP file, and printing the received results (Figure 2).

The Charts application is designed to construct sorting time dependencies on the number of members of the sorting array for different sorting methods (Figure 3).

For each testing algorithm, a preliminary analysis of how much time algorithms work, depending on the size of the input data, was carried out.

It has been found by the research that all sorting algorithms, except for threaded sort, sorting by choice, sorting by simple inserts, and "bubble" sorting, work fairly quickly. For fast algorithms (built-in sort, integer sort, bucket sort, etc.) testing with incoming data up to 1,500,000 entries was performed; for others (that work slowly) – this limit was up to 110000 entries.

From the analysed data the results of the complexity of each algorithm are obtained.

Table 1 shows the dependence of the working time (sec.) on the number of elements sorted by different algorithms (complexity of the algorithm). The language of implementation is Python.

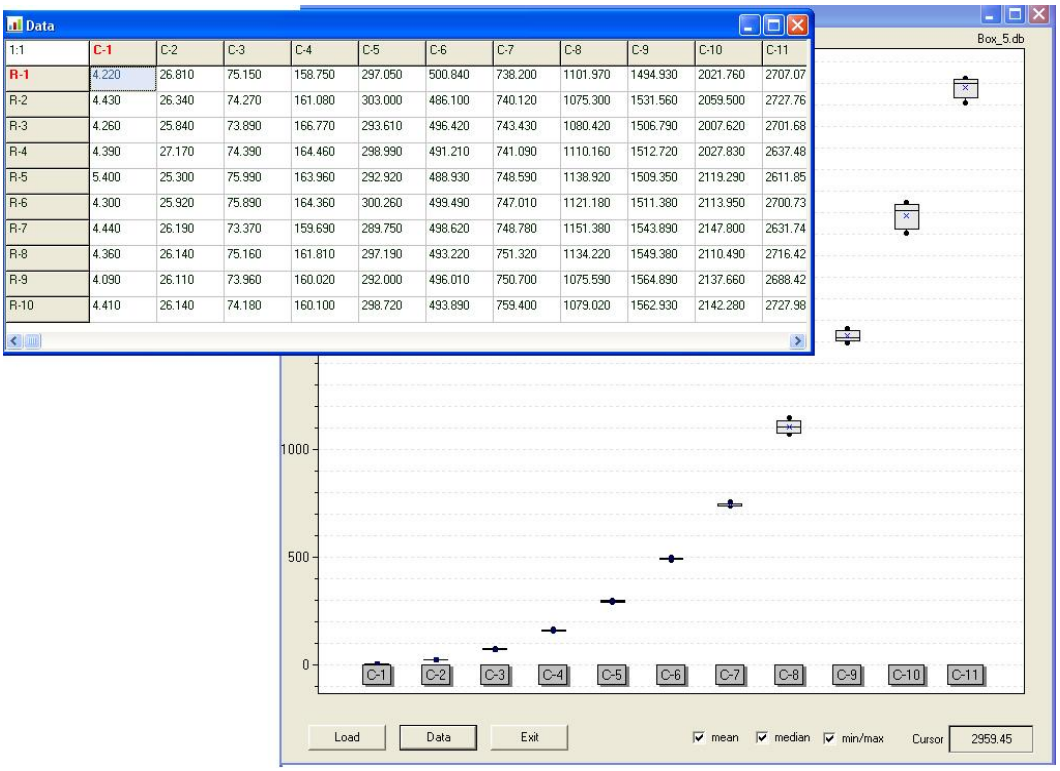

Fig. 1. Data Mining application

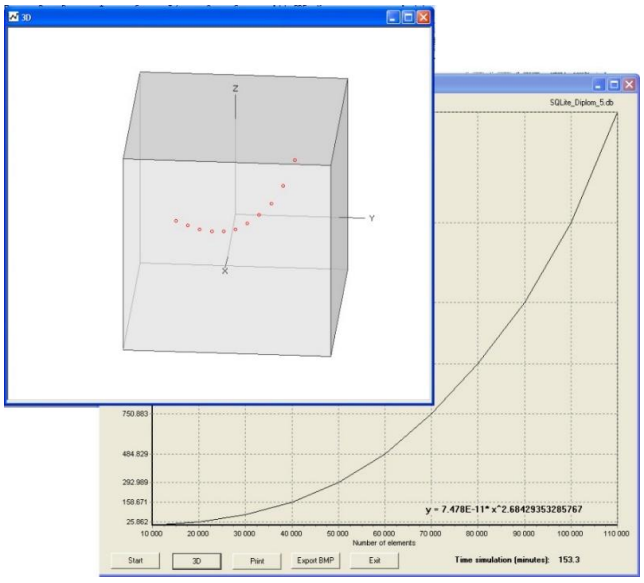

Fig. 2. The application Chart_m

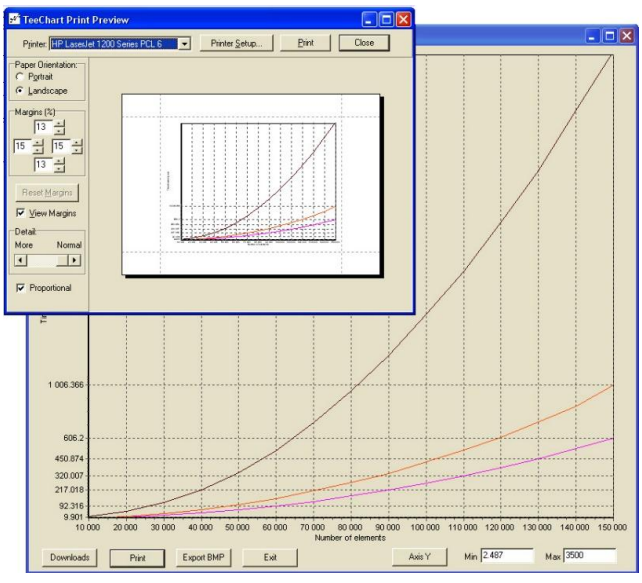

Fig. 3. The Charts application

Table 1. Dependence of the working time (sec.) on the number of elements sorted by different algorithms

Number of sorted elements	Algorithms name											
	Built-in sorting	Quicksort	Binary inserts	Merge sort	Threaded sorting	Sort by choice	Shell sort	Pyramid sort	Simple inserts	Bubble sort	Bucket sort	Sort by grade
10000	0.0083	0.092	0.277	0.1781	4.471	2.486	0.1166	0.241	13.26	4.317	0.011	0.0686
20000	0.0175	0.198	0.774	0.3781	25.862	9.901	0.2143	0.461	51.52	4.115	0.0218	0.1325
30000	0.0235	0.311	1.478	0.5867	73.461	22.26	0.3504	0.798	116.8	16.019	0.0324	0.1981
40000	0.031	0.431	2.442	0.8041	158.671	40.14	0.4584	1.077	213.3	35.415	0.0446	0.2664
50000	0.0412	0.562	3.530	1.0226	292.989	63.65	0.578	1.242	343.9	63.397	0.0571	0.3355
60000	0.055	0.691	4.828	1.2466	484.829	92.31	0.7266	1.510	512.3	101.59	0.0687	0.4042
70000	0.0567	0.817	6.258	1.4707	750.883	127.39	0.8605	1.794	722.4	146.83	0.0796	0.4759
80000	0.0661	0.959	7.937	1.7038	1087.57	169.20	0.9939	2.073	959.9	206.16	0.0924	0.5428
90000	0.076	1.087	9.834	1.9379	1502.1	217.01	1.1345	2.356	1231.7	268.33	0.1041	0.6113
100000	0.0867	1.219	11.903	2.1671	2037.53	263.05	1.2666	2.64	1539.4	339.57	0.1164	0.6812
200000	0.2051	2.614	45.241	4.6329	-	-	2.6257	5.619	-	-	0.2509	1.3716
300000	0.3316	4.067	96.237	7.1507	-	-	4.1002	8.710	-	-	0.386	2.0493
400000	0.4679	5.588	-	9.7097	-	-	5.4515	11.898	-	-	0.522	2.7254
500000	0.6084	7.111	-	12.223	-	-	7.0134	15.255	-	-	0.6609	3.4092
600000	0.7548	8.731	-	14.918	-	-	8.4102	18.398	-	-	0.7958	4.0838
700000	0.9062	10.283	-	17.796	-	-	10.236	21.748	-	-	0.9359	4.8021
800000	1.0577	11.869	-	20.516	-	-	11.721	25.116	-	-	1.0734	5.444
900000	1.2145	13.338	-	23.26	-	-	13.185	28.498	-	-	1.2114	6.1427
1000000	1.374	14.933	-	26.023	-	-	14.619	31.864	-	-	1.3499	6.8398
1500000	2.2014	23.084	-	40.095	-	-	22.002	49.392	-	-	2.0584	10.214

The following table shows that the following sorting algorithms: threaded sort, sort by choice, simple inserts, "bubble" sort, work very long in comparison with others.

The graph of the time dependence of these algorithms on the number of elements sorted is as follows (Figure 4).

From the graph it is noticeable that the algorithm of "threaded sort" is considerably inferior to others (more than 2 times).

Let's consider the running time of other algorithms.

We will start with the algorithm of binary inserts. The graph of the time dependence of this algorithm looks like this(Figure 5).

We describe the resulting curve by the equation of the form $y = ax^b$. We get y = 1.736E-8·x^1.77365. We give the similarly calculated dependencies in the four previous algorithms and in the binary insertion algorithm in Table 2.

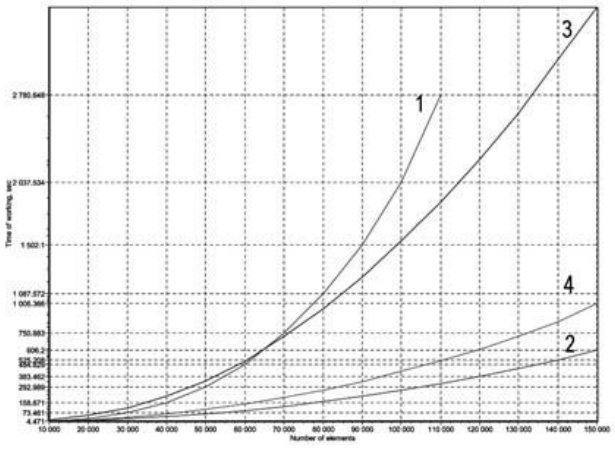

Fig. 4. Nonlinear dependence of the algorithm's running time on the number of elements that are sorted. The following algorithms are presented in the graph: 1 – Threaded sorting, 2 – Sort by choice, 3 – Simple inserts, 4 – Bubble sort

Table 2. Dependencies of the forms $y = ax^b$ for sorting algorithms

Algorithms name	Analytical equation of the curve	Coefficients	
		a	b
Threaded sorting	$y = ax^b$	7.478E-11	2,68429
Sort by choice	$y = ax^b$	1.725E-8	2,03691
Simple inserts	$y = ax^b$	5.536E-8	2.08723
Bubble sort	$y = ax^b$	3.358E-8	2,02027
Binary inserts	$y = ax^b$	1.736E-8	1.77365

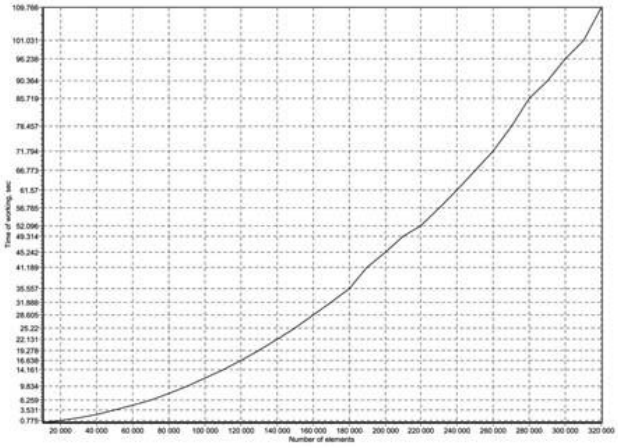

Fig. 5. The speed of the binary insertion algorithm

The binary insertion algorithm works faster than the previous four also because the constant b in this algorithm is smaller.

Let's consider a series of fast algorithms: quicksort, merge sort, Shell sort, pyramid sort (Figure 6).

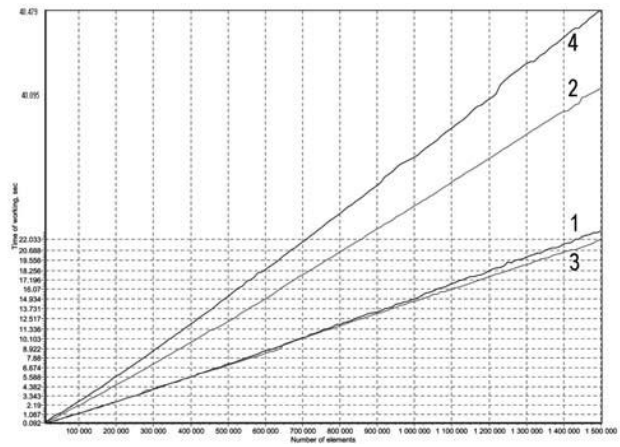

Fig. 6. The speed of algorithms: 1 – Quicksort, 2 – Merge sort, 3 – Shell sort, 4 – Pyramid sort

Accordingly, the table of coefficients of the equations for the given algorithms is as follows:

Table 3. Dependencies of the forms $y = ax^b$ for sorting algorithms

Algorithms name	Analytical equation of the curve	Coefficients	
		a	b
Quicksort	$y = ax^b$	4.151E-6	1.07562
Merge sort	$y = ax^b$	8.784E-6	1.07868
Shell sort	$y = ax^b$	6.281E-6	1.06096
Pyramid sort	$y = ax^b$	4.126E-6	1.09330

In this group the Pyramid sort Shell sort algorithm was the fastest.

The last considered algorithms:

- Sort by the built-in Python function.
- Bucket sorting.
- Sort by grade (Figure 7).

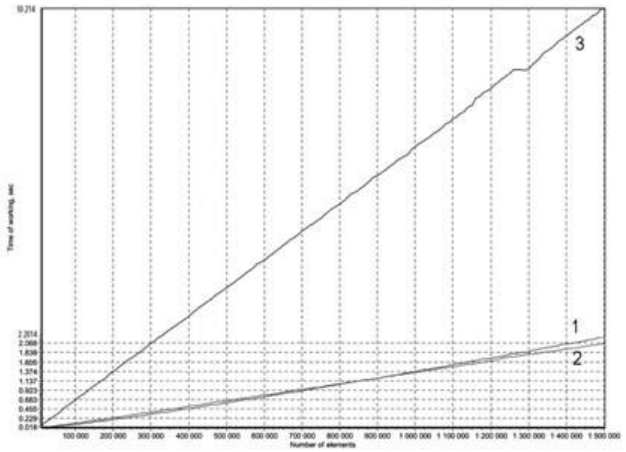

Fig. 7. The speed of algorithms: 1 – Sort by the built-in Python function, 2 – Bucket sorting, 3 – Sort by grade

Accordingly, the table of coefficients of the equations for the given algorithms is as follows:

Table 4. Dependencies of the forms $y = ax^b$ for sorting algorithms

Algorithms name	Analytical equation of the curve	Coefficients	
		a	b
Built-in Python function	$y = ax^b$	1.392E-7	1.03039
Bucket sorting	$y = ax^b$	6.609E-7	1.02246
Sort by grade	$y = ax^b$	5.478E-7	1.05756

Table 5. Total sorted table of algorithms' speed

Algorithms name	Analytical equation of the curve	Coefficients		
		a	b	b [5]
Threaded sorting	$y = ax^b$	7.478E-11	2,68429	-
Simple inserts	$y = ax^b$	5.536E-8	2.08723	2.01693
Sort by choice	$y = ax^b$	1.725E-8	2,03691	-
Bubble sort	$y = ax^b$	3.358E-8	2,02027	1.88238
Binary inserts	$y = ax^b$	1.736E-8	1.77365	2.00631
Pyramid sort	$y = ax^b$	4.126E-6	1.09330	1.08243
Merge sort	$y = ax^b$	8.784E-6	1.07868	-
Quicksort	$y = ax^b$	4.151E-6	1.07562	1.08036
Shell sort	$y = ax^b$	6.281E-6	1.06096	-
Sort by grade	$y = ax^b$	5.478E-7	1.05756	-
Built-in sorting	$y = ax^b$	1.392E-7	1.03039	1.07821
Bucket sort	$y = ax^b$	6.609E-7	1.02246	-

3. Summary

The program implementation of sorting algorithms is obtained. The program realization of complex for comparison of sorting algorithms is obtained. Using the obtained tools, an analysis of algorithms for sorting by speed was performed depending on the number of members of the data array.

References

[1] Antonova I., Karikh O.: Otsenka effektivnosti parallel'nykh algoritmov zadachi sortirovki dannykh. Promyshlennyye ASU i kontrollery 3/2010, 23–25.
[2] Kovartsev A., Popova-Kovartseva D.: Strukturnaya optimizatsiya upravlyayushchego grafa na osnove algoritma topologicheskoy sortirovki. Programmnaya inzheneriya 5/2013, 31–36.
[3] Knut D.: Iskusstvo programmirovaniya. T.3. Sortirovka i poisk. Izdatel'skiy dom "Vil'yams", Moscow 2003.
[4] Martynov V., Mironov V.: Parallel'nyye algoritmy sortirovki dannykh s ispol'zovaniyem tekhnologii MPI. Vestnik Syktyvkarskogo universiteta – Seriya 1: Matematika, Mekhanika, Informatika 16/2012, 130–135.
[5] Ovchinnikova I., Sakhnova T.: Algoritmy sortirovki pri reshenii zadach po programmirovaniyu. Informatika i obrazovaniye 2/2011, 53–56.
[6] Samun' V.: Sravneniye raboty algoritmov sortirovki, realizovannykh na yazyke Perl., 2007, http://docplayer.ru/29195102-Sravnenie-raboty-algoritmov-sortirovki-realizovannyh-na-yazyke-perl.html (available: 01.10.2017).

Ph.D. Larysa Gumeniuk
e-mail: l.gumeniuk@lntu.edu.ua

Lutsk NationalTechnical University, PhD. (technical), Head of Department of Automation and Computer – Integrated Technologies.
Research interests: Modeling ofreliability and safety ofthe automated control systems.
Has more than 60 publications in this area

Ph.D. Vladimir Lotysh
e-mail: admin@lntu.edu.ua

Lutsk National Technical University, PhD. (technical), Department of Automation and Computer – Integrated Technologies.
Scientific interests include open-source software applied for simulations of problems using distributed platforms.
Author of nearly 80 publications in this area.

Ph.D. Pavlo Gumeniuk
e-mail: p.gumeniuk@lntu.edu.ua

Lutsk NationalTechnical University, PhD. (technical), Department of Automation and Computer – Integrated Technologies.
Research interests: programming, robotics.

otrzymano/received: 21.10.2017 *przyjęto do druku/accepted: 11.05.2018*

DOI: 10.5604/01.3001.0012.0704

MODIFIED, COMPLEMENTED TAXONOMY OF FAULTS IN FAULT-TOLERANT REAL-TIME SYSTEMS

Volodymyr Mosorov, Taras Panskyi, Sebastian Biedron
Lodz University of Technology, Institute of Applied Computer Science

Abstract. *This paper presents the main definitions relating to dependability. Basic definitions including reliability, security, maintainability, etc. are described first. They are then supplemented by additional definitions, which address to the threats of dependability (faults, errors, failures). Overlapping dependability standards, renumbering and integration can cause uncertainty when using of a certain definition. For this purpose, authors present complemented fault taxonomy for fault-tolerant real-time systems to eliminate inconsistencies and to unify existing fault taxonomies.*

Keywords: fault, taxonomy, classification, dependability

ZMODYFIKOWANA, UZUPEŁNIONA TAKSONOMIA USTEREK W TOLERUJĄCYCH AWARIE SYSTEMACH CZASU RZECZYWISTEGO

Streszczenie. *W artykule przedstawiono najważniejsze definicje dotyczące słowności. Podstawowe definicje w tym niezawodność, bezpieczeństwo, obsługiwalność, itp. opisane są w pierwszej kolejności. Następnie są one uzupełniane dodatkowymi definicjami, które odnoszą się do zagrożeń słowności (usterki, błędy, awarie). Nakładające się standardy słowności, renumeracja i integracja mogą spowodować niepewność przy korzystaniu z pewnych definicji. W tym celu autorzy przedstawiają uzupełnioną taksonomię usterek w tolerujących błędy systemach czasu rzeczywistego. Celem jest wyeliminowanie niespójności oraz unifikacji istniejących taksonomii usterek.*

Słowa kluczowe: usterki, taksonomia, klasyfikacja, słowność

Introduction

The problem of reliable computing is as old as the first computers appear which used electric switches, mechanical relays, vacuum tubes, etc. The era of modern computing began with a flurry of technical development before and during World War II. Computer systems while the early 40's were slowed by various problems, including relatively unreliable components, complex equipments, cumbersome operations, and component synchronization imperfections. The invention of the transistor could be considered as an important milestone of computer system reliability. However, much more strict and demanding reliability requirements were caused by the space program in the early 60's, as well as by other real-time safety-critical practical applications where human lives could be threatened by a computer system failure.

The concept of fault tolerance unifies different approaches to system reliability by means of testing, diagnosis, prediction, redundancy in hardware and software, etc. It emerged in the late 60's when more emphasis was given to reliability testing on component and system level. Moreover, the first reliability standards were created at that time, namely military standard 781, military handbook 217. The concept of fault tolerance in 80's became more formalized due to International Organization for Standardization and its stand-alone International Electrotechnical Commission and reached maturity with the formation of the IEEE Computer Society Technical Committee on Fault-Tolerant Computing in 1969 [1].

Nowadays, there are a various combinations of national and international standards, government organizations, professional societies which have promulgated a dizzying number of system dependability standards, guidelines, recommended practices, rapports and other frameworks [4]. However, the majority of standard define only the basic term of fault, errors or failure without indentations in their properties, types, and relationships.

This paper aims to give precise definitions characterizing the various types of faults that come into play when addressing the dependability and security of computing and communication fault-tolerant systems. Furthermore, article aims to complement and unify existing fault taxonomies to eliminate inconsistencies and overlapping terms.

1. Dependability in fault-tolerant real-time system

Many terms can be used informally to describe the desired result that a system performs without going wrong. Besides the reliability, dependability is one of the key and expected system requirements. The term dependability seems not to be clearly defined. Therefore different meanings are cited:

- The original definition of dependability is the ability to deliver service that can justifiably be trusted [6]. In a broad sense, dependability includes its related attributes namely, reliability, availability, safety as well as maintainability. Fig. 1 summarizes the relationship between dependability and its principal attributes.
- According to [4] dependability is a form of availability that has the property of always being available when required. It is the degree to which a system is operable and capable of performing its required operation at any randomly chosen time during its specific operating time, on condition that the system is available at the start of the period.

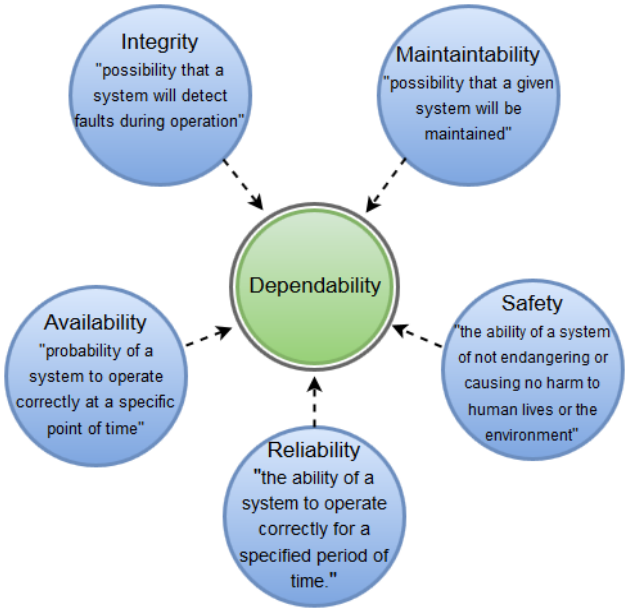

Fig. 1. Dependability and its attributes

Being fault tolerant is strongly related to what is called dependable system. A fault-tolerant real-time system is capable of performing the operations with satisfactory performance even if one or several faults, or more critically, one or several failures occur in this system [12]. Moreover, system is not only required to deliver correct results but also timely results. Thus, a system is dependable if it exhibits a *high* probability of behaving according

to its specification. How high is it? This naturally depends on the purpose of the target system: the requirements of a life-supporting system and of a game console are quite different as well as nuclear power plant control system and light control system in a residential stairwell have completely not comparable requirement levels. The consequences of a failure are much more dramatic in life-supporting systems and in nuclear power plant control systems than in a gaming machine or in living illumination systems. The knowledge of the required degree of dependability entails the awareness of the impairments to dependability, i.e., the potential causes for incorrect behavior (faults, errors, failures) and the possible ways of their elimination.

2. Threats to dependability: faults, errors, failures

A fault-tolerant real-time system provides continuous, safe operation in the presence of faults. This system must detect errors caused by faults, assess the damage caused by the fault, recover from the error, and isolate the fault. The faults the system is to be designed to tolerate must be defined based on analysis of high requirements including the probability of each fault occurring, and the impact on the system performance in general [11].

In everyday language, the terms fault, failure, and error are used interchangeably. In fault-tolerant computing, however, they have distinctive meanings. A fault is an unpermitted deviation of at least one characteristic property (feature) of the system from the acceptable, usual, standard condition. A fault corresponds to an abnormal behavior of the system, which may not affect the overall functioning of the system but may eventually lead to a failure.

A failure is a permanent interruption of a system's ability to perform a required function under specified operating conditions. Resulting from one or more faults, a failure is therefore an event that terminates the functioning of a unit in the system or a system as a whole (critical failure).

An error is a discrepancy between a computed, observed or measured value or condition, and the true, specified or theoretically correct value or condition [9]. An error within a system may be caused by fault of one or more of its components, or by the activation of a systematic fault.

According to [5] the relationship between terms fault, failure and error is illustrated in Fig. 2. That is, an error leads to a failure event (unless the error is not removed), and the last leads to the fault state.

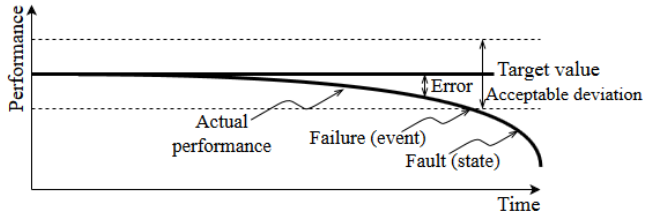

Fig. 2. The difference between failure, fault, and error

However, according to [8] an error may lead to a failure–a failure occurs when the error causes the delivered service to deviate from correct service. A fault is the cause of an error, and an error is the cause of a failure. The relationship between fault, failure and error is shown in Fig. 3.

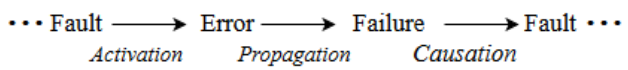

Fig. 3. The relationship between failure, fault, and error

Dependability as well as its threats differs in its meaning in some standards, e.g. MIL HDBK, IEC, DIS, etc. Organizations have different overlapping standards difficult to know which are applicable for a given situation or system. Therefore, many authors referring to the same standards confuse the reader. In this article, the authors tend to [8] explanation, where a fault is the cause of an error, and an error is the cause of a failure.

In any fault-tolerant real-time system, the range of potential fault that is quite large; enumerating all such possibilities is a vital yet formidable task in validating the system's readiness for deployment.

3. A taxonomy of faults

"A fault is an unpermitted deviation of at least one characteristic property (feature) of the system from the acceptable, usual, standard condition." [7]. Based on this definition, a fault corresponds to an abnormal behavior of the system, leading to the inability to perform as required, due to an internal state, which may not affect the overall functioning of the system but may eventually lead to a failure of one or several components. As suggested in [3] faults could be categorized in several ways according to eight basic viewpoints: phase of creation or occurrence, system boundaries, phenomenological cause, dimension, objective, intent, capability, persistence (duration). Additional viewpoints, namely extent and nature have been appeared in [4]. Classifications of faults in a tree form have been depicted in [10] with mode, domain and value viewpoints. Fig. 4 shows a complemented taxonomy of faults all aforementioned and suggested few extra viewpoints.

The new classification of faults includes several new viewpoints (classes). The classification of viewpoints is as follows:

1. The fault ***detection*** class indicates a capability of fault to be detected. Thus, faults could be distinguished as *detected* and *undetected*. Detected faults are subdivided into *targeted* and *accidentally detected* faults. Fault detection techniques are used to diagnose the presence of faults so that adequate countermeasures can be taken to prevent failures.
2. The ***simplicity*** of the faults:
   A *simple fault* is a fault that can be fixed by making a single change to a source statement. A complex fault is a fault that cannot be fixed by making a single change to a source statement. Terms simple and *complex faults* have never been formally defined, we introduce the working definitions only.
3. The ***sensitivity*** of the faults:
   According IEC 192-04-13 and IEC 192-04-14, *data sensitive fault* is a fault that is only activated when particular data are encountered. *Program sensitive fault* is a fault that is only activated when a particular sequence of program steps is executed. Generally these types of faults are for software only, but also could appear in hardware as well.
4. Two types of faults are considered relating to the ***correlation*** class: *independent* and *related* faults. Related faults result from a fault in a common specification or from dependencies in a separate design and implementation
5. The ***plurality*** class of the faults:
   Single fault is a fault caused by one adverse physical or one harmful human action. *Multiple faults* are two or more concurrent, overlapping or sequential single faults whose consequence, e.g. failures, errors, etc.
6. The ***style*** of the faults:
   An *omission fault* occurs of not doing something system should has done (the absence of actions when it should be) A *commission fault* occurs when a component generates incorrect results or when wrong actions are performed.
7. The ability to identify the activation pattern of a fault that had caused one or more errors is the ***fault activation reproducibility***. Faults can be categorized according to their activation reproducibility [2]:
   Faults whose activation is reproducible are called *solid* faults, whereas faults whose activation is not systematically reproducible are *elusive* faults.

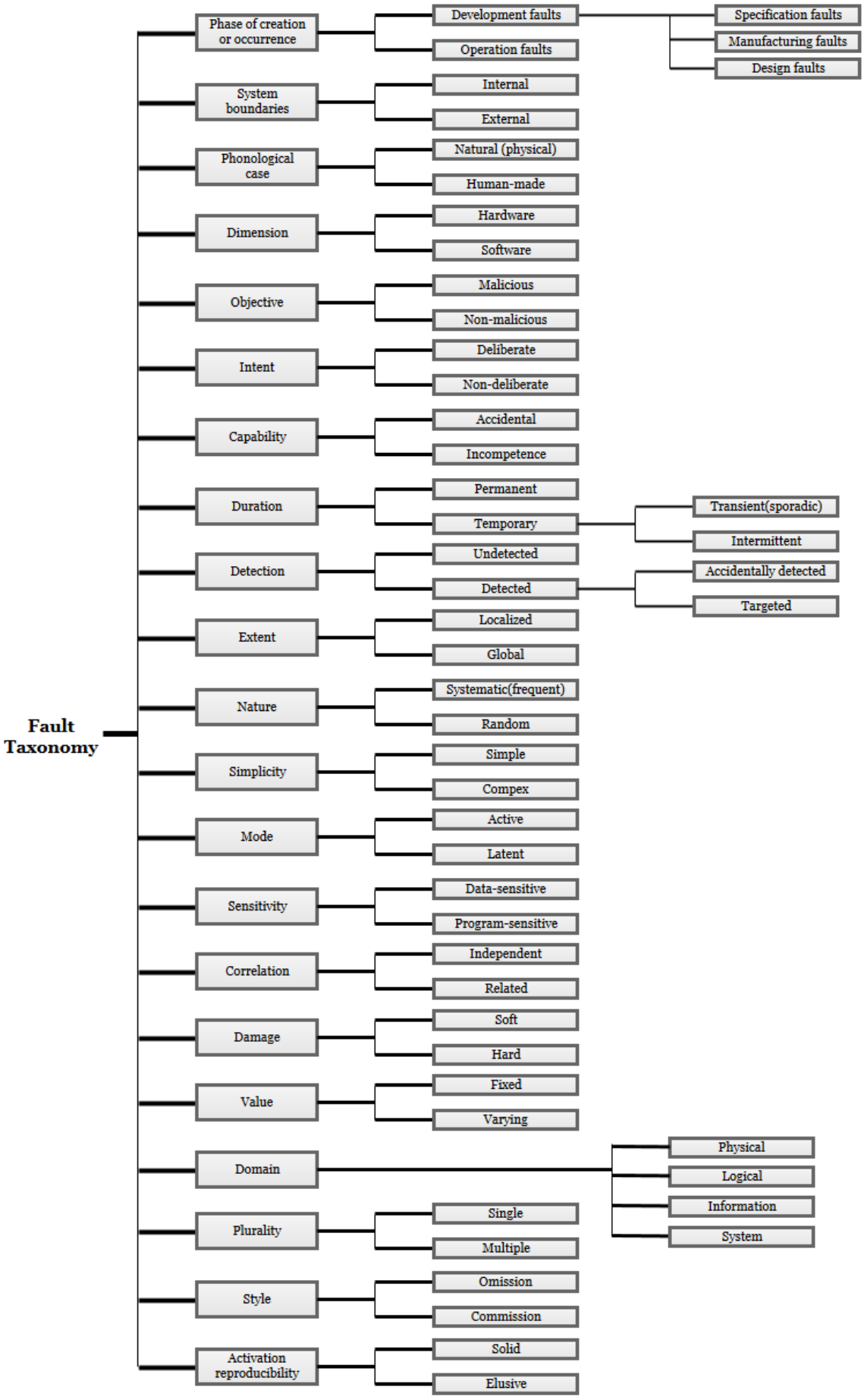

Fig. 4. Taxonomy of faults

4. Conclusion

Nowadays, developing sophisticated fault-tolerant real-time systems is required by public and private bodies. Simultaneous consideration of dependability provides a very convenient tool uniting various concerns within a single conceptual framework. Dependability includes such attributes as availability, reliability, safety, confidentiality, integrity, maintainability. However, despite the wide network of different national and international standards bodies the terminology differences are the largest potential problem. Due to consideration such as need for consistency within a set of standards, intended audience and conceptual organization, dependability as well as its attribute definitions differ in some standards, e.g. MIL HDBK, IEC and DIS. Organizations have different overlapping standards difficult to know which are applicable for a given situation. Moreover, the latest dependability standards do not outline even half of the presented fault classes. Therefore, the fault taxonomy aims to unify and to complement existing fault taxonomies to eliminate inconsistencies, renumbering and overlapping terms. Also, the taxonomy has been created to simplify the verbal description and to improve the adequacy of the models.

This article considers only elementary fault classes, however presented taxonomy does not include a complete picture of faults in fault-tolerant systems (for example authors do not consider the taxonomy of hardware or human faults). Moreover, complemented taxonomy only states the fact of its existence and does not cover the relationship between the presented fault classes.

References

[1] Avizienis A.: Fault-tolerant systems. IEEE Transactions On Computers, vol. 25, no. 12, 2006, 1304–1312.
[2] Avizienis A., Laprie J.-C., Randell B.: Dependability and Its Threats: A Taxonomy, in Building the Information Society. Springer Science + Business Media, 2004, 91–120.
[3] Avizienis A., Laprie J.-C., Randell B., Landwehr C.: Basic concepts and taxonomy of dependable and secure computing. IEEE Transactions on Dependable and Secure Computing, vol. 1, no. 1, 2004, 11–33.
[4] Bozzano M., Villafiorita A.: Design and safety assessment of critical systems. Auerbach Publications, 2010.
[5] Hoyland A., Rausand M.: System reliability theory: Models and statistical methods. John Wiley, 2009.
[6] Isermann R.: Fault-diagnosis applications. Springer-Verlag Berlin Heidelberg, 2014.
[7] Isermann R.: Fault-diagnosis systems. Springer-Verlag Berlin Heidelberg, 2006.
[8] Lee P. A., Anderson T.: Fault tolerance in Dependable Computing and Fault-Tolerant Systems. Springer Vienna, 1990.
[9] Meulen M.: Definitions for hardware and software safety engineers. Springer-Verlag London, 2000.
[10] Spitzer C.: Digital avionics handbook, Second edition – 2 volume set (electrical engineering handbook). 2nd ed. CRC Press, 2006.
[11] Tanenbaum A. S., van Steen M.: Distributed systems: Principles and paradigms. Prentice Hall, 2002.
[12] Veríssimo P., Rodrigues L.: Distributed systems for system architects in Advances in Distributed Computing and Middleware. Springer US, 2001.

D.Sc. Eng. Volodymyr Mosorov
e-mail: w.mosorow@kis.p.lodz.pl

Volodymyr Mosorov received his Ph.D. in 1998 from the State University of Lviv, Ukraine. V.Mosorov was awarded the title of Doctor of Science from AGH University of Science and Technology Krakow Poland in 2009. He is now an associate professor at the Institute of Applied Computer Science of Lodz University of Technology, Poland. His research interests include data mining and clustering. He has published more than 80 technical articles.

M.Sc. Eng. Taras Panskyi
e-mail: tpanski@kis.p.lodz.pl

Graduated from the Department of Theoretical Radio Engineering and Radio Measurement at Lviv Polytechnic National University, Ukraine. Since 2013, he has been a Ph.D. student at the Institute of Applied Computer Science of Lodz University of Technology, Poland. His research interests include data clustering, reliability and availability indexes of embedded systems, educational migration.

M.Sc. Eng. Sebastian Biedron
e-mail: sbiedron@iis.p.lodz.pl

Graduated from the Department of Science and Mathematics at Lodz University. Since 2012, he has been a court expert at the District Court at the Prague. Since 2013, he has been a Ph.D. student at the Institute of Applied Computer Science of Lodz University of Technology. The supervisor of his Ph.D. thesis is Volodymyr Mosorov, D.Sc. (dr hab. inż.), prof. PL.

otrzymano/received: 08.08.2016 *przyjęto do druku/accepted: 11.05.2018*

DOI: 10.5604/01.3001.0012.0706

THE APPLICATION OF REDUNDANCY IN LEACH PROTOCOL

Volodymyr Mosorov, Sebastian Biedron, Taras Panskyi
Lodz University of Technology, Institute of Applied Computer Science

Abstract. *Nowadays wireless sensor networks have gained much popularity due to their flexibility. This progress has enabled the use of sensor nodes on an unprecedented scale and opened new opportunities for the so-called ubiquitous computerization. The total freedom of nodes distribution within the wireless sensor network (WSN), where the wireless characteristic is one of the greatest advantages of WSN, implies its greatest weaknesses. To overcome this challenge specialized routing protocols, such as many different version of LEACH, were ushered in so as to make effective use of the energy of the nodes themselves. This article aims to show the functioning of a new author's solution, called IIS-LEACH, which uses redundancy as a basic element in increasing the reliability of WSN networks.*

Keywords: LEACH, reliability, node, IIS-LEACH

ZASTOSOWANIE NADMIAROWOŚCI W PROTOKOLE LEACH

Streszczenie. *W dzisiejszych czasach bezprzewodowe sieci czujników zyskują coraz to większą popularność ze względu na swoją elastyczność. Postęp ten, umożliwił zastosowanie węzłów sensorowych na niespotykaną dotąd skalę i otworzył nowe możliwości dla tzw. wszechobecnej komputeryzacji. Całkowita dowolność w rozmieszczeniu węzłów jak i jego bezprzewodowy charakter, stanowiący jedną z największych zalet wykorzystania bezprzewodowych sieci sensorowych, implikuje jego największą słabość – ograniczania związane z mobilnymi źródłami zasilania oraz nowymi problemami w zachowaniu niezawodności sieci. W celu efektywnego wykorzystania energii węzłów, zaczęto stosować wyspecjalizowane protokoły routingu takie jak LEACH. Celem tego artykułu będzie pokazanie nowe, zmodyfikowanej wersji tego protokołu o nazwie ISS-LEACH.*

Słowa kluczowe: LEACH, niezawodność, sensor, IIS-LEACH

Introduction

Technological progress in the twenty-first century, which resulted in the development of fields such as digital electronics, miniaturization and wireless communication devices, enabled the construction of multi-functional, economical and low-cost wireless sensor networks (WSN). Sensor networks are a new branch network, which largely differs from traditional wireless networks and IEEE 802.11 networks, such as mobile phones networks and MANET (ang. Mobile ad-hoc network) [4]. Self-organization of these networks, the management of mobility and routing has been designed so that as much as possible to ensure an appropriate level of QoS communication with the optimum use of the resources.

The first concept of such a network was proposed by Kristofer Pister, who began research in the late twentieth century as a professor at the University of California at Berkeley. Very important of further studies of wireless sensor network had rapid development of nanotechnology that was a consequence of the emergence of sensors that reach the size of up to 2.5 millimeters [7].

Sensor networks are usually homogeneous networks. Apart from base stations all nodes are identical and perform the same role. The nodes are arranged in so-called field sensors. Their number depends on the purpose of the network, and may consist from several to tens of thousands sensors. Sensor network nodes can be equipped with various types of measuring devices, which leads to perform different functions. This type of network is used to monitor the change in the weather, the state of the patient or even follow deformations or vibrations in the construction industry, where it may become an early warning system [1, 2]. This could prevent of disasters, accidents and contribute to improve the design and technology.

Putting these small devices often in such sensitive areas requires equipment protocols and algorithms used in a sensor network with the ability to quickly self-organize, and reliability features.

It should be noted that a large part of the sensor network is not possible to replace or attach the power source, and therefore the problem of use and optimal energy management is a priority in the sensor network. Such devices are usually equipped with a power supply (1.2 V). Battery consumption is equivalent to the damaged node. Depending on the construction of a network the loss of one or more nodes forces the network to reconfigure their connections. This leads to changes in the network topology and the need for re-alignment. Reconfiguration can drain more energy from still active nodes which in turn will lead to further instability. Therefore, power management becomes enormous importance. New improvements and solutions in the construction of the nodes have to allow inter alia their longer life. There are attempts to recover energy from the surrounding environment. Paul Wright developed nodes obtaining up to 200 mW of power from vibrations reaching the sensor.

Moreover, there are attempts to generate energy from light, heat and electromagnetic fields. An important factor is the proper usage of energy. Most resource is used for two tasks: data collection and communication. Pre-processing of data already in the memory of the sensor allows limiting energy-drain transmission to a minimum. Helpful is also a sensor configuration in such a way that it enter into a state of latency [3]. Sensor wakes up only to the collection, processing or data transmitting. Thereby, drastic solution significantly extends the life of the node. Despite of this, the device can run out of energy or may be damaged.

In some cases, when several sensors are damage it could separate the network into two parts that do not interact. The easiest way to prevent the degradation of a network is a dense arrangement of nodes. This solution will create a lot of potential routes for data transfer. With such a large number of connections data transmission in a disorganized manner would be a big waste of energy. Therefore, instead of a broadcast communication in the network data routing has been applied [5].

The purpose of this article is to use the redundancy in WSN using the original solution in the LEACH protocol. Redundancy in the protocol enables a reliable transmission of information to the base station. Presented IIS-LEACH protocol is a new technique to increase security in the exchange of information in WSN networks.

1. Node in a sensor network

The WSN is built from any number of sensors called nodes. Each node may be assigned different tasks, which results in a high diversity of the nodes and their structure. All nodes within a sensor network share similar features and modules. Each sensor has a power, transmission, measurement, and calculation module. A simplified diagram of the construction of a single node is shown in Figure 1.

The measurement module consists of a sensor that examines the surroundings and is the smallest element of the device. Figure 2 shows a configuration of the MEMS (Micro-Electro-Mechanical Systems). Other sensors can measure, e.g. temperature, humidity, radioactivity, speed, motion, chemical composition. The type of the measured parameter depends on the type of the sensor used. Some sensor network nodes allow the use of several types of sensors.

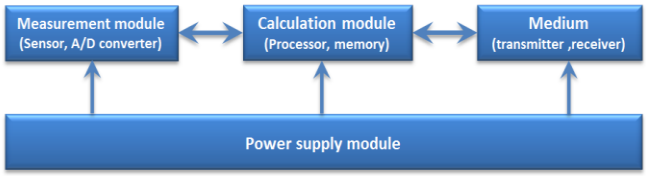

Fig. 1. Schema of a WSN node

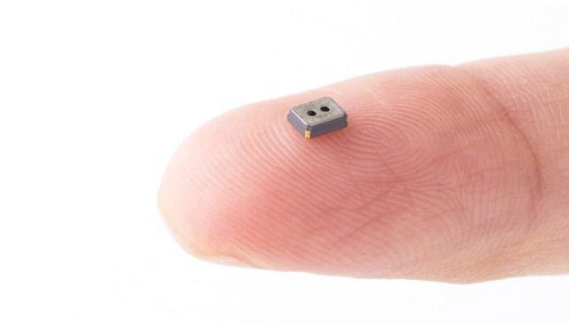

Fig. 2. FIGARO TGS8100 sensor (H_2, CO, cigarette smoke) [8]

Having completed the measurement the sensor transmits the data to the A/D converter. The purpose of the converter is to convert the signal to the digital form and forward it on. Sensor networks can be designed so that they are alert even on stand-by. This solution is applied when the network is to be continuously alert or respond to specific events only. For example, if we are interested in measuring the concentration of CO in the air, we can use appropriate filters so that we can set the sensitivity of the device. Then, the signal processed by the sensor must first penetrate through the filter. When it has met the specific requirements, the signal is passed and starts the process of activating the device.

The calculation module is one of the most important parts of the device. Its main purpose is to control the tasks and perform calculations. The module consists of a PCB board on which a microcontroller or microprocessor is integrated with the memory, interfaces and permanent record memory. The ROM, RAM and Flash memories are small in size and at best reach the size of 1 megabyte.

The medium is the most resource-consuming part of the sensor. The media are utilised by the nodes to communicate and transfer data between themselves.

The power supply module is primarily the energy storage element. The power supply system is the weakest link in the functioning of the entire platform. Depending on the size and purpose of the device different solutions are applied. Larger devices have replaceable power sources: batteries, rechargeable connectors, and many other solutions. Smaller devices are equipped with non-replaceable energy sources, solar cells and mechanisms harvesting energy from vibration or temperature differences. Still, new solutions are being sought to resolve the energy issue. Figure 4 shows energy consumption of a node in the subsequent stages.

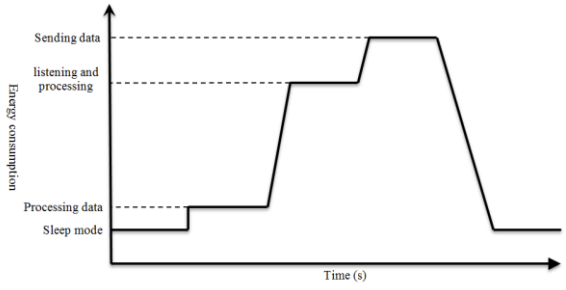

Fig. 3. Phases of energy consumption of a node

Software is one of the most important elements in the structure of the sensor, whose task is to monitor and manage the modules. The operating system which can be stored in the node's microcontroller memory can ensure response to incidents and concurrent performance of many activities conducted within sensor networks. A node can utilise, e.g. scheduler software, databases, wireless communications maintenance programme, networking programme, power management programme, and even encryption technology ensuring data confidentiality.

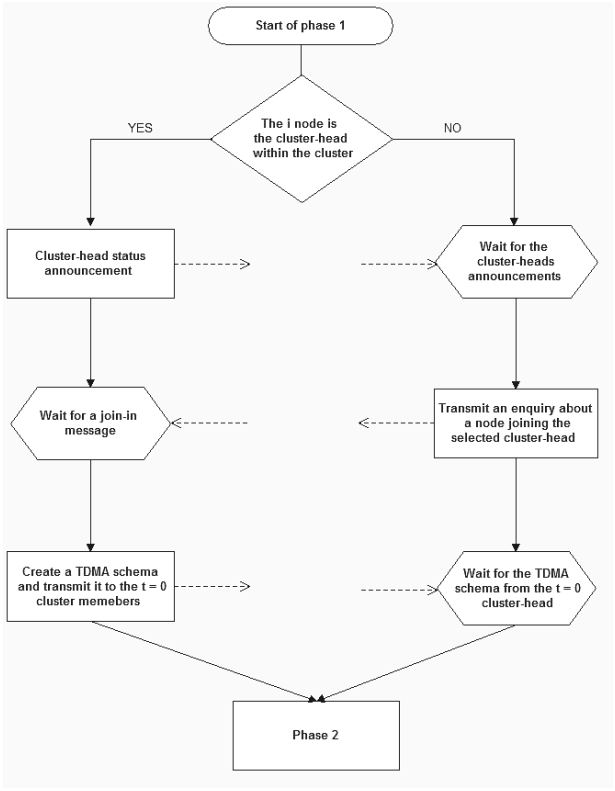

Fig. 4. Cluster-heads selection in the LEACH protocol

2. LEACH protocol

Low Energy Adaptive Clustering Hierarchy (LEACH) is a protocol that operates based on hierarchical routing protocols. The protocol creates a so-called "cluster" comprised of a group of sensors which communicate with one and the same cluster-head. The cluster-heads are selected in a random rotation, which has greatly helped to reduce energy consumption and uniformly distribute the energy load between individual network nodes. The LEACH protocol utilises location coordinates to achieve appropriate network scalability and data aggregation, which enables reduction of the amount of data flowing to the cluster-head.

The functioning of LEACH protocol [6]:

- The first phase comprises clusters formation and cluster-heads selection. Each node generates a random number between 0 and 1. If the number turns out to be less than the threshold value *T(n)* the node becomes the cluster-head of the cluster. The *T(n)* value is calculated as follows:

$$T(n) = \begin{cases} \dfrac{p}{1 - p(r \cdot \mathrm{mod}(\frac{1}{p})} & n \in G \\ 0 & otherwise \end{cases} \quad (1)$$

where, p – expected number of nodes to become cluster-heads, G – set of nodes participating in the selection process.
The newly selected cluster-head transmit a message/communication to all the nodes within the network. The nodes join those cluster-heads from which they receive the most powerful signal. When all the information regarding affiliation with the cluster-head has been transmitted, the cluster-head assigns to the sensor nodes time slots that are consistent with the TDMA technique that enable them to transmit data.

- The second phase consists in collecting and transferring data to the cluster-head that aggregate and transmit them to the base station. During this phase the nodes within the cluster perform

their tasks and then transmit the results to the cluster-head at the designated time slots. The data are transmitted to the database by the cluster-heads which aggregate the data to all the nodes within the cluster. After sometime within the WSN, the network once again passes through the first phase. In the communication process, each cluster code utilises a different CDMA code, which minimises the interference issue.

3. Redundancy in LEACH protocol

Sensor networks, given the arrangement of sensors in the field, are exposed to many risks [13, 14]. They can result from intentional damage or random failure during functioning.

In most applications, a sensor network has limited energy resources and computing capabilities of individual nodes compared to cable IP networks, so it is important to ensure an adequate level of reliability, to the environmental problems or for example hostile attack, that they can perform their functions and continue to collect data and transfer it to the base station [9].

LEACH protocol, unfortunately, does not have the mechanisms implemented in its design to ensure reliable communication in the event of random failure of the cluster-head in the cluster. Nodes in case of cluster-head failure will be still sending to it their data [11, 12].

The selection of cluster-head is determined by random system without taking the residual energy of nodes into account, so once a node with less energy is selected to be cluster-head, its energy will dissipate quickly, and then the nodes within this cluster will lose touch with its cluster-head and sink [10]. In other words, it will accelerate energy dissipation, shorten the lifetime of the network, and at worst put the network out of action.

3.1. IIS-LEACH

One of the new developments presented in modified version of LEACH called IIS-LEACH provides that much needed reliability. The functioning of the protocol IIS-LEACH as in the case of LEACH protocol consists of two phases:

Phase 1. In phase one the base station starts transmitting the test signal to all the nodes. On this basis each node calculates its distance from the base station using the following formula [14]:

$$FSPL\ (dB) = 20log10(d) + 20log10(f) + K \quad (2)$$

where, d – distance, f – frequency, K - constant that depends on the units used for d and f, $FSPL$ - Free Space Path Loss. For d and f in meters and kilohertz, respectively, the constant becomes – *87.55*. For d, f in meters and megahertz, respectively, the constant becomes – *27.55*. For d and f in kilometers and megahertz, respectively, the constant becomes – *32.45*.

$$d = 10(Free\ Space\ Path\ Loss - K - 20log10(f))/20 \quad (3)$$

The cluster-head is selected according to the following selection algorithm [6, 8]:

$$k = \sum_{i=1}^{N} P_i(t) * 1 \quad (4)$$

where, k – number of clusters during each round, N – number of nodes in the network, $P_i(t)$ – is the probability with which node i elects itself to be cluster-head at the beginning of the round r+1which starts at time t.

$$P_i(t) = \begin{cases} \dfrac{k}{N - k*(r \bmod \frac{N}{k})} & C_i(t) = 1 \\ & C_i(t) = 0 \end{cases} \quad (5)$$

where, $C_i(t)$ determines whether node i has been a cluster-head in most recent (r *mod*(N/k)) rounds.

Once the cluster-heads N has been selected, it is transmitted to all the other nodes information of their existence. While receiving this information the nodes decide which cluster they want to join. Their choice is primarily informed by the strength of the signal received from the cluster-heads. In the next step sensor nodes inform the selected cluster-heads that they will be members of their clusters by sending a message with information about their power supply status, distance from base station and cluster-head *N*. Having received such applications, each cluster-head selects its supplementary node, like shown in Figure 5, where the selection criterion is the shortest distance from the cluster-head and the appropriate condition of the power source calculated according to the following formula:

$$SM + LM + PD + SD < PS \quad (6)$$

where, *SM* – energy consumption during standby mode, *LM* – energy consumption during listening mode, *PD* – energy consumption during processing data, *PS* – power supply status, *SD* – energy consumption during sending data:

$$SD = E_{sx} d \varepsilon_{amp} \quad (7)$$

Phase 2. During phase two of the WSN network the protocol based on IIS-LEACH sets the supplementary node in the listening watch mode to collect information from the other nodes in the same way as the cluster-head. At the end of the second phase the cluster-head informs the listening node that it has sent collected data to the base station. If the cluster-head were damaged, the listening node after a certain time (t) would send the collected data to the base station

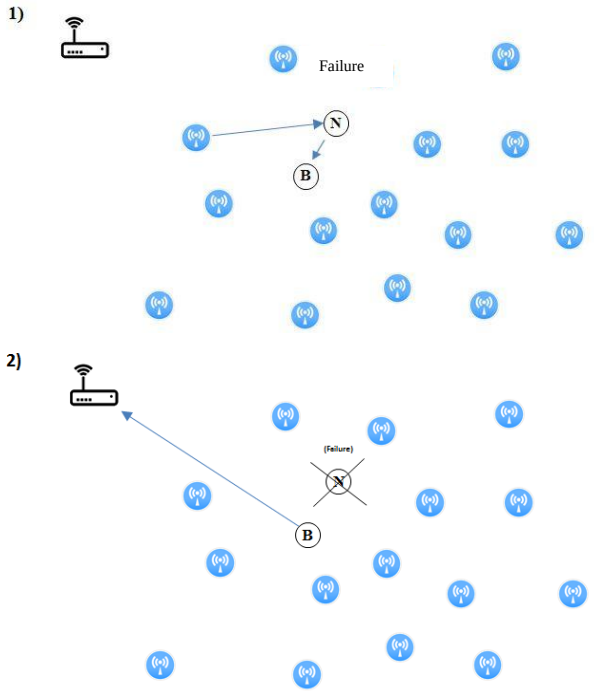

Fig. 5. Redundancy in IIS-LEACH

3.2. Simulation

The present study aims to determine how the life of a network is affected by the number of mobile sensors in the test environment using LEACH and ISS-LEACH protocol. The test involved MATLAB software using parameters from Table. 1. A test environment has been generated in which the nodes are randomly arranged upon the test. Each such node has its mobile source of energy and present energy consumption level, depending on their function and the number and distance of the transmitted data.

In the experiment, we assume:

- after the position of nodes was randomly chosen they do not change it to the end of the test;
- the supplementary node do not gather information from its monitoring equipment;
- authors do not know the physical localization of nodes in network area.

Table 1 Parameters used in test

Parameters	Value
Network area	100 m × 100 m
Number of nodes	100, 200, 300, 400, 500, 600
Number of rounds	1000
Sink location	50, 50
Initial energy	0.5 J
Packet Lenght	6400 bit
ETX (Transmitter circuit consumption)	0.00000005 J
ERX (Receiver circuit consumption)	0.00000005 J
Amplification energy	0.0000000001 J

In the experiment have been selected 1000 rounds to show visible changes in the functioning of LEACH protocol and its proposed version with the option of the redundancy – IIS-LEACH. The number of sensors is increased by 100. The purpose of this amendment is to show how changes the energy system of both protocols, when in the investigated area occurs the placement of a greater number of sensors. The sum of the energy of nodes using the protocol with redundancy IIS-LEACH and standard LEACH is shown in Figure 6. The red curve determines the functioning of the protocol IIS-LEACH. Its total energy of 1000 rounds is slightly lower than the LEACH protocol. This small difference is a result of the redundancy protocol mechanism.

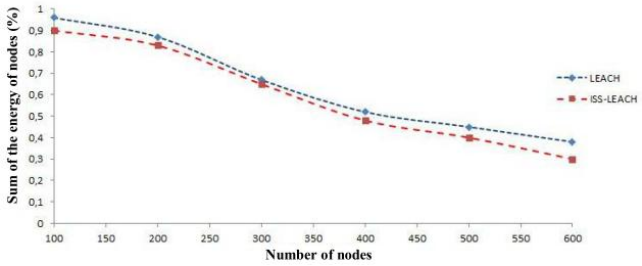

Fig. 6. Sum of energy after 1000 of rounds for networks created from different number of nodes, using IIS-LEACH and LEACH

4. Conclusion

WSN turn out to be a very interesting and forward-looking technology. Its resources and capabilities are negligible, yet the potential of the device is massive. Equipped with appropriate gauging sensors it can acquire any type of data, and with a little help from the other nodes it can process and transmit such data. The nodes can be scattered, nevertheless they will automatically activate and create a network.

Redundancy in LEACH protocol is a very useful option if it is very important periodically collect data from the area and you cannot afford that information will not be delivered. The new protocol provides this functionality, enabling thus its use in situations where the underlying protocol LEACH not meets our expectations. The experiment showed that the battery consumption increased slightly in favour of the reliability of data transmission. The next stage of the development of the said protocol will see the implementation of an even selection of the cluster-head within the cluster.

References

[1] Abbas Z., Javaid N., Khan M.A., Ahmed S., Qasim U., Khan Z.A.: Simulation Analysis of IEEE 802.15.4 Non-beacon Mode at Varying Data Rates. Seventh International Conference on Broadband, Wireless Computing, Communication and Applications (BWCCA), 2012.
[2] Ahmed S., Sandhu M.M., Amjad N., Haider A., Akbar M., Ahmad A., Khan Z.A., Qasim U.: iMOD LEACH: improved MODified LEACH Protocol for Wireless Sensor Networks, Journal of Basic and Applied Scientific Research, 2013
[3] Bakr B. A.: LEACH-SM: A Protocol for Extending Wireless Sensor Network Lifetime by Management of Spare Nodes. Fifth International Conference on Innovative Mobile and Internet Services in Ubiquitous Computing. 2011, 277–278
[4] Diane I., Kacimi R., Mammeri Z., Niang I.: Energy Optimization based on the Redundancy in WSNs. 6th Joint IFIP Wireless and Mobile Networking Conference (WMNC), Dubai, 2013, 1–7 [DOI: 10.1109/WMNC.2013.6548980]
[5] Faludi R.: Building Wireless Sensor Networks, O'Reilly Media, 2010
[6] Hayat S., Javaid N., Khan Z. A., Shareef A., Mahmood A., Bouk S. H.: Energy Efficient MAC Protocols in Wireless Body Area Sensor Networks. 5th International Symposium on Advances of High Performance Computing and Networking (AHPCN-2012), 2012.
[7] Heinzelman W., Chandrakasan A., Balakrishnan H.: Energy-Efficient Communication Protocols for Wireless Microsensor Networks. Proceedings of the 33rd Annual Hawaii International Conference on System Sciences, vol. 2, 2000 [DOI: 10.1109/HICSS.2000.926982].
[8] http://www.figaro.co.jp/en/topic/2014/03/announcement-of-new-mems-type-air-quality-sensor-tgs8100.html [19.05.2016]
[9] Lewis F.L.: Wireless Sensor Networks, Smart Environments: Technologies, Protocols, and Applications, 2004.
[10] Liao Q., Zhu H.: An Energy Balanced Clustering Algorithm Based on LEACH Protocol. Proceedings of the 2nd International Conference On Systems Engineering and Modeling (ICSEM-13), 2013.
[11] Mursleen M., Singh R.: An Improvised LEACH protocol with reduced data redundancy for wireless sensor networks, Vol 5, No 3/2014, 331–341.
[12] Najgebauer A., Dyk M.: Sieci sensorowe dla potrzeb pozyskiwania danych w symulacji wielorozdzielczej. Symulacja w Badaniach i Rozwoju, Vol. 2, No. 4/2011, 197–207
[13] Raed M., Hani B., Abdalraheem A., Ijjeh A.: A Survey on LEACH-Based Energy Aware Protocols for Wireless Sensor Networks, Journal of Communications, Vol. 8, No. 3, 2013, 192–206.
[14] Sehgal N., Kaur G.: Improved Cluster Head Selection Using Enhanced LEACH Protocol. International Journal of Engineering and Innovative Technology (IJEIT), Vol. 3, Issue 3/2013, 77–88.
[15] Tahir M., Javaid N., Iqbal A., Khan Z. A., Alrajeh N.: On Adaptive Energy Efficient Transmission in WSNs. International Journal of Distributed Sensor Networks, 2013.
[16] Zhong J., Bertok P.: A Variable Threats Based Self-Organization Scheme for Wireless Sensor Networks. Proceedings of the 2009 Third International Conference on Sensor Technologies and Applications, 2009.

D.Sc. Eng. Volodymyr Mosorov
e-mail: w.mosorow@kis.p.lodz.pl

Volodymyr Mosorov received his Ph.D. in 1998 from the State University of Lviv, Ukraine. V.Mosorov was awarded the title of Doctor of Science from AGH University of Science and Technology Krakow Poland in 2009. He is now an associate professor at the Institute of Applied Computer Science of Lodz University of Technology, Poland. His research interests include data mining and clustering. He has published more than 80 technical articles.

M.Sc. Eng. Sebastian Biedron
e-mail: sbiedron@wpia.uni.lodz.pl

A graduate of the Department of Science and Mathematics at Lodz University. From 2012 year is a court expert at the District Court at the Prague in Warsaw. From 2013, Ph.D. student at the Institute of Applied Computer Science of Lodz University of Technology. Supervisor of the Ph.D. thesis is D.Sc. (dr hab. inż.) Volodymyr Mosorov, prof. PL.

M.Sc. Taras Panskyi
e-mail: tpanski@kis.p.lodz.pl

Graduate of the Electrotechnics Department at the Lviv National Polytechnic University, Ukraine. From 2013, Ph.D. student at the Institute of Applied Computer Science of Lodz University of Technology, Poland. His research interests include data clustering, reliability and availability indexes of embedded systems, educational migration.

otrzymano/received: 05.06.2016 *przyjęto do druku/accepted: 11.05.2018*

DOI: 10.5604/01.3001.0012.0707

ANALYSIS MEDICAL AND STEREOSCOPIC IMAGES BY E-MEDICUS SYSTEM

Tomasz Rymarczyk[1,2]
[1]Netrix S.A., Research and Development Center, [2]University of Economics and Innovation in Lublin

Abstract. *In this work, there were implemented methods to analyze and segmentation medical images by using different kind of algorithms. The solution shows the architecture of the system collecting and analyzing data. There was tried to develop an algorithm for level set method applied to piecewise constant image segmentation. These algorithms are needed to identify arbitrary number of phases for the segmentation problem. With the use of modern algorithms, it can obtain a quicker diagnosis and automatically marking areas of the interest region in medical images.*

Keywords: segmentation, image analysis, level set method

ANALIZA OBRAZÓW MEDYCZNYCH I STEREOSKOPOWYCH W SYSTEMIE E-MEDICUS

Streszczenie. *W pracy zaimplementowano metody analizy i segmentacji obrazów medycznych przy użyciu różnych algorytmów. Rozwiązanie pokazuje architekturę systemu zbierającego i analizującego dane. Podjęto próbę opracowania algorytmu dla metody zbiorów poziomicowych stosowanej do fragmentarycznej, stałej segmentacji obrazu. Metody te są potrzebne do identyfikacji dowolnej liczby faz dla problemu segmentacji. Dzięki zastosowaniu nowoczesnych algorytmów można uzyskać szybszą diagnozę i automatyczne oznaczanie obszarów w regionach zainteresowania w obrazach medycznych.*

Słowa kluczowe: segmentacja, analiza obrazów, metoda zbiorów poziomicowych

Introduction

In medical clinical research and practice, imaging has become an essential part to diagnose and to study anatomy and function of the human body. The image data is of immense practical importance in medical informatics. Medical images, such as Computed Axial Tomography (CAT), Magnetic Resonance Imaging (MRI), Ultrasound, and X-Ray, in standard DICOM formats are often stored in Picture Archiving and Communication Systems (PACS) and linked with other clinical information in EHR clinical management systems. Research efforts have been devoted to processing and analyzing medical images to extract meaningful information such as volume, shape, motion of organs, to detect abnormalities, and to quantify changes in follow-up studies.

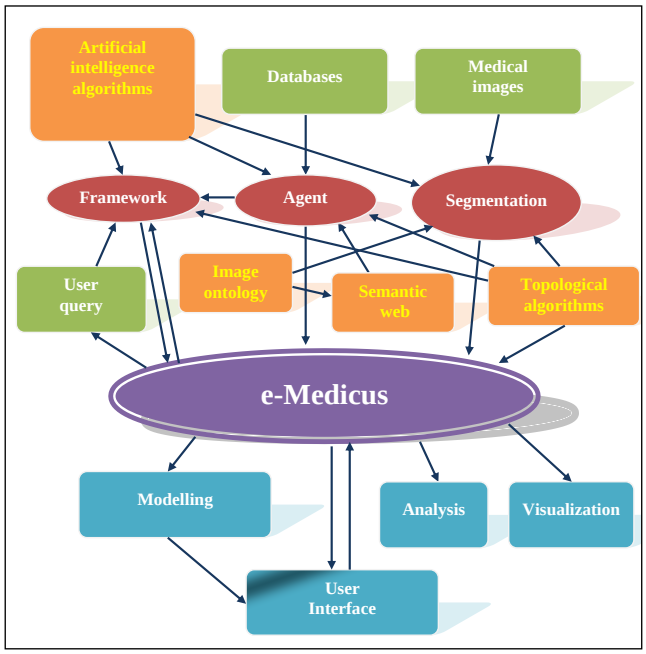

Fig. 1. The architecture of the e-Medicus system

Recent advances in a wide range of medical imaging technologies have revolutionized how we view functional and pathological events in the body and define anatomical structures in which these events take place. X-ray, CAT, MRI, Ultrasound, nuclear medicine, among other medical imaging technologies, enable 2D or tomographic 3D images to capture in-vivo structural and functional information inside the body for diagnosis, prognosis, treatment planning and other purposes. The architecture of such the medical system was projected in the Figure 1.
The e-Medicus system consists:

- artificial intelligence algorithms,
- segmentation algorithms
- the framework,
- agents,
- topological algorithms,
- databases,
- visualization systems,
- the user interface.

1. Segmentation

The image segmentation refers to the process of partitioning a digital image into multiple regions. There is typically used to locate objects and boundaries in images. The level set method is a powerful tool for representing moving or stationary interfaces. There was used the idea of the variational formulation for geometric active contours. There was used to minimization problem in image processing to compute piecewise-smooth optimal approximations of the given image. The proposed algorithm has been applied to real pictures with promising results in the image segmentation [12–18].

The level set method tracks the motion of an interface by embedding the interface as the zero level set of the signed distance function. The motion of the interface is matched with the zero level set, and the resulting initial value partial differential equation for the evolution of the level set function. The idea is merely to define a smooth function $\phi(x,t)$, that represents the interface as the set where $\phi(x,t)=0$. The motion is analyzed by the convection the ϕ values (levels) with the velocity field.

For more than two phases was introduced the multiple level sets idea by Vese and Chan. The algorithm set formulation and algorithm for the general Mumford-Shah minimization problem in image processing, to compute piecewise-smooth optimal approximations of a given image [10–11, 21].

The problem can be easily generalized to the case where the domain contains more than two materials.

$$F(s,C)=\omega \boldsymbol{L}(C)+\eta\int_{\Omega}(s_o-s)^2 d\Omega+\int_{\Omega\setminus C}|\nabla s|^2 d\Omega \qquad (1)$$

The process for minimization of the functional is the following:

$$\frac{\partial \phi}{\partial t} = \delta_{\varepsilon}(\phi)\left[\omega\nabla\cdot\left(\frac{\nabla\phi}{|\nabla\phi|}\right) - \eta_1(s_o - c_1)^2 + \eta_2(s_o - c_2)^2\right] \quad (2)$$

where coefficients c_1 i c_2 are mean values of points in the picture.

The formulation of the variational level set method consists of an internal energy term that penalizes the deviation of the level set function and an external energy term that drives the motion of the zero level set toward the desired image features. When flat or steep regions complicate the determination of the contour, the reinitialization is necessary. This reinitialization procedure is based by replacing by another function that has the same zero level set but behaves better. Variational formulation for geometric active contours that forces the level set function to be close to a signed distance function, and therefore completely eliminates the need of the costly reinitialization procedure.

The resulting evolution of the level set function is the gradient flow that minimizes the overall energy functional:

$$\boldsymbol{P}(\phi) = \int_{\Omega} \frac{1}{2}(|\nabla\phi| - 1)^2 \, dxdy \quad (3)$$

An external energy for a function $\phi(x, y)$ is defined as below:

$$\boldsymbol{E}(\phi) = \mu \boldsymbol{P}(\phi) + \boldsymbol{E}_m(\phi) \quad (4)$$

where:

$\boldsymbol{P}(\phi)$ – internal energy, $\boldsymbol{E}_m(\phi)$ – external energy.

Denoting by $\frac{\partial \mathbf{E}}{\partial \phi}$ the Gateaux derivative of the functional **E** receiving the following evolution equation:

$$\frac{\partial \phi}{\partial t} = -\frac{\partial \mathbf{E}}{\partial \phi} \quad (5)$$

In the image segmentation active contours are dynamic curves that moves towards the object boundaries. Denoting letter I as an image, and g be the edge indicator function defined by:

$$g = \frac{1}{1 + |\nabla G_{\sigma} * I|^2} \quad (6)$$

where G_{σ} is the Gaussian kernel with standard deviation σ.

The process for minimization of the functional ***E*** is the following:

$$\frac{\partial \phi}{\partial t} = \mu\left[\Delta\phi - \mathrm{div}\left(\frac{\nabla\phi}{|\nabla\phi|}\right)\right] + \lambda\delta(\phi)\mathrm{div}\left(g\frac{\nabla\phi}{|\nabla\phi|}\right) + \omega g\delta(\phi) \quad (7)$$

The formulation of the variational level set method with Mumford-Shah model is following:

$$F(\phi, c_1, c_2) = \int_{\Omega} \frac{1}{2}(|\nabla\phi| - 1)^2 \, dxdy + \omega \int_{\Omega} |\nabla H(\phi)| d\Omega + \lambda_1 \int_{\Omega} (u_o - c_1)^2 H(\phi) d\Omega + \lambda_2 \int_{\Omega} (u_o - c_2)^2 (1 - H(\phi)) d\Omega \quad (8)$$

2. E-Medicus System

E-Medicus system consists artificial intelligence algorithms, segmentation algorithms, framework, agents, topological algorithms, databases, visualization systems and user interface.

Medical image segmentation, which aims at automated extraction of object boundary features, plays a fundamental role in understanding image content for searching and mining in medical image archives. A challenging problem is to segment regions with boundary insufficiencies, i.e., missing edges and/or lack of texture contrast between regions of interest (ROIs) and background. Lately, much interest has been raised in the medical imaging community about segmentation algorithms that use active contours or surfaces. In e-Medicus use segmentation algorithms such as natural and generic networks, algorithm Beyesa, level set method, fuzzy sets and algorithm k-means (Fig. 2). The algorithms used allow to segment all pathological changes in the image. Through continuous improvement of algorithms, we come to reduce the noise in the medical image (Fig. 3) [4–9, 19].

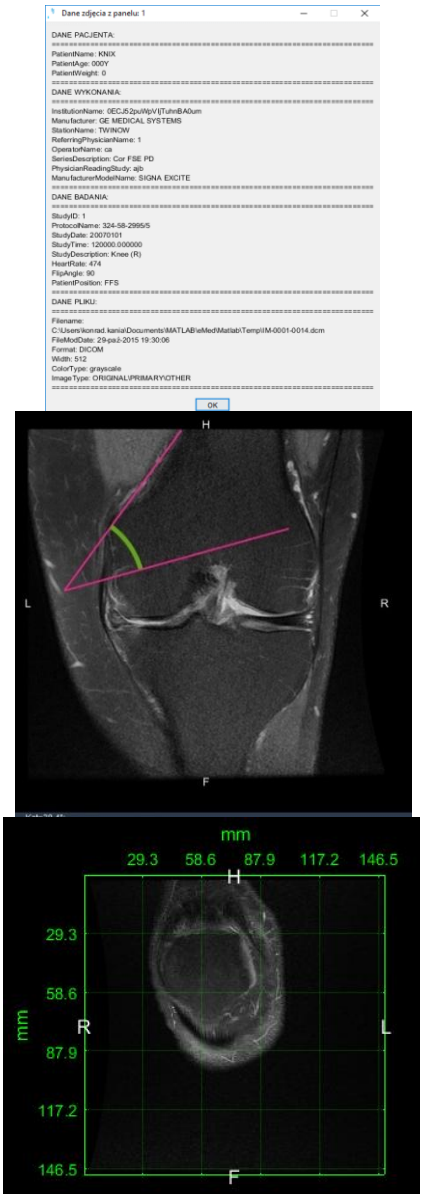

Fig. 2. Examples in e-Medicus system

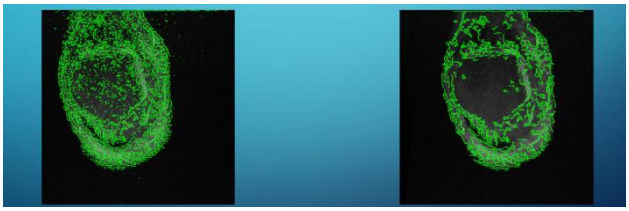

Fig. 3. On the right binarization without filtering, on the left binarization in filtering

3. System for the acquisition of stereoscopic images of skin lesions

Stereoscopic imaging techniques allow for 3D images. Simultaneous recording of two images allows for the mutual dependence of the spatial object, the distance from the observer and the depth of the scene. In order to obtain stereoscopic images a pair of two-dimensional images (stereoparas) representing a subject or scene from two points of view are made. Stereo image compositions are very similar, but they vary slightly in the way they look at objects and in the details of each object's crossing in the scene. It is these tiny differences that carry information about the third dimension. The stereoscopic skin lesion acquisition and analysis system consists of a dedicated recording device

and a computer aided image analysis program e-Medicus. The unit consists of two camera modules (101, 102), a multiadaptera camera (100), a microprocessor controller (105), an lighting unit (103) and a power supply (104). The stereoscopic image is obtained by recording the image on one and the other camera. Cameras are set at a fixed distance (D = 35 mm) from each other. This distance is determined between the main optical axes of the camera lenses. Illumination of skin lesions during shooting is accomplished through a set of LED spots (103). Illuminated dots are digitally digitally controlled eight-digit RGB LEDs. Each point can have individually set parameters such as the intensity and colour of the emitted light wave. The microprocessor controller (105) controls the multiadapter camera (100) for proper operation of the acquisition and illumination system. The connection of the cameras to the adapter is made using a flexible (flexible) tape consisting of fifteen communication wires. Figure 4 presents the device for stereoscopic images of skin lesions. Calibration and test reconstructions of stereoscopic photographs was shown in Fig. 5 and 6.

Fig. 4. Device for stereoscopic images of skin lesions

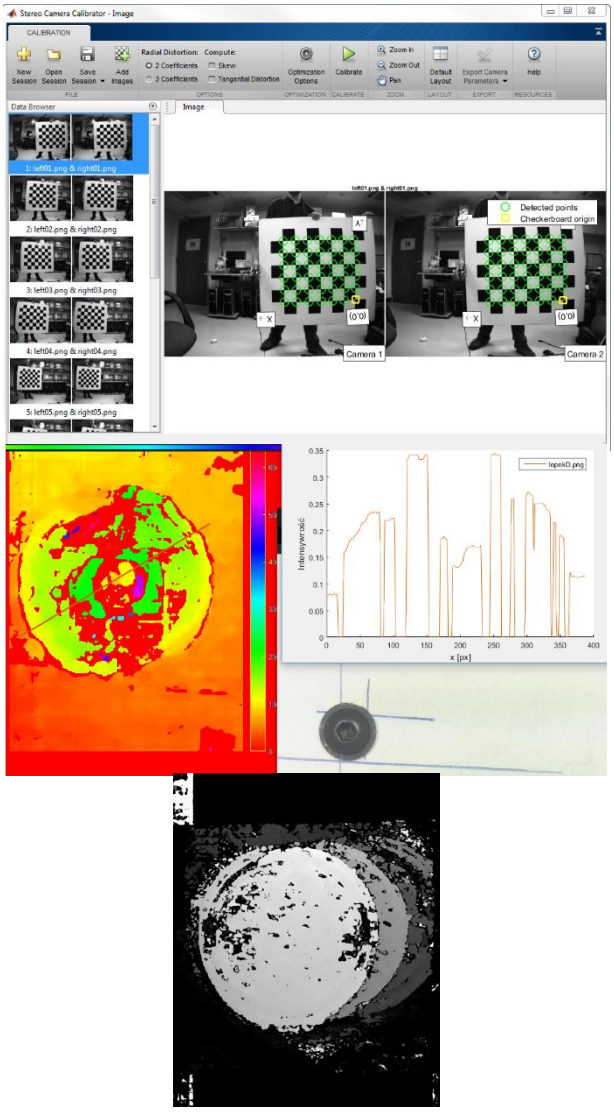

Fig. 5. Calibration process

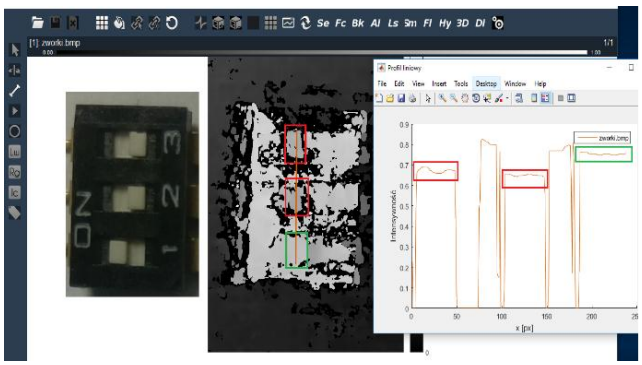

Fig. 6. Test reconstructions of stereoscopic photographs

The microprocessor controller is also responsible for communication between the recording device and a computer (109) equipped with dedicated e-Medicus software, implemented in Ethernet (108). Control of the device for image acquisition and lighting is done by dedicated e-Medicus (110) computer program. At the same time, the application allows for the qualitative analysis of stereoscopic 3D images of skin lesions, including cancerous ones.

The first step of skin surface should be identification of the lesion as melanocytic or non-melanocytic [1–3, 20]. In case of the identification of the melanocytic lesion next step should be classification as benign, malignant or "suspicious" (Fig. 7). Currently the most commonly used method for screening and the fast evaluation of the melanocytic lesions is ABCD rule, which according to Nachbar showed 92% specificity, 91% sensitivity and 80% of diagnostic accuracy in evaluation of malignant melanoma. It bases on evaluation of lesion in 4 aspects: A – Asymmetry, B – Borders, C – Colours, and D – Differential structures (Tab. 1). Figures 8 presents the image segmentation by using the level set algorithm (the pigmented skin lesions).

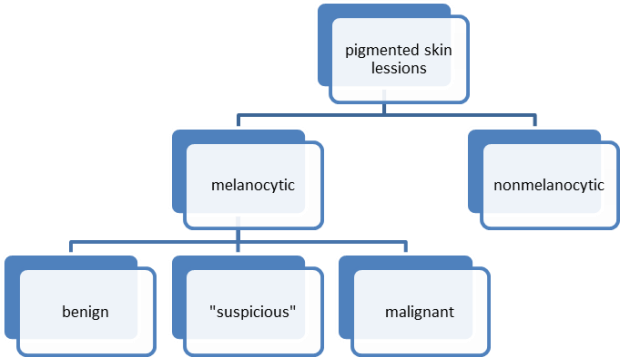

Fig. 7. The two-step procedure for the classification of pigmented skin lesions

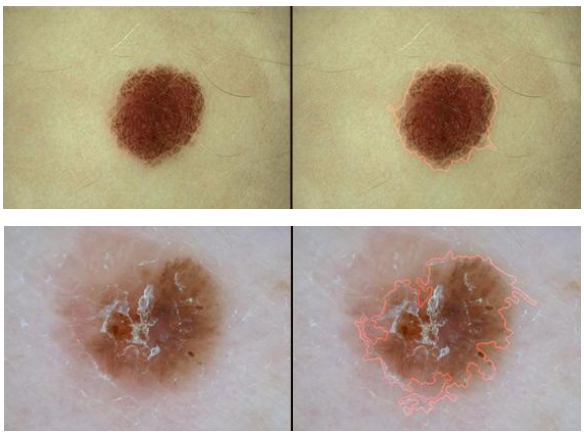

Fig. 8. The medical image analysis by Level Set Method (looking for areas with specific characteristics)

Table 1. ABCD rule parameters description

Parameter		Description	Values	TDS weight factor
A	Assymetry	Complete symmetry, asymmetry in 1 or 2 axis	0-2	1,3
B	Borders	8 segments, 1 point for abrupt cut-off of pigment	0-8	0,1
C	Colours	1 point for each color: white, red, light brown, dark brown, black, blue-gray	1-6	0,5
D	Differential structures	1 point for every structure: pigment network, structureless areas, dots, globules, streaks	1-5	0,5

4. Processing and analysis of medical images

Processing and analysis of medical images using computer comprises the following: image formation and reconstruction, image restoration, image enhancement, image compression and storage, image-based visualization, feature identification, image segmentation, shape recognition, image matching/registration, and measurement of anatomical and physiological parameters. Using an algorithm level set method and the determination of the relevant parameters, there was achieved the following results (Fig. 9).

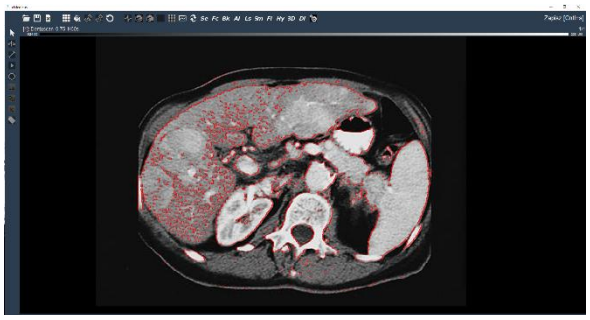

Fig. 9. Segmentation by Level Set Method

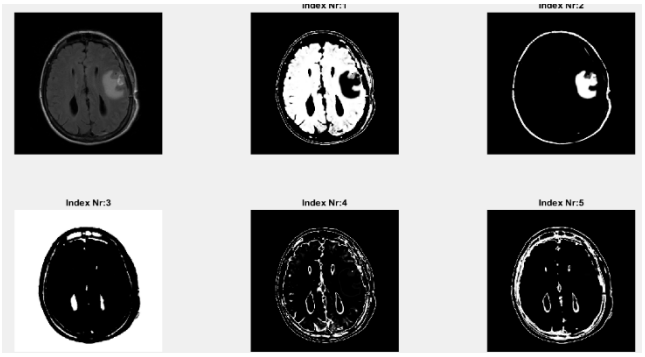

Fig. 10. Fuzzy sets

After setting the appropriate parameters, the algorithm is able to obtain satisfactory results for us. Mark not only interesting object but also the outline of the whole picture. The best algorithm that has highlighted exactly the area of interest is the Fuzzy sets (Fig. 10). As you can see in the pictures above, by indexing the medical image, the algorithm detects the appropriate scale of grays and on this basis correctly marks the object of interest, in this case changed in the brain.

5. Conclusion

In medical clinical research and practice, imaging has become an essential part to diagnose and to study anatomy and function of the human body. The proposed algorithms have been used to real pictures with promising results in the medical images segmentation. With the use of modern algorithms, the physician is able to obtain a quicker diagnosis. By automatically marking areas of interest you will notice all the changes in medical images. This will allow artificial intelligence to automatically diagnose changes and to tell the radiologist what type of disease is present in the medical image. In this work, there were developed and effective algorithms and the e-Medicus system to machine learning, analysis and compare medical images.

References

[1] Argenziano G., Soyer P.H., De Giorgi V., Piccolo D.: Interactive atlas of dermatoscopy, EDRA 2000.
[2] Balla-Arabe S., Gao X.: A Fast and Robust Level Set Method for Image Segmentation Using Fuzzy Clustering and Lattice Boltzmann Method. IEEE Trans Cybern. 43(3), 2013.
[3] Braun R.P., Rabinovitz H.S.: Dermoscopy of pigmented skin lesions. J. Am. Acad. Dermatol. 52, 2005, 109–121.
[4] Gdula A., Rymarczyk T.: Application Computational Algorithms for Analysis of Dental Image. Proc. of WD 2015.
[5] Jajuga K.: Statystyczna teoria rozpoznawania obrazów. PWN. Warszawa 1990.
[6] Johr R.H.: Dermoscopy: Alternative melanocytic algorithms-the ABCD rule of dermatoscopy, Menzies scoring method, and 7-point checklist. Clin Dermatol. 20(3), 2002, 240–247.
[7] Kamińska J., Winciorek G.: Dermatologia cyfrowa. Cornetis. Wrocław 2008.
[8] Kurzyński M.: Rozpoznawanie obiektów. Metody statystyczne. Oficyna Wydawnicza Politechniki Wrocławskiej. Wrocław 1997.
[9] Li C., Kao C., Gore J. C., Ding Z.: Minimization of Region-Scalable Fitting Energy for Image Segmentation. IEEE Trans. Image Processing 17 (10), 2008, 1940–1949.
[10] Mumford D., Shah J.: Optimal approximation by piecewise smooth functions and associated variational problems. Communications on Pure and Applied Mathematics 42(5), 1989, 577–685 [DOI: 10.1002/cpa.3160420503].
[11] Osher S., Fedkiw R.: Level Set Methods and Dynamic Implicit Surfaces. Springer. New York 2003.
[12] Osher S., Sethian J.A.: Fronts Propagating with Curvature Dependent Speed: Algorithms Based on Hamilton-Jacobi Formulations. Journal of Computational Physics 79, 1988, 12–49.
[13] Ossowski S.: Sieci neuronowe do przetwarzania informacji. Politechnika Warszawska. Warszawa 2006.
[14] Osowski S., Markiewicz T., Kruk M., Kozłowski W.: Metody sztucznej inteligencji do wspomagania diagnostyki patologii tkanek. WAT. Warszawa 2011.
[15] Rymarczyk T.: Characterization of the shape of unknown objects by inverse numerical methods. Przegląd Elektrotechniczny 7b/2012, 138–140,
[16] Rymarczyk T., Osior K.: E-Medicus System for Analysis and Images Segmentation. Proc. of. IIPhWD 2013.
[17] Rymarczyk T., Filipowicz S.F., Sikora J., Polakowski K.: A piecewise-constant minimal partition problem in the image reconstruction. Przegląd Elektrotechniczny 12/2009, 141–143.
[18] Sethian J.A.: Level Set Methods and Fast Marching Methods. Cambridge University Press, 1999.
[19] Stąpor K.: Metody klasyfikacji obiektów w wizji komputerowej. Wydawnictwo Naukowe PWN. Warszawa 2011.
[20] Stolz W., Braun-Falco O.: Color atlas of dermatoscopy. Blackwell Science, 1994.
[21] Vese L. Chan T.: A new multiphase level set framework for image segmentation via the Mumford and Shah model. CAM Report 01-25, UCLA Math. Dept., 2001.

Acknowledgments

Projekt współfinansowany przez Unię Europejską z Europejskiego Funduszu Regionalnego. Działanie 1.4 – wsparcie projektów celowych. Umowa nr UDA-POIG.01.04.00-06-022/11-00. Nazwa Beneficjenta – Netrix S.A. dawniej Net-Art Paweł Rymarczyk. Tytuł projektu „Stworzenie prototypu aplikacji e-Medicus opartej na funkcjach zbiorów poziomicowych oraz algorytmach inteligencji obliczeniowej" (2012-2015).

Ph.D. Eng. Tomasz Rymarczyk
e-mail: tomasz.rymarczyk@netrix.com.pl

Director in Research and Development Center Netrix S.A. His research area focuses on the application of non-invasive imaging techniques, electrical tomography, image reconstruction, numerical modelling, image processing and analysis, process tomography, software engineering, knowledge engineering, artificial intelligence and computer measurement systems.

otrzymano/received: 02.03.2018 *przyjęto do druku/accepted: 11.05.2018*

DOI: 10.5604/01.3001.0012.0713

ANALYSIS OF THE EFFECTIVENESS OF SELECTED SEGMENTATION METHODS OF ANATOMICAL BRAIN STRUCTURES

Róża Dzierżak, Magdalena Michalska
Lublin University of Technology, Institute of Electronics and Information Technologies

Abstract*. An important aspect of analysis medical images is acknowledging the role of the segmentation process of individual anatomical structures. This process allows to show the most important diagnostic details. Owing to the segmentation the areas of interest (ROI) it is possible to adapt the methods of further image analysis considering the specification of selected elements. This process has been widely used in medical diagnostics. The article presents the use of segmentation by thresholding, segmentation by region growth and by edge detection to extract the parts of the human brain the user is interested in. The series of MRI (magnetic resonance imaging) images were used. The aim of the research was to develop the methods that would allow comparing the effectiveness various types of anatomical brain structures' segmentation in two dimensions. The above methods present the different impact that selected types of segmentation, masks or parameters have on the most accurate depiction of a selected human brain element.*

Keywords: brain imaging, image segmentation, magnetic resonance imaging

ANALIZA SKUTECZNOŚCI WYBRANYCH METOD SEGMENTACJI STRUKTUR ANATOMICZNYCH MÓZGU

Streszczenie. *Istotnym aspektem analizy obrazów medycznych jest dostrzeżenie roli procesu segmentacji poszczególnych struktur anatomicznych. Proces ten pozwala na ukazanie najistotniejszych pod względem diagnostycznym szczegółów. Dzięki segmentacji obszarów zainteresowania (ROI) możliwe jest odpowiednie dostosowanie metod dalszej analizy obrazów uwzględniając specyfikę wybranych elementów. Proces ten znalazł rozległe zastosowanie w diagnostyce medycznej. W artykule przedstawiono wykorzystanie segmentacji przez progowanie, przez rozrost regionów oraz przez wykrywanie krawędzi, w celu wyodrębnienia interesujących użytkownika części ludzkiego mózgu. Wykorzystano serie obrazów MRI (rezonans magnetyczny). Celem badań było opracowanie metod, które pozwolą porównać skuteczność różnych typów segmentacji struktur anatomicznych mózgu w dwóch wymiarach. Zaprezentowane metody pokazują różny wpływ wybranych rodzajów segmentacji, masek czy parametrów na dokładniejsze ukazanie poszczególnych elementów ludzkiego mózgu.*

Słowa kluczowe: obrazowanie mózgu, segmentacja obrazu, rezonans magnetyczny

Introduction

Medical imaging is currently one of the most dynamically developing issues in biomedical engineering. Owing to the use of technical and IT solutions, the correct assessment of patients' condition is better than ever. Various imaging diagnostics techniques allow method to be adapted to character of the examined objects [1, 5, 12].

The tests allow patient's body image to be obtained along with the characteristics of his internal organs. The test results usually involve more structures than are evaluated. Therefore, it is necessary to isolate the area of interest in order to adapt further methods of image analysis appropriate to the studied area [1, 11].

Segmentation is a process aimed at extracting from the results the elements that are to be further analyzed. The processing of medical images makes it necessary to distinguish the tested object from the rest of the less important details of the image. All elements that do not belong to ROI (Region of Interest) can be included in the background [8, 11, 12].

Currently used medical imaging techniques allow to obtain an image on which tissues have similar properties [14]. This creates a problem regarding the precise separation of the examined structures from other elements. In order for the obtained results to have a diagnostic value, the isolated objects must be in accordance with the actual interpretation of the medical image [3, 9].

The scope of the article is the analysis of the effectiveness of the three segmentation types. The adopted measure of effectiveness is the operator's ability to distinguish between the anatomical structures of the brain, complexity of the selected segmentation algorithm and calculation effort.

1. Methods

The selecting of the particular segmentation technique should begin by considering the nature of the diagnostic problem and image origin [9, 11]. In the initial stages of the research on the segmentation process, the main method was to perform image binarization. It was performed by thresholding, which allowed to distinguish the examined object and background [7, 9].

1.1. Segmentation based on thresholding

Segmentation by thresholding is the most popular and the most commonly used method of extracting objects from an image. The most important part of the process is to determine the threshold value T in the image brightness scale. The calculated value divides pixels into two groups: image points $f(x, y) \geq T$ and background points $f(x, y) < T$. The result of this operation is to obtain a binary image [8].

Threshold values can be determined based on the entire image (this is the so-called global brightness threshold), or depending on spatial coordinates (x, y) (the so-called dynamic brightness threshold). The threshold may also depend on a certain image feature such as average brightness in a certain environment. The determined value is then called the local brightness threshold [10].

For segmentation by thresholding, a matrix representing the input image is used, a matrix representing the threshold result (int) containing positions of pixels greater than a given threshold [13].

1.2. Segmentation by region growth

The region segmentation algorithm checks the neighboring pixel grains and decides on the basis of the assumed range if a given pixel should be added to the current region. The process runs iteratively, as in the data clustering algorithms.

The first step in creating the region is determining grains. They are determined on the basis of a previously specified criterion. The region grows from the grain to the adjacent pixel depending on the level of gray. These values are determined based on the histogram of the image..

During the initial stage of dividing the areas, the whole image is treated as one region. Then the uniformity of the region is checked. If the area does not meet the given criterion, it is divided into equal parts and the iterative step is terminated. In the next stage, all four regions are considered. If one of them does not meet the criterion of uniformity, it is automatically divided into four. This process is repeated until all areas meet the required criterion [2].

The correct grain selection is very important. Depending on the desired effect, the placement of grains in the same image can be different. The more data is known, the easier it is to choose grains and thresholds. An important issue is the scope, i.e. predetermined level, below which the algorithm assigns pixels to the common region [4]. Segmentation by the growth of regions gives the possibility to define the threshold and range, which allows specifying the particular parameters required to carry out the segmentation. The input parameters of the function used in Matlab are matrix representing a segmented image, parameter defining the location of starting points (grains) for the region's proliferation procedure and the value of threshold set by the user. When the difference between the value of image element and the grain exceeds threshold value, the region's growth in given direction is completed.

1.3. Segmentation by edge detection

Segmentation by edge detection determines threshold and mask that allow specifying the particular, parameters needed to perform the segmentation [6]. Implemented in masks are: Prewitt, Sobel, Roberts. The result of the function to segment the image using the edge algorithm is a matrix representing the image resulting from segmentation. It takes logical values 0 and 1. The input parameters of function used are the matrix representing segmented image, the matrix of mask used and threshold value.

2. Materials

To analyze the segmentation methods, a series of 64 T1-size images of size 256×256 saved in the gray scale was used. Images were obtained by magnetic resonance imaging (MRI). Cross-sections are made every 3 mm. The GE Medical Systems 1.5 T. was used to obtain image data. The times used are TR = 35, TE = 5. The results were recorded in the DICOM standard. An important step in the segmentation algorithm is to create a histogram image, based on its analysis, the user decides on the chosen type of segmentation.

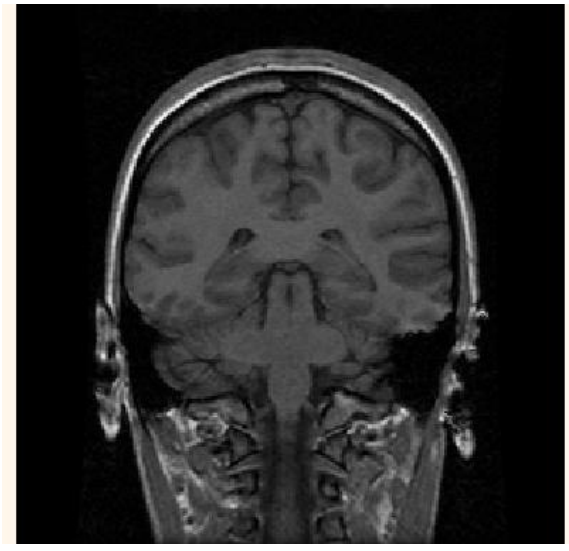

Fig. 1. Original MRI brain image

3. Results

The results of the experiments carried out are images created as a result of the segmentation by thresholding, the segmentation by edge detection and the segmentation by region growth. Each set of image data is represented by values from 0 to 255 (according to the MATLAB indexing method, the intensity values in this image take the values 1 – 256). A black and white image is an M×N matrix containing only 0 and 1. The images in the program are gray images representing its matrix size M×N with values from the set [0,255], which corresponds to 256 shades of gray.

The first experiment was the segmentation by thresholding. In Figure 2 (a) we can see a significant area of the cerebellum and the initial segment of the spinal cord. As can be seen in the segmented images, the extended core has the shape of a cone with the base pointing upwards and it passes into the spinal cord. The limitations of the spinal cord are: the lower edge, the pyramid intersections and the starting point of the spinal cord of the first cervical spinal nerve pairs. The pons appears on the abdominal side of brain as a thick, wide band laterally outside the cerebral peduncles of brain. Its lateral parts penetrate the cerebellum as branches.

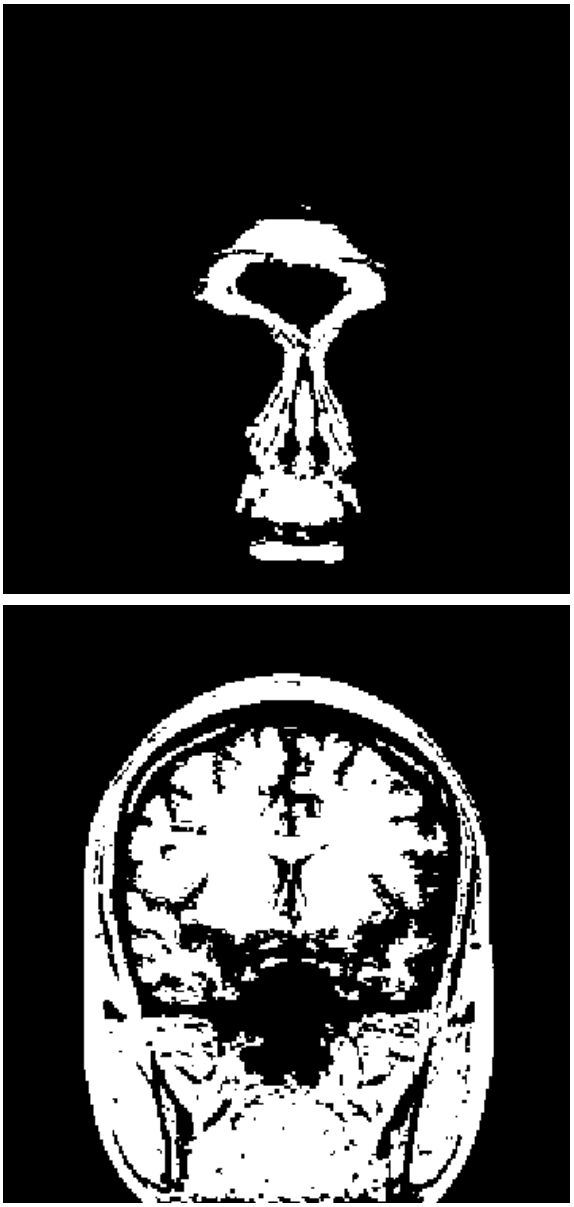

Fig. 2. Segmentation by thresholding images with preset thresholds: (a) 40, (b) 60

Figure 3 illustrates segmentation by edge detection. Despite the same value of the factor by which the pixels of image subjected to filtration are multiplied, each of the masks gives a different effect. The Sobel mask more clearly detected edges around the spinal cord, where there are many more areas of varying intensity than the Prewitt mask. Each of masks perfectly shows the outline of the skull, the boundaries between each of three meninges, the contour of white matter and soft tissues surrounding the skull. Determining the smaller parameter of selected mask gives better detection of each edge. The brains and spinal cord are covered with three meninges. The outer cover creates dura mater which consists of two plaques. Under the dura

mater there is an arachnoid, which is separated from the dura mater by a slit. A pia mater lies under the arachnoid, which covers the surface of the cortex and the spinal cord. The pia mater and arachnoid are connected by delicate beams; between them, there are spaces filled with cerebrospinal fluid.

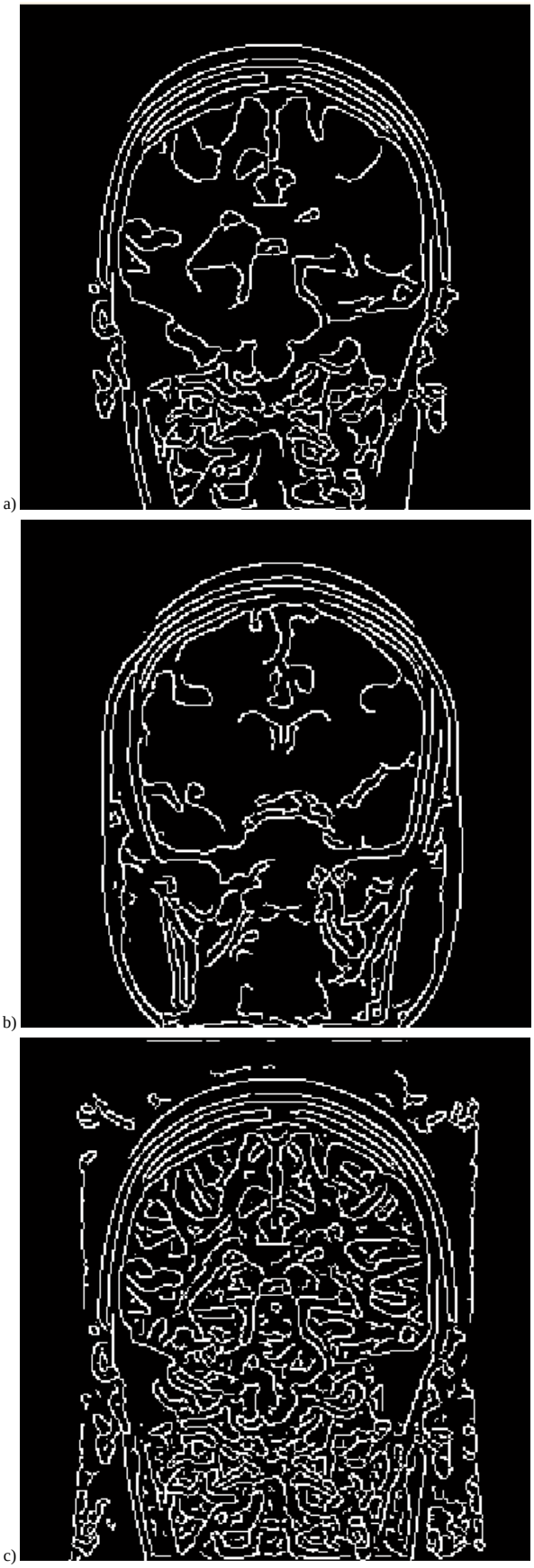

Fig. 3. Segmentation by edge detection: images with given parameters and masks (a) Threshold: 0.16 Prewitt, (b) 0.16 Sobel, (c) 0.02 Roberts

Parameters used during segmentation by region growth give the effects visible in Figure 4. They show the gray matter of brain (Figure 4a) and the white matter of brain along with the pons (Figure 4b).The hemispheres of human brain are surrounded by a gray matter that forms a cortex; there is a white matter within cortex that also contains the endbrain nucleior or subcortical nuclei.

Segmentation methods carried good results in the case of T1-dependent images. It was observed that reducing the (threshold) coefficient with selected mask causes detection of more edges. The optimal range was 0.16–0.2. It allows showing the main edges in the image for each of the selected masks. In the event, where it is important to show more details, one should reduce the threshold value until a satisfactory result is obtained. The Canna mask gives a more satisfying segmentation effect comparing to the Sobel mask. Even the low value of the coefficient does not detect the noise in the image. For the same value of the coefficient it finds better mainly the edges in the image.

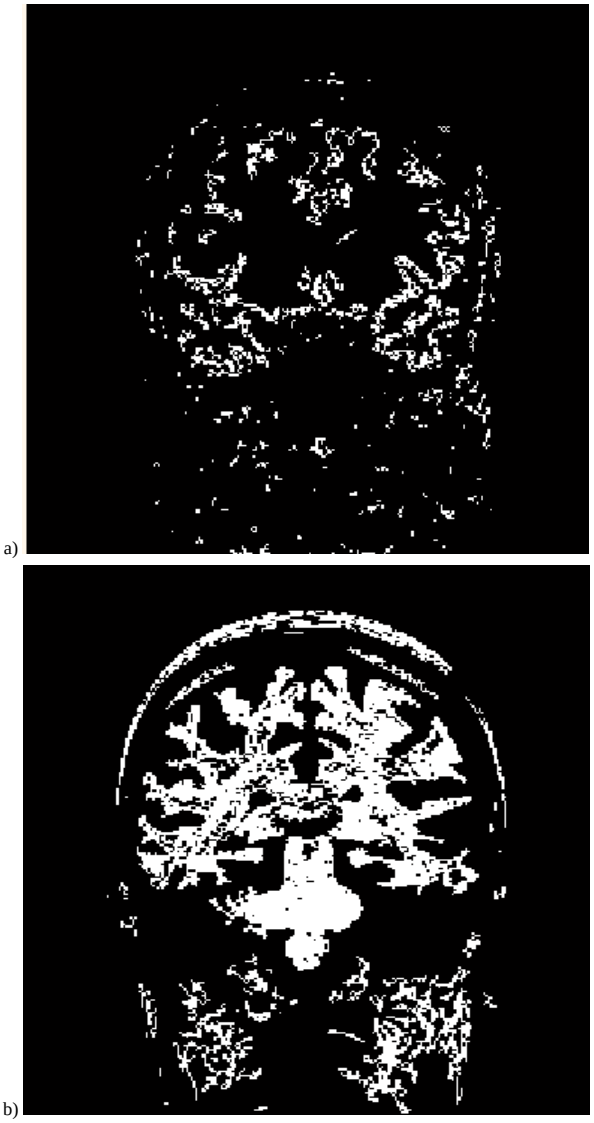

Fig. 4. Segmentation by region growth: images with given parameters Threshold/range:(a) 60/3,(b) 80/10

4. Conclusions

Each of the selected segmentation methods gives different effects for areas showing different anatomical structures. Using correctly selected algorithms allows to obtain correct segmentation of individual tissues. An effective type of segmentation is considered to be one that allows to distinguish a larger number of relevant elements. The segmentation methods

presented in the article allow for different efficiencies. Its measure is the time of performing the operation, the complexity of the algorithm and the ability to recognize anatomical structures in the segmented images.

Analyzing the effectiveness of segmentation methods presented in the article, it can be concluded that the advantage of segmentation of the brain structures by the region's growth method is the high correctness of pixel assignment of features common to one region. The simplicity of the algorithm and the flexibility of parameter selection are also important. Segmentation by region for complex images tends to create a large number of small areas. However, it allows to distinguish small anatomical structures, which are many in the human brain.

Edge segmentation with the use of Prewitt mask revealed that it is an effective tool. Specifies the size and orientation of the edges in human brain MRI images. The Sobel operator performs the averaging operation of the lead, making it less sensitive to image distortions than Robert's mask, and smoothing it better than Prewitt mask.

Many problems related to the efficiency of segmentation of medical images have not yet been resolved. Research is ongoing on more precise segmentation of anatomical elements, especially the smallest ones, such as blood vessels. The search for new segmentation algorithms is an important research challenge in field of computer image analysis. In future studies, the effectiveness analysis may be subjected to segmented structures derived from other types of imaging, eg USG or CT, and visualize them in 3D.

Bibliography

[1] Avrunin O. G., Tymkovych M. Y., Moskovko S. P., Romanyuk S. O., Kotyra A., Smailova S.: Using a priori data for segmentation anatomical structures of the brain. Przegląd Elektrotechniczny 93/2017, 102–105.

[2] Bellon O. R., Silva L.: New improvements to range image segmentation by edge detection. IEEE Signal Processing Letters 9/2002, 43–45.

[3] Bernstein M. A., King K. F., Xiadhong J. Z.: Handbook of MRI pulse sequences. Amsterdam. Elsevier, 2004.

[4] Boskovitz V., Guterman H.: An adaptive neuro-fuzzy system for automatic image segmentation and edge detection. IEEE Transactions on Fuzzy Systems 10/2002, 247–262.

[5] Hidayatullah R. R., Sigit R., Wasista S.: Segmentation of head CT-scan to calculate percentage of brain hemorrhage volume. Knowledge Creation and Intelligent Computing (IES-KCIC), IEEE, 2017, [DOI: 10.1109/KCIC.2017.8228603].

[6] Kaganami H. G., Beiji Z.: Region-Based Segmentation versus Edge Detection. Intelligent Information Hiding and Multimedia Signal Processing IIH-MSP'09. Fifth International Conference, 2009.

[7] Rebouças E. S., Braga A. M., Sarmento R. M.: Level Set Based on Brain Radiological Densities for Stroke Segmentation in CT Images. Computer-Based Medical Systems (CBMS), IEEE 2017 [DOI: 10.1109/CBMS.2017.172]

[8] Sharma N., Aggarwal L. M.: Automated medical image segmentation techniques. J. Med. Phys. 35/2010, 3–14.

[9] Suri J. S., Setarehdan S. K., Singh S.: Advanced Algorithmic Approaches to Medical Image Segmentation. Springer, 2002.

[10] Tadeusiewicz R., Korohoda P.: Komputerowa analiza i przetwarzanie obrazów. Wydawnictwo Postępu Telekomunikacji, Kraków 1997.

[11] Tadeusiewicz R., Śmietański J.: Pozyskiwanie obrazów medycznych oraz ich przetwarzanie, analiza, automatyczne rozpoznawanie i diagnostyczna interpretacja. Wydawnictwo Studenckiego Towarzystwa Naukowego, Kraków 2011.

[12] Ulagamuthalvi V., Kulanthaivel G.: An novel approach for segmentation using brain images. International Conference on Control, Instrumentation, Communication and Computational Technologies (ICCICCT), IEEE, 2017.

[13] Wróbel Z., Koprowski R.: Praktyka przetwarzania obrazów z zadaniami w programie Matlab. Akademicka Oficyna Wydawnicza EXIT, Warszawa 2012.

[14] Yahiaoui A. F. Z., Bessaid A.: Segmentation of ischemic stroke area from CT brain images, Signal, Image, Video and Communications (ISIVC), IEEE 2017 [DOI: 10.1109/ISIVC.2016.7893954].

M.Sc. Róża Dzierżak
e-mail: r.dzierzak@pollub.pl

Ph.D. student at the Electrical Engineering and Computer Science Faculty. Assistant in the Institute of Electronics and Information Technology of Lublin University of Technology. Recent graduate Biomedical Engineering and Computer Science. Her research interests include medical image processing.

M.Sc. Magdalena Michalska
e-mail: magdalena.michalska@pollub.edu.pl

Ph.D. student at the department of Electronics and Information Technology, Lublin University of Technology. Recent graduate Biomedical Engineering and Electronic at Warsaw University of Technology.
Research field covers wide variety of 3D modeling, medical image processing, spectrophotometry.

otrzymano/received: 24.04.2018 *przyjęto do druku/accepted: 11.05.2018*

DOI: 10.5604/01.3001.0012.0714

ANALYSIS OF METROLOGICAL PROPERTIES FIBER BRAGG GRATINGS WITH A CONSTANT AND VARIABLE PERIOD

Tomasz Zieliński, Piotr Kisała
Lublin University of Technology, Institute of Electronics and Information Technology

Abstract. *The paper presents periodic structures in terms of metrological properties in the distinction for a fiber Bragg grating (FBG) with a constant and changeable period. The process of their formation and characteristics as well as applications in many areas have been described. On the basis of the literature, the results of research and measurements of measurable quantities such as temperature and stress made by periodic structures applied to the fiber of the optical fiber are presented. Analysis of the presented measurements allowed to mark the ranges and accuracy of measurements of individual applications.*

Słowa kluczowe: fiber Bragg grating, optical sensors, uniform fiber Bragg grating, chirped fiber Bragg grating

ANALIZA WŁAŚCIWOŚCI METROLOGICZNYCH SIATEK BRAGGA ZE STAŁYM I ZMIENNYM OKRESEM

Abstract. *W pracy przedstawiono struktury periodyczne pod kątem własności metrologicznych w rozróżnieniu na światłowodowe siatki Bragga (FBG – ang.: Fiber Bragg Grating) o stałym i zmiennym okresie. Opisano proces ich powstawania oraz cechy charakterystyczne jak i zastosowania w wielu dziedzinach. W oparciu o literaturę zaprezentowano wyniki badań i pomiarów takich wielkości mierzalnych jak temperatura i naprężenie dokonywanych strukturami periodycznymi naniesionymi na włókno światłowodu. Analiza zaprezentowanych pomiarów pozwoliła nakreślić zakresy oraz dokładności pomiarów poszczególnych aplikacji.*

Keywords: światłowodowa siatka Bragga, czujnik optyczny, jednorodna światłowodowa siatka Bragga, chirpowa światłowodowa siatka Bragga

Introduction

The phenomenon of photosensitivity in optical fiber is the main phenomenon involving the fabrication of Bragg gratings in the fiber core, which for the first time showed K.O. Hill et al. In 1978 [14]. However, only eleven years later (1989), published by G.Meltz and colleagues [39], a pioneering work in the production of Bragg grids, has become a milestone for fiber optic sensors. It describes a method for producing bragga nets using two intersecting UV rays, directed to the side of an optical fiber falling on its cladding. This method enabled the creation of a mesh with a fixed period and depth of modulation, while being much more efficient in comparison to previous methods that did not give such possibilities to change the parameters of the mesh [16].

The information that contains the aforementioned publications initiated the dynamic development of optical fiber technology around the world. In a short time, many new methods for the production of Bragg grids arose, and as a result, their quality and the number of potential applications drastically increased.

The replacement of the first methods of producing periodic structures such as internal writing [14] and holographic technique [39], phase mask technique [2, 15] allowed for a significant reduction in manufacturing costs through the use of cheaper devices in the production process while increasing product quality. The disadvantage of the phase mask technique is the need to use a separate mask for each other Bragg wavelength. However, it is possible to tune the wavelengths by tensioning the fibers during the photocoding process; the Bragg wavelength of the loosened fiber will vary by 2 nm [16].

The phase mask technique ensures not only high-quality periodic structures, but is very flexible, it can be used to produce meshes with controlled spectral characteristics. For example, the typical spectral response of a uniform Gragge (uniform grating), one that has a constant period of refractive index and a constant depth of modulation along the length of the fiber, has side bands/secondary maxima on both sides of the main reflection peak. In applications such as wavelength division multiplexing, this type of response is not desirable [16]. Along with the use of the phase mask technique, it is possible to silence the sidebands with the apodization procedure, the change in modulation depth [1, 37].

The phase mask technique has also been adapted to produce periodic structures with variable periods, those that have a variable period of refractive index along the length of the mesh to extend their spectral response.

Another method that enabled the development of fiber optic sensors is the point-by-point (PbP) method. Despite the first presentation of the structure made in this PbP method in 1993 [36], it did not arouse much interest until the use of light sources with femtosecond pulse lengths [46]. This technique allows the recording of Bragg grids in photonic fibers [28]. The advantage of this technique is also the possibility of using the produced periodic structures at temperatures close to 1000°C due to structural modifications of the glass during their production [38].

The use of fiber-optic periodic structures as a sensor is very popular due to the possibility of using them in flammable and chemically aggressive environments, their great advantage is that they are insensitive to changes in the electromagnetic field. Negligible weight and size make it possible in most cases to omit their influence on the object under study [26].

Thanks to continuous research on the use of fiber optic Bragg grids as measuring sensors, many methods have been developed for their application. Most of the methods presented in the published works are based on the multiple use of FBG sensors in a single application.

Simple batch structures such as homogeneous Bragg gratings, thanks to the properties of linear processing of magnitude measured on the Bragg wave shift, are great transducers of physical quantities such as temperature and stress [24, 35], displacement [48] or force [10]. These structures are also widely used in the study of many physical quantities simultaneously, eg: elongation and temperature [25], or strength and temperature [22].

Homogeneous optical fiber optical sensors are also tested for their application in the measurement of stress values occurring in the structures of aircraft wings, masts of sea-going ships, or examination of the condition of bridge structures – constructions particularly exposed to the influence of external forces. Noteworthy is the use of this structure in the field of medicine. The optical sensor allows you to monitor the vibrations of the body caused by basic life activities, such as the rhythm of the heartbeat and breathing. This use of periodic structure gives a lot of possibilities in the field of monitoring the physiological state of the examined person without the need of direct contact with the skin of the patient (gel or dry electrodes) [7].

In addition to the use of homogeneous Bragg grids as sensors, tests are also carried out in the field of their use as optical switches based on optical bistability. The first works describing the optical bistability phenomena using the Bragg's single lattice appeared in 1995. They present the optical switching threshold, which

occurred for the input optical grid signal of 200 W, which is a much higher value than the optical switching power level [43].

An article from 2015 proposes an optical bistable system that uses two homogeneous Bragg grids and an erbium doped optical fiber. It has been shown that the level of switching power of the system can be reduced to 12.5 mW by increasing the length of the erbium fiber characterized by a high value of the non-linear refractive index, and it was noted that the change in the length of the grid from 5 mm to 4 mm causes almost double increase in switching power [21].

Bragg grids with a variable period have many applications. Particularly linear periodic structures of this type have found a special place in optics: as devices for correcting dispersion and compensation. This application has also resulted in the production of very long, high-quality wide-band meshes, intended for high-speed transmission over long distances [27, 33], and in WDM transmission [8, 11, 40]. Some of the other applications include high order fiber dispersion compensation, ASE attenuation, amplifier gain flattening, bandpass filters [20] and Fourier transform in real time [3].

A very interesting application of CFBG is its use in an application to replace an optical spectrum analyzer. In the article from 2017. presents a CFBG interrogation system that can simultaneously measure positive/negative deformations and temperature changes, with a resolution of about 1με (thanks to a photodiode with a sensitivity of 0.3–0.4 nW). A chirp of 5 nm can provide a strain measurement range of around ± 4000 με [34].

Bragg's chirp grids have also found their application as measuring courts used to measure impact velocity, detonation velocity, shock wave profile or pressure profile in inert and energetic materials. The diameter of the measuring judge using the chirp structure does not exceed 150 μm, which allows it to be placed directly in the material without interfering with physical phenomena. The sensor placed in this way enables the shockwaves to be traced inside the material using the Bragg wavelength. In this application, the speed (several km/s) and measurements of the shockwave profile are carried out by recording the reflected spectrum from the CFBG [4].

Common application of the sensor using the Bragg mesh with a constant and variable period is presented in the publication from 2012. The author presented a method enabling the simultaneous measurement of deformation and temperature using a single, uniform Bragg mesh with a properly selected chirp zone. Providing the same sensitivity to temperature and different sensitivity to deformation of two parts of the sensor and experimental measurements of the quality of the proposed system made it possible to state that the presented application is fully functional. The sensor grid was placed in such a way that its half was in the zone of variable axial stresses induced by changes in the cross-section of the sample, while the other half was in the zone with a constant cross-section of the sample and constant strain value. In this work, the author also presented the obtained nonlinear errors in the processing characteristics for measuring the deformation and temperature of the proposed system, amounting to 2.7% and 1.5% respectively, with the sensitivity factors for strain and temperature being respectively 0.77×10^{-6} m/ε and 4.13×10^{-12} m/K. The maximum differences shown between the values obtained from the intermediate measurement and the set values were 110 με for the deformation and 3.8ºC for the temperature, while for the deformation 2,500 με and the temperature 40°C [23].

While discussing the subject of Bragg grids with a constant and variable period, it is worth mentioning the possibility of transforming homogeneous FBG into chirp using, for example, strain gradient or temperature along the length of a homogeneous FBG. The deformation or temperature gradient can be produced by various methods:

- combining FBG with the base using a soft adhesive, which gradually relieves the stress of the mesh [12],
- narrowing of the external FBG diameter using acid [42],
- using a cantilevered beam with non-uniform cross-section [13],
- deposition of different thicknesses of the retaining film on the FBG surface with a constant period [9].

The paper presents issues concerning optical parameters of homogeneous periodic structures and variable-period structures, and their use as transducers for temperature and stress measurement.

1. Optical parameters of periodic structures with a uniform and variable period

The Bragg fiber optic mesh is referred to as glass regions with different refractive index values stored in the single-mode optical fiber core.

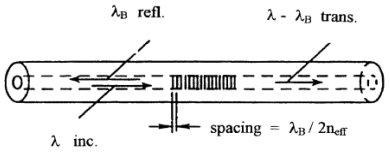

Fig. 1. Schematic of optical fiber with the Bragg mesh applied [20]

These periodic changes have a sinusoidal character, which characterizes their period Λ, and their amplitude Δn. Propagation of a beam of light in a fiber with a direction perpendicular to the Bragg grating causes the reflection of a specific wavelength from the beam incident on it. The structure in question is capable of backward reflection of the wavelength satisfying the Bragg condition [20]:

$$m\,\lambda_B = 2 \bullet n_{eff} \bullet \Lambda \quad (1)$$

where: m – natural number defining the order of reflection of radiation, λ_B – Bragg wave length, n_{eff} – the average value of the modulation component of the refractive index modulation in the Bragg structure, Λ – Bragg grid.

Reflected rays add in the phase creating a ray obliterated from the Bragg structure on the principle of constructive interference, while the remaining part of radiation, which does not meet the condition (1) is subject to further lossless propagation [20].

Considering the fixed network and the distribution of the refractive index inside the periodic structure, we are able to list different types of Bragg grids. In the further part of the work, two types of fiber-optic Bragg nets will be discussed, homogeneous and chirpova in terms of metrology.

The homogeneous Bragg mesh is the basic type of this type of structures. It is characterized by a constant value of modulation depth and a constant period of refraction along the fiber axis, as shown in Fig. 2.

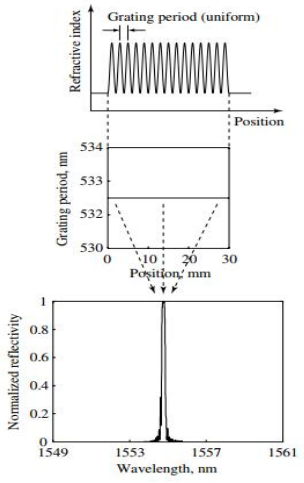

Fig. 2. Diagram of a single FBG with its corresponding spectrum [20]

A structure that has a heterogeneous value of the period along its length has been called Chirp. Chirp can take many different forms, it can differ symmetrically, growing or decreasing in the

period. Chirp may be linear, square or may have spikes over a period of time. The grid may also have a period that changes randomly along its length. In Figure 3. the diagram of the Bragg's chirp grid and its corresponding spectrum are shown.

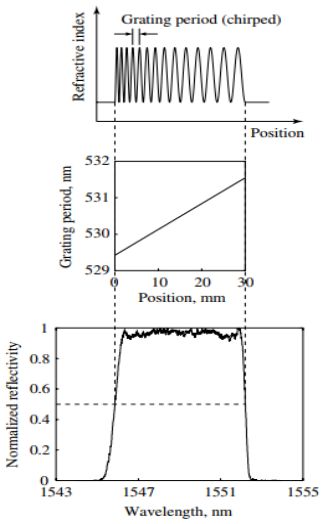

Fig. 3. Chirp FBG diagram with the corresponding spectrum [20]

Proper analysis of metrological properties should be based on qualitative indicators of optical fiber periodic structures. The assessment is made by analyzing the spectral spectra obtained in the result of the tests, these may be transmission or reflection spectra.

One of the qualitative indicators is the reflectance of the periodic structure. In Figure 4, the reflectance value R is indicated, which is the ratio of the difference in power values for the part of the characteristic out of the transmission peak, which is the reference power and the minimum power value at the summit point of the transmission peak to the reference power value. Spectral changes in the power level of the spectrum in the real measurement of the spectral characteristics result from the light source used to measure. The method to minimize the impact of the shape of the spectral characteristic of the source is to use the quotient of two measured spectra, the optical fiber spectrum without the recorded periodic structure and the spectral characteristics of the Bragg structure [20].

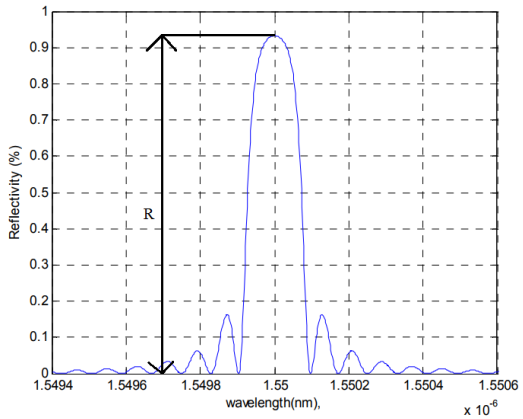

Fig. 4. Determination of FBG reflectance based on its reflection characteristics

The actual spectral characteristics of the Bragg structures differ from the ideal characteristics. Deformation consists in the occurrence of sidebands on both sides of the reflective peak and the slope of the slope of the same reflective peak of the net as shown in Fig. 5.

The RL sideband reflexivity is an important qualitative indicator affecting the applicability and accuracy of the Bragg structure used. It was defined as the ratio of the amplitude of the reflection of the radiation of the first-order ribbon and the main peak. Obtaining minimal reflectance of the first-order lateral webs (with the highest amplitude) in the Bragg structure manufacturing process indicates high quality of the obtained structure.

The reason for the formation of side bands that are part of the spectrum are the extreme areas of the Bragg structure with a steep slope of the refractive index. The method for leveling the sidebands is to change the shape of the refractive index profile along the optical fiber axis (apodization) during the Bragg structure fabrication process.

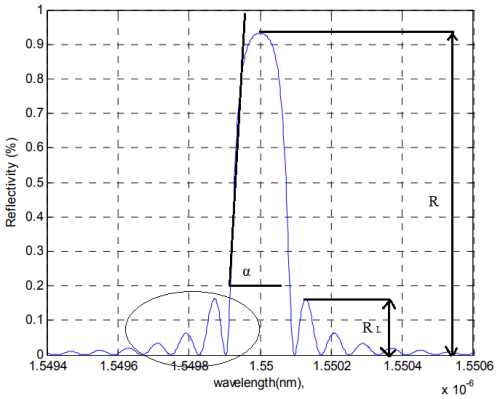

Fig. 5. The spectral characteristics of the Braga structure with marked slope line and sidebands and determination of their reflectance

The research results presented in the literature prove that for a Bragg structure with a length of L = 5 mm, the maximum reflectance is about 60%, while for a structure with a length of L = 25 mm, the maximum reflectance is already 99.98%. However, increasing the length of the grid, despite obtaining high reflectance, causes a drastic increase in the refinement of the sidebands [17]. After applying apodization of the Bragg structures, the mesh with a length of L = 10 mm obtained a reflectance of about 60%, while a reflectance of 99.99% was indicated with a Bragg structure equal to L = 45 mm. Despite the necessity to increase the length of Bragg structures after apodization in order to achieve the highest possible reflectance, nearly ideal spectra were obtained that were not burdened with side bands [17].

Half width FWHM (Full Width at Half Maximum), is a qualitative indicator defining the spectral width of the reflection of the periodic structure.

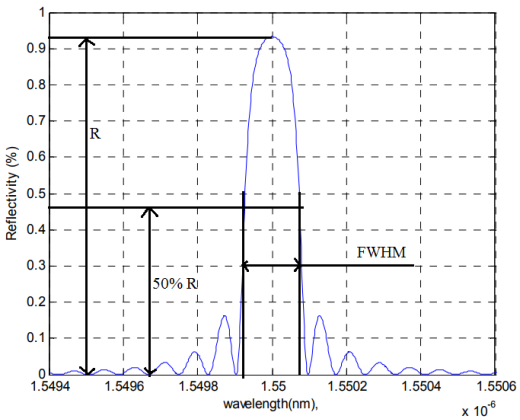

Fig. 6. Reflection spectrum with marked half width FWHM

Figure 6 shows the reflection spectrum with the half-width FWHM indicated, which is defined as the spectral distance between two points of the main peak of the reflection grid, at which the course takes half of peak values [20].

The studies presented in the literature define a range of typical FWHM half-width values, starting at 10 pm for Bragg structures with a constant period [6], and ending with CFBG grids, reaching a FWHM value equal to 100 nm [38].

Half-width measured in fixed-term structures is a very important parameter considering the use of the Bragg fiber optic mesh in sensor applications. The narrowing of the FWHM width makes it possible to increase the detection range leading to the measurement of very small deformations. As an example, it is worth citing a special type of mesh, πFBG, whose spectrum reflects the discontinuity caused by the π-phase cut in the central part of the mesh. Thanks to the application of πFBG in the sensor application, a half width equal to FWHM = 10 pm can be achieved, and the use of the π phase shift area allows to reduce the effective length of the sensor, making it particularly suitable for detecting high frequency ultrasound [6].

Each of the qualitative parameters described above marked in Fig. 4, Fig. 5, Fig. 6, presented as reflection spectra for a Bragg structure with a fixed period, can be directly related to a structure with a variable period as shown in Fig. 7.

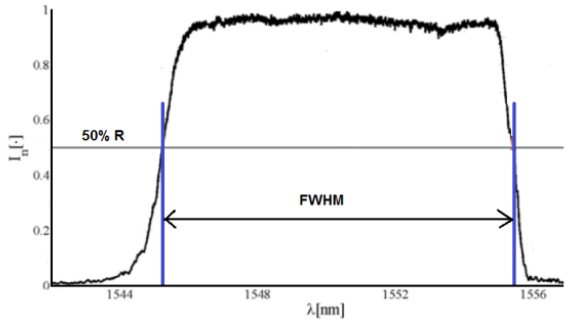

Fig. 7. Reflectance spectrum of CFBG structure with marked half width FWHM, side bands and reflectance

2. Uniform and chirp grids as transducers for temperature and stress measurement

Analyzing the research presented in the publications, we can observe a great interest in sensors based on Bragg fiber optic nets. Among the many applications, FBG sensors are particularly useful for measuring stresses or temperatures, since both stress and temperature information are encoded in the optical fiber as a wavelength shift.

An important parameter conditioning the use of the Bragg structure as a measuring transducer is a typical measuring range. In this part of the article a typical measuring range will be described for the temperature measured with different types of Braaga structure.

Uniform Optic Bragg type I fiber mesh, characterized by a monotonic increase in the depth of the refractive index modulation as a function of the amount of energy delivered to the fiber in the recording process. They are usually used at temperatures up to 300°C because of their strength [30].

Bragg type II grids are created by increasing the energy of radiation during the recording process which can lead to physical damage in the fiber core or at the edge of the shell and core. A characteristic feature of this type of mesh is high temperature resistance, exceeding 800°C, and in some cases reaching 1200°C. This high temperature resistance was achieved due to the fabrication of the structures under investigation with the use of laser pulses of femtosecond lengths [39, 40]. In 2002, for the first time, the type IA structure was described, which is characterized by a higher temperature resistance compared to type I mesh, reaching the limit of 500°C [5, 32].

Another group of FBG structures are type IIA grids. Their temperature resistance fluctuates within 500°C, yet they are characterized by the highest temperature sensitivity from all types of meshes, taking into account stresses [19, 41].

Analyzing publications published in recent years, we can notice other types of Bragg's products. Table 1. shows all types of fiber optic Bragg grids with respect to the maximum temperature at which they can be used.

The fact that data relating to temperature and stress is signaled by the shift of the wavelength in a fiber optic cable forces the execution of a system that allows measuring the stress of the examined element, distinguishing the influence of the ambient temperature and the tested element. The Bragg wavelength of the FBG sensor depends mainly on the deformation, but varies with the change in temperature. At a temperature change of 1°C, the measured stress usually has an error of 11 με [45].

Tab. 1. Types of fiber optic Bragg grids [5]

Grids type	Thermal durability
Type I	~320°C
Type IIA; (Type In)	800°C
Type I (H_2); (Type IH)	< 320°C
Type IA; (Type IHp)	500°C
Type IHs	600°C
Type II	>1000°C
Type R	>1000°C

To achieve higher accuracy, FBG sensors require temperature compensation. Many methods have been developed to measure stresses with temperature compensation. One of the first methods published in 1995 is the use of a stretched net in a packet containing two materials with different coefficients of thermal expansion. As the temperature rises, stress gradually releases, compensating for the temperature dependence on the Bragg wavelength. The Bragg fiber optic mesh mounted in the above-mentioned package, 50 mm long and 5 mm in diameter, showed a total variation of Bragg wavelength 0.07 nm in the temperature range of 100°C, compared with 0.92 nm for uncompensated mesh as shown in Figure 8 [18].

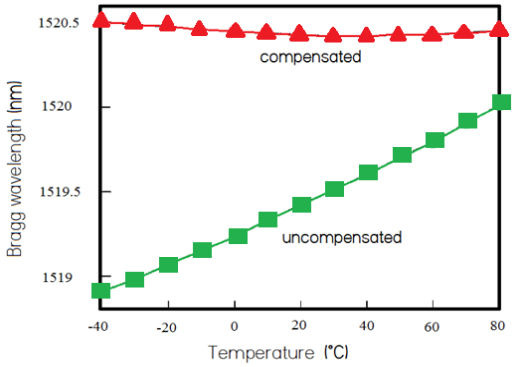

Fig. 8. Bragg wavelength graph with respect to the temperature with marked values for Bragg mesh without compensation and temperature compensation [47]

The high interest in fiber-optic temperature and stress sensors translates into published works in which we can distinguish many methods and applications of these periodic structures. The results of publications that outline the accuracy and measurement ranges of given structures will be presented below.

One of the first publications is the article from 1996. describing the technique of simultaneous, independent temperature and deformation measurement using the Bagga fiber optic sensors. Two structures with closely spaced mid-wavelengths are recorded on both sides of the weave between two fibers of different diameters (Corning PMF-38 – 80 μm and Snectran FS SMC-A0780B – 125 μm). Batch structures exhibit similar temperature sensitivity but different strain reactions to applied stresses. The maximum error is ± 17 με and ± 1°C for a measuring range of 2,500 με and 120°C. The test results are presented in the form of graphs Fig. 9 and Fig. 10 [18].

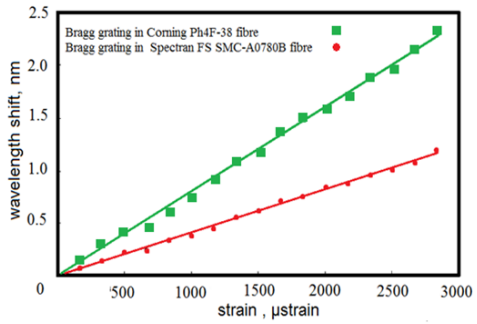

Fig. 9. Graph showing the stress response of a pair of periodic structures [18]

Analyzing the above graphs, we can notice that the stress response of both periodic structures differs to a large extent from each other. The gradient of the stress graph shown is $0.42\pm5\times10^{-3}$ pm/µstrain for the Bragg mesh made on Corning fiber and $0.81\pm7.8\times10^{-3}$ pm/µstrain for the Bragg mesh made on the Spectran fiber [18].

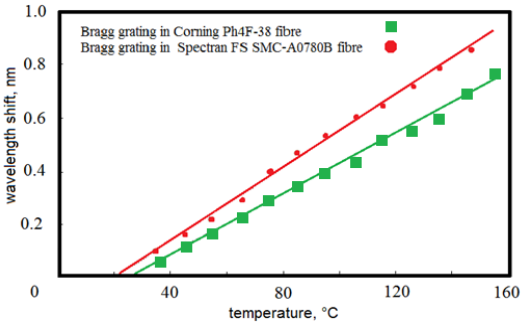

Fig. 10. Graph showing the temperature response of a pair of periodic structures [18]

In the case of a graph showing the temperature response, we can observe that the responses of individual periodic structures are very similar to each other. The gradient of the temperature response graph is 7.0±0.1 µm/°C of the Brgg mesh made on the Corning fiber and 5.7±0.1 pm/°C for the Brgg mesh made on the Spectran fiber [18].

The temperature and stress can also be measured with one Bragg fiber optic mesh. The publication from 2010 presents a method of simultaneous measurement of both these quantities using a single periodic structure made on a tapered fiber. The implementation of a homogeneous periodic structure on a tapered optical fiber allows to obtain a heterogeneous (chirp) structure after undergoing stress. The existence of stress-induced chirp allowed the authors to collect information encoded not only in Bragg's wavelength but also in the FWHM grid. An important feature of the periodic structure, related to the insensitivity of FWHM to temperature changes, allowed to measure temperature and strain with uncertainty of ±1.9°C and 15.3 µε respectively. The measurement was carried out at a constant stress of 1500 µε and a temperature change in the range from 20 to 65°C, and at a constant temperature of 40°C and variable tension [31].

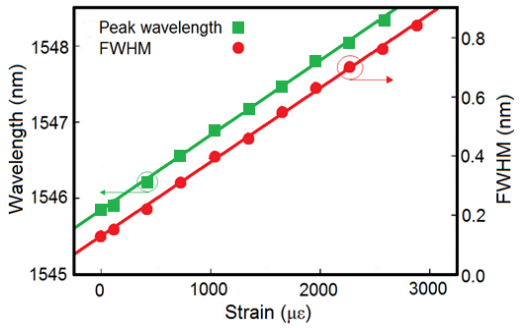

Fig. 11. Graph showing the response of the sensor to different stress values [31]

The above Figure 11 shows the response of the sensor to different values of the applied strain, which reveals the linear dependence of FWHM on the applied strain. The peak wavelength response is also linear with the applied strain [31].

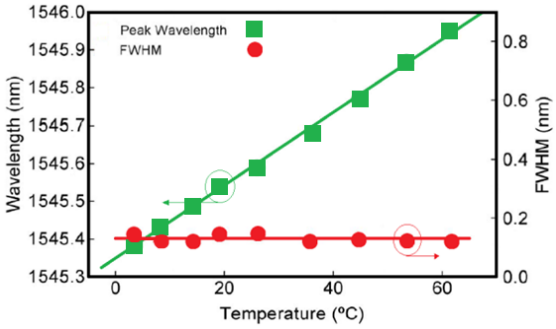

Fig. 12. Graph showing the response of the sensor to different temperature values [31]

Figure 12 shows the temperature response of the sensor head. It can be seen that as the temperature rises, the peak wavelength also increases linearly, but FWHM remains relatively at around 0.13 nm [31].

3. Conclusion

The literature examples cited in the paper clearly indicate the very accurate use of fiber-optic periodic structures in the technique of measuring non-electrical quantities such as temperature and stress. Presentation of fiber optic Bragg grids through the spectrum of metrology enabled accurate scratching of measurement intervals, presentation of features affecting the accuracy of measurement and various types of periodic structures themselves, that is grids with a constant and variable period. Taking into account the described research results taken from the literature, it is clearly visible that periodic structures work well in the role of measuring transducers of temperature and stress. The described applications thanks to the use of fiber-optic periodic structures in various configurations also enable their adaptation to other scientific fields.

Reference

[1] Albert J., Hill K.O., Malo B., Theriault S., Bilodeau F., Erickson L.E.: Apodization of the spectral response of fiber Bragg gratings using a phase mask with variable diffraction efficiency. Electron. Lett. 31, 1995, 222–223.
[2] Anderson D.Z., Mizrahi V., Erdogan T., White A. E.: Production of in-fiber gratings using a diffractive optical element. Electron. Lett. 29, 1993, 566–568.
[3] Azaña J., Chen L.R., Muriel M.A., Smith P.W.E.: Experimental demonstration of real-time Fourier transformation using linearly chirped fiber Bragg gratings. Electron. Lett. 35(25), 1999, 2223–2224.
[4] Barbarin Y.: Dynamic measurements of physical quantities in extreme environment using fiber Bragg grating. 27th Optical Fiber Sensors Conference (OFS), IEEE, 2017, 1–4.
[5] Canning J.:Fibre gratings and devices for sensors and lasers. Laser & Photonics Reviews 2(4), 2008, 275–289.
[6] Deepa S., Bhargab D.: Pico-strain-level dynamic perturbation measurement using πFBG sensor. arXiv preprint arXiv:1710.04206, 2017.
[7] Dziuda Ł., Krej M., Lewandowski J., Różanowski K., Skibniewski F.: Światłowodowy czujnik czynności oddechowej i rytmu serca. Polski Przegląd Medycyny i Psychologii Lotniczej 3(17), 2011.
[8] Eggleton B.J., Nielsen T.N., Rogers J.A., Westbrook P.S., Strasser T.A., Hansen P. B., Dreyer K.F.: Dispersion compensation in 20 Gbit/s dynamic nonlinear lightwave systems using electrically tunable chirped fiber grating. Electron. Lett. 35, 1999, 832–833.
[9] Eggleton B.J., Rogers J.A., Westbrook P.S., Strasser T.A.: Electrically tunable power efficient dispersion compensating fiber Bragg grating. IEEE Photonics Technology Letters 11(7), 1999, 854–856.
[10] Fernandez A.F., Berghmans F., Brichard B., Mégret P., Decréton M., Blondel M., Delchambre A.: Multi-component force sensor based on multiplexed fibre Bragg grating strain sensors. Meas. Sci. Technol. 12(7), 2001, 810.
[11] Garrett L.D., Gnauck A.H., Forgherieri, Scarano D.: 8 X 20 Gb/s–315 km–480 km WDM transmission over conventional fiber using multiple broadband fiber gratings. Tech. Digest of Conf. On Opt. Fiber Commun. OFC '98, Post-Deadline paper, PD18, 1998, 1–4.
[12] Hill P.C., Eggelton B.J.: Strain gradient chirp of fibre Bragg gratings. Electronics Letters 30(14), 1994, 1172–1174.

[13] Hill K.O., Bilodeau F., Malo B., Kitagawa T., Thériault S., Johnson D. C., Albert J., Takiguchi K.:Chirped in-fiber Bragg gratings for compensation of optical-fiber dispersion. Opt. Lett. 19(17), 1994, 1314–1316.
[14] Hill K.O., Fujii Y., Johnson D.C., Kawasaki B.S.: Photosensitivity in optical fiber waveguides: Application to reflection filter fabrication. Appl. Phys. Lett. 32, 1978, 647–649.
[15] Hill K.O., Malo B., Bilodeau F., Johnson D.C., Albert J.: Bragg gratings fabricated in monomode photosensitive optical fiber by UV exposure through a phase mask. Appl. Phys. Lett. 62, 1993, 1035–1037.
[16] Hill K.O., Meltz G.: Fiber Bragg grating technology fundamentals and overview. J. Lightwave Technol. 15, 1997, 1263–1275.
[17] Ikhlef A.: Uniform Fiber Bragg Grating modeling and simulation used matrix transfer method. International Journal of Computer Science Issues 9(1), 2012, 368–374.
[18] James S.W., Dockney M.L., Tatam R.P.: Simultaneous independent temperature and strain measurement using in-fibre Bragg grating sensors. Electronics Letters 32(12), 1996, 1133–1134.
[19] Kalli K., Simpson G., Dobb H., Komodromos M., Webb D., Bennion I.: Annealing and temperature coefficient study of type IA fibre Bragg gratings inscribed under strain and no strain-implications to optical fibre component reliability. Proc. SPIE 6193, 2006.
[20] Kashyap R.: Fiber Bragg Gratings. New York, Academic, 1999.
[21] Kisała P., Klimek J., Skorupski K.: W pełni optyczny przełącznik wykorzystujący jednorodne światłowodowe siatki Bragga. Przegląd Elektrotechniczny 91(11), 2015, 266–270.
[22] Kisała P., Cięszczyk S.: Method of simultaneous measurement of two direction force and temperature using fbg sensor head. Appl. Opt. 54, 2015, 2677–2687.
[23] Kisała P.: Generation of a zone chirp in uniform Bragg grating as a way of obtaining double functionality of a sensor. Metrology and Measurement Systems 4, 2012, 727–738.
[24] Kisała P.: Method of simultaneous measurement of bending forces and temperature using Bragg gratings. Proc. SPIE 9506, Optical Sensors, 2015.
[25] Kisała P.: Optoelectronic sensor for simultaneous and independent temperature and elongation measurement using Bragg gratings. Przegląd Elektrotechniczny 11a, 2012, 343–346.
[26] Kisała P.: Periodyczne struktury światłowodowe w optoelektronicznych czujnikach do pomiaru wybranych wielkości nieelektrycznych. Politechnika Lubelska, 2012.
[27] Laming R.I., Ibsen M., Durkin M., Cole M.J., Zervas M.N., Ennser K.E., Gusmeroli V.: Dispersion compensation gratings. Bragg Gratings, Photosensivity, and Poling in Glass Fibers and Waveguides, Applications and Fundamentals. OSA Technical Digest Series (Optical Society of America, Washington, DC) 17, Paper BTuA7, 1997, 271–273.
[28] Lazaro J.M., Quintela A., Tarnowski K., Wojcik J., Urbanczyk W., Lopez-Higuera J.M.: Experimental characterization of the spectral effective index dependence of index-guided photonic crystal fibers. Meas. Sci. Technol. 21, Paper 055111, 2010.
[29] Li Y., Yang M., Wang D.N., Lu J., Sun T., Grattan, K.T.: Fiber Bragg gratings with enhanced thermal stability by residual stress relaxation. Optics express 17(22), 2009, 19785–19790.
[30] Liao C., Li Y., Wan, D.N., Sun T., Grattan K.T.V.: Morphology and Thermal Stability of Fiber Bragg Gratings for Sensor Applications Written in H_2-Free and H_2-Loaded Fibers by Femtosecond Laser. IEEE Sensors Journal 10(11), 2010, 1675–1681.
[31] Lima H.F., Antunes P.F., de Lemos Pinto J., Nogueira R.N.: Simultaneous measurement of strain and temperature with a single fiber Bragg grating written in a tapered optical fiber. IEEE Sensors Journal 10(2), 2010, 269–273.
[32] Liu Y., Williams J.A.R., Zhang L., Bennion, I.: Abnormal spectral evolution of fiber Bragg gratings in hydrogenated fibers. Optics letters 27(8), 2002, 586–588.
[33] Loh W.H., Laming R.I., Robinson N., Cavaciuti A., Vaninetti, Anderson C.J., Zervas M.N., Cole M.J.: Dispersion compensation over distances in excess of 500 km for 10 Gb/s systems using chirped fibre gratings. IEEE Photon. Technol. Lett. 8, 1996, 944.
[34] Maheshwari M., Tjin S.C., Yang Y., Asundi A.: Wavelength-shifted chirped FBGs for temperature compensated strain measurement. Sensors and Actuators A: Physical. 2017.
[35] Majumder M., Gangopadhyay T.K., Chakraborty A.K., Dasgupta K., Bhattacharya D.K.: Fiber Bragg gratings in structural health monitoring–prezent status and applications. Sensors and Actuators 147, 2008, 150–164.
[36] Malo B., Hill K.O., Bilodeau, F., Johnson D.C., Albert J.: Point-by-point fabrication of micro-Bragg gratings in photosensitive fiber using single excimer pulse refractive-index modification techniques. Electron. Lett. 29, 1993, 1668–1669.
[37] Malo B., Theriault S., Johnson D.C., Bilodeau F., Albert J., Hill K.O.: Apodised in-fiber Bragg grating reflectors photoimprinted using a phase mask. Electron. Lett. 31, 1995, 223–224.
[38] Martinez A., Khrushchev I.Y., Bennion I.: Thermal properties of fibre Bragg gratings inscribed point-by-point by infrared femtosecond laser. Electron. Lett. 41, 2005, 176–178.
[39] Meltz G., Morey W.W., Glenn W.H.: Formation of Bragg gratings in optical fibers by a transverse holographic method. Opt. Lett. 14, 1989, 823–825.
[40] Ouellette F., Krug P.A., Stephens T., Dhosi G., Eggleton B.J.: Dispersion compensation using chirped sampled fibre Bragg gratings. Electronics Lett. 31, 1995, 899–901.
[41] Prakash O., Kumar J., Mahakud R., Agrawal S.K., Dixit S.K., Nakhe S.V.: Enhanced Temperature (~800°C) Stability of Type-IIa FBG Written by 255 nm Beam. IEEE Photonics Technology Letters 26(1), 2014, 93–95.
[42] Putnam M.A., Williams G.M., Friebele E.J.: Fabrication of tapered, strain-gradient chirped fibre Bragg gratings. Electronics Letters 31.4, 1995, 309–310.
[43] Shi Ch.X.: Optical Bistability in Reflective Fiber Gratings. IEEE Journal of Quantum Electronics 31, 1995, 2037–2043.
[44] Takubo Y., Yamashita S.: High-speed dispersion-tuned wavelength-swept fiber laser using a reflective SOA and a chirped FBG. Optics express 21(4), 2013, 5130–5139.
[45] Tanaka N., Okabe Y., Takeda N.: Temperature-compensated strain measurement using fiber Bragg grating sensors embedded in composite laminates. Smart materials and structures 12(6), 2003, 940.
[46] Williams R.J., Voigtländerv C., Marshall G.D., Tünnermann A., Nolte S., Steel M.J., Withford M.J.: Pointby-point inscription of apodized fiber Bragg gratings. Opt. Lett. 36(15), 2011, 2988–2990.
[47] Yoffe G.W., Krug P.A., Ouellette F., Thorncraft D.A.: Passive temperature-compensating package for optical fiber gratings. Applied Optics 34(30), 1995, 6859–6861.
[48] Zhu HH., Yin JH., Zhang L., Jin W., Dong JH.: Monitoring internal displacements of a model dam using FBG sensing bars. Advances in Structural Engineering 13(2), 2010, 249–262.

M.Sc. Tomasz Zieliński
e-mail: tomasz.zielinski.1992@gmail.com

Graduated from the Faculty of Electrical Engineering at Lublin University of Technology. Received his Master of Science degree in 2016. Title of Thesis: The analysis of sensory platform for use in the Internet of Things. Areas of interest: IoT, mobile systems in mechatronics, mobile system, fiber Bragg grating.

D.Sc., Ph.D. Piotr Kisała
e-mail: p.kisala@pollub.pl

Piotr Kisała is currently a professor in the Department of Institute of Electronics and Information Technology of Lublin University of Technology (LUT), Lublin, Poland. In 1997, he received a diploma in Informatics and Computer Networks from the Maria Curie-Skłodowska University, Poland. He received the Ph.D. degree in 2009 and habilitation degree in 2013 from LUT. He is currently head of Optoelectronic & ICT Department at LUT. His research interests include optical sensors projects, fabrication and testing as well as designing and developing of unconventional FBG sensors. He has authored over 70 journal publications and conference contributions and 2 patents.

otrzymano/received: 23.09.2017 *przyjęto do druku/accepted:11.05.2018*

DOI: 10.5604/01.3001.0012.0715

A COMPARISON STUDY OF THE FEATURES OF DC/DC SYSTEMS WITH SI IGBT AND SIC MOSFET TRANSISTORS

Karol Fatyga, Łukasz Kwaśny, Bartłomiej Stefańczak
Lublin University of Technology, Faculty of Electrical Engineering and Computer Science, Department of Electrical Drives and Machines

Abstract. *This paper presents a comparison of the efficiency of two bidirectional DC/DC converters based on dual H-bridge topology. Tested converters were built using Si-based IGBT transistors and SiC-based MOSFETs. The results of the research are efficiency characteristics, taken from tests at the frequency range of 10÷60 kHz. Analysis of the results points to a massive advantage of the SiC-based design over the Si-based one.*

Keywords: IGBT, SiC, Transistor, MOSFET, DC/DC converter

BADANIA PORÓWNAWCZE SPRAWNOŚCI UKŁADÓW DC/DC Z TRANZYSTORAMI SI IGBT ORAZ TRANZYSTORAMI SIC TYPU MOSFET

Streszczenie. *W artykule zaprezentowano badania porównawcze sprawności dwóch dwukierunkowych przekształtników DC/DC wykonanych w topologii podwójnego mostka H. Badane przekształtniki wykonano w technologii krzemowej z tranzystorami IGBT oraz w technologii węglika krzemu z tranzystorami SiC MOSFET. Rezultatem badań są charakterystyki sprawności uzyskane z testów przy częstotliwości pracy w zakresie 10÷60 kHz. Analiza uzyskanych wyników wskazuje na zdecydowaną przewagę rozwiązania wykonanego w technologii węglika krzemu nad rozwiązaniem z tranzystorami krzemowymi IGBT.*

Słowa kluczowe: IGBT, SiC, Tranzystor, MOSFET, przekształtnik DC/DC

Introduction

Technological advancements, government actions and developer initiatives the during last few years resulted both in a massive boom in technology and an intensive interest in e-mobility. Both contact and contactless charging technologies are being developed or improved, along with more efficient energy storage devices. Advancements in semiconductor technology also help in developing new solutions in terms of energy supply and electric drives.

One of the most significant factors impeding development of e-mobility is the lack or shortage of electric vehicle charging infrastructure. Charging the vehicle, according to IEC-62196-1, assumes that galvanic isolation between the utility grid and an electric vehicle will be provided by using isolating elements. Using a grid-frequency transformer in a device with output power rated at 50 kW (fast-charging device) [2], will drastically increase both the size and production cost of the charging system. Because of this, high-frequency transformers are used and entire devices are built around them, creating high-frequency isolated DC/DC converters, which work in conjunction with AC/DC converters to deliver power to electric vehicle (Fig. 1) [4].

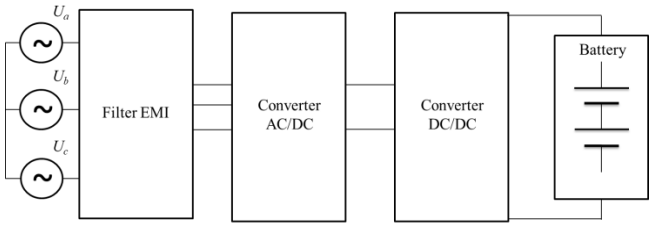

Fig. 1. Block diagram of the charging system

In isolated DC/DC converter systems, several different topologies are used, consisting of two to eight transistor switches [6], where eight-switch systems, so called dual active bridges (Fig. 2) [1] can achieve the highest power density and allow soft switching to be implemented into the system, further increasing its efficiency [7].

Systems using such topology also allow energy flow in both directions, which enables the use of an electric vehicle's battery as distributed energy storage, assuming that there are enough electric vehicles connected to chargers at any given time [3].

Using modern Silicon Carbide based semiconductors allows a further decrease in the size of DC/DC converters. This is caused by a wider bandgap, allowing transistor operation in higher frequency ranges. Since the frequency is increased, less magnetic materials and smaller capacitors are required for their proper operation. This reduces both the size and the cost of a DC/DC converter.

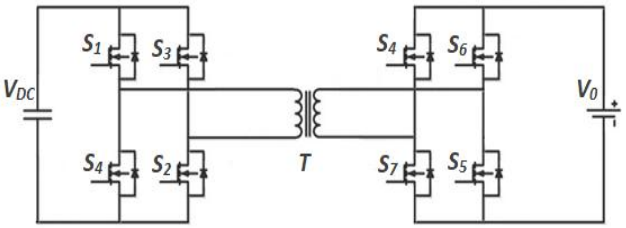

Fig. 2. Scheme of a DC/DC bidirectional converter

Using SiC semiconductor technology in fast charging systems is relatively new, because only for a few years have transistors been available that can withstand currents ranging from tens to hundreds of Amperes, while at the same time keeping high isolation voltage. Of course, since those devices are cutting-edge technology, their price is higher than IGBT Silicon semiconductors, and because of limited availability of SiC semiconductors, IGBTs will still be used for a long time before they get obsolete.

When choosing semiconductor technology for DC/DC converters it is important to know about the efficiency of both the technologies discussed. This paper presents their comparative laboratory tests. It consists of an introductory part, describing the topology and control scheme of the converter tested. Next, the main parameters of the tested converters are presented. The test results, their evaluation and analysis make the final and most important part, concluding the paper and suggesting an answer to the problem contained in the title.

1. Analysis of the operation of a DC/DC converter

To depict the operation of a bidirectional DC/DC converter, each conducting cycle are shown in Figure 3. Transistor driving signals as well as transformer voltage and current waveforms are presented in Figure 4. For clarity of discussion, the control scheme selection debate is skipped, and the paper is focusing on the efficiency of SiC-based and Si-based DC/DC converters.

High frequency DC/DC converters are usually frequency controlled or phase controlled, with a trend to implement switching transistors during a zero current period. This allows to achieve very high efficiency. The prototype laboratory system was

phase-controlled: the H-bridge driving the primary side was the active control element, while the H-bridge on the secondary side was used passively: transistor switches were all driven low, and only the diodes from the transistor modules were used as a passive Graetz rectifier (Fig. 3).

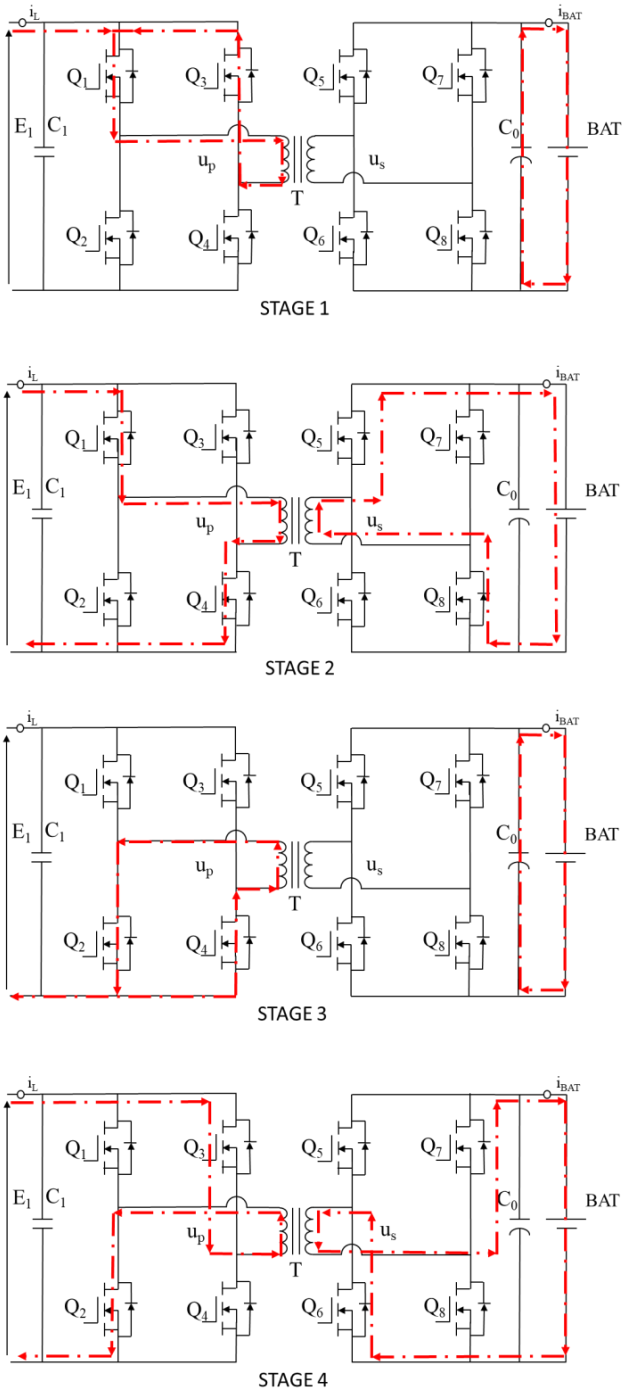

Fig. 3. Current flow through the transformer in subsequent stages of the operation

On the primary side, the H-bridge can be divided into a left half-bridge and a right half-bridge. The left half-bridge is responsible for shutting the energy transfer window, while the right one is responsible for opening it. Transistors in one half-bridge are driven with 50% fixed width pulse. The right half-bridge driving signals are phase-shifted in relation to the left half-bridge. At the first stage of the operation the transformer is connected to DC bus + through the Q1 and Q3 switches. At the second stage, the current flows through switch Q1, the transformer's primary winding, and switch Q4. During this stage the voltage across the transformer is $+V_{DC}$. In stage three the transformer is connected through the Q2 and Q4 switches to DC bus -. In stage 4 the current flows through Q3, the transformer's primary winding, and Q2. During this stage the voltage across the transformer is $-V_{DC}$. The current in stages two and four flows through the transformer's windings in opposite directions, creating an alternating high frequency current. By changing the phase-shift between the left and right half-bridge, it is possible to lengthen or shorten the transfer window, and therefore control how much energy is transferred through the transformer. The transistor driving signals, primary winding voltage and the current are presented in Figure 4.

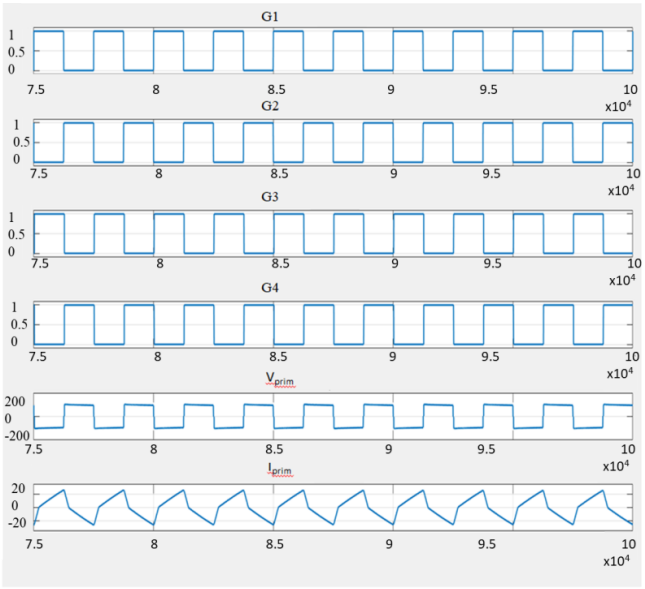

Fig. 4. Phase control of transistor inverters with voltage and current diagrams V_{prim} and I_{prim}

2. Prototype test systems

Laboratory tests were performed on DC/DC converters built on two types of transistors. One DC/DC converter was built on bipolar transistors with isolated gate (IGBT), using silicon semiconductors. The other DC/DC converter was based on Silicon Carbide MOSFET (Metal-Oxide Semiconductor Field-Effect Transistor) semiconductors. Two test systems were built, based on the structure presented in Figure 5.

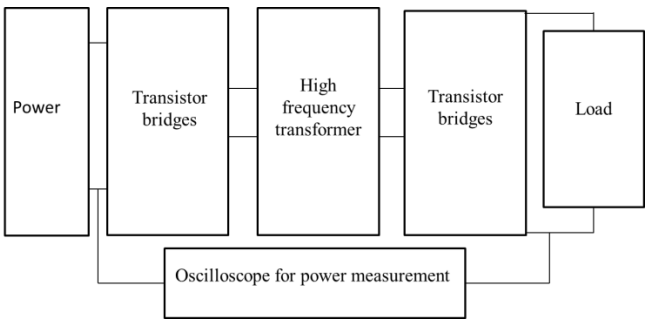

Fig. 5. Block diagram of the power measurement system

To perform tests with the IGBT-based converter, Mitsubishi CM200DX-24S modules were used. A single module consists of 2 transistors and can be used as a half-bridge. These modules have been in production since 2013. Their parameters are as follows: rated collector current $I_c = 200$ A, collector-emitter voltage $V_{ces} = 1200$ V and maximum junction operating temperature $T_{jmax} = 175$°C. According to the datasheet, the collector-emitter voltage drop is 2.25 V maximum. This defines power losses of 450 W while operating under maximum load. In the IGBT-based DC/DC converter, a single-phase transformer was used, with the rated power of $P_Z = 30$ kVA and the switching frequency of $f_z = 25$ kHz. The system is depicted in Figure 6.

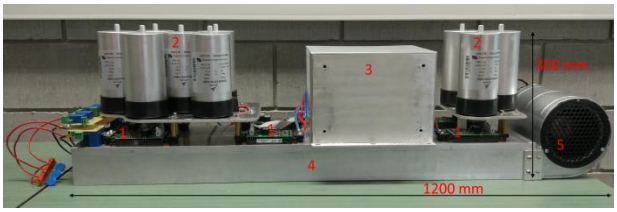

Fig. 6. Measurement system built of IGBT silicon transistors: 1 – transistors, 2 – condensers, 3 – transformer, 4 – heatsink, 5 – fan

Another type of transistor used for DC/DC converters was the Silicon Carbide based MOSFET transistor. For laboratory tests, Infineon FF11MR12W1M1_B11 transistors were used. These were introduced to the market in 2017. Their parameters: drain-source voltage V_{DDS} = 1200 V, drain current I_D = 100 A, operating temperature T_v = 150°C and drain-source junction resistance R_{DS} = 11 mΩ. To provide galvanic isolation a single-phase transformer was used, with the output power of 20 kVA and the nominal frequency of 100 kHz. The prototype is depicted in Figure 7.

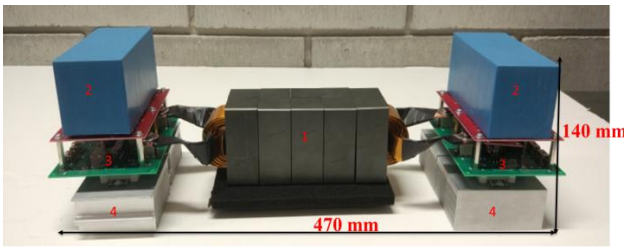

Fig. 7. Test system built of MOSFET SiC transistors: 1 – transformer, 2 – capacitors, 3 – transistor bridge, 4 – radiators

An important parameter during DC/DC converter efficiency testing are transistor switching losses. According to the datasheet, an IGBT transistor requires 30.07 mJ of energy to turn it on, and 21.5 mJ to turn it off. For comparison, SiC MOSFET requires 1.4 mJ to create a conduction channel, and 0.645 mJ to shut it down.

3. Analysis of the results

In order to perform results tests in as wide a frequency range as possible, and at the same time ensure safety of the equipment, the supply voltage for both systems was dropped to 165 V. The transformer's primary current was controlled by the controlling phase in the primary side H-bridge. Tests were performed for four different transistor switching frequencies: 10 kHz (Fig. 8), 20 kHz (Fig. 9), 40 kHz (Fig. 10) and 60 kHz (Fig. 11).

The characteristics were derived on the basis of measurements with a Yokogawa PX8000 oscilloscope.

It is clearly noticeable from the presented characteristics that SiC MOSFET based converters have a higher efficiency for every switching frequency. The IGBT-based converter achieved its peak efficiency at 10 kHz switching frequency, while the SiC MOSFET based converter achieved 95.87 efficiency at 20 kHz. Another matter is the shape of the characteristics: for smaller loads IGBT-based converter efficiency drops significantly. This effect is not so severe for the SiC MOSFET based design.

The reason for this are the switching losses. The cost of elements used for both devices needs to be taken into consideration. The cost of the IGBT transistor based design is significantly higher than the SiC MOSFET design. Despite using cheaper switches, well established on the semiconductor market, the cost of magnetic elements, additional capacitors or a massive radiator, which can dissipate power losses that turn into heat from transistors, makes the IGBT design more expensive than the SiC MOSFET system, which uses transistors that are a few times more expensive. Another matter is the size of the device. The SiC-based system is less than half the size of the IGBT-based system. The size difference is presented in Figure 12.

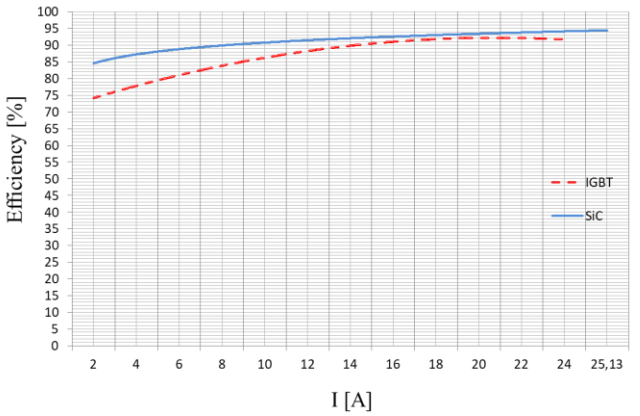

Fig. 8. Efficiency characteristics of Silicon IGBT and Silicon Carbide MOSFET for 10 kHz switching frequency

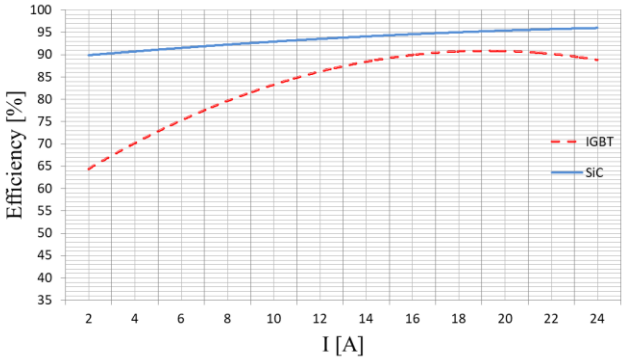

Fig. 9. Efficiency characteristics of Silicon IGBT and Silicon Carbide MOSFET for 20 kHz switching frequency

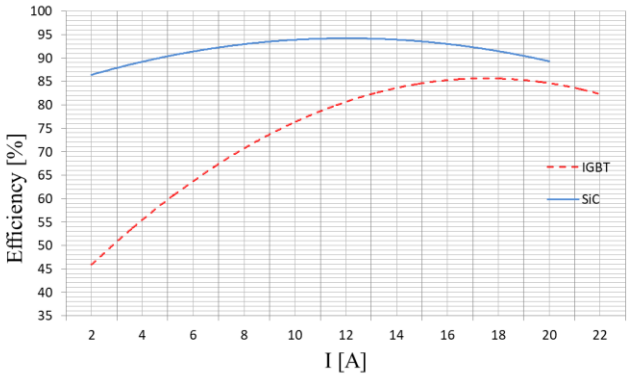

Fig. 10. Efficiency characteristics of Silicon IGBT and Silicon Carbide MOSFET for 40 kHz switching frequency

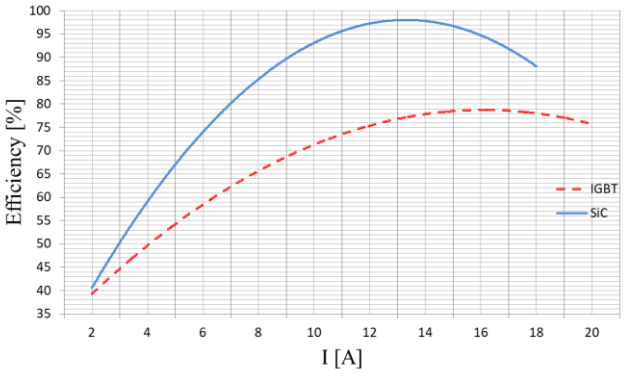

Fig. 11. Efficiency characteristics of Silicon IGBT and Silicon Carbide MOSFET for 60 kHz switching frequency

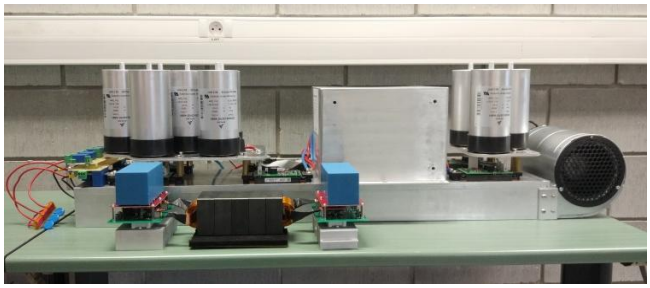

Fig. 12. Photograph of both the SiC MOSFET and Si IGBT converter – comparison of sizes

Thanks to the MOSFET properties and the Silicon Carbide technology it was possible to reduce the radiator size. The ability to switch transistors at 100 kHz frequency allowed to significantly reduce the magnetic elements.

In summary, DC/DC converters made with silicon carbide semiconductor technology have a significant advantage over their IGBT silicon based counterparts. Their most significant features are small size, greater energy density and lower switching losses. This gives them a great potential and makes them a good alternative to IGBT converters in high-power systems.

Bibliography

[1] Barlik R., Nowak M., Grzejszczak P.: Power transfer analysis in a single phase dual active bridge. Bulletin of the Polish Academy of Sciences, Technical Sciences 61(4), 809–828.

[2] Dobrzański D.: Overview and characteristics of the EV fast charging connector systems. Maszyny Elektryczne: Zeszyty problemowe 3/2017, 91–96.

[3] Fatyga K., Mroczek B.: Charakterystyki pracy dwukierunkowej przetwornicy DC/DC do pojazdów elektrycznych i architektura jej komunikacji w systemie operatora sieci elektroenergetycznej. Maszyny Elektryczne: Zeszyty problemowe 3/2017 83-89.

[4] Inoue S., Akagi H.: A bi-directional isolated DC/DC converter as a core circuit of the next-generation medium-voltage power conversion system. 37th IEEE Power Electronics Specialists Conference – Jeju, 2006, 1–7.

[5] Zdanowski M., Rąbkowski J., Barlik R.: Design issues of the high-frequency interleaved DC/DC boost converter with Silicon Carbide MOSFETs. 16th European Conference on Power Electronics and Applications, 2014.

[6] Zhao B., Song Q., Liu W., Sun Y.: Overview of Dual-Active-Bridge Isolated Bidirectional DC–DC Converter for High-Frequency-Link Power-Conversion System. IEEE Transactions on Power Electronics 29(8), 4091–4106.

[7] Zieliński D., Tokovarov M.: Simulation and comparison of selected fast charger topologies. Informatyka, Automatyka, Pomiary w Gospodarce i Ochronie Środowiska – IAPGOŚ 3/2017, 23-28.

M.Sc. Eng. Karol Fatyga
e-mail: k.fatyga@pollub.pl

Graduated from the Faculty of Electrical Engineering and Computer Science of the Lublin University of Technology in 2016. Since then also employed as assistant lecturer at the university's Department of Electrical Drives and Machines. His research focuses on power converters, specifically on electric vehicle chargers and converters for coupling utility grid with energy storage. He is a member of the team working on NCBiR (National Centre for Research and Development) projects.

M.Sc. Eng. Łukasz Kwaśny
e-mail: l.kwasny@pollub.pl

Graduated from the Faculty of Electrical Engineering and Computer Science of the Lublin University of Technology. Since 2016 employed at the Department of Electrical Drives and Machines there. His work revolves around simulation, design and assembly of power converters used in cooperation with renewable energy sources, and electric vehicle charging stations. He is a member of the team working on NCBiR (National Centre for Research and Development) projects.

B. Eng. Bartlomiej Stefańczak
e-mail: bartlomiej.stefanczak@pollub.edu.pl

Undergraduate of the Lublin University of Technology with a Bachelor's degree in Engineering in Mechatronics. Currently pursuing his career by working for a Master's Degree at the Faculty of Electrical Engineering and Computer Science. He is employed in NCBiR (National Centre for Research and Development) funded projects undertaken at the university's Department of Electrical Drives and Machines. His interests combine power electronics and computer science. In his limited leisure time he is an active tennis player and swimmer.

otrzymano/received: 11.04.2018 *przyjęto do druku/accepted: 11.05.2018*

DOI: 10.5604/01.3001.0012.0716

PROPOSAL FOR MANAGING ELECTRIC ENERGY QUALITY IN THE LV GRID USING ON-LOAD TAP CHANGER WITH A STATIC SYNCHRONOUS COMPENSATOR

Bartłomiej Mroczek, Karol Fatyga
Lublin University of Technology, Faculty of Electrical Engineering and Computer Science, Department of Electrical Drives and Machines

Abstract. *The paper proposes the use of auxiliary equipment in the low voltage network: an on-load tap changer and a static synchronous compensator (STATCOM) to improve the quality of energy supply to end users. As part of the research, a section of medium and low voltage power grid was modelled using Matlab & Simulink software, which was tested in three scenarios. The first scenario presents the operation of the power grid with the on-load tap changer installed in the transformer block. The second scenario uses the STATCOM for local reactive power compensation. Additionally, the third scenario is the combined work of the on-load tap-changer along with the STATCOM. According to the authors, the method discussed does not bring the expected results in the area of voltage quality improvement, indicating that further research is required, including tests with energy storage.*

Keywords: On-Load Tap Changer (OLTC), Static Synchronous Compensator (STATCOM), energy quality

PROPOZYCJA ZARZĄDZANIA JAKOŚCIĄ NAPIĘCIA Z WYKORZYSTANIEM PODOBCIĄŻENIOWEGO PRZEŁĄCZNIKA ZACZEPÓW TRANSFORMATORA I KOMPENSATORA STATCOM

Streszczenie. *W artykule zaproponowano zastosowanie pomocniczych urządzeń w sieci niskiego napięcia: podobciążeniowego przełącznika zaczepów oraz kompensatora mocy biernej (STATCOM) w celu poprawy jakości energii dla odbiorców końcowych. Zamodelowano fragment sieci elektroenergetycznej średniego i niskiego napięcia za pomocą oprogramowania Matlab & Simulink, który został poddany badaniu w ramach trzech scenariuszy. Pierwszy scenariusz prezentuje pracę sieci elektroenergetycznej z podobciążeniowym przełącznikiem zaczepów zainstalowanym w kadzi transformatora. Drugi scenariusz wykorzystuje STATCOM do lokalnej kompensacji mocy biernej. Natomiast trzeci scenariusz jest to jednoczesna praca podobciążeniowego przełącznika zaczepów wraz ze STATCOM. Zaprezentowany sposób według autorów nie przyniósł oczekiwanych rezultatów w zakresie poprawy jakości napięcia i wskazuje na dalszą potrzebę badawczą z wykorzystaniem magazynów energii.*

Słowa kluczowe: podobciążeniowy przełącznik zaczepów transformatora, STATCOM, jakość energii

Introduction

Due to disturbances caused by dissymmetric operation, short circuits, or power shortages, the quality of energy supplied from utility grid can be disturbed. The utility grid operator simply cannot guarantee the quality of energy supply. For example, the utility grid cannot provide enough energy in the case of a voltage drop. This may cause disturbances in the operation of the device on the end user side. In severe cases, it can cause unpredicted shutdowns and stops – actions that are not welcome especially in industry. Additionally, when a local electrical installation is equipped with an undervoltage safety system, it creates a local shutdown for all the devices supplied from that grid.

A phenomenon described as a rapid voltage reduction dropping below the set threshold value in no shorter time than 10 ms and ending by voltage returning back to normal is called a voltage sag [9]. Two types of incidents can cause a voltage sag to occur. The first of them are short circuits in the utility grid, when there is a rapid impedance drop, and as a consequence the grid current rises up to the short circuit current value. The other type is events connected with starting industrial processes, which require large starting power – and large inrush currents. During these processes the grid load changes dynamically along with the impedance of the receivers [4].

In practice, counteracting voltage sags or, to be more precise, handling their consequences is based on using additional devices, which aim to keep the voltage in the range of ±10% of the rated grid voltage. The choice of the devices, as well as their location, have a direct impact on the final effect of voltage regulation and the improvement of energy quality. Moreover, the choice of the device type, according to its ability to store energy, can influence the reduction of voltage sag consequences, and even protect from energy shortages [16].

1. Influence of the load profile change on energy quality

In Europe, grid management and development is beginning to drift towards so called "smart grid" solutions, and control of energy quality in real time [2]. Energy supply quality at user connection point is a service quality indicator, and according to § 38 act 3. p 2 of regulation [5], every week at least 95% of 10-minute average RMS voltage values has to fall between ±10% of the rated grid voltage for connection groups III-V.

The occurrence of short voltage sags that are allowed by the cited regulation is inconvenient for end users. Because of that, it is advisable to use devices that reduce the impact of short voltage sags on end users.

Power demand during the day is not constant. It is influenced by the time of day, season of the year and current end-user demands. Because of that, temporary, or constant energy demand that is higher than the one for which the grid was designed causes a drop in the quality of energy supply that exceeds the limit permissible in the regulation [14].

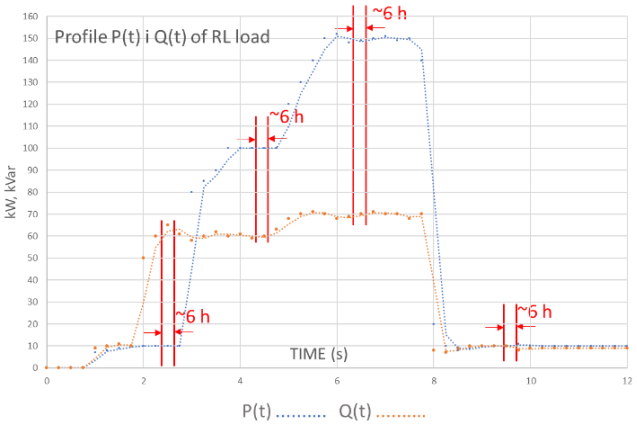

Fig. 1. Active power profile P (navy blue) and reactive Q (orange) for the tested part of the distribution network (LV line, load)

In order to create temporary voltage values in the chosen utility grid points, the end-user group profile was defined for both active power *P* and reactive power *Q*, which is shown in Figure 1.

The existing connection system of the distribution network for both the medium voltage (MV) and low voltage (LV) can be modelled as a simplified circuit, shown in Figure 2.

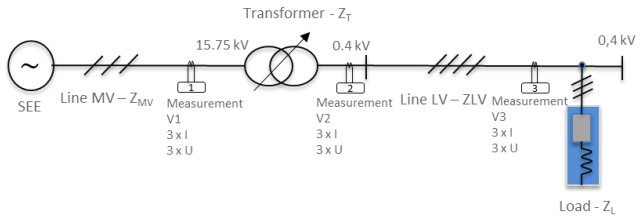

Fig. 2. Schematic diagram of part of the distribution network, where: SEE – power system, Z_{MV} – MV line impedance, Z_{LV} – LV line impedance, Z_T – transformer impedance, Z_L – load impedance, V1 – voltage side of the primary side of the transformer, V2 – voltage secondary side measurement of the transformer, V3 – voltage measurement at the receiving energy

The impedance of the exemplary distribution network fragment was derived separately for an MV line, an MV/LV transformer, an LV line and a load with RL characteristics.

Table 1. Nominal data of the MV and LV fragment of the power grid

Power network parameters	Value
Frequency	50 Hz
Voltage phase to phase MV	15 kV
Type of wire MV	AFL 3 × 70 mm^2
Length of the MV line	10 km
St – power of transformer	100 kVA
P_{Fe} – non-load loss	199 W
P_{cu} – load loss	1920 W
U_z – short-circuit voltage	4%
Transformer ratio	GN:15,75 DN:0,4 ±10 %
Connection system	Dyn5
Type of the LV wire	AFL 4 × 35 mm^2
L of the LV line	1,5 km
Active and Reactive Power RL Load	P = 150 kW, Q = 60 kVar

To simplify the control algorithm for both active and reactive power, a transformation from stationary into rotating orthogonal reference frame *dq* occurs. The definition of voltage vector V_s in a synchronously rotating reference frame is:

$$\underline{V_S} = V_d + j\,V_q = (V_\alpha + j\,V_\beta)\,e^{-j\omega t} \quad (1)$$

where: V_d – active component in the *dq* frame, V_q – reactive component in the *dq* frame, V_α – voltage component in the *αβ frame*, V_β – voltage component in *αβ*, ω – grid angular frequency.

Using the Clarke transform, three phase signals (U_a, U_b, U_c) are transformed into a 2-phase orthogonal stationary frame *αβ*:

$$V_\alpha + j\,V_\beta = \frac{2}{3}\left(U_a + U_b\,e^{\frac{j2\pi}{3}} + U_c\,e^{\frac{-j2\pi}{3}}\right) \quad (2)$$

Next, using the Park transform, 2-phase signals are transformed from stationary frame *αβ* into rotating reference frame *dq*. *The* Vd, Vq signals can be defined as:

$$\begin{bmatrix} V_d \\ V_q \end{bmatrix} = \frac{2}{3}\begin{bmatrix} \sin(\omega t) & \sin\left(\omega t - \frac{2\pi}{3}\right) & \sin\left(\omega t + \frac{2\pi}{3}\right) \\ \cos(\omega t) & \cos\left(\omega t - \frac{2\pi}{3}\right) & \cos\left(\omega t + \frac{2\pi}{3}\right) \end{bmatrix} \times \begin{bmatrix} U_a \\ U_b \\ U_c \end{bmatrix} \quad (3)$$

This transform allows changing from a stationary three-phase reference frame into a rotating orthogonal reference frame on the *dq* plane [17].

Based on grid parameters presented in Table 1, voltage waveforms in points *V1* (Fig. 3), *V2* (Fig. 4), *V3* (Fig. 5) were derived.

They represent relational voltage values in synchronously rotating reference frame dq, related to the rated voltage of the primary and secondary side of the transformer.

First, exemplary voltage waveforms *V*d and *V*q for the primary side of the transformer – *V*1, with simulated load profile change is presented (Fig. 3).

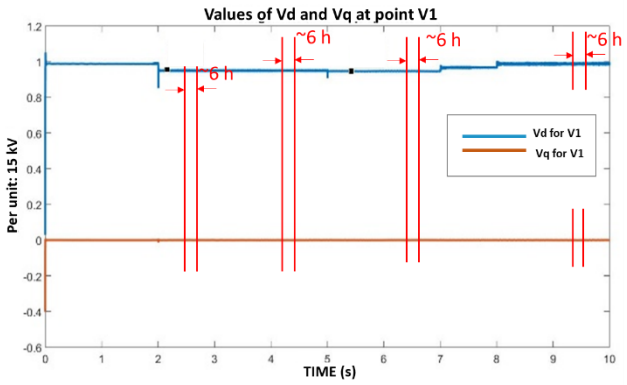

Fig. 3. Values of V_d and V_q at point V1

The voltage drop that can be observed between t = 2 s to t = 8 s is caused by the load profile change according to assumptions from Figure 1. It is still in the range of ±10% of the grid's rated voltage. The null value of component V_q=0 shows full synchronization with the grid on the medium voltage side of the transformer.

For exactly the same disturbance, the voltage in the V2 measurement point behaves similarly. The V_d and V_q component values are presented in Figure 4.

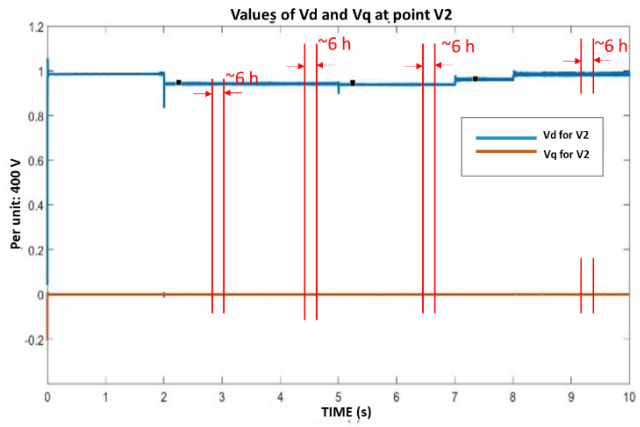

Fig. 4. Values of Vd and Vq at point V2

Just as in the case of measurement point *V*1, a change of load profile in point *V*2 did not cause voltage sags exceeding the threshold of ±10% of the rated grid voltage.

The situation changes when we consider the influence of the load profile change in measurement point *V*3 (Fig. 5).

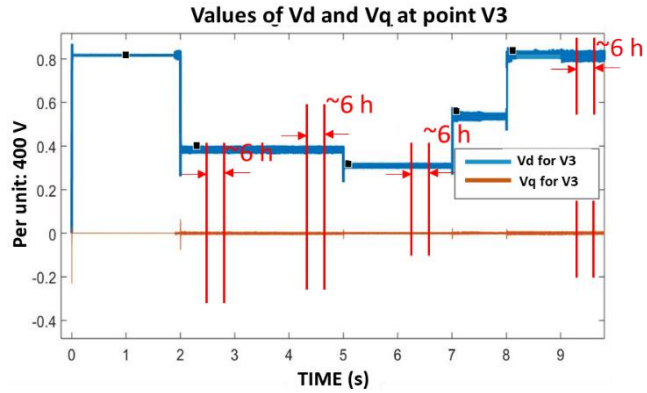

Fig. 5. Values of V_d and V_q at point V3

In *V*3 measurement point, being the closest to the distribution grid load, a large voltage sag can be observed, which exceeds the allowable ±10% of the rated grid voltage. This is connected to end users exceeding their load profiles *P* and *Q*.

Taking these results into account, consideration of the quality of energy supply in MV and LV distribution grids, as well as the strategy of its management, has to be connected with deep analysis of several grid measurement points. It has to be pointed out that a load profile change is followed by voltage drops in impedance elements, and the farther the load is from the supply, the larger the voltage sag. From this, a scientific problem arises, consisting in the need to judge technological decisions and point in the direction of strategy development for energy quality in low voltage grids [6].

2. Energy quality improvement solution analysis

The proposed solution for the scientific problem defined in the previous section is equipping the utility grid presented in Figure 2 with additional devices that greatly improve energy quality in the low voltage grid. The first device is the On-Load Tap Changer (OLTC) [3], the other is the Static Synchronous Compensator (STATCOM) [12]. To control the operation of these devices a central control unit AVC (Automatic Voltage Control) is needed, which acts as an automated system for voltage management in a low voltage grid LV [5]. The idea of implementing additional equipment into the grid is presented in Figure 6.

Using an On-Load Tap Changer aims to apply step compensation of voltage sags in MV line – *V*1, and on transformer impedance – *V*2. The task assigned for the STATCOM is reactive current compensation in a grid fragment that is monitored at the *V*3 measurement point.

For the operating grid, a suitable reaction, and as a consequence voltage regulation in each of the points *V*1, *V*2, *V*3, is of paramount importance. Using both the OLTC and STATCOM in same grid fragment requires developing rules and conditions for their independent or cooperative operation. In a fully developed solution, these should be implemented into the main controller AVC.

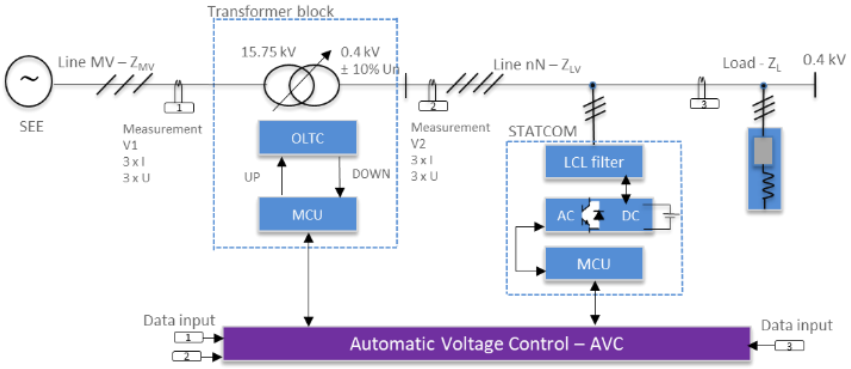

Fig. 6. Schematic diagram of part of the distribution network with OLTC and STATCOM, where: OLTC – on-load tap changer, MCU – microcontroller, AC/DC – power inverter

2.1. Operating conditions of the On-Load Tap Changer

A commonly used device in the distribution grid is a transformer equipped with tap changers that are placed in the transformer tank [8]. These allow to change voltage on the secondary side of the transformer. Due to lower current values, a tap changer is installed on the primary side of the transformer. The tap-changer position switch changes the number of turns on the primary side of the transformer, which – combined with the constant number of turns on the secondary side – causes change in the transformer ratio. This enables control of the secondary side voltage by changing the primary side voltage in the range of $\pm U_N$ % of the rated grid voltage. Currently, two types of tap changers are used: off-load tap changers, used only in no voltage states of the transformer – these are commonly found in distribution stations [8], or on-load tap changers, which allow turn change without any power breaks [7]. The control mechanism, which is responsible for changing transformer taps is implemented into a MCU microcontroller, and operates in real time, based on voltage value on the low-voltage side. The microcontroller acts on the transformer by using a tap selector with transition resistors. To ensure proper voltage regulation on the secondary side of the transformer, four conditions for OLTC switching were defined as follows:

Condition 1: Tap-changer position switch:

$$n = n_0 + \Delta n\, f(z_n) \tag{4}$$

where: z_n – OLTC work interval range between states, n – state of the OLTC, n_0 – nominal position of the OLTC.

The above condition has additional mechanical restrictions of the number of n positions, bound to the transformer construction and regulation needs. The description of the OLTC's condition 1 is:

$$OLTC.1(n_n) = \begin{Bmatrix} TAP\ 1\ UP,\ if:\ \frac{U_N}{n_n} < U_{current\ value} \\ TAP\ n_0,\ if:\ U_N = U_{current\ value} \\ TAP\ 1\ DOWN, if:\ \frac{U_N}{n_n} > U_{current\ value} \end{Bmatrix} \tag{5}$$

where: U_N – the nominal value for a given voltage level.

Condition 1 is the base algorithm for the state space machine allowing the voltage control mechanism to operate properly over time.

Condition 2: The limit of position changes as a method to prolong the tap changer's lifecycle:

$$OLTC.2 = \sum_k k_{OLTC2} \le k_p \tag{6}$$

where: $k_p(t)$ – the number of switching cycles (0 : +∞) in time t, $k_{OLTC2}(t)$ – the number of switching cycles that the OLTC performed at t time.

Condition 2 is an algorithm that reduces mechanical wear and prolongs the OLTC's lifecycle.

Condition 3: Time limit, state space machine lock.

$$OLTC.3(n_n, T_0) = \begin{Bmatrix} TAP\ 1\ UP, if:\ \frac{U_N}{n_n} < U_{current\ value}\ i\ T_0 \ge 1 \\ TAP\ n_0, if: U_N = U_{current\ value}\ i\ T_0 \ge 1 \\ TAP\ 1\ DOWN, if:\ \frac{U_N}{n_n} > U_{current\ value}\ i\ T_0 \ge 1 \end{Bmatrix} \tag{7}$$

where: T_0 – blocking time of the OLTC <0 : +∞).

Condition 3 aims to reduce so-called hazard states [1], where due to different reaction times, in certain points of the distribution grid, contradicting or doubling decisions can be made. This condition was proposed due to cooperation with the STATCOM, whose reaction time is measured in milliseconds.

Condition 4: OLTC limitation due to voltage fluctuation caused by the load profile change of quick active power P or reactive power Q:

$$OLTC.4 = \sum_{T_n}^{n_n} k_{OLTC1} \le k_n(T_n) \tag{8}$$

where: T_n – time in which the number of repetitions of a given position of the tap-changer is measured n [s], $k_n(T_n)$ – set point of repetitions in time T_n, k_{OLTC1} – number of OLTC positions (counted separately for each position of tap) according to condition no. 1

AVC – controller managing the grid voltage, measuring the number of repeating tap changer positions in set time *t*. Due to the protection of mechanical parts of the OLTC and the device's reaction time, the AVC locks the states of repeating fluctuation of the tap changer.

2.2. Operating conditions of the STATCOM system

The Static Synchronous Compensator (STATCOM) is a step forward from the device known in the literature as VAR-Compensator. The STATCOM is based on power electronics, built by using fully controlled IGBT or MOSFET switches. The task of the STACOM compensator is reactive power compensation on a local scale.

To present a mathematical model of the STATCOM, the Clarke and Park transforms were used [11]. These allowed to transform input voltages from a three-phase stationary reference frame into the orthogonal rotating reference frame *dq*.

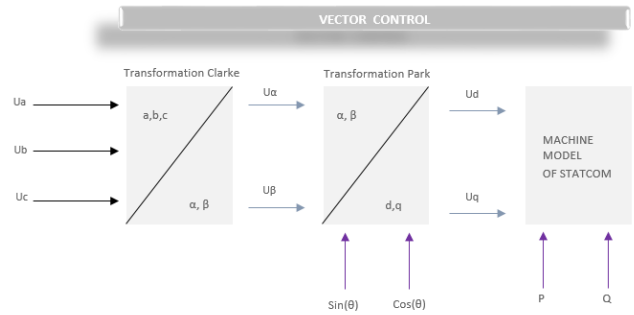

Fig. 7. The Clarke and Park transformation mechanism, where the angle θ is the angle of synchronization with the power grid

The Clarke and Park mathematical transforms, described with equations (2) and (3), as well as depicted in Figure 7, allow the calculation of an instantaneous voltage positive component in the *dq* reference frame.

An assumption was made that U_a, U_b and U_c are sampled in the grid, and as a result, discrete waveforms are used in the calculations. These are used in the transformation to the rotating reference frame *dq*. This mechanism is applied in the STATCOM or Energy Storage solutions. In the case of the STATCOM device, additional current vector control is required. It is controlled as follows:

$$I_d^{ref} = 0 \tag{9}$$

The active current component I_d^{ref} in the STATCOM systems is always equal to zero. The passive component is defined as:

$$I_q^{ref} = k_p\left(1 + \frac{1}{sT_i}\right)(Q - \left(\frac{1}{\sqrt{3}}\right)(U_{ab}i_c + U_{bc}i_a + U_{ca}i_b) \tag{10}$$

where: k_p – the proportional gain factor, T_i – integral time.

Using equation (10), voltage control vectors are calculated for the STATCOM output:

$$V'd = 0 \tag{11}$$

$$V'q = V_q + \left(i^{ref}{}_q - i_q\right)\left(k_p + \frac{k_p}{sT_i}\right) + i_d\omega L \tag{12}$$

The STATCOM operation can be divided into two stages. In the first stage, the device synchronises with the utility grid, calculating vectors V_d and V_q [10]. Next, the converter is started up. Its reference values are calculated on the basis of vectors V_d and V_q and measured I_d and I_q currents. These values are then transformed using the Park transform, and converted into PWM control signals by an SVM modulator. The conversion mechanism is shown in Figure 8.

Using the Clarke and Park transforms described above, and controlling the reactive power value Q, it is possible to achieve the reactive component of the current for a low voltage grid fragment [15].

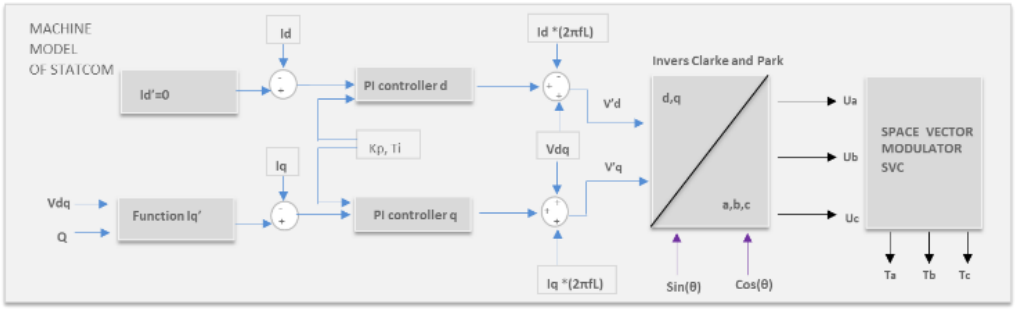

Fig. 8. The STATCOM work mechanism

3. Schematic diagram of the grid model

In order to perform the research, a distribution grid fragment (only the low voltage part) presented in Figure 6 was modelled as a simplified circuit. This will allow to define the initial conditions and evaluate the final results.

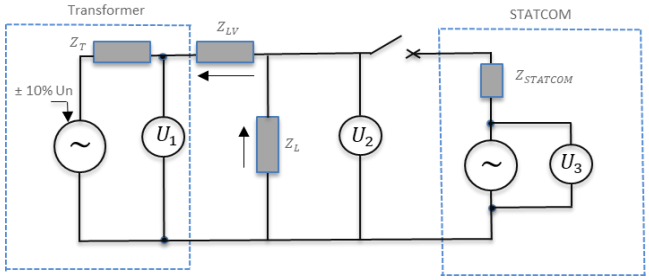

Fig. 9. Schematic diagram of part of the distribution network with the OLTC and STATCOM, where: U_1 – measurement of the secondary side voltage of the transformer, U_2 – voltage value at the RL load point, U_3 – voltage value at the STATCOM connection point, Z_T – transformer impedance, Z_L – load impedance, Z_{LV} – LV line impedance, $Z_{STATCOM}$ – STATCOM own impedance

Research, based on grid equipment, will be performed for two test cases:

The grid fragment works with a nominal voltage value – U_N, then:
$U_1 = U_N$
$U_2 \approx U_N$
$U_3 = 0$;

the grid fragment works out of the nominal voltage range – U_N, because Z_0 has a strong inductive characteristic, then:
$U_1 < U_N$
$U_2 \approx U_3 \rightarrow f(Q^+)$
$U_3 \approx U_1$.

Additionally, an important matter is deriving the set value Q for the grid, which will then be used to calculate the value *V'*q. The Q value is calculated on the basis of on equation:

$$S(Q) = \frac{(U_1 - U_2)^2}{Z_T + Z_{LV} + Z_L + Z_{STATCOM}} \times jsin\varphi \tag{13}$$

where: φ – the phase of the signal source voltage U_1 relative to the source U_2.

3.1. Model and test scenarios

The research carried out was based on the Matlab & Simulink software, most of it based on Simscape: Power Systems library. These tools allow simulation of electric grid dynamics [13]. A model of the grid fragment is presented in Figure 10.

The basic initial conditions and simulation parameters are presented in Table 2.

Three scenarios were designed during the research, which should be sufficient to provide the answer regarding the strategy choices of voltage control using the OLTC and STATCOM. The starting point for the test are the V_d and V_q (Fig. 4 & 5) values when there is no additional control. In each scenario, the same load profile was used, as depicted in Figure 1.

Three sets of simulations were carried out, where:

I – active OLTC only;
II – active STATCOM only;
III – active OLTC and active STATCOM.

Table 2. Simulation parameter data

Simulation parameters	Value
Simulation step	1e-5 s
Simulation time	10 s
Filter STATCOM - L	0.0012 H
Filter STATCOM - C	0.2 mF
$Q_{STATCOM}$	-10e3 Var
z_n	2.5 %

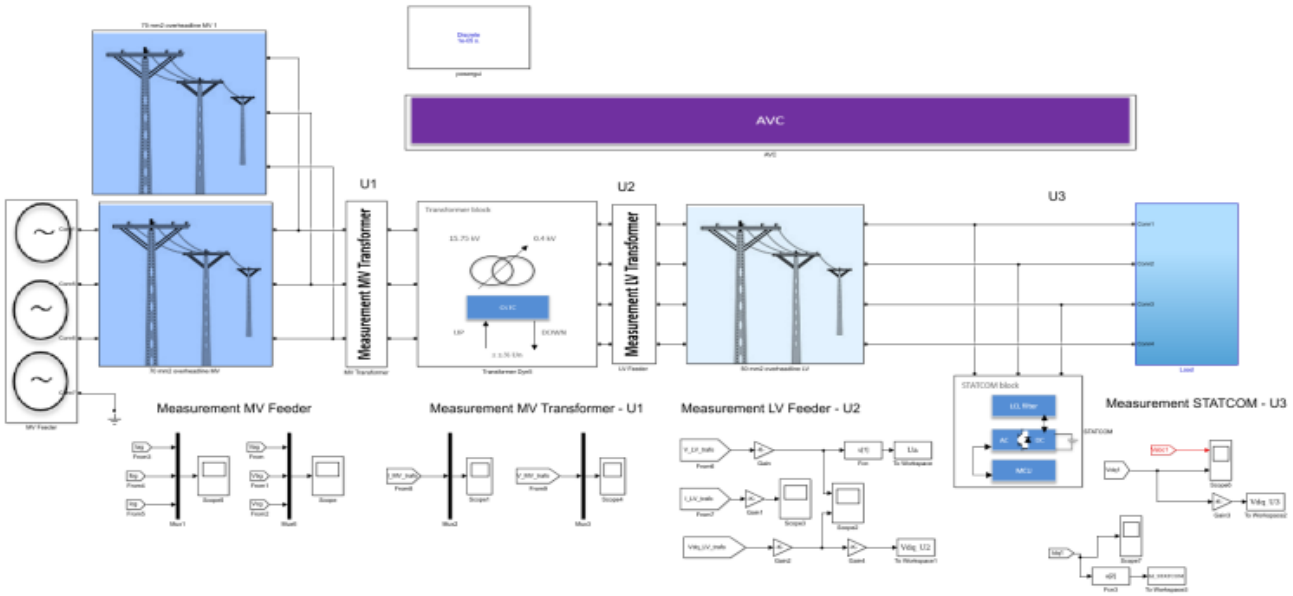

Fig. 10. Model of the OLTC and STATCOM grid in Matlab & Simulink

3.2. Test results

In terms of the V_d and V_q result presentation for each scenario, these values are presented in relation to the rated voltage of 400 V. To present rapid impedance change, and voltage drop on impedance elements, the grid is overloaded on the MV side with active power P = 20 kW, and on the LV side according to the graph in Figure 1.

Scenario 1. Simulation results in point V2:

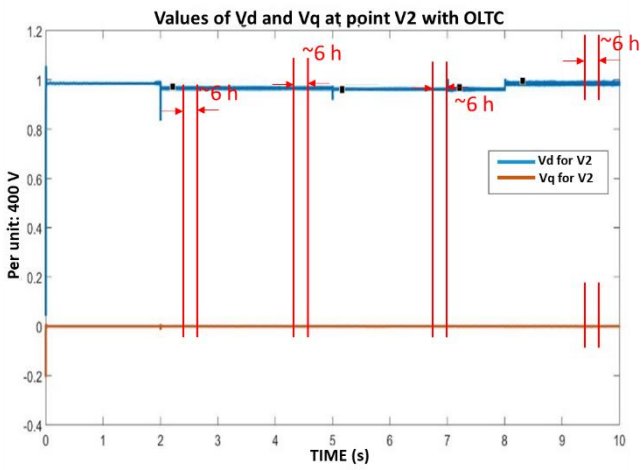

Fig. 11. Values of V_d and V_q at point V2 with OLTC, scenario 1

The voltage value V_d related to the base value was improved by about 1.5%. V_d is in the admissible range of voltage quality.

Scenario 1. Simulation results in point V3:

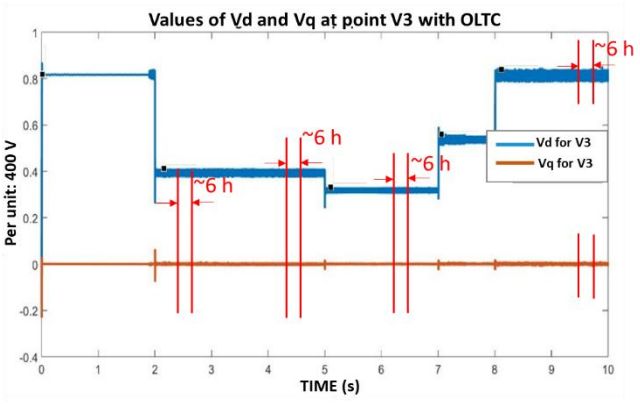

Fig. 12. Values of V_d and V_q at point V3 with OLTC, scenario 1

The voltage value V_d in relation to the base value was improved by 2.7%. The V_d values are not in the admissible range of voltage quality.

The simulation performed shows that using the OLTC increases the voltage value on the secondary side of the transformer, even in the case of the loading grid on both the MV and LV sides. However, using the OLTC does not improve the voltage value at load point.

Scenario 2. Simulation results in point V2:

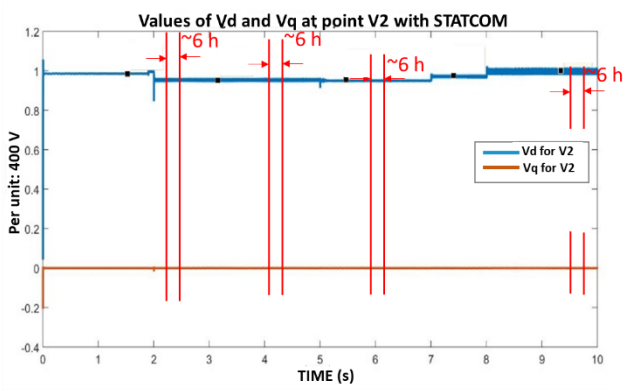

Fig. 13. Values of V_d and V_q at point V2 with STATCOM, scenario 2

Voltage value V_d related to base value was improved by about 1%. V_d are in admissible range of voltage quality.

Scenario 2. Simulation results in point V3:

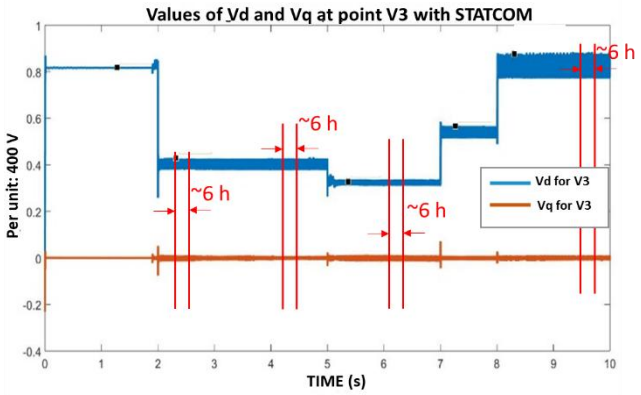

Fig. 14. Values of V_d and V_q at point V3 with STATCOM, scenario 2

The voltage value V_d in relation to the base value was improved by 7.5%. The V_d values are not in the admissible range of voltage quality. The inductive character of the load was compensated.

The simulation performed shows that using the STATCOM increases voltage values, even in the case of loading the grid on both the MV and LV sides. However, using the STATCOM does not raise the voltage value at load point for RL type loads with the coefficient cos φ > 0.85.

Scenario 3. Simulation results in point V2:

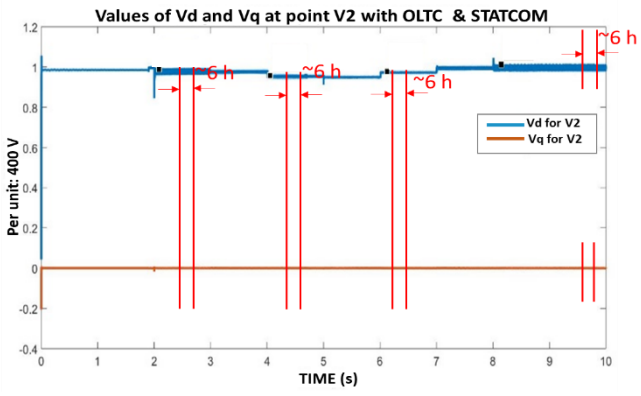

Fig. 15. Values of V_d and V_q at point V2 with OLTC & STATCOM, scenario 3

The voltage value V_d in relation to the base value was improved by 2.6%. The V_d values are not in the admissible range of voltage quality.

Scenario 3. Simulation results in point V3:

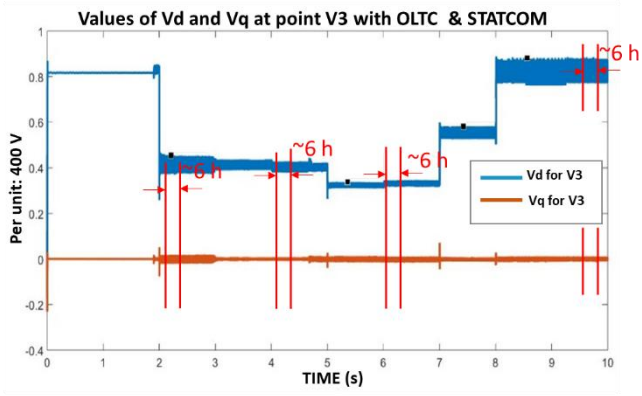

Fig. 16. Values of V_d and V_q at point V3 with OLTC & STATCOM, scenario 3

The value of the V_d voltage in relation to the base value improved temporarily by around 12.5%. The inductive character of the line and reception was compensated. The OLTC raised the voltage value on the secondary side. The V_d values are not within the permissible voltage quality range.

4. Summary

The choice of the voltage control strategy in the LV grid is dependent on a few initial conditions. First, the active power P and reactive power Q load profile has to have a regulating potential (reactive power reduction). Otherwise, using either the OLTC or STATCOM is unreliable. Next, the depth of the voltage sag and its time needs to be repeatable over a prolonged period and to have a significant impact on the voltage quality. Another thing is that specific conditions need to be established, for example tap switching limitations in a set amount of time t and so on.

Simulation of the OLTC and STATCOM operation on the selected and modelled grid fragment shows limited abilities of active and reactive power transfers using a cable with set cross-section. There should exist an option to control inductive reactive power (resistance systems will not be controlled in the passive part). The management strategy should be based on power electronic devices. It is recommended that those devices are located deep in the grid – close to the isolated fragments, where voltage changes are more significant. Moreover, power electronic devices should first work as voltage regulation devices, and then only with the OLTC. The cases analysed show a need for further research which would include additional devices such as local energy storage. It would then be possible to compensate voltage sags in the LV grid by injecting the active component of current I_d at connection point.

Bibliography

[1] Arif M. A., Ndoye M., Murphy G. V., Kennedy A.: A cooperative game theory algorithm for distributed reactive power reserve optimization and voltage profile improvement. 2017 North American Power Symposium (NAPS), Morgantown 2017, 1-6 [DOI: 10.1109/NAPS.2017.8107250].

[2] Benysek G., Kaźmierkowski M., Popczyk J.: Power electronic systems as a crucial part of Smart Grid infrastructure – a survey. Bulletin of the Polish Academy of Sciences, Technical Sciences 4/2011, 455–473 [DOI:10.2478/v10175-011-0058-2].

[3] Bettanin A., Coppo M., Savio A., Turri R.: Voltage management strategies for low voltage networks supplied through phase-decoupled on-load-tap-changer transformers. 2017 AEIT International Annual Conference, Cagliari, 2017, 1–6 [DOI: 10.23919/AEIT.2017.8240492].

[4] Bobrowska-Rafał M., Krzysztof R., Kaźmierkowski M.: Zapady napięcia – kompensacja przy zastosowaniu urządzeń energoelektronicznych typu FACTS. Elektroenergetyka: Współczesność i Rozwój 7/2012, 49–65.

[5] Borase P. B., Akolkar S. M.: Energy management system for microgrid with power quality improvement. 2017 International conference on Microelectronic Devices, Circuits and Systems (ICMDCS), Vellore, 2017, 1–6 [DOI: 10.1109/ICMDCS.2017.8211710].
[6] Cieślik S.: Analiza symulacyjna strat mocy czynnej w elektroenergetycznej sieci niskiego napięcia z mikroinstalacjami z podobciążeniową regulacją napięcia. Poznan University of Technology Academic Journals. Electrical Engineering 82/2015, 101–111.
[7] Deng J., Zhang G., Geng Y., Wang J.: Design of intelligent on-load tap changer controlled by permanent magnetic actuator. 2017 1st International Conference on Electrical Materials and Power Equipment (ICEMPE), Xi'an, 2017, 270–274 [DOI: 10.1109/ICEMPE.2017.7982082].
[8] Gao C., Redfern M. A.: A review of voltage control techniques of networks with distributed generations using On-Load Tap Changer transformers 45th International Universities Power Engineering Conference UPEC2010, Cardiff, Wales, 2010, 1–6.
[9] Hanzelka Z.: Zapady napięcia i krótkie przerwy w zasilaniu. Automatyka – Elektryka – Zakłócenia 2/2010, 55–70.
[10] Jarzyna W., Zieliński D.: The impact of converter's synchronization during FRT voltage recovery in two-phase short circuits. 2015 Selected Problems of Electrical Engineering and Electronics (WZEE), Kielce, 2015, 1–6.
[11] Kaplon A., Rolek J., Tunia H.: The method for reducing harmonics in input currents of rectifier using a modulation in interphase transformer. 5th IEEE Annual International Energy Conversion Congress and Exhibition (ECCE), Melbourne 2013, 117–121.
[12] Khan I., Verma K.S., Balgopal Faheemullah, Rafi M.: STATic synchronous COMpensator(STATCOM) using FCMLI - A devices for power system security and efficiency Enhancement. 2011 International Conference on Computer, Communication and Electrical Technology (ICCCET), Tamilnadu, 2011, pp. 444–449, [DOI: 10.1109/ICCCET.2011.5762516].
[13] Murali M., Gokhale A., Pandey A.V.; Sharma E.: Modelling, design and comparison of PI and PID controllers for Static Synchronous Compensator (STATCOM). 2016 IEEE 1st International Conference on Power Electronics, Intelligent Control and Energy Systems (ICPEICES), Delhi, 2016, 1–6 [DOI: 10.1109/ICPEICES.2016.7853563].
[14] Rozporządzenie Ministra Gospodarki z dnia 4 maja 2007 r. w sprawie szczegółowych warunków funkcjonowania systemu elektroenergetycznego. Dz. U. Nr 93, poz. 623 z póź. zm.
[15] Zieliński D.: Dynamiczna regulacja mocą przekształtników sieciowych, Informatyka, Automatyka, Pomiary w Gospodarce i Ochronie Środowiska – IAPGOŚ 1/2016, 59–62.
[16] Zieliński D., Zielińska K.: The impact of a power electronics converter in phase failure work on the power system network. Acta Energetica 3/2016, 155–161.

M.Sc. Eng. Bartłomiej Mroczek
e-mail: b.mroczek@pollub.pl

In 2002 graduated from the Faculty of Electrical Engineering, Automatics, Computer Science and Electronics* of the AGH University of Science and Technology. From 2018 employed at the Department of Electrical Drives and Machines at the Faculty of Electrical Engineering and Computer Science of the Lublin University of Technology. Studies the dynamics of the changes of energy quality in microgrids by using electric machines and converter systems dedicated to energy storage and reactive power control.

M.Sc. Eng. Karol Fatyga
e-mail: k.fatyga@pollub.pl

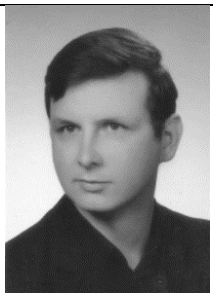

In 2016 graduated from the Faculty of Electrical Engineering and Computer Science of the Lublin University of Technology. Since then employed as assistant lecturer at the university's Department of Electrical Drives and Machines. His research focuses on power converters, specifically on electric vehicle chargers and converters for coupling the utility grid with energy storage. He is a member of the team working on NCBiR (National Council for Research and Development) projects.

otrzymano/received: 11.04.2018 *przyjęto do druku/accepted: 11.05.2018*

DOI: 10.5604/01.3001.0012.0717

OCENA RUCHU PALIWA W PROCESIE SPALANIA NA PODSTAWIE OBRAZU CYFROWEGO

Łukasz Pater
Politechnika Wrocławska, Wydział Elektroniki, Katedra Automatyki Mechatroniki i Systemów Sterowania, Zakład Systemów Wizyjnych i Teorii Sterowania

Streszczenie. *Artykuł dotyczy sposobu wskazania rodzaju ruchu przy pomocy przetwarzania i analizy obrazu cyfrowego na przykładzie sekwencji przemieszczania się pyłu węglowego. Prezentowane podejście ma poszerzyć perspektywę zastosowania systemów wizyjnych w kontroli procesów spalania, podnosząc tym samym ich efektywność. Wyniki pokazały właściwe odzwierciedlenie rzeczywistego ruchu paliwa na dyskretnej powierzchni pól wektorowych przy zastosowaniu metody przepływu optycznego. Dołączenie metody numerycznej, do analizy pól wektorowych, pozwoliło wyznaczyć sześć rodzajów ruchu. Obserwacje, obejmujące fragmentu badanego zjawiska, wyczerpują wszystkie przypadki oceny przemieszczenia cząstek paliwa.*

Słowa kluczowe: analiza ruchu na obrazie, przemysł węglowy, metoda różnic skończonych, pola wektorowe

ASSESSMENT OF FUEL MOVEMENT IN COMBUSTION PROCESS BASED ON THE DIGITAL IMAGE

Abstract. *The article refers to the method of indicating the type of movement by means the digital image processing and analysis on the example of a coal dust movement sequence. Presented approach is broaden the perspective of use the vision systems in the combustion processes control, thus increasing their effectiveness. The results showed a correct reflection of the real fuel movement in the discrete surface of the vector fields using the optical flow method. Including a numerical method for vector field analysis allowed to indicate six types of movement. Research, covering a fragment of the studied phenomenon, exhaust all cases of assessing the fuel particles displacement.*

Keywords: image motion analysis, coal industry, finite difference methods, vector fields

Wstęp

Jednym ze stosowany paliw w produkcji jest węgiel. Dostarcza on ponad 30% zapotrzebowania na energię oraz 40% zapotrzebowania na elektryczność w skali świata. Bierze udział w produkcji 70% stali w skali światowego rynku [6, 12].

W dobie rosnącego zapotrzebowania i stosowania energii odnawialnych [11], węgiel nadal ma największe znaczenie w produkcji, a jego zużycie stale rośnie. Paliwem może być zarówno sam sproszkowany węgiel [3], nazywany pyłem węglowy, jak i mieszanki pyłu węglowego z innymi produktami spalania [1, 9]. Do takich mieszanek należą biopaliwa, które pozwalają na zmniejszanie kosztów produkcji oraz zmniejszenie emisji substancji szkodliwych. Stale rozwijane proporcje i rodzaje mieszanek, bez istotnych zmian układów spalania wymagają stałej kontroli.

Automatyzacja pomiaru procesu spalania za pomocą obrazu rejestrowanego przez kamery, od ultrafioletu po podczerwień, jest dobrze znana i stale rozwijana. Jak pisze Hobson i in. [8] zmiany ekonomiczne wpływają na rodzaj węgla w elektrowniach. Przeprowadzają oni badania kontroli jakości paliwa przez analizę obrazu cyfrowego, w zakresie światła widzialnego, wskazując różnice tekstury węgla względem innym skał. Carter i in. [5] przedstawiają wyniki pomiaru cząstek paliw, dostarczanych na bieżąco do kotła spalania, za pomocą kamery cyfrowej umieszczonej w rurociągu dolotowym. Znanych jest również wiele badań analizy samego płomienia podczas spalania paliwa [7].

W niniejszym artykule przeprowadzono badanie oceny rodzaju ruchu naturalnego paliwa stałego, na podstawie zarejestrowanej sekwencji obrazu cyfrowego w zakresie światła widzialnego. Motywacją badania jest wpływ podania i ruchu paliwa na przebieg spalania.

1. Metodyka

Badanym stałym paliwem opałowym był pył węglowy. Ruch pyłu węglowego wymuszono przez zasilenie palnika o szerokości ok. 80 mm (element 4, rys. 1a). Do badań, palnik umieszczono nad rurą opadową, o szerokości 130mm (element 5, rys. 1b). Palnik wyposażony jest w trzy kanały wlotowe (elementy 1 – 3, rys. 1a). Jednym z kanałów, centralnym (element 1, rys. 1a), dostarczane jest paliwo. Pozostałymi dwoma kanałami (element 2 i 3, rys. 1a) dostarczana jest mieszanka gazowa, tlenu i dwutlenku węgla. Gaz pełni funkcję transportową, wpływa na ruch paliwa oraz bierze udział w procesie spalania paliwa. Ilość dostarczanego paliwa oraz gazu, wykorzystanie kanałów dolotowych gazu czy też proporcja mieszanki gazowej jest w pełni kontrolowana. Na zarejestrowanej sekwencji (rys. 1c), pył węglowy porusza się z góry na dół. Prędkość badanego paliwa mieści się w zakresie od 3 do 8 m/s. Pozostawiając przestrzeń na rejestrację obrazu oraz zbieranie wylatującego paliwa (rys. 1), pył węglowy nie jest spalany.

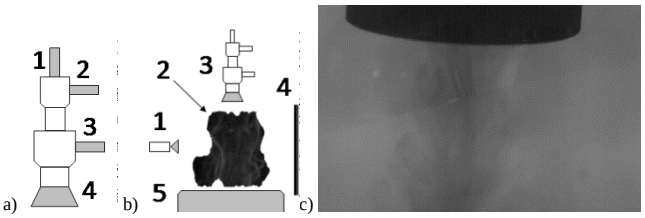

Rys. 1. Poglądowe rysunki a) palnika doprowadzającego paliwo: 1 – doprowadzenie paliwa, 2, 3 – gazu transportowego, 4 – wylot palnika, b) sposobu rejestracji przeprowadzanego badanego zjawiska: 1 – kamera rejestrująca, 2 – rejestrowany pył węglowy, 3 – palnik doprowadzający paliwo, 4 – tło zwiększające kontrast ruchu paliwa, 5 – rura opadowa zbierająca paliwo oraz c) jedna z zarejestrowanych ramek sekwencji o rozdzielczości 752×480 px.

Analiza ruchu paliwa w sekwencji obrazu została podzielona na cztery kroki. Pierwszym krokiem jest odfiltrowanie zakłóceń urządzenia rejestrującego oraz sposobu rejestracji zjawiska. Drugim krokiem jest wyznaczenie pola wektorowego, opisującego w przybliżeniu ruch rzeczywisty. Trzecim punktem jest obliczenie wartości pochodnych cząstkowych z dyskretnej przestrzeni pól wektorowych. Czwartym, ostatnim krokiem są obliczenia na pochodnych cząstkowych w celu prezentacji dywergencji i rotacji ruchu. Wynik obliczeń, dywergencji oraz rotacji, jest opisem rodzaju przemieszczenia paliwa.

Do odfiltrowania ramek sekwencji, zaproponowano usunięcie tła (1) oraz wyrównanie histogramu. Usunięcie tła jest różnicą ramki wzorcowej i ramki aktualnie przetwarzanej:

$$I_{PRZETWORZONY} = I_{BADANY} - I_{WZORCOWY} \quad (1)$$

gdzie: $I_{PRZETWORZONY}$ – ramka wynikowa po przetworzeniu, I_{BADANY} – aktualnie analizowana ramka, $I_{WZORCOWY}$ – ramka wzorcowa, na której nie został zarejestrowany ruch paliwa. Na obrazie różnicy, obrazie przetworzonym pozostaje ruch pyłu węglowego. Z powodu małego kontrastu badanego zjawiska, tylko połowa zakresu kwantyzacji, dodatkową filtracją ramki jest wyrównanie histogramu. Dla sekwencji odfiltrowanych ramek wyznaczana jest sekwencja pól wektorowych.

Z kolejno występujących po sobie, dwóch ramkach sekwencji, wyznaczono pole wektorowe. Wybrano metodą przepływu

optycznego (ang. optical flow) Lucas-Kanade [4]. Jak pokazują wyniki pozostałych metod przepływu optycznego [2], metoda Lucas-Kanade wyznacza dość dobrze pola wektorowe dla obrazów rzeczywistych. Jest to lokalna metoda gradientowa. Polega ona na wyznaczeniu, z punktów sąsiednich, wektora ruchu. Dla większości punktów ramki, poza brzegowymi, wyznaczany jest wektor metodą najmniejszych kwadratów. Metoda liczy wektor w lokalnej przestrzeni, tzw. okna. Na podstawie punktów sąsiednich, znajdujących się w oknie, zakładamy, że przesunięcie nastąpiło w tym samym kierunku dla wszystkich punktów okna. Mniejsze okno wymaga krótszego czasu obliczeń, jednak wyznaczony wektor może znacznie odbiegać kierunkiem i długością od wektorów sąsiednich. Przyjęta wielkość okna, dla badanego zjawiska, to 40×40 pikseli. Wynikiem obliczeń jest sekwencja pól wektorowych.

Do przybliżenia wartości pochodnych składowych wektorów, w przestrzeni dyskretnej, zastosowano metodę różnic skończonych [10] (ang. finite difference method). Metoda numeryczna oblicza pochodne cząstkowe przez przybliżenia algebraiczne oparte o punkty sąsiednie. Punkty sąsiednie występują zarówna na jednej ramce, jak i na sąsiednich ramkach sekwencji, w przypadku liczenia pochodnej po czasie *t* (rys. 2).

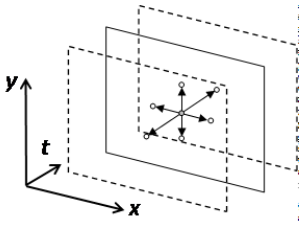

Rys. 2. Wizualizacja pobrania wartości sąsiednich, na osi x, y oraz czasu t dla metody różnic skończonych z trzech kolejnych ramek sekwencji obrazu

Dla dalszych obliczeń, wyprowadzone zostały wzory (2 – 4) składowych wektora dla każdego przypadku przesunięcia względem dyskretnej przestrzeni:

$$\frac{\partial P}{\partial x} = \frac{P(x+1,y,t) - P(x-1,y,t)}{2} \qquad (2)$$

$$\frac{\partial Q}{\partial x} = \frac{Q(x+1,y,t) - Q(x-1,y,t)}{2}$$

$$\frac{\partial P}{\partial y} = \frac{P(x,y+1,t) - P(x,y-1,t)}{2} \qquad (3)$$

$$\frac{\partial Q}{\partial y} = \frac{P(x,y+1,t) - P(x,y-1,t)}{2}$$

$$\frac{\partial P}{\partial t} = \frac{P(x,y,t+1) - P(x,y,t-1)}{2} \qquad (4)$$

$$\frac{\partial Q}{\partial t} = \frac{Q(x,y,t+1) - Q(x,y,t-1)}{2}$$

gdzie: *P* i *Q* – składowe wektora przemieszczenia, *x* – położenie punktu względem osi x, *y* – położenie punktu względem osi y, *t* – numer ramki z sekwencji. W dalszych krokach, powyższe obliczenia można przekształcić do maski, i obliczeń konwolucji obrazu. Wynikiem jest sekwencja pochodnych cząstkowych.

Przeprowadzone badania obejmują opis przemieszczeń paliwa w dwóch rodzajach ruchu. Pierwszym rodzajem ruchu jest dywergencją, na którą składają się trzy typu ruchu (rys. 3). Drugim rodzajem ruchu jest rotacja, na którą składają się trzy typu ruchu, z których dwa są kluczowe (rys. 4).

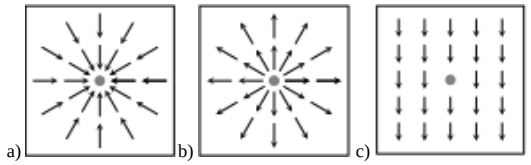

Rys. 3. Rodzaje badanych typów dywergencji: a) napływ, b) odpływ, c) przepływ

Pierwszym opisem przemieszczenia jest dywergencja, obliczana wzorem (5).

$$divF = \nabla \circ F = \frac{\partial P}{\partial x} + \frac{\partial Q}{\partial y} \qquad (5)$$

gdzie: *F* – wektor przemieszczenia punktu, *P*, *Q* – składowe wektora przemieszczenia. Za jej pomocą badamy czy sąsiednie obiekty napływają do punktu źródłowego (źródło ujemne) (rys. 3a), odpływają od niego (źródło dodatnie) (rys. 3b), czy też poruszają się stale bez zauważalnego napływu lub odpływu (bezźródłowe) (rys. 3c). Odpowiednio dywergencja w tym punkcie przyjmuje wartości mniejsze do zera, większe od zera oraz równe zeru.

Drugim opisem przemieszczenia jest funkcja wektorowa, rotacja, obliczana wzorem (6):

$$rotF = \nabla \times F = -i\left(\frac{\partial Q}{\partial t}\right) - j\left(\frac{\partial P}{\partial t}\right) + k\left(\frac{\partial Q}{\partial x} - \frac{\partial P}{\partial y}\right) \qquad (6)$$

gdzie: *F* – wektor przemieszczenia, *P*, *Q* – składowe wektora przemieszczenia, *i, j, k* – wektory jednostkowe. Wskazuje ona że sąsiednie punkty, względem obliczanego, poruszają się ruchem zgodnym ze wskazówkami zegara (rys. 4a) lub przeciwnie (rys. 4b). Rotacja w tym punkcie, jest odpowiednio dodatnia lub ujemna. Jeżeli nie zachodzi ruch okrężny, wartość rotacji jest zerowa.

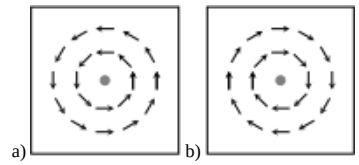

Rys. 4. Rodzaje badanych typów rotacji a) lewoskrętnej oraz b) prawoskrętnej

2. Wyniki

Obszar rejestracji kamerą, w zakresie światła widzialnego, obejmuje powierzchnię większą niż obserwowane zjawisko. Zarejestrowana ramka poza ruchem paliwa zawiera fragmenty zbędnych informacji. Należy do nich fragment palnika, przestrzeń, w której nie zachodzi ruch pyłu węglowego czy odbicie pyłu przed przejściem do rury opadowej.

Każdy krok, opisanej analizy ruchu, powoduje nieznaczne skrócenie sekwencji oraz zmniejszenie wielkości każdej ramki. Założenie wykonania badania dla całej sekwencji wejściowej nie jest możliwe. Jednak wielkość każdej ramki oraz długość sekwencji nie wpływa negatywnie na wskazanie właściwego obszaru zjawiska.

Do przedstawienia wyników, kolejnych kroków analizy ruchu paliwa, wybrano fragment ramki oraz fragment sekwencji. Wybrany fragment ramki ma wielkość 100×140 px co w przeliczeniu na rzeczywiste wymiary daje obszar 14×20 mm. Z całej sekwencji wybrano dwie, występujące po sobie, ramki (rys. 5), które reprezentują w pełni zaobserwowane zjawisko. Pomiędzy tymi ramkami można zaobserwować wyraźnie ruch i dokonać oceny empirycznej otrzymanych wyników.

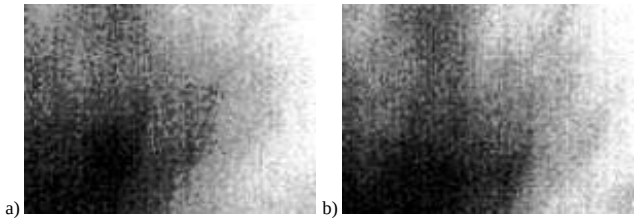

Rys. 5. Dwie: a) 200 oraz b) 201 wybrane do badania ramki sekwencji o wymiarach 100×140px

Zaproponowana filtracja ramki miała zwiększyć dokładność wyznaczenia pola wektorowego. W przeprowadzonym badaniu ruch paliwa przechodzi płynnie pomiędzy kolejnymi ramkami oraz pomiędzy sąsiednimi obszarami. Widocznym efektem filtracji ramki było zwiększenie kontrastu zjawiska oraz poprawna

czytelności przebiegu zjawiska. Jednak po wyznaczenie pola wektorowego, dla odfiltrowanej sekwencji, wynik wskazuje na brak płynności ruchu cząstek pyłu węglowego.

Na przedstawionym, przykładowym polu wektorowym (rys. 6), można zaobserwować wektory wskazujące na przesunięcie w kierunku punktów sąsiednich. W kilku przypadkach, wskazany punkt sąsiedni, który powinien być kontynuacją ruchu, wskazuje na prędkość zerową lub wręcz, jego zwrot jest skierowany o 90° w kierunku odmiennym. Patrząc globalnie na ten problem, wektory z prawej części rysunku (rys. 6) wskazują na ruch obiektów w lewą stronę. W połowie szerokości następuje nagła zmiana ruchu. Za to, wektory z lewej części rysunku, zmieniają nagle kierunek, wskazując na ruch obiektów w dół. Pomiędzy tymi grupami wektorów brakuje płynnego przejścia. Nie jest to zgodne z rzeczywistym postrzeganiem ruchu badanego paliwa. Po wyłączeniu filtracji, otrzymane pole wektorowe, dla tych samych ramek sekwencji, jest bliższe postrzeganemu ruchowi rzeczywistemu.

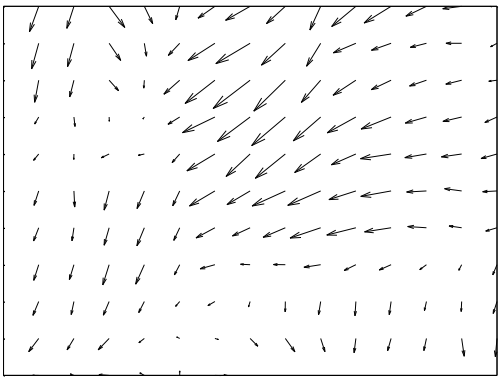

Rys. 6. Pole wektorowe ramki 200 i 201 wyznaczone po filtracji

Dobranie prawidłowej wielkości okna, podobnie jak filtracja, polegało na obserwacji płynności otrzymanego pola wektorowego. Zbyt małe okno metody Lucas-Kanade, poniżej 20×20 px, uniemożliwiło identyfikację ruchu jakiejkolwiek grupy punktów (rys. 7). Z takiego pola wektorowego wynika, że każdy punkt porusza się w kierunku oraz z prędkością niezależna od punktu sąsiedniego. Okno zbyt duże, powyżej 40x40px, powoduje, że w grupach punktów można dostrzec płynną zmianę kierunku wektorów przesunięcia, jednak trudno jest dostrzec różnicę prędkości tych grup. Nie jest to odzwierciedleniem ruchu rzeczywistego. Prędkość oraz rozdzielczość badanej sekwencji obserwowanego zjawiska pozwoliła wyznaczyć przedział okna metody Lucas-Kanade, między 20×20 px, a 40×40 px. Dalsze wyniki oparte są o pole wektorowe jest obliczane dla wielkości okna 40×40 px (rys. 8).

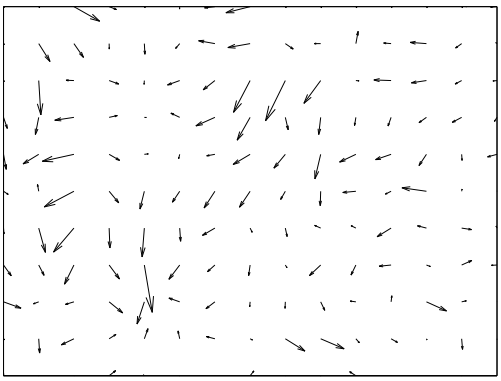

Rys. 7. Pole wektorowe ramki 200 i 201 dla okna 10x10 metody Lucas-Kanade

Pochodne cząstkowe obliczone metodą różnic skończonych (2 – 4), tworzą kolejne sekwencje danych. Dla każdej składowej wektora, względem jednej ze zmiennych, otrzymujemy sześć sekwencji pochodnych cząstkowych, równych wielkości ramki i długości sekwencji wejściowej. Z tak przygotowanych pochodnych można wykonać podsumowanie wyników, określających rodzaj ruchu.

Jedno z dwóch równań, opisane na pochodnych cząstkowych, określa ruch w formie dywergencji. Dla każdego punktu ramki obliczana jest dywergencja (5). Dla całej sekwencji powstaje sekwencja powierzchni dywergencji. Kontynuując analizę fragmentu ramek 200 i 201 otrzymujemy wizualizację dywergencji (rys. 9). Jedna powierzchnia mapy kolorów obrazuje trzy rodzaje przemieszczenia dywergencji. Jasny kolor mapy wskazuje na napływ paliwa do punktu. Ciemny kolor oznaczone miejsca z których paliwa odpływa. Miejsca przepływu, dywergencja zerowa, nie zostały zaobserwowane. Dla takiego rodzaju ruchu należy założyć pewien zakres wartości bliskich zeru.

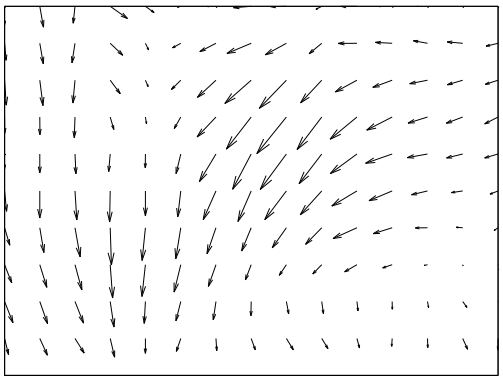

Rys. 8. Pole wektorowe ramki 200 i 201 dla okna 40x40 metody Lucas-Kanade

Drugim równaniem, opisującym rodzaj ruchu oraz składającym się z pochodnych cząstkowych jest rotacja. Rotacja liczona jest, dla każdego punktu ramki, równaniem (6). Dla całej sekwencji obrazu wejściowego, powstaje sekwencja powierzchni rotacji. Podtrzymując badanie fragmentu ramki i sekwencji otrzymujemy wizualizację rotacji (rys. 10). Powierzchnia ta, poprzez odcień koloru, obrazuje trzy rodzaje ruchu rotacyjnego. Jasny odcień zielonego, rotacja dodatnia, wskazuje na ruch przeciwny do ruchu wskazówek zegara. Ciemny odcień, rotacja ujemna, wskazuje na ruch zgodny z ruchem wskazówek zegara. Wartość zerowa, wskazująca na brak dowolnej rotacji, nie wystąpiła w przeprowadzonych obliczeniach. Można empirycznie wskazać, tak samo jak dla dywergencji, pewien zakres wartości bliskich zeru świadczących o braku rotacji.

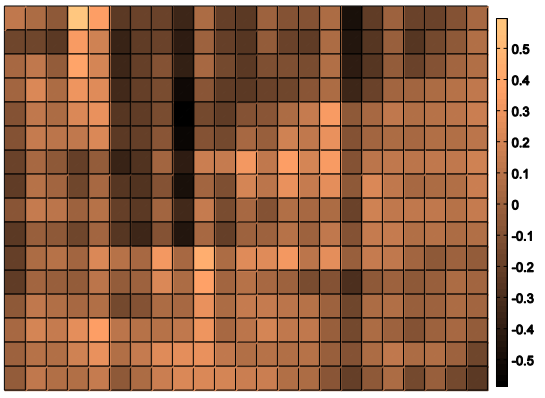

Rys. 9. Wizualizacja dywergencji badanego pola wektorowego

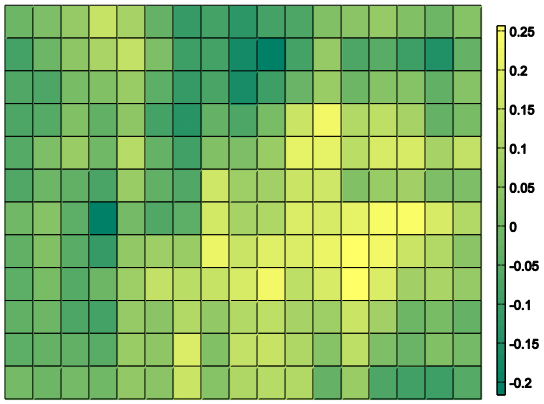

Rys. 10. Wizualizacja rotacji badanego pola wektorowego

3. Wnioski

Filtracja, w postaci różnicy ramek oraz wyrównania histogramu, badanej sekwencji wejściowej, pomimo poprawy kontrastu i wyeksponowania detali zarejestrowanego zjawiska, wpływa negatywnie na wyznaczenie pól wektorowych. Obserwując obliczone pole wektorowe, występuje brak ciągłości zarówno kierunku jak i długości wektorów sąsiednich. Jest to sprzeczne z rzeczywistym ruchem paliwa.

Metoda Lucas-Kanade bardzo dobrze sprawdziła się przy wyznaczaniu pola wektorowego. Do badanego zjawiska, prędkości oraz wielkości przemieszczających się cząstek pyłu węglowego, wymagane było dobranie odpowiedniej wielkości okna.

Nie jest możliwe, z rzeczywistej sekwencji, otrzymanie dywergencji lub rotacji zerowej. Aby wskazać miejsca przepływu dywergencji lub braku rotacji na obrazie, należy wyznaczyć przedział wartości bliskich zeru.

Jeżeli dla metody różnic skończonych zostanie wybrana pojedyncza wartość punktu sąsiedniego, dywergencja lub rotacja przyjmuje wartości znacznie odstające od punktów sąsiednich. Wyznaczanie pochodnych cząstkowych wymagało obliczenia wartości średniej z punktów sąsiednich, co wygładziło szum i zwiększyło płynność ruchu cząstek pyłu węglowego.

Na tym etapie badań, trudne jest określenie szczegółowych parametrów doboru paliwa czy mieszanki paliwowo-gazowej. Do opisania zależności między zaobserwowanym ruchu, a kontrolą dostarczania paliwa, badanie wymaga dokładnego opisu czynności dostarczenia paliwa, powiązanego z czasem rejestrowanej sekwencji. Prezentowane badania mają na celu wskazanie narzędzi oraz sposobu pomiaru ruchu pyłu węglowego. Otwiera ono możliwości dokładnych badań określających wpływ ruchu paliwa na parametry procesu spalania.

Podziękowania

Badania były finansowane z grantu: 2012/07/B/ST7/01216 Narodowego Centrum Nauki.

Autor kieruje podziękowania dla zespołu naukowego prof. Haliny Pawlak-Kruczek za wykonanie eksperymentu oraz dla dr inż. Wojciecha Rafajłowicza za rejestrację oraz udostępnienie zebranych materiałów.

Literatura

[1] Altawell N.: Co-Firing Issues. Wiley-IEEE Press, 2014.
[2] Barron J.L., Fleet D.J., Beauchemin S.S., Burkitt T.A.: Performance of optical flow techniques. Proceedings 1992 IEEE Computer Society Conference on Computer Vision and Pattern Recognition, Champaign, IL, 1992, 236–242 [DOI: 10.1109/CVPR.1992.223269].
[3] Branning R.L., Peizer M.J.: Profiting from pulverising. Power Engineer 21(1)/2007, 28–33.
[4] Bruce D.L., Takeo K.: An iterative image registration technique with an application to stereo vision. Proceedings of the 7th international joint conference on Artificial intelligence –IJCAI'81, Vol. 2. Morgan Kaufmann Publishers Inc., San Francisco, CA, USA, 1981, 674–679.
[5] Carter R.M., Yan Y.: Digital imaging based on-line particle sizing of 'green' biomass fuels in power generation. 2007 IEEE Instrumentation & Measurement Technology Conference IMTC 2007, Warsaw, 2007, 1-4 [DOI: 10.1109/IMTC.2007.379414].
[6] Coal Facts 2014. IEA Coal Information 2014, BP Statistical Review of World Energy 2014, September 2014.
[7] Duo Sun, Gang Lu, Hao Zhou, Yong Yan, Shi Liu: Quantitative assessment of flame stability through image processing and spectral analysis. IEEE Transactions on Instrumentation and Measurement 64(12)/2015, 3323–3333.
[8] Hobson D.M., Carter R.M., Yong Yan, Zhixin Lv.: Differentiation between coal and stone through image analysis of texture features. IEEE International Workshop on Imaging Systems and Techniques, IST2007, Krakow 2007.
[9] Li Xiao-yu, Yang Xiao-xi, Gong Bo, Feng Hong-qing, Cheng Gang, Liu Xiao-jie. Optimal ratio of oil-sludge and coal mixed fuel. International Conference on Materials for Renewable Energy & Environment, Shanghai, 2011, 1650–1653 [DOI: 10.1109/ICMREE.2011.5930650].
[10] Mitchell A.R., Griffiths D.F.: The finite difference method in partial differential equations. Wiley, Chichester [Eng.], New York 1980.
[11] Patel V., Saha B., Chatterjee K.: Fuel saving in coal-fired power plant with augmentation of solar energy. International Conference on Power, Control and Embedded Systems (ICPCES), 2014, 1–5.
[12] World Coal Institute. The coal resource: A comprehensive overview of coal. UK London, September 2005.

Mgr inż. Łukasz Pater
e-mail: lukasz.pater@pwr.edu.pl

Wykształcenie wyższe techniczne zdobył na Wydziale Elektroniki Politechniki Wrocławskiej w specjalności Zastosowanie Inżynierii Komputerowej w Technice. Dyplom magistra uzyskał w 2011 roku. Zainteresowania naukowe to analiza i przetwarzanie obrazów. Obecnie doktorant w Zakładzie Systemów Wizyjnych i Teorii Sterowania

otrzymano/received: 15.06.2016 *przyjęto do druku/accepted: 11.05.2018*

DOI: 10.5604/01.3001.0012.0821

NONLINEAR ANALYSIS OF HIGH Q RADIO FREQUENCY ENERGY HARVESTING NETWORKS

Christian Merz, Gerald Kupris
Deggendorf Institute of Technology, Faculty of Electrical Engineering, Media Technology and Computer Science

Abstract. *The paper focuses on nonlinear analysis of high and low Q RF energy harvesting circuits. The analysis is made mathematically and by large signal simulation via Keysight Advanced Design System. The mathematical analysis of the nonlinear harvesting circuits is done by using the Galerkin method and the simulations are performed using the harmonic balance method, which is a special version of the Galerkin method.*

Keywords*: Galerkin method, high Q impedance matching, nonlinear circuit analysis, radio frequency energy harvesting*

NIELINIOWA ANALIZA SIECI ZBIERAJĄCYCH ENERGIĘ W ZAKRESIE RADIOWYM O WYSOKIM WSPÓŁCZYNNIKU DOBROCI Q

Streszczenie. *Artykuł poświęcony jest nieliniowej analizie obwodów zbierających energię o wysokim i niskim współczynniku dobroci Q, w zakresie częstotliwości radiowych. Z użyciem Keysight Advanced Design System wykonano analizę wielkosygnałową. Przeprowadzono również matematyczną analizę nieliniowych obwodów zbierających energię z użyciem metody Galerkina oraz symulacje za pomocą metody balansu harmonicznego, która jest wersją metody Galerkina.*

Słowa kluczowe: metoda Galerkina, dopasowanie impedancji o wysokim współczynniku dobroci, analiza obwodów nieliniowych, zbieranie energii o częstotliwościach radiowych

Introduction

The previous work of the authors has focused on high Q impedance matching for harvesting circuits. It could be shown in a former publication [3] that the use of a high Q resonator as an inductor in the matching network can lead to an improvement of the harvester efficiency.

This work focuses on the mathematical description of the output voltage in dependence on the input power for two example high Q and low Q harvester networks. Because of the nonlinear behavior of the diodes, which are used to rectify the harvested AC voltage, the dependence of the output voltage on the input power is also nonlinear. Because of this, the mathematical description of the harvester network leads to a nonlinear differential equation and a numerical method has to be used to approximate a solution. In this work, the Galerkin Method is used to find an approximated solution.

1. Method

The following harvester circuit is analyzed mathematically and by simulation.

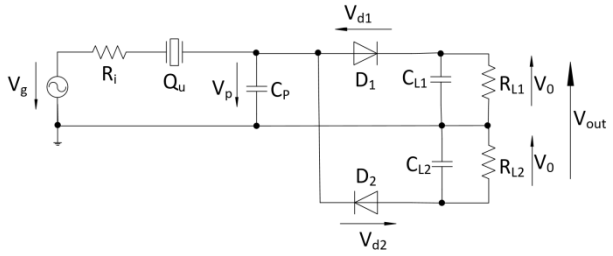

Fig. 1. RF energy harvesting circuit with Delon rectification (high Q)

The circuit consists of a RF generator block, a high Q matching circuit in L-topology and a Delon rectifier. The RF generator block represents the equivalent circuit of the antenna of the harvester circuit and consists of a RF voltage source V_g and a resistance R_g. The high Q matching circuit is comprised of a crystal resonator in the series leg and a capacitance in the parallel leg.

A crystal resonator is a resonant circuit with an equivalent circuit (see Fig. 2) consisting of a series motional resistance (R_1), a series motional inductance (L_1), a series motional capacitance (C_1) and a shunt static capacitance (C_0).

These parameters are also called Butterworth-van-Dyke (BVD) parameters. The three motional devices form a series resonance circuit and the static shunt capacitance forms a parallel resonance circuit together with L_1 and C_1.

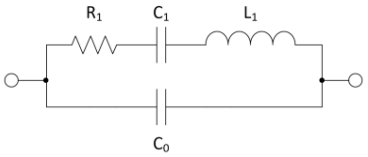

Fig. 2. Equivalent circuit of a resonator

The following figure shows the reactance diagram of a crystal resonator.

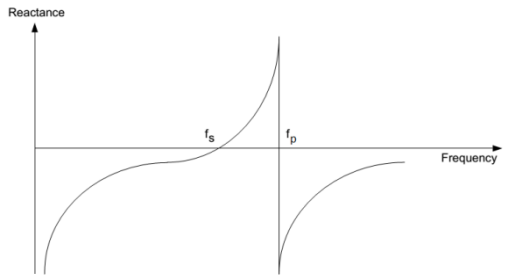

Fig. 3. Reactance diagram of a crystal resonator

The diagram in Fig. 3 shows that the resonator has an inductive behavior between the series resonance frequency (f_S) and the parallel resonance frequency (f_P). The series resonance frequency (f_S) and the parallel resonance frequency (f_P) can be calculated as follows:

$$f_S = \frac{1}{2\pi\sqrt{L_1 C_1}} \tag{1}$$

$$f_P = \frac{1}{2\pi\sqrt{L_1 \frac{C_1 C_0}{C_1 + C_0}}} \tag{2}$$

The rectifier includes two HSMS-282 diodes from Avago Technologies and the capacitors C_{L1} and C_{L2}. The two resistors R_{L1} and R_{L2} represent the load of the harvester circuit. In the following, it is assumed that the load resistors and rectifier capacitors have the same values, that means $R_{L1} = R_{L2} = R_L$ and $C_{L1} = C_{L2} = C_L$.

The diodes can be modeled as varistors with a series resistor R_j and a junction capacitance C_j. The following figure shows the equivalent circuit of the diode.

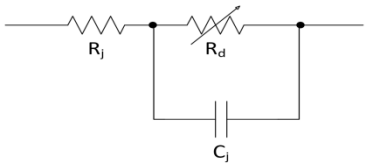

Fig. 4. Equivalent circuit of a diode [2]

The parameters of the HSMS-282 diode are:

- series resistance $R_j = 6\ \Omega$,
- saturation current $I_S (T = T_0 = 300\ \text{K}) = 22\ \text{nA}$,
- junction capacitance C_j ($V_D = 0\ \text{V}$) = 0.7 pF,
- ideality factor $n = 1.08$,
- metal-semiconductor energy gap $E_G = 0.69\ \text{eV}$.

The current through the diode I_D and the diode voltage V_D have the following nonlinear relation:

$$I_D = I_S(T) \cdot \left[\exp\left(\frac{q \cdot V_D}{n \cdot k \cdot T} \right) - 1 \right] \tag{3}$$

where I_D is the diode current, V_D represents the diode voltage, $q = 1.06 \cdot 10^{-19}$ C denotes the elementary charge and $k = 1.3806 \cdot 10^{-23}$ J/K the Boltzmann constant.

Using the equivalent circuits of the diode and the resonator, the harvester circuit (see Fig. 1) can be designed as illustrated in Fig. 5.

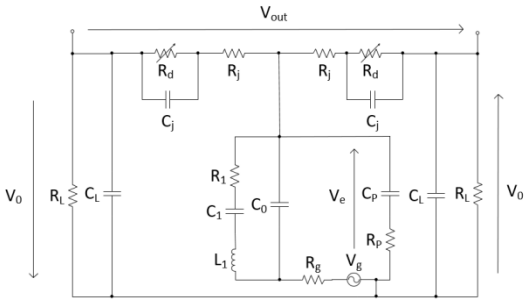

Fig. 5. Harvester circuit with the equivalent circuits of the resonator and the diodes

To simplify the analysis of the harvester network, the following partial network has firstly to be taken into account.

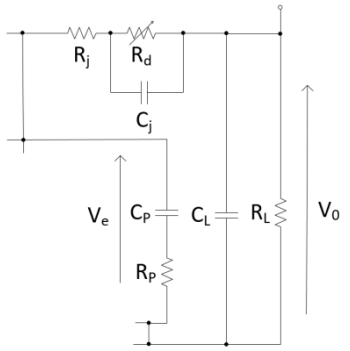

Fig. 6. Partial harvester network

The straightforward analysis of the partial harvester network leads to the following nonlinear differential equation of second order:

$$\begin{aligned} & I_S \left\{ \exp\left[\alpha \left(v_e(t) + \beta v_o(t) + \gamma \frac{dv_0(t)}{dt} - v_0(t) \right) \right] - 1 \right\} \\ & + C_j \frac{dv_e(t)}{dt} + \delta \frac{dv_0(t)}{dt} + \zeta \frac{d^2 v_0(t)}{dt^2} - C_j \frac{dv_0(t)}{dt} \\ & = \frac{v_0(t)}{R_L} + C_L \frac{dv_0(t)}{dt} \end{aligned} \tag{4}$$

where

$$\alpha = \frac{q}{n \cdot k \cdot T},\ \beta = \frac{R_j}{R_L},\ \gamma = R_j C_L,\ \delta = \frac{R_j C_j}{R_L} \text{ and } \zeta = R_j C_j C_L.$$

It is not possible to find a closed form of the solution for the differential equation. Because of this, a numerical method has to be used to find an approximated solution. A suitable numerical approximation method is the so called Galerkin method. To apply this method, the differential equation has to be brought into the form

$$\xi\left[x, y, t, \frac{d}{dt}, \frac{d^2}{dt^2} \right] \equiv 0 \tag{5}$$

In equation (5) ξ is a nonlinear operator. The exact solution cannot be determined, but is approximated by an assumed solution $\tilde{y}(t)$, which can be expressed with equation (6).

$$\tilde{y}(t) = \sum_{k=1}^{N} a_k \phi_k(t) \tag{6}$$

$\phi_k(t)$ are N linearly independent functions and a_k are N arbitrary constant coefficients. The assumed solution $\tilde{y}(t)$ does not in general satisfy the differential equation exactly. Therefore, the expression obtained by substituting equation (6) into equation (5) is no longer equivalent to zero.

Instead

$$\xi\left[x, \tilde{y}, t, \frac{d}{dt}, \frac{d^2}{dt^2} \right] = \varepsilon(t) \neq 0 \tag{7}$$

where $\varepsilon(t)$ is called the residual and is a measure of the deviance of the exact solution and therefore represents the incurred error. This error can be minimized if the residual satisfies the so called Ritz conditions:

$$\int_{t_1}^{t_2} \xi\left[x, \tilde{y}, t, \frac{d}{dt}, \frac{d^2}{dt^2} \right] \cdot \Phi_k(t) dt = 0 \tag{8}$$

$$k = 1,2,\ldots,N$$

This conditions result in a system of N algebraic equations with N variables. To reduce this system of equations to one equation, the ripple of the output voltage has to be neglected, so that the assumed solution changes to

$$\tilde{y} = V_0 \tag{9}$$

The input forcing function x can be expressed as follows:

$$x = v_e(t) = \hat{V}_e \cdot \cos(\omega t) \tag{10}$$

Here $\hat{V}_e$ is the amplitude of the input function and the parameter ω represents the angular frequency of the RF source.

This simplification leads to only one Ritz condition:

$$\int_{t_1}^{t_2} \xi\left[\hat{V}_e \cdot \cos(\omega t), V_0, t, \frac{d}{dt}, \frac{d^2}{dt^2} \right] dt = 0 \tag{11}$$

If the assumed input and output functions, represented by the equations (10) and (9), are inserted into the differential equation (see equation (4)) the residual leads to the following formula:

$$\varepsilon(t) = I_S \left\{ \exp\left[\alpha\left(\hat{V}_e \cdot \cos(\omega t) + V_0(\beta - 1) \right) \right] - 1 \right\} - C_j \cdot \hat{V}_e \cdot \sin(\omega t) - \frac{V_0}{R_L} \tag{12}$$

Carrying out the integration specified in equation (11) and taking equation (12) into account, we get the following nonlinear relation between the input and output value:

$$I_0\left(\alpha \cdot |\hat{V}_e| \right) = (1 + \mu \cdot V_0) \cdot \exp(\alpha \cdot \nu \cdot V_0) \tag{13}$$

where $\nu = \frac{R_j + R_L}{R_L}$ and $\mu = \frac{1}{R_L \cdot I_S}$.

To get the expression formulated in equation (13), the following formula has been used [1]:

$$I_0(z) = \frac{1}{\pi} \int_0^{\pi} \exp\left[\pm z \cdot \cos(\Theta) \right] d\Theta = \frac{1}{2\pi} \int_0^{2\pi} \exp\left[\pm z \cdot \cos(\Theta) \right] d\Theta \tag{14}$$

Here $I_0(z)$ is the zero-order modified Bessel function of first kind with argument z.

It has to be mentioned that the capacitances C_j and C_L do not appear in equation (13). This is the consequence of ignoring the ripple component of the output voltage $v_0(t)$.

The relation between the absolute value of the input amplitude $|\hat{V}_e|$ and the amplitude of the RF generator source voltage $\hat{V}_g$ can be calculated as follows:

$$\left| \hat{V}_e \right| = \left| \frac{\hat{V}_g \cdot \left(\frac{1}{j\omega C_p} + R_p \right)}{R_g + Z_Q + \frac{1}{j\omega C_p} + R_p} \right| \tag{15}$$

The impedance of the crystal resonator Z_Q is:

$$Z_Q = \frac{R_1 + j\omega L_1 + \frac{1}{j\omega C_1}}{\left(R_1 + j\omega L_1 + \frac{1}{j\omega C_1}\right)\cdot j\omega C_0 + 1} \tag{16}$$

The relationship between $\hat{V}_g$ and the incident power P_{in}, which is fed in at the antenna, can be expressed with the equation

$$\hat{V}_g = \sqrt{8 \cdot R_g \cdot P_{in}} \tag{17}$$

The output voltage of the harvester system V_{out} is twice as much as the output voltage of the partial network V_0:

$$V_{out} = 2 \cdot V_0 \rightarrow V_0 = \frac{V_{out}}{2} \tag{18}$$

2. Results

2.1. High Q matching

The insertion of the formulas (15), (17) and (18) into formula (13) results into the following equation, which describes the nonlinear relation between the output voltage V_{out} and the input power P_{in}:

$$I_0\left(\alpha \cdot \left|\frac{\sqrt{8 \cdot R_g \cdot P_{in}} \cdot \left(\frac{1}{j\omega C_P} + R_P\right)}{R_g + Z_Q + \frac{1}{j\omega C_P} + R_P}\right|\right) = \left(1 + \frac{\mu V_{out}}{2}\right) \cdot \exp\left(\frac{V_{out}}{2} \cdot \alpha \cdot \nu\right) \tag{19}$$

The equation (19) has been plotted (see Fig. 7) using the following parameters.

- Generator resistance R_g = 50 Ω,
- Equivalent series resistance of the matching capacitor R_P = 2.5 Ω,
- Matching capacitor C_P = 9.3 pF,
- Series motional resistance R_1 = 9.78 Ω,
- Series motional inductance L_1 = 9.3 mH,
- Series motional capacitance C_1 = 14.82 fF,
- Shunt static capacitance C_0 = 3.3 pF,
- Operational frequency f_a = 13.562966967 MHz,
- Load resistance R_L = 1 MΩ.

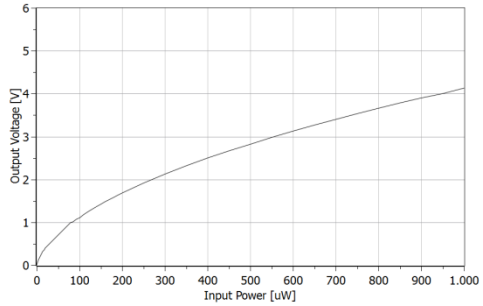

Fig. 7. Calculated output voltage versus input power (high Q)

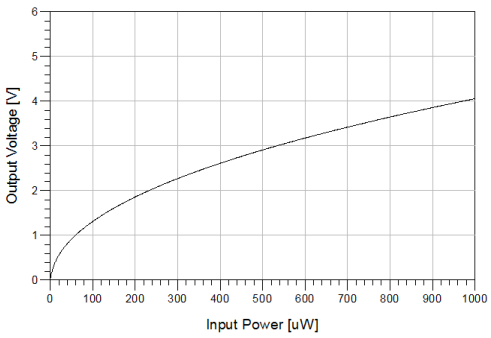

Fig. 8. Simulated output voltage versus input power (high Q)

The output voltage in dependence on the input power has been simulated with Keysight Advanced Design System. The simulation result is shown in Fig. 8. The same parameters like in the calculations have been used.

The simulated and the calculated relation of the output voltage on the input power differs. The reasons for this are the simplifications which are made at the calculations and that not all parameters of the harvester networks have been taken into account to reduce the complexity of the calculations. The simulation was performed with the so called harmonic balance method, which is a special version of the Galerkin method.

Fig. 9 shows the spectrum of the output voltage of the partial network V_0. The first harmonic has a magnitude of -47.85 dBV and the DC component has a magnitude of -6.373 dBV, which leads to a ripple factor of 0.6%. This shows that the neglection of the harmonics of the output voltage is suitable and does not influence the result significantly.

The value of the matching capacitor C_P has been chosen so that the input port voltage reflection coefficient of the harvester network has a minimum between the series resonance frequency (13.556 MHz) and the parallel resonance frequency (13.586 MHz) of the crystal resonator at an input power of 10 µW. The resonant frequencies have been calculated with the formulas (1) and (2).
The following figure shows the input port voltage reflection coefficient versus the frequency at an input power of 10 µW.

The above figure shows that the input port voltage reflection coefficient has a value of 1.3% at the operational frequency f_a.

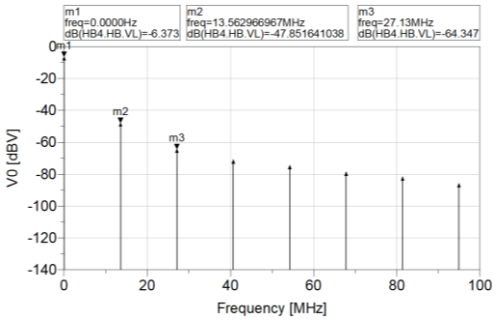

Fig. 9. Spectrum of the output voltage of the partial network V_0

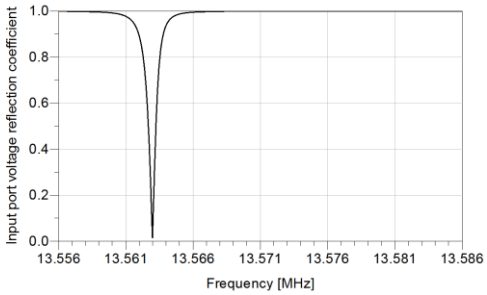

Fig. 10. Simulated voltage reflection coefficient versus frequency at an input power of 10 µW (high Q)

2.2. Low Q matching

By substituting the crystal resonator with an off-the-shelf inductor, the high Q harvester network (see Fig. 1) is changed as indicated in Fig. 11.

Due to the substitution of the crystal by an inductor, the equation (19) changes as follows:

$$I_0\left(\alpha \cdot \left|\frac{\sqrt{8 \cdot R_g \cdot P_{in}} \cdot \left(\frac{1}{j\omega C_P} + R_P\right)}{R_g + j\omega L_S + R_S + \frac{1}{j\omega C_P} + R_P}\right|\right) = \left(1 + \frac{\mu V_{out}}{2}\right) \cdot \exp\left(\frac{V_{out}}{2} \cdot \alpha \cdot \nu\right) \tag{20}$$

L_S represents the inductance of the matching inductor and R_S is the associated equivalent serial resistance. The component quality factor of the matching inductance, represented by the symbol Q_L, can be calculated with:

$$Q_L = \frac{\omega L_S}{R_S} \tag{21}$$

By optimizing with Advanced Design System with the goal to minimize the input port voltage reflection coefficient, the matching inductance results into a value of 8.6 µH and the matching capacitor leads to a value of 14.8 pF. For the coil a component

quality factor of 20 is assumed, which is a typical value for off-the-shelf inductors in the µH-range. By using equation (21), the equivalent series resistance of the matching inductor leads to a value of 37 Ω.

The simulated input port voltage reflection coefficient versus the frequency at an input power of 10 µW for the low Q matching circuit is shown in Fig. 12. The same parameters like in the high Q circuit have been used (except the matching component values) to ensure the comparability between the low Q and the high Q circuit.

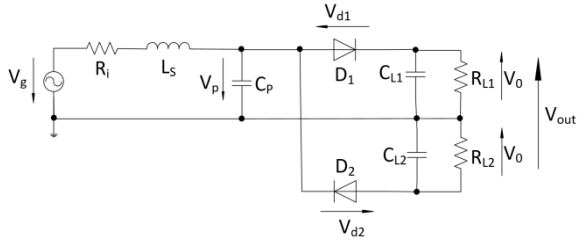

Fig. 11. RF energy harvesting circuit with Delon rectification (low Q)

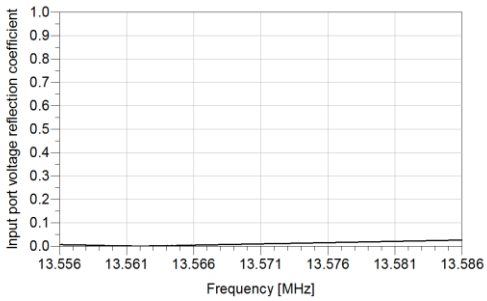

Fig. 12. Simulated voltage reflection coefficient versus frequency at an input power of 10 µW (low Q)

The above figure shows that the input port voltage reflection coefficient has a value of 0.14% at the operational frequency and the value remains quite constant between 13.556 MHz and 13.586 MHz.

The plot of the calculated output voltage of the low Q circuit in dependence on the input power, which is represented by equation (20), is visualized in Fig. 13.

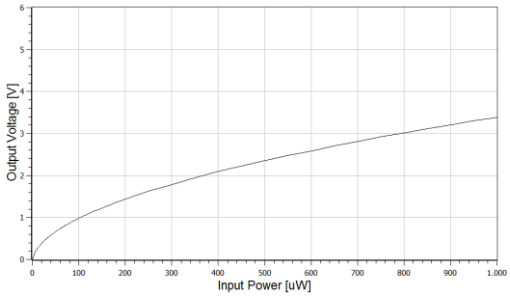

Fig. 13. Calculated output voltage versus input power (low Q)

The output voltage in dependence on the input power has been simulated for the low Q circuit. The simulation result is shown in Fig. 14.

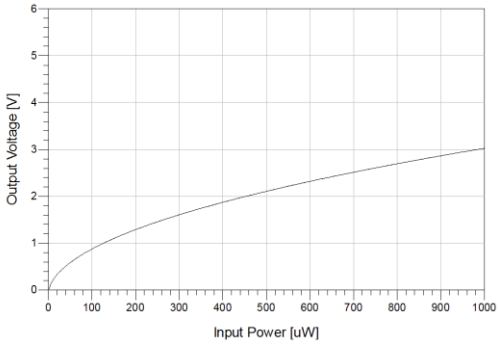

Fig. 14. Simulated output voltage versus input power (low Q)

The difference of the output voltage between the high Q and the low Q circuit (represented by the parameter dV) in dependence on the input power is plotted in Fig. 15.

The voltage difference increases with rising input power. At an input power of 1000 µW, the voltage difference has a value of 0.75 V. This indicates that the benefit of the usage of a high Q resonator as inductor in the matching circuit gets higher with increasing input power.

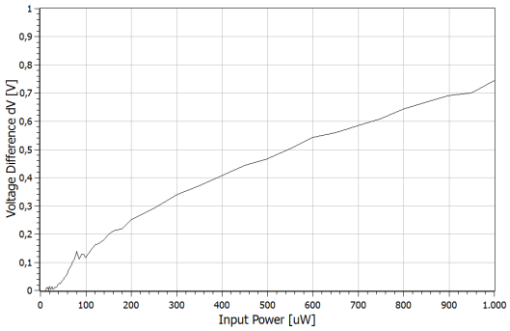

Fig. 15. Calculated voltage difference between high Q and low Q output voltage versus input power

3. Discussion

In this paper, an approximated solution of a nonlinear differential equation of second order has been found by using the Galerkin method. The nonlinear relation between the output voltage of the harvester and the input power has been plotted and simulated with a harmonic balance simulation using Keysight Advanced Design System.

The same calculations and simulations have been carried out for the low Q version of the harvester network. The usage of a high Q resonator as an inductor in the matching circuit has led to an increase of the output voltage of the harvester.

The difference of the output voltage of the high Q and low Q harvester increases with rising input power.

In the future, this phenomenon has to be examined for different matching points, for example at lower load resistances and higher input powers.

References

[1] Abramowitz M., Stegun I.: Handbook of Mathematical Functions. National Bureau of Standards, 1964.
[2] Avago Technologies: HSMS-282x Surface Mount RF Schottky Barrier Diodes. Data Sheet, 2009.
[3] Merz C., Kupris G.: High Q Impedance Matching for RF Energy Harvesting Applications. The 3rd IEEE International Symposium on Wireless Systems within the Conference on Intelligent Data Acquisition and Advanced Computing Systems, Offenburg, Germany, 2016.

M.Sc. Merz Christian
e-mail: christian.merz@th-deg.de

Mr. Merz has studied electrical engineering at the Deggendorf Institute of Technology. Currently he is a scientific researcher at the Deggendorf Institute of Technology in the field of energy harvesting, high Q impedance matching and nonlinear circuit analysis. He has published 11 papers about these topics.

Prof. Dr.-Ing. Kupris Gerald
e-mail: gerald.kupris@th-deg.de

Professor Kupris is the dean of the Faculty of Electrical Engineering, Media Technology and Computer Science at the Deggendorf Institute of Technology. He is researching on the field of internet of things, bluetooth low energy and energy harvesting.

otrzymano/received: 08.12.2017 *przyjęto do druku/accepted: 11.05.2018*